

Beam Position Monitor System for Proton-LINAC for FAIR

DISSERTATION
ZUR ERLANGUNG DES DOKTORGRADES
DER NATURWISSENSCHAFTEN

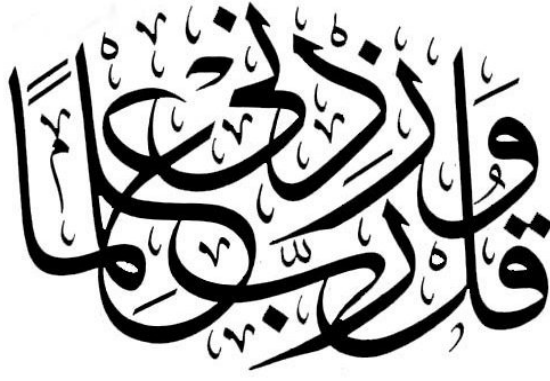


vorgelegt beim Fachbereich Physik
der Johann Wolfgang Goethe-Universität

von
Mohammed Heneen Almalki
aus Bani Malk, Saudi Arabia

Frankfurt am Main 2015

D30



My Lord, increase my knowledge

vom Fachbereich Physik

der Johann Wolfgang Goethe-Universität als Dissertation angenommen.

Dekan: Prof. Dr. Rene Reifarth

Erster Gutachter: Prof. Dr. Oliver Kester

Zweiter Gutachter: Prof. Dr. Holger Podlech

Datum der Disputation: --.2015

Dedication

This thesis is dedicated to the memory of my father, Heneen.

my dear mother, Matarh, for being my first teacher

and my lovely wife, Dalal, for her love, endless support and encouragement.

Zusammenfassung

- Motivation

Einer der wesentlichen Forschungsschwerpunkte des in Darmstadt geplanten Beschleunigerzentrums FAIR (Facility for Antiproton and Ion Research) ist die Physik mit Antiprotonen. Zur Erzeugung von Antiprotonen ist eine Protonenstrahl hoher Intensität vorgesehen, der von einem dedizierten Protonen-Linearbeschleuniger (LINAC) bereitgestellt werden wird. Dieser LINAC wird Protonen bei 70 MeV kinetischer Energie mit ~ 35 mA Strahlstrom liefern und mit einer Beschleunigungsfrequenz von 325 MHz betrieben werden. In solchen Beschleunigern ist die Messung der Strahlposition und des Strahlenergie mit hoher Präzision notwendig.

Strahlpositionsmonitore (BPMs) werden zur Bestimmung dreier wichtiger Strahlparameter eingesetzt. Dies sind der transversale Strahlschwerpunkt durch die Differenz der Signale zweier Elektroden, die Strahlenergie (genauer die mittlere Geschwindigkeit der Protonen) durch eine Time-Of-Flight-Methode (TOF) sowie der relative Strahlstrom aus der Summe der Signale der vier BPM Platten. Die Anforderungen an das System betragen 0,1 mm räumliche Auflösung für die transversal Positionsbestimmung und 8,5 ps (entsprechend 1° @ 325 MHz) für die Time-Of-Flight Messungen.

Wie in Abbildung (Figure 1) dargestellt werden die Strahlpositionsmonitore (BPMs) als nicht-strahlstörendes Diagnosegeräte entlang des Proton LINACs an 14 Stellen installiert. Passend zu den Einbauorten wurde das BPM System für Strahlrohrdurchmesser von 30 mm (neun Stellen) und 50 mm (fünf Stellen) optimiert, wobei der Energiebereich von 3 bis 70 MeV und die begrenzte Einbaulänge für die BPM Installation berücksichtigt wurde. Auf Grund der günstigen mechanische Realisierung und der kurzen Einbaulänge wurden so genannte kapazitive Button Pickup-Elektroden gewählt.

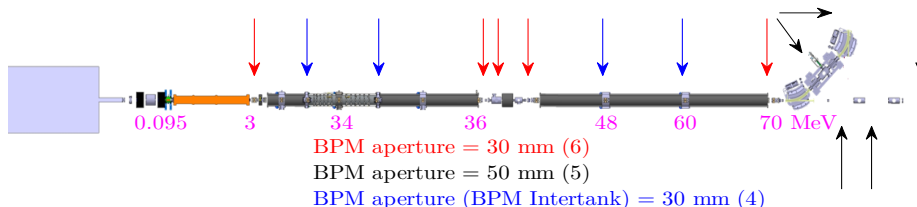


Figure 1: Der FAIR Protonen Linearbeschleuniger ist dargestellt mit den Einbauorten der 14 BPMs mit einem Strahlrohrdurchmesser von entweder $\text{\O} 30$ mm (neun Stellen) oder $\text{\O} 50$ mm (fünf Stellen). Vier BPMs werden in der Zwischentank-Sektion zwischen den Beschleunigungskavitat installiert. Weiterhin ist Strahlenergie an spezifischen Positionen angegeben.

- BPM Zwischentank-Sektion

An vier Stellen bilden die BPMs innerhalb eines evakuierten Gehäuses zusammen mit den magnetischen Triplett-Linsen einen integralen Bestandteil der Zwischentank-Sektionen zwischen den CCH- oder CH-Kavitäten, siehe Abbildung (Figure 2, links). Die begrenzte Einbaulänge erlaubt nur 62 mm Abstand zwischen der CCH-Kavität und dem Gehäuse der Triplett-Magnete, so dass die Mitte des BPMs nur einen Abstand von 48 mm von dem Ende der Kavität aufweist. Numerische Simulationen wurden durchgeführt um die aus der Kavität austretende Hochfrequenzamplitude (HF) abzuschätzen sowie um die HF Abschirmeigenschaften zu bestimmen. Das Ergebnis ist in Abbildung (Figure 2, rechts) dargestellt. Mit einer Länge des Kegels und des Rohrs von jeweils 20 mm wurde das Störsignal der Pickup-Elektrode auf 10 mV Amplitude reduziert. Dieser Wert ist zufriedenstellend im Vergleich zur Signalspannung von ~ 1 V für den nominalen Strahlstrom von 35 mA.

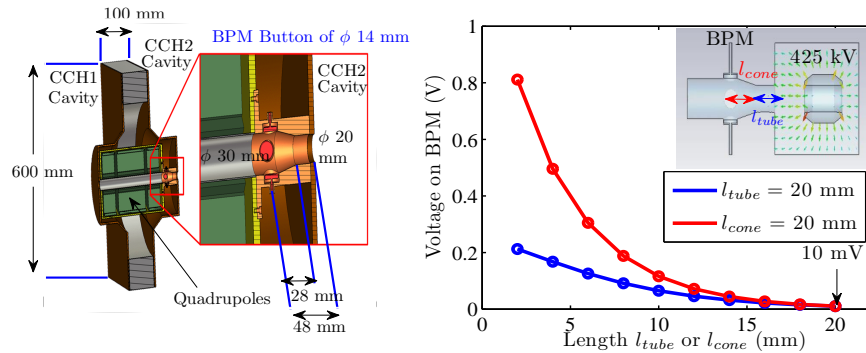


Figure 2: Links: Das technische Layout der Zwischentank-Sektion. Rechts: Berechnung der Abschirmeigenschaften in Abhängigkeit von der Länge des Kegels (rot) für eine festgehaltene Länge des Rohres sowie in Abhängigkeit der zylindrischen Rohrlänge (blau) für feste Kegellänge. Für die Berechnungen mit dem CST elektro-statischen Solver wurde die erste Driftröhre innerhalb der Kavität auf eine Spannung von 425 kV gelegt.

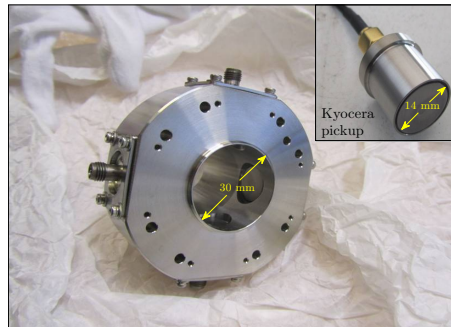


Figure 3: Der erste Prototyp der BPM Installation für die Zwischentank-Sektion mit vier Button-Elektroden.

Der erste Prototyp der BPM Mechanik für eine Intertank-Sektion mit dem Strahlrohrdurchmesser von \varnothing 30 mm wurde hergestellt. In Abbildung (Figure 3) ist der BPM Prototyp bestehend aus vier Pickup-Elektroden von \varnothing 14 mm, produziert von der Firma Kyocera, in einem Edelstahlgehäuse gezeigt. Dieser Prototyp wird für BPM Tests mit einem Draht in coaxialer Anordnung bei CEA/Saclay und für die Messungen des HF-Störsignals an dem Prototyp der CCH-Kavität bei GSI eingesetzt werden.

- Numerische Simulation mit CST STUDIO SUITE

Detaillierte Simulationen der BPM Designparameter wurden mit dem Simulationsprogramm CST durchgeführt. Der CST ELECTROMAGNETIC STUDIO - Solver wurde benutzt um die Kapazität der Pickup-Elektroden als Funktion der Dicke der Elektrode sowie des Abstands zwischen Elektrode und Schirm zu berechnen. Die elektrischen Eigenschaften des Pickup-Design, insbesondere die Impedanzanpassung an die koaxiale Signalleitung, wurden durch den CST MICROWAVE STUDIO Solver durch Auswertung der zeitabhängigen Refraktometrie (TDR) untersucht. Die Simulation zur Pickup-Optimierung hat gezeigt, dass gegenüber dem ursprünglichen Design von Kyocera ein größerer Abstand zwischen Elektrode und Schirm und eine geringe Dicke der Elektrode erforderlich sind, um die Störung der Signalausbreitung zu reduzieren und damit das Verhalten des Pickups zu verbessern.

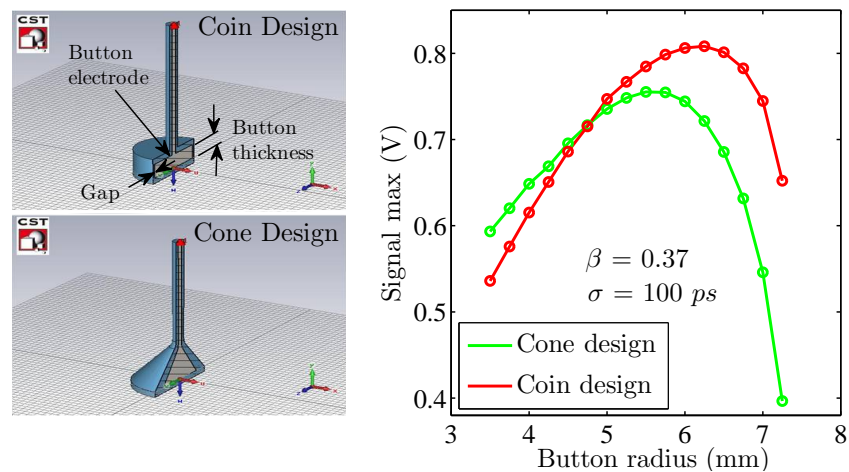


Figure 4: Die Optimierung des so genannten Münz- und Kegel-Designs mit dem CST PARTICLE STUDIO zeigt, dass die höchsten Signale mit einem Münze Radius von 6,25 mm (Button Dicke = 0,5 mm) und einem Kegel Radius von 5,5 mm erzeugt werden.

Der Wakefield Solver in CST PARTICLE STUDIO wurde verwendet, um die Signalform des BPMs für verschiedene Geometrien und verschiedene Strahlparameter zu untersuchen. Die Anregungsquelle wird durch eine Gauß-förmige longitudinale Ladungs-

verteilung mit variabler Länge σ_{bunch} in Flugrichtung und einer Ladung von 1 nC definiert. Die zeitabhängigen Signale und deren Frequenzspektren wurden extrahiert und verglichen. Ein sogenanntes Münz- und ein Kegel-Design, deren Einbaulänge 15 mm beträgt, wurden durch die Variation des Durchmessers der Pickup-Elektrode optimiert. Abbildung (Figure 4) zeigt die Optimierungskurven für das Münz- und das Kegel-Design. Das maximale Signal für das Münz-Design wurde bei einem Radius von 6,25 mm und für das Kegel-Design bei einem Radius von 5,5 mm erhalten. Basierend auf der Simulation wurde festgelegt, die Pickup-Elektrode in Münzenform (0,5 mm Dicke, 5,5 mm Radius und 1,5 mm Abstand) zu verwenden.

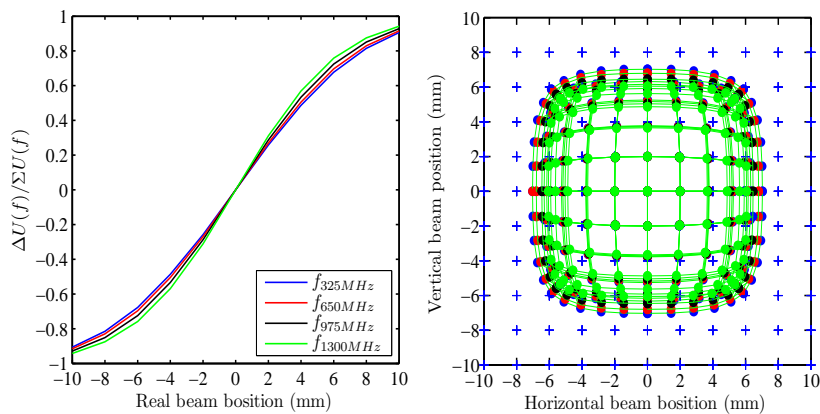


Figure 5: Links: Vertikale Strahlpositionskurven unter Verwendung des Differenz-durch-Summe-Verfahrens bei unterschiedlichen Auswertefrequenzen mit $\beta = 0,27$ für eine Bunchlänge von $\sigma_{bunch} = 150$ ps. Rechts: Die BPM Positionskarte.

Ausführliche CST-Simulationen wurden durchgeführt um die Signalveränderungen in Bezug auf unterschiedliche Bunchlängen, Pickuptiefen in Bezug auf die Wand des Strahlrohrs, Buttongrößen und Strahlrohrdurchmesser zu bestimmen. Die BPM Positionsempfindlichkeit, die BPM Positionskarte und die Änderung der Strahlphase in Abhängigkeit von der Strahlposition wurden damit systematisch untersucht. Diese Simulationen sind auch nützlich für die Auslegung der analogen Bandbreite der weiteren Signalverarbeitung. Die Ergebnisse aus den Rechnungen mit Variation der Bunchlängen zeigen eine lineare Beziehung zwischen der Signallänge und der Bunchlänge ab eines von der Strahlenergie abhängigen Grenzwertes. Unterhalb dieses zeitliche Wertes bleibt das Signal im Wesentlichen konstant. Außerdem zeigen die Simulationen, dass im Frequenzband der zweiten Harmonischen der Beschleunigungsfrequenz eine ausreichende Signalstärke in den Spektren vorhanden ist.

Die Empfindlichkeitskurven für die Positionsmessung und die Positionskarten wurden für jeweils vier Harmonische der Beschleunigungsfrequenz bei $\beta = 0,08; 0,27$ und $0,37$ erstellt. In Abbildung (Figure 5) sind als Beispiel die Empfindlichkeitskurven und Positionskarten für die vier Harmonischen bei $\beta = 0,27$ dargestellt. Die Phase der Signale als Funktion der Strahlposition wurden durch eine Verschiebung entlang der vertikalen Achse und entlang einer diagonalen Linie untersucht. Die Ergebnisse zeigen, dass die Variation der Strahlphase in dem interessierenden Bereich des BPM von ± 6 mm unter $0,1^\circ$ liegt.

- BPM Elektronik und Signalverarbeitung

Ein strahlbasierter Test wurde am GSI UNILAC durchgeführt, um die prinzipielle Eignung des vorgesehenen Libera SPH Elektroniksystems der Firma Intrumentation Technology [1] für die Strahlpositions- und Phasenmessungen zu untersuchen. Die Libera SPH beinhaltet einen hochauflösenden ADC (16 bit nominal) und wendet die Technik des so genannten "Under-sampling" mit einer Abtastrate von 117,4 MSa/s an. Die Strahlposition, die Strahlenergie and der relativer Strahlstrom wird mit Hilfe einer FPGA-basierten Digitalelektronik berechnet. Das Experiment wurde unter Verwendung eines Ca^{10+} Strahls aus dem Hochladungsinjektor (HLI) mit einer Energie von 1,4 MeV/u bei einer Beschleunigungsfrequenz von 108,408 MHz durchgeführt. Die optischen Elemente der Strahlführung erlauben es, die Strahlposition durch Variation eines Dipols sowie die Bunchform durch Variation eines Debunchers zu verändern.

Zunächst wurde für die Libera SPH die Auflösung bezüglich der Strahlposition und Strahlphase getestet. Die Ergebnisse zeigen stabile Werte für Positionsmessungen vor allem bei großen Signalamplituden mit einer Standardabweichung von $\sigma_x \sim 50 \mu m$; damit ist die Systemanforderung erfüllt. Die Ergebnisse der Phasenmessungen zeigen, dass deren Auflösung amplitudenabhängig ist und nur für einige Signalformen und Signalstärken die notwendige Standardabweichung von weniger als 1° erreicht wird.

Anschließend wurde die Genauigkeit der Phasenmessung durch die Untersuchung der Phasenkorrelation zwischen Libera SPH und andere Methoden, im speziellen im Zeitbereich durch Berechnung des Nulldurchgangs des Signals, durch Fourier-Transformation des Signals und Phasenauswertung, sowie durch I/Q Demodulation, bestimmt. Ein einzelner BPM wurde als sogenannter Bunch-Ankunftsmonitor verwendet und die Phasenabhängigkeit anhand von sechs Strahlen mit unterschiedlichen Bunchformen getestet. Im Zeitbereich wurden die Daten mit einem 10 GSa/s Oszilloskop (LeCroy Waverunner 6200A) aufgenommen. Wie in Abbildung (Figure 6) gezeigt, bestehen zwischen den

verschiedenen Methoden eine klare Korrelation, wobei aber die Libera SPH Phasenmessungen große Fluktuationen aufweist. Die Ergebnisse zeigen, dass die vorgesehene Elektronik der Libera SPH vielversprechend ist, obwohl bisher die Anforderungen noch nicht vollständig erfüllt sind. Einige Änderungen der Elektronik könnten zu der gewünschte Genauigkeit führen; dies ist dann durch weitere Untersuchungen zu bestätigen.

Abschließend wurde die mit der Libera SPH erreichbare Genauigkeit für die Messung der Strahlposition durch den Vergleich mit dem Strahlprofil aus der Messung mit einem Sekundärelektronen Monitor (SEM) Profiltgitter für verschiedene Strahlparameter untersucht. Die Ergebnisse zeigen, dass die digitale Elektronik der Libera SPH für die Strahlpositionsbestimmung geeignet ist.

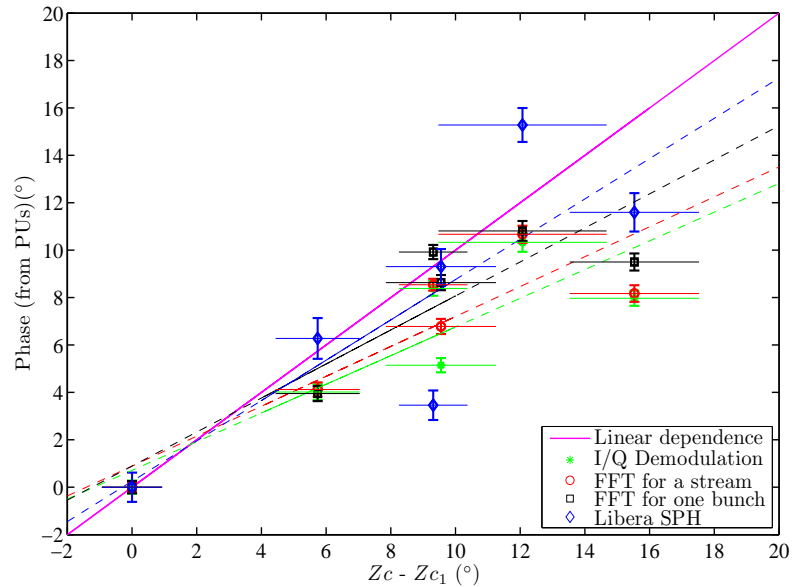


Figure 6: Darstellung der Signalphasenmessung für verschiedene Bunchformen. Dargestellt ist auf der y-Achse die Phasenmessung mit der Libera SPH, die Phase der Fourier-Transformation für einen einzelnen Bunch und für eine Folge von Bunchen, sowie die Phase mit Hilfe der I/Q-Demodulation als Funktion der im Zeitbereich aufgezeichneten Bunche charakterisiert durch den jeweiligen Nulldurchgang $Z_c - Z_{c_1}$ (Bunchform 1 dient als Referenz).

Contents

angenommen	i
Dedication	iii
Zusammenfassung	v
1 Introduction	2
1.1 Motivations	2
1.2 Thesis Structure	3
1.3 GSI and FAIR: An Overview	4
1.3.1 The GSI Facility	4
1.3.2 The Future FAIR Project	6
1.3.3 The FAIR Proton LINAC Injector	7
2 RF Linear Accelerators	12
2.1 General Parameters	12
2.2 Cavity Design of Linear Accelerators	15
2.3 Beam Dynamics in Linear Accelerators	18
2.3.1 Transversal Beam Dynamics	18
2.3.2 Longitudinal Beam Dynamics	19
2.3.3 KONUS Beam Dynamics	21

2.4	Radio Frequency Quadrupole (RFQ)	23
2.5	The FAIR Proton Linac Injector : Design and Main Parameters	24
2.5.1	Beam Diagnostics System of the FAIR Proton Linac	27
3	Beam Position Monitors (BPMs)	30
3.1	Principle and Sensing Mechanism	30
3.2	Signal Treatment and Estimation	33
3.3	Signal Analysis Using the Discrete Fourier Transform	35
3.4	Transverse Beam Position Determination	37
3.5	The Time-of-flight (TOF) and Beam Energy Determination	38
4	The BPM System for the FAIR Proton Linac	42
4.1	Specifications and Main Parameters	42
4.2	Beam Properties at BPM Locations	44
4.3	The BPM Intertank Section	50
4.3.1	RF-Leakage Calculations	50
4.3.2	The BPM intertank Prototype : Design and Fabrication	55
5	BPMs Numerical Simulation with CST STUDIO SUITE	60
5.1	Problem Statement	61
5.2	Pickup Simulations	61
5.2.1	Pickup Capacitance	62
5.2.2	Pickup Electrical Properties	63
5.3	BPM Response Investigations	68
5.4	Button Design Investigations	71
5.5	BPM Optimizations	75
5.6	Button Depth and Size Investigations	79

5.7	Bunch Length Investigations	82
5.8	BPM Sensitivity, Linearity and Map	88
5.9	Signal Phase Investigation	92
6	BPM Electronic and Signal Processing	96
6.1	Motivations	96
6.2	Signal Processing Methods	97
6.3	Amplitude and Phase Detection in BPM Digital Systems	99
6.3.1	The Sampling Theorem	99
6.3.2	Phasor Representation of RF Signal	100
6.3.3	I/Q modulation and Digital Down Conversion (DDC)	101
6.3.4	I/Q Demodulation	104
6.3.5	Libera SPH Digital Electronics for Proton LINAC	105
6.4	Experimental Setup	107
6.4.1	Libera SPH Data Evaluation	110
6.5	Test of Libera SPH Resolution	112
6.5.1	Position Measurements	112
6.5.2	Phase Measurements	113
6.6	Beam Phase Evaluation by Different Methods	114
6.6.1	Libera SPH Phase Evaluation	116
6.6.2	FFT Analytical Approach	117
6.6.3	<i>I/Q</i> Demodulation method	120
6.6.4	Time Domain Evaluation	121
6.6.5	Data Evaluation and Results	127
6.7	Beam Position Evaluation	129
7	Summary and Outlook	132

7.0.1	Summary	132
7.0.2	Outlook	135
8	Appendix	138
9	Bibliography	144
	List of Figures	154
	List of Tables	168
	Acknowledgements	170

Introduction

1.1 Motivations

The research in this thesis is motivated by the planned accelerator center Facility for Antiproton and Ion Research (FAIR). A major part of the experimental program at FAIR is dedicated to antiproton physics which requires a high intensity proton beam. The primary proton beam needed for anti-proton production chain will be supplied by a proton linac injector. The proton linac will deliver a ~ 35 mA proton beam accelerated up to 70 MeV with an operating frequency of 325 MHz. In such a dedicated accelerator, a high precision and a high resolution beam position and beam energy system is essential.

This work focuses on building a reliable beam position monitor (BPM) system for the FAIR proton linac injector. The BPM system will serve for beam position determination and for beam energy from the Time-of-flight (TOF) method. The system's specifications are 0.1 mm spatial resolution for the transverse beam position determination and 8.5 ps for the time-of-flight measurements which corresponds to a phase difference of 1° with respect to the accelerating frequency of 325 MHz.

The Beam Position Monitors (BPMs) as non-destructive devices will be installed at 14 locations along the proton linac. They will measure three beam quantities, namely the beam displacement, the mean beam energy and the relative beam current. The main objectives of this work can be classified in three divisions. The first objective is to perform detailed simulations for BPM design parameters with the finite element code CST. The second is the mechanical design and realization of the BPM intertank section and the production of the first BPM prototype. The third objective is to introduce and develop a novel digital signal processing system for beam position and beam phase determination.

1.2 Thesis Structure

This thesis is structured into 5 chapters:

- Chapter 1 gives an overview about the GSI facility and its main components. It discusses briefly the FAIR project and the milestone of its scientific programs.
- Chapter 2 is a revision of some important concepts in RF linear accelerators such as cavity design, electromagnetic fields distribution and beam dynamic. The last section focusses on the proton linac injector layout and discusses its main parameters and some design aspects.
- Chapter 3 reviews the basic principles of BPMs as described in standard references and papers and discusses some important definitions and concepts related to the BPMs sensing mechanism and signal estimation. The transverse beam position determination and beam energy calculations from the Time-of-flight (TOF) are described. Most of the theory within this chapter is well known and it is presented to be used in subsequent chapters.
- Chapter 4 introduces the layout and the main parameters of the BPM System for the proton linac and the particle distribution at the BPMs along the proton linac as well as the calculation as the beam is drifted. Next, the BPM intertank section case where the BPM has to be inserted between the CCH and CH cavities within an evacuated housing and the related calculations of the rf-leakage generated by cavity excitation are discussed. The mechanical design and the fabrication of the first prototype of the BPM intertank section are presented.
- Chapter 5 is dedicated to CST simulations (CST EM STUDIO, CST MICROWAVE STUDIO and CST PARTICLE STUDIO) for the button pickup BPM. These simulations include Time Domain Refractometry (TDR) measurements, impedance matching characteristics, pickup capacitance, time and frequency-domain response of the BPM output signals reflects the BPM's interaction with the beam, non-linearity, sensitivity and position map. The results of these simulations and the BPM performance with different geometries and with varying beam parameters are presented.
- Chapter 6 discusses digital signal processing of the BPM system. The detection algorithm of amplitude and phase in digital systems are discussed. The experimental setup and the results of the beam-based test at UNILAC for beam position and phase using Libera SPH electronic are presented.

1.3 GSI and FAIR: An Overview

1.3.1 The GSI Facility

The GSI Helmholtzzentrum für Schwerionenforschung (Helmholtz center for heavy ion research) is a facility for fundamental research with ion beams. It was founded in 1969 as the Society for Heavy Ion Research (Gesellschaft für Schwerionenforschung) and funded by the Federal Republic of Germany and the state of Hessen. It performs various basic and applied researches in physics such as plasma physics, atomic physics, nuclear structure and reactions research, biophysics and medical research and accelerator development [2,3]. The GSI complex comprises the Universal Linear Accelerator (UNILAC) commissioned in 1975 and the heavy ion synchrotron (Schwerionensynchrotron) (SIS18), the Experimental Storage Ring (ESR), the FRagment Separator (FRS), the Petawatt High-Energy Laser for Heavy Ion EXperiments (PHELIX) as well as several systems of spectrometers, detectors and medical irradiation units for cancer therapy.

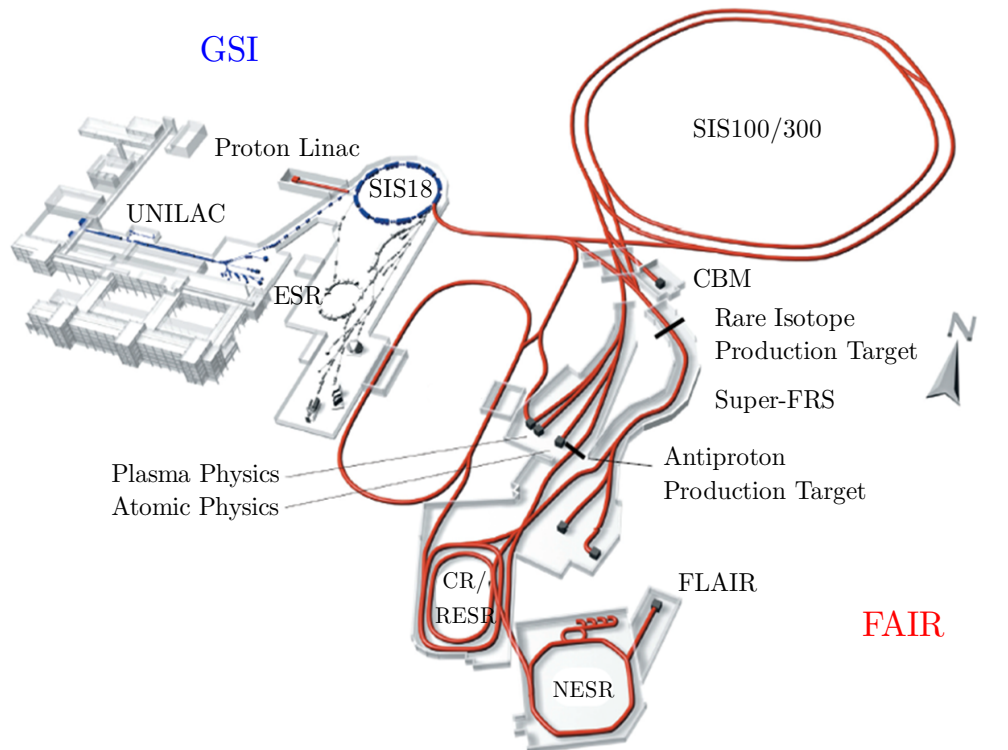


Figure 1.1: Layout of the existing GSI facility (UNILAC, SIS18, ESR) on the left and the planned FAIR facility on the right (proton linac, SIS100 and SIS300, CR, RESR, NESR, the rare isotope production target, Super-FRS, the antiproton production target, HESR, FLAIR and the experimental stations for plasma physics and atomic physics)

The three main components of the present GSI facility are the UNILAC, SIS18 and ESR as schematically shown in figure 1.1. The UNILAC [4,5] can deliver all types of ion beams from hydrogen to uranium with energies up to 11.4 MeV/u. The final energy of the beam is determined based on the charge state and ion species. It was designed to accelerate all ion species with mass over charge ratios of up to 8.5 ($m/z < 8.5$). Various ion sources are constructed, namely CHORDIS/MUCIS/MEVVA/VARIS [6] to feed the UNILAC with different types of ion species. The first acceleration stage for the ions is accomplished by the high current injector (HSI) [4] to reach an energy up to ~ 1.4 MeV/u. The HSI accelerating structure consists of a radio-frequency quadrupole (RFQ) and two Interdigital H-type drift tube structures (IH) operating with a frequency of 36 MHz. The HSI is followed by a stripping section where the charge state of the ions is increased. After the stripping section, a High Charge State Injector (HLI) [7] is coupled with the UNILAC delivering in parallel highly charged ion beams with an energy of 1.4 MeV/u. The HLI is equipped with an ECR (Electron cyclotron resonance) ion source, RFQ and an IH structure. In the second stage, the ions are further accelerated up to an energy of 11.4 MeV/u by Alvarez DTL poststripper operating at 108 MHz. Then, the ions are injected by slow extraction to the low-energy Experimental Hall (EH). In the EH some experiments are directly performed such as the production of super-heavy elements and the examination of exotic nuclei in traps. Otherwise, the beam is directed by fast extraction into the transfer channel (TK) to be finally fed into the SIS18.

The SIS18 has a circumference of 216.72 m with a maximum magnetic rigidity of 18 Tm. The upgraded SIS18 will serve as boosters for the FAIR's new synchrotron (SIS100). The technical parameters of SIS18 can be found in [8]. The ions are accelerated to an adjustable energy based on their mass-to-charge ratio. The SIS18 is equipped with two radio frequency cavities. They are used to accelerate ions to a maximum energy of 1 GeV/u for U^{73+} ions and 4.5 GeV for protons. The beam is then extracted and transported to the ESR. The ESR [9] is the third major infrastructure at the GSI. It has two arcs and two straight sections and a circumference of 108.36 m. Inside the ring many detectors, particle counters and experiment specific targets are installed. It features a high quality vacuum, an electron cooler [10] and a stochastic cooler [11]. Many experiments are conducted in very unique conditions where the beam is cooled and stored over long time periods. The goals of these experiments are mainly the investigation of atoms, complex nuclei, elementary particles and the forces acting between them, matter under extreme heat and pressure, and the synthesis of the elements in stars.

1.3.2 The Future FAIR Project

The international Facility for Antiproton and Ion Research (FAIR) facility was founded in 2010 as an extension to the existing GSI facility [12–14](see figure 1.1). It aims to match the demand from the scientific community for higher beam energy and intensity which is beyond the capabilities of the GSI facility. Currently it is under construction [15, 16]. The new facility FAIR will host a proton linac injector, upgraded UNILAC, several storage rings, beam targets and many detectors. FAIR will enable a wide range of new opportunities for scientists to perform more advanced experiments in various research areas. Moreover, it opens new frontiers for answering many unsolved questions in fundamental physics concerning the structure of matter and the evolution of the universe.

A superconducting double-synchrotron, the SIS 100/300, is the essential part of the FAIR facility [17]. It has a circumference of 1083 m and designed for a magnetic rigidity of 100/300 Tm as indicated by the name. A new high current proton LINAC and the upgraded UNILAC [18] will serve as ion injectors providing proton and heavy ion beams with unprecedented intensity and luminosity. The SIS18 synchrotron in the existing GSI facility will be upgraded to accommodate such high beam energy and intensity to function as a booster for the FAIR accelerator complex. A unique infrastructure and experimental sites will be available for nuclear- atomic-, astrophysics and high density plasma physics opening new fields in research. The parallel operation is one of the essential features of the FAIR facility which allows the users to accelerate different ions species and run up to four scientific programs at the same time [19]. The general scientific objectives can be grouped into four fields [12, 14]:

- 1- physics with high energy antiprotons (Anti-Proton Annihilation at Darmstadt - PANDA).
- 2- physics of radioactive nuclei and nuclear matter physics (Compressed Baryonic Matter - CBM).
- 3- Nuclear Structure, Astrophysics and Reactions (NuSTAR).
- 4- Atomic, Plasma Physics and Applications (APPA).

1.3.3 The FAIR Proton LINAC Injector

There was a significant activity in the development of LINAC during the last 20 years to investigate the capability of this type of accelerators to deliver high intensity, high duty factor, proton and ion beams. This was triggered by the demand from nuclear, material, and biological sciences for neutron beams with energy and time spectra different from that available by power plants. Many LINAC designs have been proposed and developed such as SNS [20], ESS [21], FRIB [22], FRANZ [23], EUROTRANS [24], IFMIF [25], JPARC [26] and at CERN (LINAC4 [27]). The LEDA machine [28] at Los Alamos demonstrated the first successful test which showed the possibility to accelerate a 100 mA proton beam at a frequency of ~ 350 MHz. The most actual projects based on a high intensity proton injector are FAIR (Germany), SNS at ORNL (USA), CERN LINAC4 (Switzerland), JPARC (Japan) and ESS (Sweden).

The SNS is the first spallation neutron source driven by a LINAC instead of a synchrotron or by a cyclotron. It consists of a LINAC, an accumulator ring and a high power target station to perform materials and biological research. The LINAC begins with room temperature Drift tube LINAC (DTL) and coupled-cavity LINAC (CCL) operating at two different frequencies (402.5 & 805 MHz) to accelerate the beam up to 187 MeV [20]. Subsequently, the superconducting LINAC (SCL) consists of 11 medium- β cryomodels ($\beta = 0.61$) and 12 high- β cryomodels ($\beta = 0.82$) to provide the final beam energy of 968 MeV. The beam is collected into the accumulator ring and then injected into the liquid mercury target station.

The LINAC4 at CERN [27] comprises a DTL, a CCL and a Side Coupled LINAC (SCL) while the operating frequency is switched from 352 to 704 MHz. The proton beam is extracted at 95 keV from the source and then accelerated by a 4-vane RFQ to 3 MeV to 3 DTL cavities which bring the beam energy to 40 MeV. After the DTL the beam is accelerated to 90 MeV by 8 CCL modules. The beam then passes into the 704 MHz SCL for the final acceleration up to 160 MeV.

The JPARC is a multi purposes facility consists of a LINAC, a 3 GeV rapid cycling synchrotron and a 50 GeV synchrotron [26]. The ion source delivers 50 keV proton beam which is further accelerated by an RFQ structure to energy of 3 MeV. The main LINAC of 324 MHz accelerates the beam to the final energy of 181 MeV. Four experimental areas are foreseen which are nuclear waste transmutation, materials and life science, hadron beam physics and neutrino generation.

The ESS is a high current proton LINAC delivers an average power of 5 MW to the target in the nominal design [21]. An ECR source produces a macro-pulses of up to 2 ms in length and currents of up to 62 mA. A 4-vane RFQ resonates at 352.2 MHz will increase the beam energy from 75 keV to 3 MeV. The DTL works at the same frequency as the RFQ, accelerating the proton beam from 3 MeV to 50 MeV in three tanks. A half wave Superconducting Spoke Resonators will be used in the acceleration section after the DTL from 50 MeV to 200 MeV [1]. The superconducting elliptical cavities operate at 704.4 MHz will be used with medium β cavities accelerating from 200 MeV to 500 MeV and high β cavities from 500 MeV to 2500 MeV.

The antiproton physics program at FAIR demands a primary proton beam which is much beyond the capabilities of the existing UNILAC. For this reason a dedicated proton LINAC has to be used as injector into the SIS 18/100 synchrotrons. An ECR source delivers up to 100 mA proton beam which is accelerated by an RFQ up to energy of 3 MeV. The main LINAC is based on CH-type cavities which accelerate the beam to 70 MeV. The design and the main parameters of the FAIR proton linac are presented in chapter 2 of this thesis. Table 1.1 summarizes and compares the main features of the above described facilities characterized by a high intensity of the beam, in the order of 10^{12} proton per pulse. The FAIR proton injector is the only LINAC based on a single structure.

Table 1.1: A comparison between some of the most recent worldwide LINAC accelerators

Parameter	FAIR	CERN	SNS	JPARC	ESS
Output energy [MeV]	70	160	968	181	2500
Peak current [mA]	35	40	38	30	62
Proton per pulse [10^{12}]	7.8	100	9.3	93	200
Frequency [MHz]	325	352 - 704	402.5 - 805	325 - 975	352.2 - 704.4
Beam pulse length [μs]	36	160	1000	500	2000

At FAIR it is planned to produce the antiprotons in a collision of a bunch of 29 GeV protons with a target. A primary proton beam is produced by proton LINAC injector with 2×10^{16} protons per hour and an energy of 70 MeV [29]. The proton beam is transported to SIS18 for further acceleration before it is injected into SIS100 where the final acceleration stage is achieved to reach a maximum energy of 29 GeV. The beam

is then extracted and bombarded at a metal target to produce an intense anti-proton \bar{p} beam. The anti-protons beam is collected, accumulated and cooled in the Collector Ring (CR) and the accumulator / decelerator ring RESR before it is transferred either to the New Experimental Storage Ring (NESR) or to the High Energy Storage Ring (HESR) for the experiments. The HESR and the NESR will be equipped with both stochastic and electron cooling to provide high luminosity and high resolution beams. The HESR hosts the PANDA detector which is one of the key experiments at the FAIR experiment. The scientific programme of PANDA covers charmonium spectroscopy, search for gluonic excitations, open charm spectroscopy, hypernuclear and electroweak physics, and electromagnetic processes.

RF Linear Accelerators

2.1 General Parameters

A linear accelerator (LINAC) is a type of particle accelerator in which charged particles acquire energy moving on a linear path by applying an electric field. In radio frequency (RF) linacs the acceleration up to the required final energy is provided by time-varying electric fields [30–32]. The beam is delivered from the source at a given length τ and a repetition frequency f . The product of these quantities gives the beam duty cycle which is a key design of any accelerating machine.

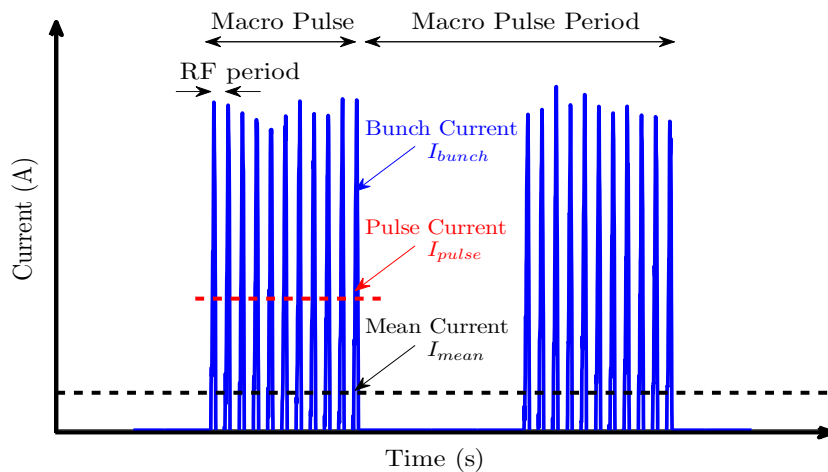


Figure 2.1: The time structure of the beam at a pulsed linac and the definition of different currents (according to [33]).

The beam current in pulsed linac can be characterized by three definitions, the mean current I_{mean} , the pulse current I_{pulse} and the bunch current I_{bunch} [33]. The mean current is the current averaged over the full RF macropulse including both the macropulse time

and the time between the macropulses. The pulse current is the value averaged over the RF macropulse. The bunch current (micro pulse) refers to the number of particles per bunch ($I = qNf$). A typical time structure of a pulsed linac is shown in figure 2.1.

The drift tube RF linear accelerator is made of a sequence of resonating cavities of variable length. Each cavity consists of a series of drift tubes separated by accelerating gaps. A longitudinal electric field used for particles acceleration can be generated in the gaps by an rf-field. As the field is reversed, the particles are shielded inside the drift tubes. **The Electric Field** E_z generated on z axis between two gaps can be written as [30]

$$E_z = E(0, z)\cos(\omega t(z) + \phi) \quad (2.1)$$

where $t(z) = \int_0^z dz/v$ is the traveling time taken by a particle with velocity v to reach position z . Figure 2.2 illustrates an accelerating gap of length g and its on axis electric field distribution. The field distribution is confined within $\pm L/2$ where L is the gap effective length and a is the drift aperture. Assuming that the particle with charge q

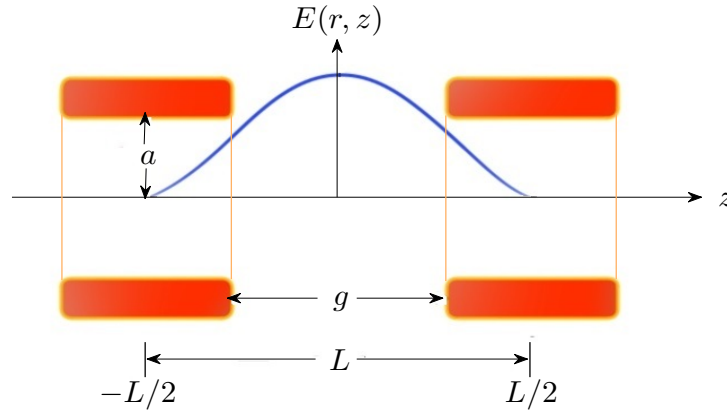


Figure 2.2: Schematic of the axial electric field $E_z(r, z)$ in an accelerating gap

reaches the the gap center at $t = 0$ with phase ϕ with respect to the field crest. **The Total Energy** gained as the particle crosses the gap is [30]

$$\Delta W = q \int_{-L/2}^{L/2} E(0, z)\cos[\omega t(z) + \phi]dz = qV_0T \cos(\phi) \quad (2.2)$$

where $V_0 = \int_{-L/2}^{L/2} E(0, z)dz$ is the RF axial voltage and T is the **Transit Time Factor** [30]. The **Transit Time Factor** gives the reduction in energy gain caused by the sinusoidal variation of the electric field with respect to a DC voltage of amplitude V_0 which is defined as [30]

$$T = \frac{\int_{-L/2}^{L/2} E_0\cos\omega t(z)dz}{\int_{-L/2}^{L/2} E_0(z)dz} \quad (2.3)$$

The electrical power transferred to the particle beam during the acceleration process in all accelerating cavities defines the total beam power P . In each cavity the current I_{beam} times the voltage V_{eff} gives the RF power absorbed by the beam. The **Total Beam Power** produced by a linac can also be expressed as [32]

$$P = \sum V_{eff} \cdot I_{beam} \cdot duty\ cycle \quad (2.4)$$

where V_{eff} is the effective voltage (corrected with the transit time factor on the cavity gaps) seen by the beam in all the RF cavities.

One important quantity to estimate the quality of the resonator is called the **Quality Factor** (Q – *value*) determined by the bandwidth of the resonance frequency at -3 dB from the maximum value $Q = f_0/\Delta f(-3dB)$. It can be expressed also in terms of the ratio between the stored energy W and the dissipated RF power P in the cavity at the resonance frequency as $Q = \omega W/P$, where ω is the angular resonance frequency.

Another important parameter of a room temperature cavity is the **Shunt Impedance per Unit Length** Z . It measures the capability of a cavity with length l to produce an axial voltage V_0 for a given dissipation power expressed in $M\Omega/m$ as

$$Z = \frac{(\int_0^l E(0, z) dz)^2}{P \cdot l} \quad (2.5)$$

Maximizing the energy gain per the dissipated power is an important purpose for the accelerating cavity design. Therefore, the efficiency of a linac is calculated by the **Effective Shunt Impedance per Unit Length** Z_{eff} from the shunt impedance and the Transit Time Factor T as

$$Z_{eff} = Z T^2 \cdot \cos^2(\bar{\phi}) \quad (2.6)$$

where $\bar{\phi}$ is the averaged accelerating RF phase inside the cavity. Moreover, the ratio of Effective Shunt Impedance to the quality factor Z_{eff}/Q indicates the capability of the resonator to concentrate the electric field in the acceleration region expressed as

$$\frac{Z_{eff}}{Q} = \frac{(\int_0^l E(0, z) dz \cdot T)^2}{\omega W} \quad (2.7)$$

The ratio Z_{eff}/Q measures the accelerating efficiency per stored energy at a given frequency [30].

2.2 Cavity Design of Linear Accelerators

The field patterns in the accelerating cavities are classified based on the configuration of the RF magnetic and electric fields, namely Transverse Electric (TE), Transverse Magnetic (TM) and Transverse ElectroMagnetic (TEM) modes. The name of the mode indicates which transverse fields oscillates on the direction of propagation.

The distribution of electric and magnetic fields in a resonating cavity of radius R and length L in z -direction can be analyzed by solving Maxwell equations in cylindrical coordinates system (ϕ, r, z) . Depending on the boundary conditions of the cavity certain modes are permitted, named TM_{mnp} or TE_{mnp} -modes (TE_{mnp} -modes known as H -mode in Germany). m, n, p are integers define the excited mode where m ($m = 0, 1, 2, \dots$) is the number of full period variations in ϕ of the field components in the range $0 < \phi < \pi$, n ($n = 1, 2, 3, \dots$) is the number of zeros of the axial field component in the radial direction in the range $0 < r < R$, excluding $r = 0$ and p ($p = 0, 1, 2, \dots$) is the number of half period variations in z of the fields $0 < z < L$. The simplest form of a resonant cavity is the ideal pillbox cavity as shown in figure 2.3(left). The resulting electric and magnetic field distribution of a TE -mode and TM -mode are out of the scope and they can be found in [30], see an example in figure 2.3 (right).

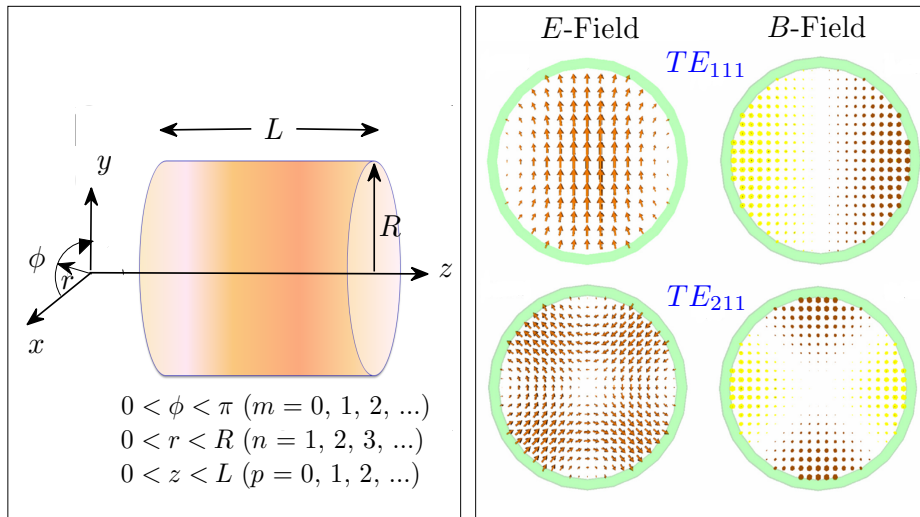


Figure 2.3: A cylindrical and a pillbox cavity (left). The distribution of electric and magnetic fields in an empty cylindrical cavity excited in TE_{111} – mode in IH-cavity and TE_{211} – mode in CH-cavity (right), from [34].

The resonance frequency for TM_{mnp} and TE_{mnp} cavities are given by [34]

$$f_{mnp}(TM - mode) = c\sqrt{\left(\frac{x_{mn}}{2\pi R}\right)^2 + \frac{1}{4}\left(\frac{p}{L}\right)^2} \quad (2.8)$$

$$f_{mnp}(TE - mode) = c\sqrt{\left(\frac{x'_{mn}}{2\pi R}\right)^2 + \frac{1}{4}\left(\frac{p}{L}\right)^2} \quad (2.9)$$

where x_{mn} the zeros of the Bessel functions J_m , and x'_{mn} are the zeros of the derivatives of the Bessel functions J'_m (for IH : $x'_{11} = 1.841$ and for CH: $x'_{21} = 3.054$ [30]).

As the cavity is being designed the operating frequency differs from the resonance frequency for the empty cylinder calculated from equations 2.8 and 2.9 due to introducing drift tubes and stems in the cavity. The presence of the drift tubes leads to a significant increase of the capacitance of the cavity. This extra capacitance is localized between the drift tubes and modifies the resonance frequency efficiency.

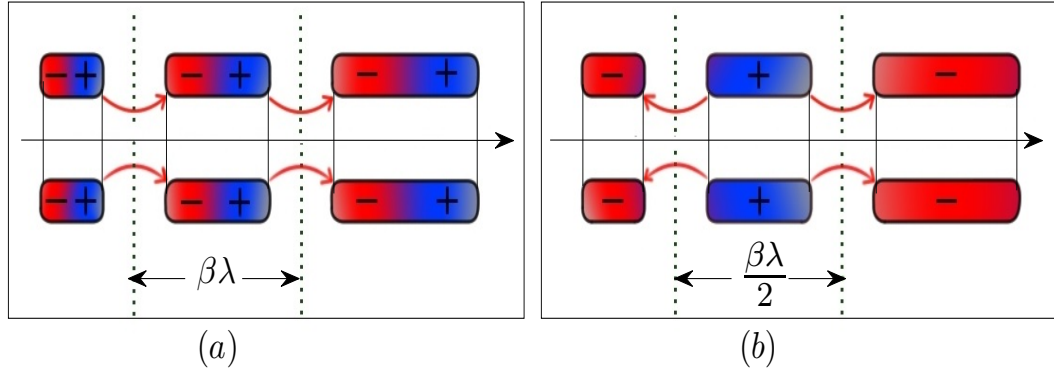


Figure 2.4: The resulting electric field in adjacent gaps in a cavity : a) 2π - mode or $\beta\lambda$ structure, b) π - mode or $\beta\lambda/2$ structures.

The resulting electric field in the gaps needed for beam acceleration can oscillate in phase like in TM -mode and the classical Alvarez structure (2π mode or $\beta\lambda$ structure), or in opposite phase like in TE -mode cavities (π mode or $\beta\lambda/2$ structure) as depicted in figure 2.4. In the Alvarez-type the cavity is excited in the Transverse Magnetic Mode (TM -mode) to provide the longitudinal electric field components required for beam acceleration [35].

In contrast, TE -type cavities are excited in the Transverse Electric Mode (TE -mode) and the accelerating components are generated by the stems which carry the surface current and support the drift tubes. The stems have to be carefully designed so that the surface current on the stems establish the magnetic field. The change of the magnetic field on the drift tubes establish an alternating electric field which can produce the longitudinal

electric field component needed for beam acceleration near the beam axis. The magnetic field is oriented parallel and antiparallel to the direction of beam propagation, so that the field lines are connected with opposite orientation at the cavity ends to provide the closed loops [36,37].

The major advantage of TE -cavities in comparison with the Alvarez-type is the high shunt impedance. This allows to increase the RF power efficiency in the low-medium β range. Thus, the slim drift tubes design allows to reduce the loading capacitance and concentrates the accelerating field close to the beam axis [38]. Additionally, increasing the cross section of the stems can be used to increase the shunt impedance due to decrease in surface current density. Such compact design offers high effective field gradients (up to 10 MV/m [39–41]) and higher resonance frequency for low and medium β acceleration.



Figure 2.5: The IH cavity $TE_{11(0)} - mode$ (left) [42]. The CH cavity $TE_{21(0)} - mode$ of the FAIR proton linac injector operates at 325 MHz (right) (Courtesy of R. Brodhage).

The Interdigital- H structure (IH) and the crossbar- H structure (CH) are two common types of TE -mode as shown in figure 2.5. For instance, the IH ($TE_{11(0)} - mode$) is efficient for an energy range from 100 keV/u to 30 MeV/u [36] whereas the CH ($TE_{21(0)} - mode$) is suitable for beam energies between 3 MeV/u and 150 MeV/u [36]. However, for a resonance frequency higher than 300 MHz, a realistic design of an IH structure is difficult to be achieved in terms of mechanical construction and maintenance [40]. The CH structure consists two stems per drift tube and operates in TE_{210} -mode which can be used to reach up to 800 MHz resonance frequency. Therefore, CH-structure shown in figure 2.5 (right) was proposed for the FAIR proton injector which operates at 325 MHz as a potential alternative in the low-medium β range and at higher frequencies with respect to the IH and Alvarez structures [38].

2.3 Beam Dynamics in Linear Accelerators

The design of the linac cavities is based on the concept of synchronous particle. The synchronous particle has to arrive at each gap center with an energy W_s and a well-defined phase ϕ_s in respect to the applied electric field. Thus, the distances between the gaps and drift tubes have to be adapted to the increase in particle velocity and the bunch must be synchronous with the accelerating wave to gain the right amount of energy. In the following two subsections the transversal and longitudinal beam dynamics are discussed.

2.3.1 Transversal Beam Dynamics

As a bunch of particles crosses the gap between two drift tubes, it experience an axial and a radial electric field components. The off-axis particles will be subjected to radial electric field components which are focussing in the first half of the gap and defocussing in the other half as shown in figure 2.6.

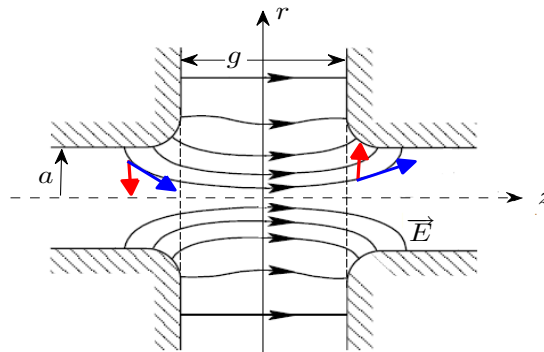


Figure 2.6: Accelerating field lines in an accelerating gap of length g .

It is important to know that the oppositely directed radial electric components in the two halves of the gap do not cancel each other as the total radial momentum is caused by two facts [30]. First, as will be discussed in the next subsection, the phase of synchronous particle ϕ_s must be negative for the purpose of longitudinal stability. The fields vary in time as the particle crosses the gap, thus, most particles experience higher electric field in the second half than in the first. Second, particles do not spend equal times in each half of the gap due to increasing velocity, thus, the energy of the off-axis particles is higher in the second half gap than in the first.

Both mechanisms result in a defocusing effect, known as the RF-defocusing force which can eventually cause the loss of the beam. Therefore, it is necessary to keep the off-axis particles confined within an acceptable range and to compensate the defocusing forces which generate a net radial impulse. The radial momentum impulse near the axis in an accelerating gap is given by [30]

$$\Delta p_r = -\frac{q\pi E_0 T L \sin(\phi_s)}{mc^2 \gamma^2 \beta^2 \lambda} r \quad (2.10)$$

where λ is the wavelength of the RF frequency, $E_0 T$ is the effective accelerating gradient, L is the gap effective length, ϕ_s is the synchronous phase and r is the particle offset from the beam axis.

The defocusing effect produced by the radial electric forces (particle interaction with the accelerating field) and the defocusing resulting from space charge forces (particle-particle interactions) developed inside the beam have to be compensated. This is achieved by applying an external focusing force commonly provided by an array of quadrupoles lenses or magnetic solenoids along the accelerator. The standard solution is to place a focusing element (typical for *TM*-mode cavities) inside the drift tube. However, this limits the achievable accelerating gradient and reduces the structure shunt impedance.

An innovative focusing scheme to reduce the defocusing effect is the KONUS (KOMbinierte NULL grad Struktur Combined Zero Degree Structure) beam dynamics proposed by U. Ratzinger [43]. A complete description of the KONUS concept can be found in [44–46]. In this approach the transverse focusing is provided by compact electric or permeant magnet quadrupole lenses or magnetic solenoid placed at the end of every cavity section. The FAIR proton injector is designed based on KONUS beam dynamics [38].

2.3.2 Longitudinal Beam Dynamics

The acceleration is achieved by a series of accelerating cavities where each consists of a series of drift tubes and accelerating gaps as shown in figure 2.4. As a first approximation it is assumed that passing from two successive gaps centers the particles velocity β remains constant so that the energy gain through a single gap is small compared to the particle energy. All particles in the same bunch will oscillate around the synchronous particle during the acceleration process, so called synchrotron oscillations. These oscillations describe particles motion in the longitudinal phase plane. The motion of each individual particle forms an ellipse representing its energy and phase difference with respect to the synchronous particle.

Assuming a synchronous particle arrives a certain gap in the correct phase ϕ_s with an energy W_s and a velocity β_s and an arbitrary particle in the same bunch reaches the same gap with different phase ϕ_i , energy W_i and velocity β_i . The energy and phase difference between the two particles are given by $\Delta W_{i,s} = W_i - W_s$ and $\Delta\phi_{i,s} = \phi_i - \phi_s$, respectively. For describing the longitudinal bunch stability one defines so called the stable region in $\Delta W_{i,s}$ and $\Delta\phi_{i,s}$ phase space given by [30]

$$\frac{Aw^2}{2} + B(\sin\phi - \phi\cos\phi_s) = \text{const} = H_\phi \quad (2.11)$$

where $w = \delta\gamma = (W - W_s)/mc^2$, $A = 2\pi/(\gamma_s^3\beta_s^3\lambda)$ and $B = qE_0T/mc^2$. H_ϕ in equation 2.11 is a constant and it can be interpreted as the Hamiltonian or total energy. The kinetic energy is the first term ($K.E = Aw^2/2$) while the second term describes the potential energy ($V_\phi = B(\sin\phi - \phi\cos\phi_s)$). The potential well is defined if $-\pi \leq \phi_s \leq 0$. The acceleration only can happen in the region $-\pi/2 \leq \phi_s \leq \pi/2$. Thus, the stable motion is confined in a region which extends from $\phi_2 \leq \phi \leq -\phi_s$ as depicted in figure 2.7 (a, b). ϕ_s in good approximation is $\sim 2\phi_s$. The potential V_ϕ has the maximum at $\phi = -\phi_s$, therefore, the phase change with respect to the synchronous particle is then $\phi' = \phi - \phi_s = 0$ and $w = 0$. Thus, equation 2.11 can be rewritten by defining the constant H_ϕ at $\phi = \phi_s$ as following [30]

$$\frac{Aw^2}{2} + B(\sin\phi - \phi\cos\phi_s) = -B(\sin\phi_s - \phi_s\cos\phi_s) \quad (2.12)$$

Equation equation 2.12 represents the separatrix equation which separates the longitudinal phase space into a stable and an unstable region. The maximum allowed energy spread from the synchronous energy on the separatrix can be determined by solving the equation of separatrix at $\phi = \phi_s$ [30]

$$w_{max} = \frac{W - W_s}{mc^2} = \sqrt{\frac{2qE_0T\gamma_s^3\beta_s^3\lambda}{\pi mc^2}(\phi_s\cos\phi_s - \sin\phi_s)} \quad (2.13)$$

If the injection phase corresponds to the crest of the wave ($\phi = 0^\circ$ in the linac definition) for maximum acceleration, particles having slightly higher or lower phases will gain less energy. As a result, they will slowly lose synchronicity until they are lost. Therefore, the beam has to be injected at a slightly lower phase in respect to the crest of the applied electric field in the the stable phase region $-\pi/2 < \phi_s < 0^\circ$. The reason is that the particles arriving earlier than the synchronous particle gain less energy, and particles arriving later will gain more energy.

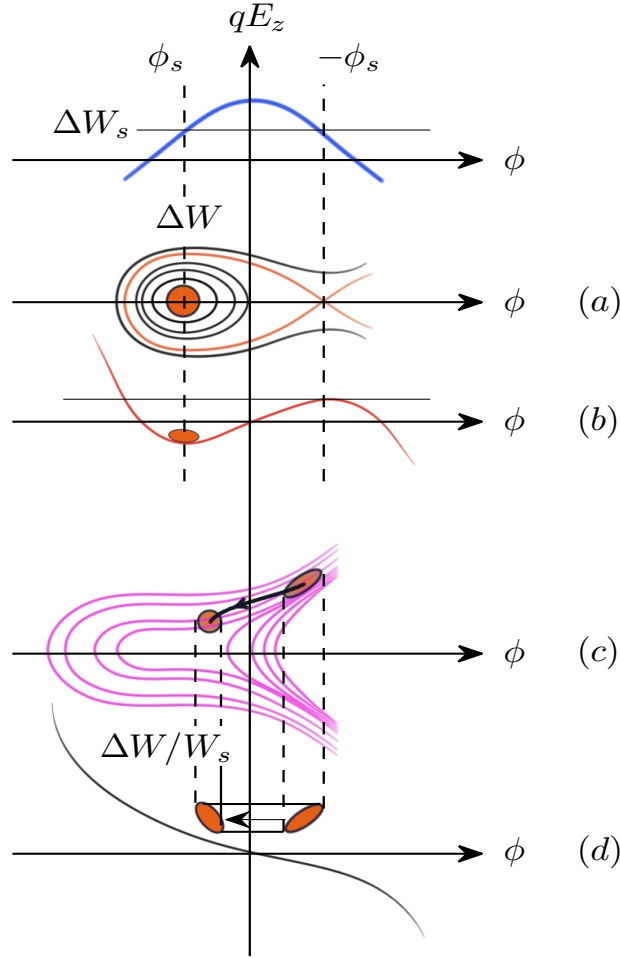


Figure 2.7: On top the accelerating electric field E_z as a cosine function of the phase ϕ where the synchronous phase ϕ_s is shown as negative value. Some trajectories in the longitudinal phase space are shown including the separatrix and the limit trajectory for stable motion (a). The potential function has its minimum at $\phi = \phi_s$ illustrating the meaning of the synchronous phase in the phase space (b). The particle motion in the longitudinal phase space for zero synchronous phase 0° (c) and the longitudinal potential well (d) as applied in KONUS beam dynamics.

It can be concluded that the synchronous phase has to be chosen between $-\pi/2 \leq \phi_s \leq 0$ and stable motion of any arbitrary particle with phase ϕ_i has to be $-2|\phi_s| \leq \phi_i \leq \phi_s$. The typical values of the synchronous phase ϕ_s are between -20° and -35° [32].

2.3.3 KONUS Beam Dynamics

The condition of negative injection phase for a longitudinal stable motion implies a defocusing effect on the beam in transverse direction. The KONUS longitudinal-focusing method was invented to overcome the effect of RF-defocusing forces and to ensure a stable motion of the beam [43]. The KONUS beam dynamic shown in figure 2.7 (c, d) provides

transverse and longitudinal beam focusing for relatively long TE -mode linac sections without hosting quadrupole focusing lenses in the drift tubes. The long drift section without focusing elements allows to design very compact and cost efficient structures with a high field gradient.

The KONUS lattice shown in figure 2.8 is designed using LORASR code (LONGitudinale und RADiale Strahldynamikrechnungen mit Raumladung) [47,48]. LORASR Code simulates the beam with space charge along $\beta\lambda$ and $\beta\lambda/2$ accelerating sections, quadruple, dipole magnets and solenoidal lenses.

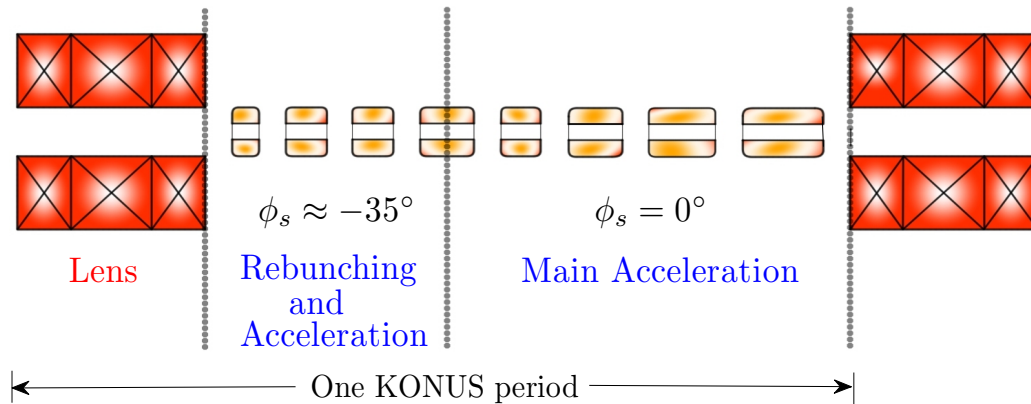


Figure 2.8: A schematic representation of KONUS period in H-DTL. A KONUS period consists of a transverse focusing element, longitudinal focusing and matching section with negative synchronous phase (rebunching) and the main acceleration stage with a multi gap 0° - synchronous phase.

KONUS defines the main acceleration stage on a 0° synchronous phase to maximize the acceleration efficiency and to minimize the defocusing in transverse planes. This is done by adjusting the gap-to-gap spacings so that the synchronous phase for each gap is 0° , which means that a synchronous particle arrives at the center of each gap when the field is maximum.

The essential of the KONUS scheme is to inject the beam into the accelerating section with energy larger than the energy of the synchronous particle on the boundary between the first and second quadrant as shown in figure 2.7 (*c, d*). As the particles advance from gap to gap, the particles will move along the second quadrant counterclockwise in longitudinal phase space. As the particles advance to reach the third quadrant the section is ended and followed by transversal focussing element [30]. The same approach will be applied to fulfill a proper initial condition for the acceleration stage in the next drift tube section. Figure 2.8 illustrates a schematic of KONUS period [40].

2.4 Radio Frequency Quadrupole (RFQ)

The Radio Frequency Quadrupole (RFQ) is a linear accelerator that offers special geometry which allows the electric field to bunch, accelerate and focus the beam at the same time [49]. This can be achieved using electric RF fields of four alternately loaded electrodes following the principles introduced by Kapchinskiy and Tepliakov in 1970 [50]. The beam is accelerated and bunched by longitudinal RF electric field while the beam is transversely focused by RF electric-quadrupole fields.

Currently, the RFQ is the standard solution for the first acceleration step after the ion source replacing the conventional electrostatic accelerators like Van-de-Graaff or Cockcroft-Walton [51]. The RFQ is used typically to accelerate a DC high-current beams up to an energy of ~ 5 MeV/u [52]. The field in the RFQ structure is determined by the electrode design described as either rods or vanes depending on the type of geometry. A detailed discussions about the properties of the four-vane and four-rod structures can be found in [30, 49, 51].

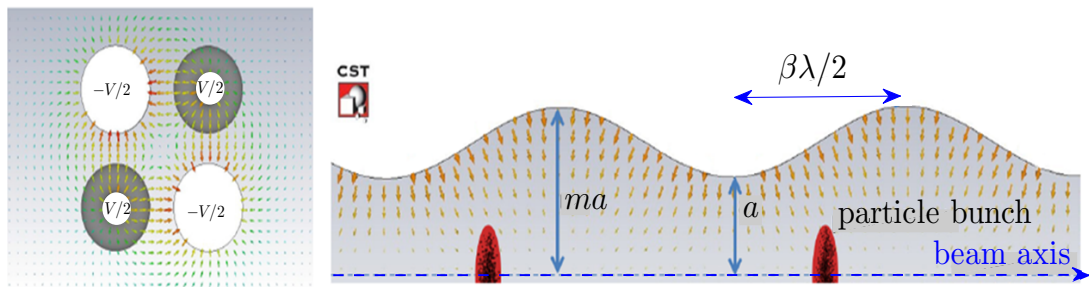


Figure 2.9: a quadrupole field of the RFQ (left). A sinusoidal modulated electrode form acceleration cells with a mid to mid distance of $\beta\lambda/2$ where the bunch to bunch distance is $\beta\lambda$ (right) [from [53]].

In the RFQ structure, the electrodes are alternately loaded with a potential of $\pm V/2$ to form a quadrupole field as shown in figure 2.9 (left) [53]. The electrodes change sign as the beam travels through the structure due to the RF resulting in an alternating focusing and defocusing force in one plane. This chain of lenses results in an overall focusing effect following the Alternating Gradient Focusing method [54].

The axial electric field component required for particle acceleration can be produced by varying the transverse-electrode displacements along the axis [30]. A sinusoidal modulated electrode form acceleration cells with a mid to mid distance of $\beta\lambda/2$ where the bunch to bunch distance is $\beta\lambda$ as shown in figure 2.9 (right) [53]. The wave profile of the

electrode is described by the aperture a which is the minimum distance from the beam axis and the modulation factor m shown figure 2.9 (right). The product ma is the maximal distance in an acceleration cell. The length of the acceleration cell, a and m have to be adapted to β increase along the RFQ structure.

2.5 The FAIR Proton Linac Injector : Design and Main Parameters

The antiproton physics program at the FAIR requires an intensity up to $7 \times 10^{10} \bar{p}/h$ which needs a primary proton beam of $2 \times 10^{16} p/h$ if the \bar{p} production and cooling rate taken into account [29, 55–57]. The primary proton beam will be delivered by a chain of accelerators comprising a dedicated proton linac injector and two synchrotrons, SIS18 and SIS100. The proton linac injector will accelerate a 70 mA proton beam to an energy of 70 MeV before injecting into SIS18. The primary proton beam intensity delivered by the injector is limited by the Space Charge Limit of the synchrotron SIS18 expressed as [38]

$$N_{SIS18} = 4.305 \times 10^{13} \beta^2 \gamma^3 \quad (2.14)$$

where γ is the relativistic factor ($\gamma = 1/\sqrt{1 - \beta^2}$). The main design parameters are listed in table 2.1 [38].

The FAIR proton linac injector will be the first room temperature linac based on crossed-bar H-mode (CH) cavities applying a KONUS beam dynamics scheme [56]. According to the layout in 2012 [58] the entire accelerator consists of an ECR source, Low Energy Beam Transport (LEBT), an RFQ, rebuncher for longitudinal beam matching and a Drift Tube Linac (DTL) as shown in figure 2.10.

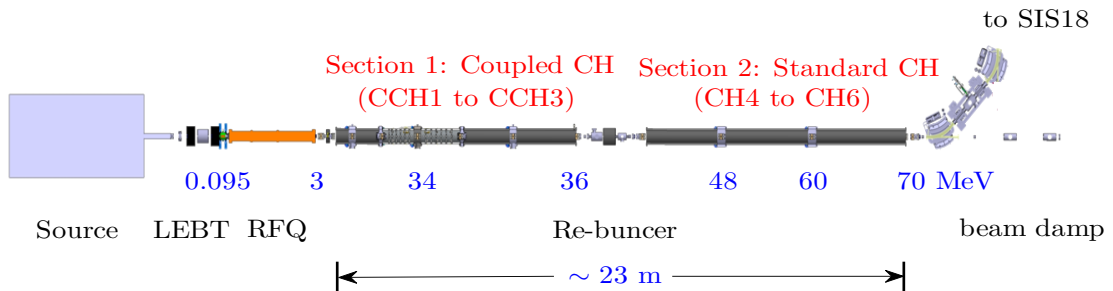


Figure 2.10: The conceptual layout of the FAIR proton linac

The ECR source consists of a five electrode extraction system to produce protons with a maximum beam current of 130 mA and an energy of 100 keV [59]. The Low Energy Beam Transport (LEBT) of ~ 2.3 m long consists of two solenoids, steerers for the horizontal and vertical beam position adjustment and a diagnostic chamber between the two solenoids [60]. A diagnostic chamber is equipped with the Wien filter, Allison scanner, SEM, profile grid, IRIS, 4-grid analyzer and beam stopper. Subsequently, the generated proton beam is bunched and accelerated up to the energy of 3 MeV by an RFQ [61]. Following the RFQ is the MEFT consisting of a single quadruple lens, a rebuncher cavity and a quadruple triplet injects the beam into the first CH-DTL.

Table 2.1: The FAIR Proton Linac Parameters

Parameter	Value
Final energy	70 MeV
Frequency	325.25 MHz
Max. pulse current	70 mA
Protons per pulse	7×10^{12}
Macro pulse length	30 to 100 μs
Repetition rate	4 Hz
Output Emittance (Long.)	$\varepsilon_{95\%} = 21.8$ keV ns $\varepsilon_{rms} = 2.56$ keV ns
Output Emittance (X-X')	$\varepsilon_{95\%} = 3.71$ mm mrad $\varepsilon_{rms} = 0.61$ mm mrad
Output Emittance (Y-Y')	$\varepsilon_{95\%} = 4.00$ mm mrad $\varepsilon_{rms} = 0.61$ mm mrad
Trans. beam emittance	4.2 μm (tot. norm.)

The length of proton linac is ~ 23 m. It is based on three coupled CH-cavities (CCH) followed by three CH's cavities [62]. Each two CH-cavities are connected by an intertank section which hosts a magnetic triplet and distributes the input power between the cavities [38]. The first coupled CH (CCH) power prototype is currently under preparation at GSI. A drawing of the cavity is presented in figure 2.11. The main parameters of this CCH-prototype are summarized in table 2.2 [58].

The first three coupled cavities accelerate the beam up to an energy of 37 MeV. Subsequently, about 60 cm will be reserved to a dedicated diagnostics section, discussed in

Sec. 2.5.1. A quadrupole triplet will then refocus the beam before the further acceleration in the second part of the linac to bring the beam to the final energy of 70 MeV and finally transferred to the SIS18.

The transverse focusing along the linac is ensured by electromagnetic quadrupole triplets (EMQ). Four different types of quadrupole lenses are used along the linac and the beam transport sections. All quadrupoles used along the linac have the same aperture with gradients resulting in pole tip fields below 1 T.

Table 2.2: The main parameters of the second CCH cavity of the FAIR proton injector

Parameter	Value
No. of Gaps	27
Frequency (MHz)	325.25
Energy Range (MeV)	11.7 - 24.4
Beam Loading (kW)	882.6
Heat Loss (MW)	1.35
Total Power (MW)	2.2
Q_0 - value	15300
Effective shunt Impedance ($M\Omega/m$)	60
Average E_0T (MV/m)	5.8-6.4
Kilppatrick Factor	2.0
Coupling Constant (%)	0.3
No. of Plungers	11
Beam Aperture (mm)	20
Inner Total Length (mm)	3000

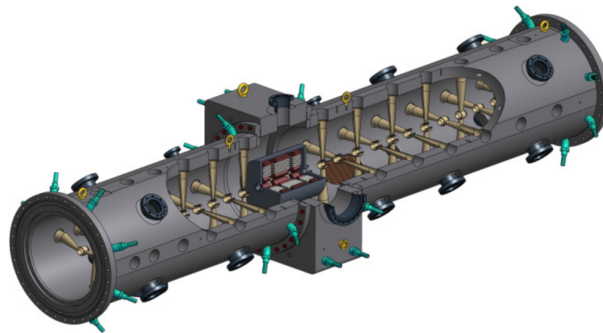


Figure 2.11: 3D Sketch of the CCH power prototype

2.5.1 Beam Diagnostics System of the FAIR Proton LINAC

The KONUS beam dynamics shows the capability of the CH structures to accelerate a proton beam efficiently with a proper quality to the required final energy. However, the beam inside the vacuum pipe of the machine during acceleration is very sensitive to any deviation from the optimal design. Moreover, the situation is rather complicated in reality if all possible imperfections of a technical installation are included. Therefore, beam diagnostics is essential part in proton LINAC providing the means of visualizing beam characteristics and behaviour in the real conditions.

The proton LINAC will be equipped with diagnostic devices along the LINAC to keep all the beam parameters under control during operation. Various beam parameters have to be observed such as the beam current, the transversal and longitudinal profile (size and shape of the bunch), the beam energy and the beam position [33]. Different physical processes and working principles are used for beam observation. For instance, the electro-magnetic influence of moving charges and the coulomb interaction of charged particles penetrating matter [63].

In general, beam diagnostic devices can be destructive or non-destructive. In the destructive beam diagnostic, the beam is lost after it interacts with the matter inside the device such as Faraday cups and SEM-grid. The non-destructive beam diagnostic are sometimes referred to as beam monitors such as beam current transformers and beam position monitors (BPM).

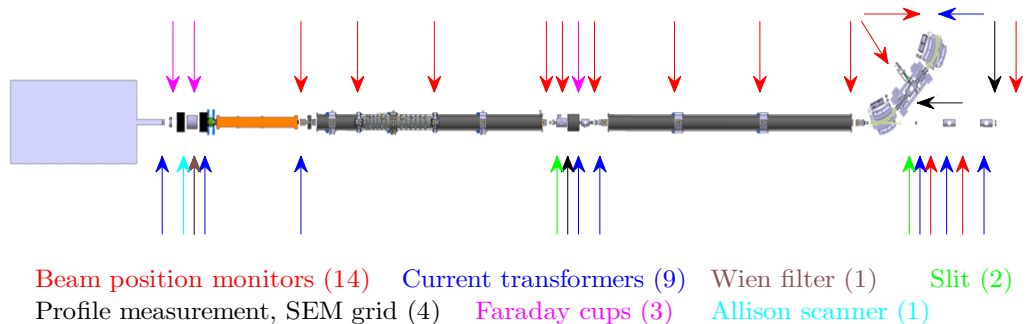


Figure 2.12: The scheme for the diagnostics along the proton LINAC.

Due to the compact structure of the two CH sections all devices will be installed in three drift regions except four BPMs will be installed between the CH modules, together with the magnetic triplet lenses. First, in the LEBT, behind the RFQ (rebuncher section), charge state analysis will be performed with a Wien Filter, while the emittance is measured

with an Allison scanner. Second, after the third CCH a dedicated diagnostics section of 70 cm length will contain the most common diagnostics devices to control the beam quality such as a Faraday cup, a slot grid array for emittance measurements, a BPM, a current transformer and a beam profile monitor. Third, behind the accelerator after the last quadrupole triplet, beam diagnostics elements are placed in the transfer line to the SIS18 as well as in a straight line in the beam dump. A horizontal scraper (8 mm aperture) is placed between two bending magnets before the injection to SIS18 in order to clean the beam from outer particles. For determination of longitudinal emittance a wire based bunch shape monitor is foreseen [64].

The BPM system will be a major diagnostic tool in the test bench during the machine commissioning phase. A typical setup of the test bench involves a complete set of diagnostic devices such as Faraday cup, SEM grid, BPM, current transformer ...etc. The test bench will be placed behind each cavity and the signal from the BPMs downstream (e.g. on a test-bench) will be measured. Additionally, for time-of-flight measurements a drift between two BPMs will be used (typically, 2 to 5 m) to determine the mean energy of the beam.

Beam Position Monitors (BPMs)

Beam Position Monitor (BPM) consists of sensing electrodes called pickups (PUs). These electrodes serve to observe the proximity of the beam inside the vacuum pipe. The goal is to determine the transverse beam position. BPM's electrodes can be designed in different geometrical shapes. However, it is important that the electrodes provide an adequate signals without unduly disturbing of the beam itself. Beam parameters must be considered when the BPM is being designed in order to achieve the required sensitivity and the optimum linearity response.

This chapter presents the theoretical concepts for beam position determination in particle accelerators and discusses the BPM system for the FAIR proton LINAC. The chapter is divided into two major parts; the first part reviews the basic fundamentals of the BPM sensing mechanism and the way to obtain the beam position from the BPM output signals. The discussions in this part essentially follow from the following sources [33, 63, 65–67].

3.1 Principle and Sensing Mechanism

A bunched beam is a time-varying current, therefore, it will be accompanied by both a magnetic field and an electric field. All types of beam monitors are based on electromagnetic effects either the capacitive or inductive (magnetic) one [65]. From Maxwell equations of induction, there are two methods to extract a signal induced by a bunched beam [67]. The first method is to measure the voltage $V(t)$ induced by the magnetic field \vec{B} of the beam particles in a winding of length l surrounding an area A as shown in figure 3.1 (left) so called a loop monitor by

$$V(t) = -\frac{d}{dt} \int \vec{B} d\vec{A} = -\frac{d}{dt} \int B_{\Phi} dA = -\frac{d}{dt} \oint \vec{A}_p d\vec{l} \quad (3.1)$$

where \vec{A}_p is the vector potential. The second method is to measure the current $I_{im}(t)$ induced by the electric field \vec{E} of the beam particles on an insulated metal plate of an area A as shown in figure 3.1 so called a capacitive pickups (PUs) given by

$$I_{im}(t) = \frac{d}{dt} \int_{area} \epsilon \vec{E} d\vec{A} \quad (3.2)$$

where \vec{E} is the electric field of the moving charged particles. For beam position determination as well as the longitudinal bunch shape profile the capacitive pickups are employed [67]. The idea of the BPMs is to pick up a signal from the electric fields produced by beam through a particular segment of the accelerator. In a BPM, four pickup electrodes are mounted orthogonally around the vacuum pipe aperture. The signals of two opposite pickups are subtracted to measure how far the beam is from each in order to determine beam position.

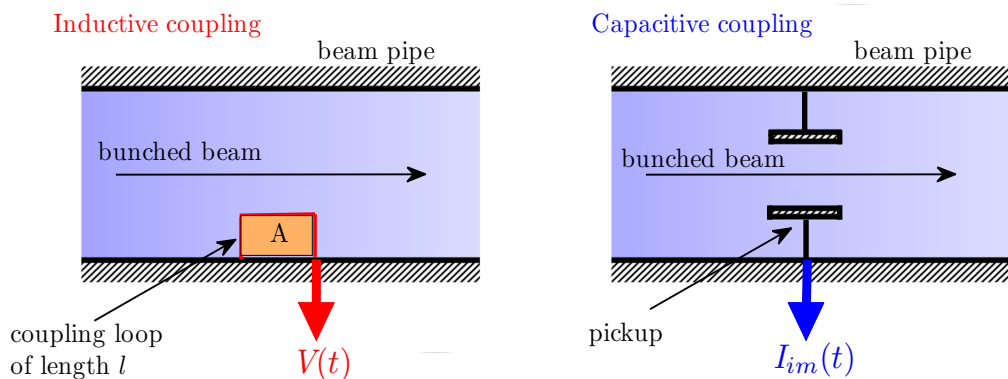


Figure 3.1: Scheme of inductive (left) and capacitive (right) signal extraction [67].

Capacitive pickups type in BPMs bases its sensing mechanism on the image current $I_{im}(t)$ flowing through the electrode which is driven in an opposite polarity of the beam direction as depicted in figure 3.2 (left). The image current amplitude is a function of the distance of the electrode from the beam and the solid angle subtended on the beam [66]. The image current flowing from the pickup into the circuit can be estimated by summing up the weighted contributions of point charges moving inside the pickup [67]. If the beam is displaced from the center the magnetic and the electric fields reaching the pickups are modified and thus the produced image current. The closer distance to one of the opposite electrodes leads to a higher signal so called **The Proximity Effect** [65], figure 3.2 (right). The induced signal is then coupled via an amplifier for further processing. This basic sensing mechanism allows one to determine the beam position from the pickups signals as will be described in the next sections. It serves as well to monitor non-destructively the longitudinal profile of the bunch during the routine operation of the accelerator.

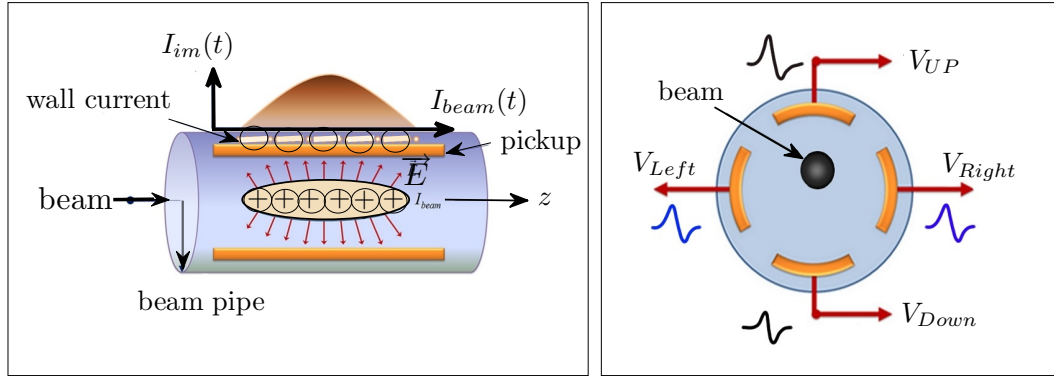


Figure 3.2: Extracting a signal from moving charged particles bunches by measuring the image current flowing with reverse polarity to the beam current (left). Four electrodes mounted orthogonally around the vacuum pipe aperture to measure how far the beam is from each in order to determine beam position (right).

The electromagnetic fields generated by the beam and thus the time evolution of the signal coupled out by the pickup depend on beam velocity as shown in figure 3.3. In the limit of very high beam energy or relativistic velocities the generated beam fields are pure transverse electric and magnetic known as Transverse Electric and Magnetic (TEM) mode. A TEM mode has an electric and magnetic field vector perpendicular to the propagation direction. Thus, the electric field is longitudinally concentrated above and below the beam [65, 66]. For moderate beam velocities $\beta > 0.9$ the resulting field can be also approximated to first order by TEM field distribution and the image current mirrors the same time behavior as the beam is traveling. At low beam velocities $\beta < 0.5$, the electromagnetic field is no longer a TEM wave [66]. The resulting transverse field component is proportional to the Lorentz factor $\gamma = 1/\sqrt{1 - \beta^2}$ compared to the values within the beam's rest frame. The resulting signal shape can be described by the **Transfer Impedance** Z_t as will be discussed in the next section.

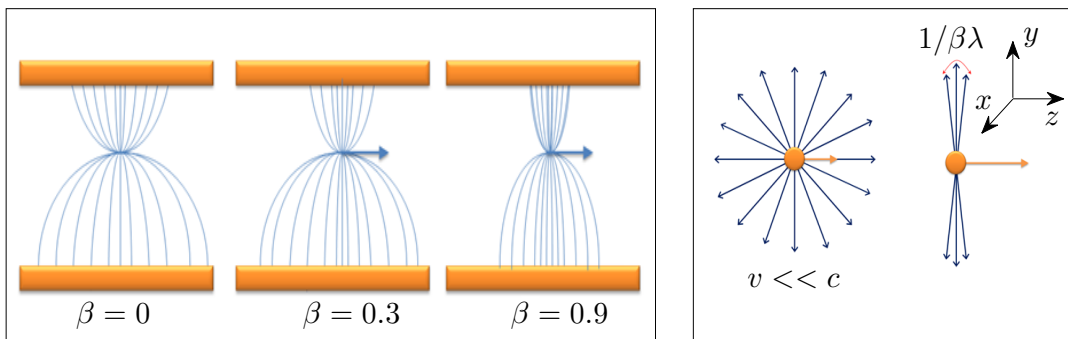


Figure 3.3: Schematic plot for the relativistic increase of the transverse electric field (left). The electric field lines of charged particle beam moving at much less than the speed of light and close to the speed of light (right)

3.2 Signal Treatment and Estimation

Assuming a pickup has an area of A and a length in longitudinal direction of l mounted at a certain distance a from the beam center. The image current $I_{im}(t)$ appears on the pickup electrode driven by the image charge $Q_{im}(t)$ is given by [65, 66]

$$I_{im}(t) = \frac{dQ_{im}}{dt} = -\frac{A}{2\pi al} \cdot \frac{dQ_{beam}(t)}{dt} \quad (3.3)$$

If the beam has a velocity β the derivative of the beam charge $dQ_{beam}(t)/dt$ is written as

$$\frac{dQ_{beam}(t)}{dt} = \frac{l}{\beta c} \frac{dI_{beam}(t)}{dt} = -\frac{l}{\beta c} \cdot i\omega I_{beam}(\omega) \quad (3.4)$$

where $I_{beam}(t)$ is the current of a centered pencil beam and the beam current is expressed as in frequency domain as $I_{beam}(t) = I_0 e^{-i\omega t}$. The frequency of the periodic beam bunches is the carrier of the beam position and phase information. The corresponding image current can be written as

$$I_{im}(t) = -\frac{A}{2\pi a\beta c} \cdot i\omega I_{beam}(\omega) \quad (3.5)$$

Using the voltage drop at a resistor R , the voltage signal on the pickup in frequency domain $V_{im}(\omega)$ is expressed by the product of the current out of the pickup and the impedance seen by this current

$$V_{im}(\omega) = R \cdot I_{im}(\omega) = Z_t(\omega, \beta) \cdot I_{beam}(\omega) \quad (3.6)$$

where $Z_t(\omega, \beta)$ is the transfer impedance which relates the beam current and the pickup voltage. It depends on frequency and the relative velocity of the beam and on geometrical factors. The transfer impedance can be characterized from the equivalent circuit of an electrostatic pickup shown in figure 3.4. It involves an input resistor of the amplifier R and a pickup electrode with a certain capacitance C determined by the distance between the pickup and the beam pipe and a capacitance contributed by the cable between the pickup and the amplifier input. The value of the impedance Z is $R/(1 + i\omega RC)$ and the resulting output voltage is [65]

$$V_{im}(\omega) = \frac{1}{\beta c} \frac{1}{C} \frac{A}{2\pi a} \frac{i\omega RC}{1 + i\omega RC} \cdot I_{beam}(\omega) \equiv Z_t(\omega, \beta) \cdot I_{beam}(\omega) \quad (3.7)$$

The length of the transformed beam current $\tilde{I}_{beam}(\omega)$ in frequency domain is given by $\sigma_f = (2\pi\sigma_t)^{-1}$ in case of a Gaussian distribution. The absolute value of the transfer impedance is given by [65]:

$$|Z_t| = \frac{A}{2\pi a C \beta c} \frac{\omega/\omega_{cut}}{\sqrt{1 + \omega^2/\omega_{cut}^2}} \quad (3.8)$$

the phase relation $\varphi = \arctan(\omega_{cut}/\omega)$.

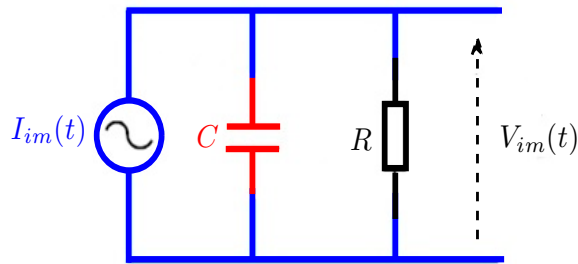


Figure 3.4: The equivalent circuit of the electrostatic pickup device.

In general The response or output signal shape can be characterized using the transfer impedance concept as schematically shown in figure 3.5. The pickup circuit reacts as high pass filter with the cut-off frequency calculated by $f_{cut} = 1/(2\pi RC)$ determined by pickup's geometry and the input resistor.

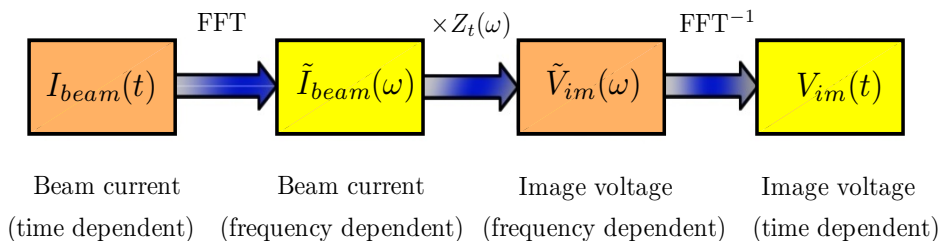


Figure 3.5: The beam current $I_{beam}(t)$ is Fourier transformed resulting $\tilde{I}_{beam}(\omega)$ and then multiplied by $Z_t(\omega)$ to give the frequency dependent voltage $\tilde{V}_{im}(\omega) = Z_t(\omega) \cdot \tilde{I}_{beam}(\omega)$. Next, the inverse Fourier transformation is applied to get back the time dependent signal $V_{im}(t)$.

The signal at the amplifier output depends on the frequency range as compared to the cut-off frequency. If the bunch spectrum ranges far above the cut-off frequency ($f \gg f_{cut}$) the multiplication by the transfer impedance $Z_t(\omega)$ does not change the spectral shape of image voltage $\tilde{V}_{im}(\omega)$ significantly. The inverse transformation leads to a proportional image voltage $V_{im}(t)$ so that the pickup signal is direct image of the bunch time structure without a phase shift, $\varphi = 0$. The time dependence of the output signal at R follows the shape of the beam current according to

$$Z_t \propto \frac{i\omega/\omega_{cut}}{1 + i\omega/\omega_{cut}} \sim 1 \quad \Rightarrow V_{im}(t) \simeq \frac{A}{2\pi a C \beta c} \cdot I_{beam}(t) \quad (3.9)$$

If the bunch spectrum ranges is far below the cut-off frequency ($f \ll f_{cut}$), the multiplication by $Z_t(\omega)$ leads to a strong modification of the spectrum and the inverse Fourier

transformation leads to a derivative behavior. The output signal is bipolar and proportional to the derivative of the beam current $V_{im}(t) \propto dI/dt$. The voltage across R in this case is

$$Z_t \propto \frac{i\omega/\omega_{cut}}{1 + i\omega/\omega_{cut}} \sim i \frac{\omega}{\omega_{cut}} \quad \Rightarrow V_{im}(t) \simeq \frac{RA}{2\pi aC\beta c} \cdot \frac{dI_{beam}(t)}{dt} \quad (3.10)$$

If the main bunch frequency components are in the same cut-off frequency band the multiplication by $Z_t(\omega)$ leads to significant modification of the image voltage spectrum $\tilde{V}_{im}(\omega)$. The behavior of the output signal $V_{im}(t)$ is more complex with some proportional and some differentiating components which results a signal deformation in time domain.

Therefore, the pickup design should match the interesting frequency range given by the acceleration frequency and the bunch length [65]. The working region of the BPM should be chosen in which the cut-off frequency of the pickup circuit is larger than the acceleration frequency to avoid the signal deformation.

3.3 Signal Analysis Using the Discrete Fourier Transform

Fourier transformation is a very common and powerful tool in the field of digital signal processing. It reveals the frequency content of the time domain signal. The continuous Fourier transform $X(f)$ is defined as [68]:

$$X(f) = \int_{-\infty}^{\infty} x(t)e^{-i2\pi ft} dt \quad (3.11)$$

where $x(t)$ is the continuous time domain signal. However, in the real world the processed signals in the electronic components are digitized in a discrete manner. The discrete Fourier transformation (DFT) defined as the discrete frequency domain sequence $X(m)$ written

$$X(m) = \sum_{n=0}^{N-1} x(n)e^{-i2\pi \frac{nm}{N}} \quad (3.12)$$

$$= \sum_{n=0}^{N-1} x(n) [\cos(2\pi \frac{nm}{N}) - i \sin(2\pi \frac{nm}{N})] \quad (3.13)$$

where $x(n)$ is a discrete sequence of time domain sampled values of the continuous variable $x(t)$, $X(m)$ is the m th DFT output component, m is the index of the DFT output in the frequency domain, n is the time domain index of the input samples and N is the number of samples of the input sequence. The indices for the input samples n and the DFT output samples m always range from 0 to $N - 1$ in the standard DFT notation. The Fourier

transformation $X(f)$ of a real signal results in complex numbers and always plotted as amplitude and phase spectrum versus frequency.

The Fast Fourier Transform (FFT) [69] is an algorithm optimization of the Discrete Fourier Transform which removes the redundant calculations if the number of samples N to be transformed is an exact power of two, $N = 2^k$, where k is a positive integer. The value of N is an important parameter when the FFT is performed. It determines how many input samples are needed, the resolution of the frequency domain results and the amount of processing time necessary for the calculation.

The data collection time interval must be long enough to satisfy the desired FFT frequency resolution for the given sample rate f_s . Additionally, the number of sample N of the input sequence $x(n)$ and the sampling frequency f_s has to be carefully chosen to meet the desired FFT bin spacing or so called the analytical frequencies $f_a(m)$. The FFT produces a correct results only when the input data sequence contains weight precisely at the analysis frequencies given by [70]

$$f_a(m) = m \frac{f_s}{N} \quad (3.14)$$

where $m = 0, 1, 2, \dots, N - 1$. It shows that the exact frequencies of the different sinusoids depend on both the sampling frequency rate f_s at which the original signal is sampled, and the number of samples N .

As mentioned previously the FFT is constrained to operate on a finite set of $N = 2^k$ input values sampled at a sample rate f_s . It produces then an N -point transform whose discrete outputs are associated with the individual analytical frequencies $f_a(m)$. The longer we sample at a fixed f_s sample rate, the finer the frequency resolution can be obtained. An important hint when the FFT is performed is to use an integer number of cycles of the input signal to avoid the so called DFT leakage [70]. The FFT bin spacing will be the ratio of the sampling rate over the number of points in the FFT, f_s/N . If the FFT's input samples are real, the $X(m)$ outputs from $m = 0$ to $m = N/2$ are

$$X(m) = X_r(m) + iX_i(m) \quad (3.15)$$

where $X_r(m)$ and $iX_i(m)$ are the real and the imaginary component of the FFT, respectively. The magnitude $X_{mag}(m)$ and the phase angle $X_\phi(m)$ of the FFT bin frequencies output are given by

$$X_{mag}(m) = |X(m)| = \sqrt{X_r^2(m) + X_i^2(m)} \quad \text{and,} \quad X_\phi(m) = \tan^{-1}\left(\frac{X_i(m)}{X_r(m)}\right) \quad (3.16)$$

This process can be reversed to obtain the original time domain signal $x(n)$. This is implemented by performing the inverse discrete Fourier Transform (IDFT) on the $X(m)$ frequency domain values expressed [70],

$$x(n) = \frac{1}{N} \sum_{m=0}^{N-1} X(m) e^{-i2\pi \frac{nm}{N}} \quad (3.17)$$

$$= \frac{1}{N} \sum_{m=0}^{N-1} X(m) \left[\cos\left(2\pi \frac{nm}{N}\right) - i \sin\left(2\pi \frac{nm}{N}\right) \right] \quad (3.18)$$

3.4 Transverse Beam Position Determination

The levels of the output voltages produced by the PUs depend directly on the beam proximity to each electrode through the image current as shown in figure 3.2 (right). The image current induced on the electrode surface gets higher with the beam closer to an electrode. Assuming a BPM with four electrodes distributed orthogonally around the vacuum pipe aperture, the image current will be uniformly distributed on the electrodes as long as the beam is in the BPM center. Otherwise it increases or decreases from the central value as the beam approaches or moves away from the PU due to an arbitrary beam position displacement. The horizontal and vertical beam position coordinates (x, y) are determined by the difference between two signals of opposite pairs $[\Delta U_x, \Delta U_y]$ in the BPM. The difference $\Delta U_x = U_{x+} - U_{x-}$ where U_{x+} and U_{x-} are signals coming from left and right pickups representing the horizontal plane while for ΔU_y ; U_{y+} and U_{y-} are up and down pickups signals for the vertical one. Both signals are normalized to their sum $[\Sigma U_x, \Sigma U_y]$ to make the position measurement independent of the beam current. The normalized horizontal H and vertical V beam position are given by [66]

$$H = \frac{\Delta U_x}{\Sigma U_x} \quad \text{and,} \quad V = \frac{\Delta U_y}{\Sigma U_y} \quad (3.19)$$

This method commonly used for deriving the normalized beam position signal from BPM signals; called the difference-over-sum (Δ/Σ) processing. A linear fit is used to characterize the BPM and, thus, obtain the beam position coordinates (x, y) from the output signals written as

$$x = E_x + k_x \cdot \frac{\Delta U_x}{\Sigma U_x} \quad \text{and,} \quad y = E_y + k_y \cdot \frac{\Delta U_y}{\Sigma U_y} \quad (3.20)$$

where k_x and k_y , defined as $S_x = 1/k_x$ and $S_y = 1/k_y$ respectively, are the characteristic slopes which depend on the BPM sensitivity to the beam position changes in each plane. They give basically the variation of ΔU_x and ΔU_y signals when the beam changes

its position in the vertical or horizontal directions. E_x and E_y are the electric off-sets from the PU mechanical center for both coordinates. In the BPM characterization tests, the position is known and the parameters for both planes are obtained. Therefore, the sensitivity parameters are obtained from the inverted linear fit equations

$$\frac{\Delta U_x}{\Sigma U_x} = n_x + S_x x \quad \text{and,} \quad \frac{\Delta U_y}{\Sigma U_y} = n_y + S_y y \quad (3.21)$$

where x and y are the positions, n_x and n_y are the parameters deviation when the beam is in the center, which are directly related to the electric off-sets obtained from the linear fit relations in equation 3.20 .

3.5 The Time-of-flight (TOF) and Beam Energy Determination

The common approach for beam energy determination in a non-relativistic velocities regime is the Time-of-flight (TOF) method. Two BPMs (or phase probes) separated by a well defined distance L are installed in a straight section as schematically shown in figure 3.6. Each BPM acts as phase probe detecting the bunch center-of-mass determined by the zero-crossing point of the sum of pickups signals. The phase difference between the BPMs signals corresponds to the time of passage of the beam.

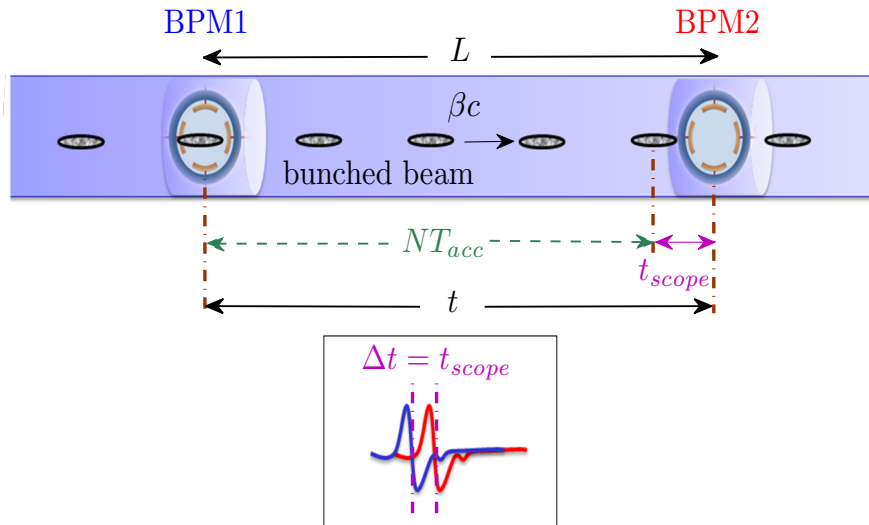


Figure 3.6: Principle of the Time-of-flight (TOF) measurements using two BPMs

In the time domain conventional method, both signals can be recorded, displayed on an oscilloscope to be compared to a reference signal [67]. The velocity is calculated for the measured time t_{scope} from [33, 67]

$$\beta c = \frac{L}{NT_{acc} + t_{scope}} \quad (3.22)$$

where T_{acc} is the bunch repetition time ($T_{acc} = 1/f_{RF}$), and N the number of bunches between the two BPMs. To determine the number of bunches a third BPM is installed at a distance l close to one of the BPMs where l has to fulfill the condition $l = \beta\lambda_{acc}$. The corresponding beam energy can be calculated from [67]

$$E(\text{MeV}/u) = mc^2[\text{MeV}/u] \cdot (\gamma - 1) \quad (3.23)$$

where γ is the relativistic factor ($\gamma = 1/\sqrt{1 - \beta^2}$).

Presently, a state-of-the-art digital processing scheme is developed for the BPM of the proton LINAC. The digital electronics are foreseen to replace the analogue time domain approach. The BPM signals will be digitally processed to obtain the beam position information and beam phase with respect to rf master oscillator. In this case, t_{scope} described in equation 4.5 is used to calculate beam velocity and therefore beam energy. The phase difference between two BPMs corresponds to the time-of-flight with respect to the accelerating frequency of 325 MHz ($1^\circ = 8.5$ ps).

The BPM System for the FAIR Proton Linac

4.1 Specifications and Main Parameters

The beam position monitor (BPM) is an essential diagnostic tool in the FAIR proton LINAC [58]. Fourteen Beam Position Monitors (BPMs) will be installed along the LINAC as schematically shown in figure 4.1 [71]. These monitors will be used to determine three beam quantities, namely the beam displacement, the mean beam energy and the relative beam current. The main measurement is to determine the beam displacement with a spatial resolution of 0.1 mm averaged on a macro pulse of 36 μs duration by calculating the ratio of the difference over sum voltage between two opposite buttons. The beam energy will be measured from the Time-of-flight (TOF) of bunches between two BPMs with an accuracy of 8.5 ps corresponding to a phase difference of 1° at 325 MHz. The relative beam current is determined for the sum signal of the four BPM plates [72].

A capacitive button type pickup from Kyocera [73] with 14 mm diameter has been proposed for its easy mechanical realization and for the short insertion length. These design properties are required due to beam dynamics requirements and compactness of the beamline in proton LINAC. In particular, four BPMs will be an integral part of the intertank section between the CCH or CH cavities as shown in figure 4.1. Moreover, the same type of button electrode is foreseen along the LINAC.

Depending on the location the BPM design has to be optimized taking into account an energy range from 3 MeV to 70 MeV and limited space for installation at the 30 mm (nine locations) or 50 mm (five locations) beam pipe aperture [64, 74]. In the case of the intertank sections and the beamline (the region of matching sections between the RFQ and the first CH and between the third and fourth CH) and directly behind the last CH,

the BPM aperture is 30 mm. In the inflection region, the transfer line to SIS18 and before the beam dump, the BPM aperture of 50 mm is required. The design parameters of the proton LINAC BPM are summarized in table 4.1.

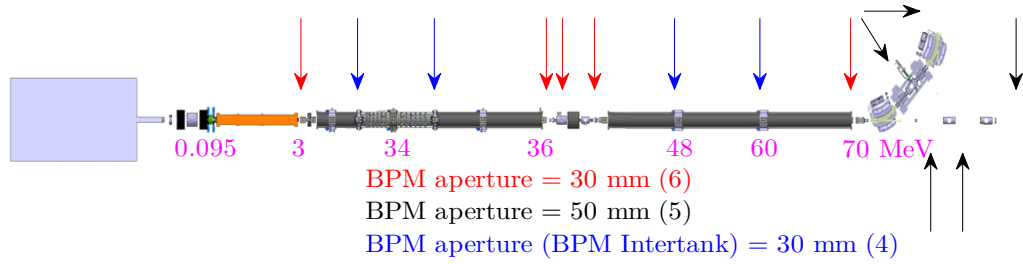


Figure 4.1: The FAIR proton LINAC, showing the positions of the 14 BPMs for the 30 mm (nine locations) or 50 mm (five locations) beam pipe aperture. Four of these BPMs are located in the intertank section between two coupled cavities. The proton beam energy is given as well

Table 4.1: Parameters for the BPM system for the LINAC

Parameter	Value
Beam energy	3 to 70 MeV
Accelerating frequency	325.224 MHz
Beam pulse length	36 μ s nominal, 70 μ s maximum
Bunch length	150 ps (average)
Average current (mA)	35 mA nominal, 70 mA maximum
Beam pipe diameter	30 mm or 50 mm
BPM type	Four-fold button
Position resolution (rms)	0.1 mm averaged over 36 μ s
Operation range	\pm 5 mm
Phase resolution	1° averaged over 36 μ s
Pre-amplifier gain	0 ... 40 dB
Total Dynamic range	60 dB

4.2 Beam Properties at BPM Locations

Signals produced by the BPM pickups demonstrate the longitudinal profile of the bunch which depends on bunch shape and its particle distribution. The knowledge of bunch characteristics at the BPM locations along the proton LINAC is very important for the layout of the BPM system. This information has to be considered for the related technical layout of the BPM such as bandwidth of the the analog chain and amplifiers. Additionally, the bunch parameters are required in order to estimate the produced pickup signal using CST simulation. This section presents bunch characteristics at 12 locations along the proton LINAC and the longitudinal bunch profile after some drifts.

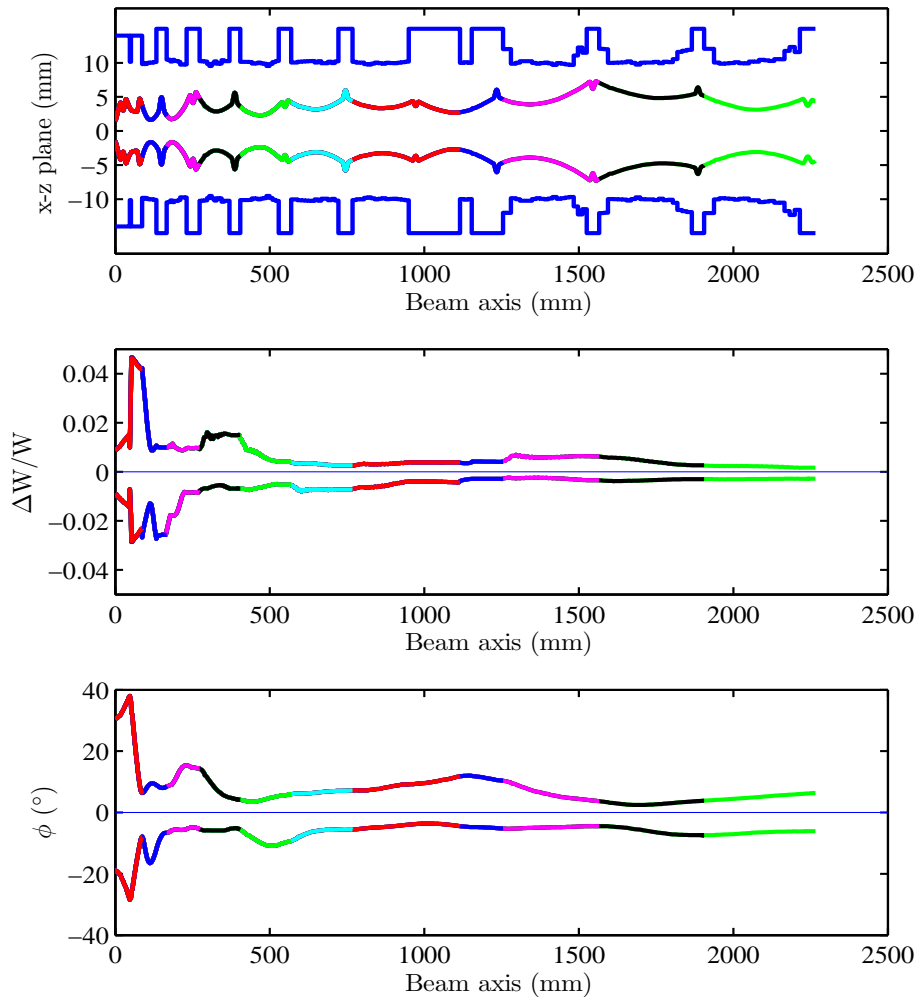


Figure 4.2: 95% transversal beam envelope along the proton LINAC in XZ plane (Up). 95% beam energy envelope with respect to the bunch center (Middle). 95% beam phase envelope with respect to the bunch center (Down).

The BPMs will be installed in the most cases behind quadrupoles (doublet or triplet) along the proton LINAC so that the beam will be focussed before the beam position and beam energy are determined. Since the BPMs are located just a few millimeters behind the quadrupoles, it is sufficient as a first approximation to consider that the particle distribution does not change significantly at the BPM locations. The transversal ($x - z$ plane) and the longitudinal beam envelopes in the complete 6D phase space along the proton LINAC is shown in figure 4.2.

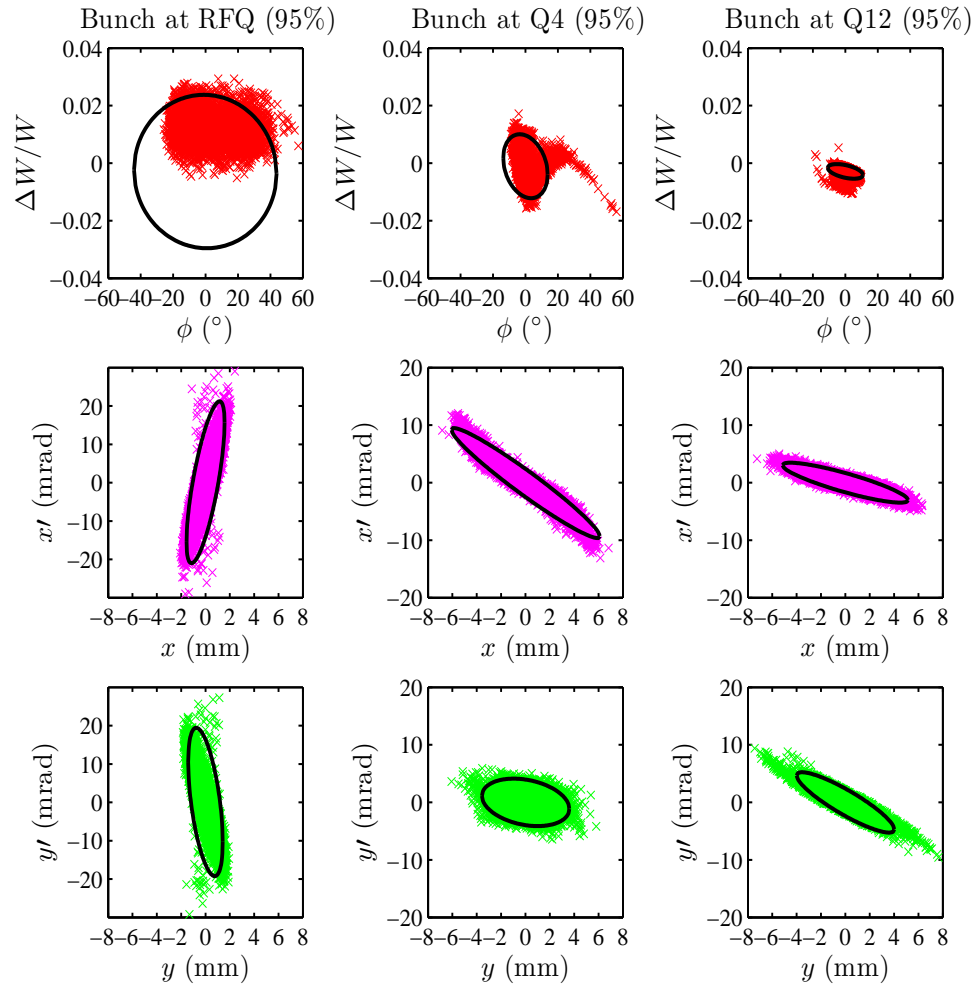


Figure 4.3: Phase space distribution at three locations. The output phase space after RFQ at 3 MeV (Up), The output phase space at after Q4 at 20 MeV (Middle), the output phase space after Q12 at 70 MeV (Down).

The particle distribution in phase space ($x - x'$, $y - y'$, $\phi - \Delta W/W$) was produced at 12 locations along the LINAC for ~ 10000 particles [75]. These locations correspond to the exist of each quadrupoles starting from the output distribution of the RFQ to the quadrupole located behind the last CH cavity as demonstrated in figure 4.5. Figure 4.3 illustrates particle distribution in transverse and longitudinal phase space only at three locations; after the RFQ, Q4 and Q12. The phase projection (histogram) of the particles distribution after the RFQ, Q4 and Q12 is shown in figure 4.4. RFQ output distribution in longitudinal phase space shows a large phase spread of about $\sim 50^\circ$ rms, while the beam is divergent in the $x - x'$ plane and converges in the $y - y'$ plane.

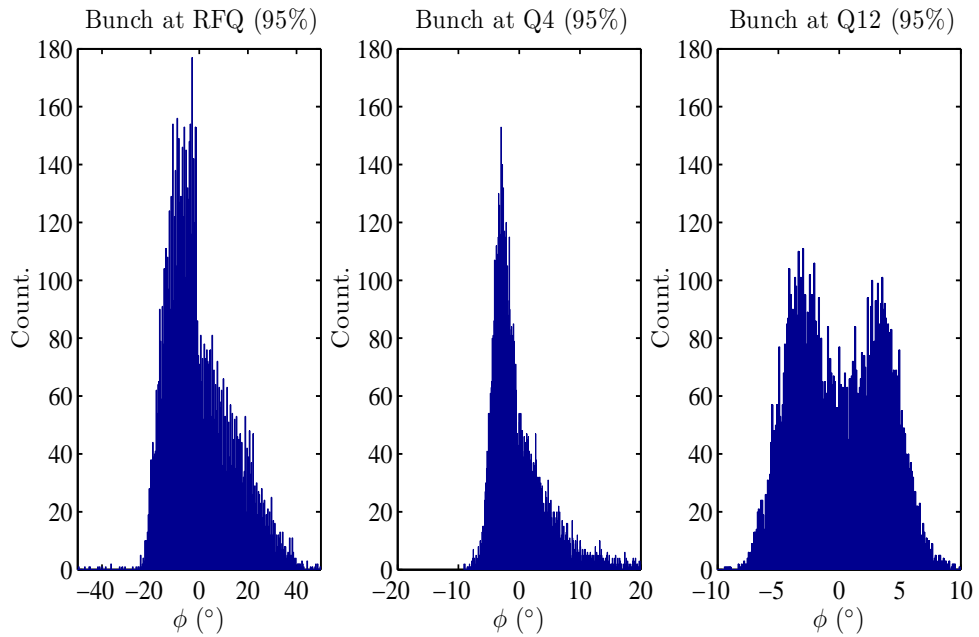


Figure 4.4: The phase projection (histogram) of the particles distribution after the RFQ, Q4 and Q12.

The bunch lengths are estimated by the rms values of the phase projection (histogram) of the particles distribution in $\phi - \Delta W/W$. The dynamic range of rms bunch lengths at the exit of each quadrupole is illustrated in figure 4.5. Based on these simulations it is clear that rms bunch length is fluctuating around $\sim 5^\circ$ (corresponding to 41.2 ps at 325 MHz) except the bunch after the RFQ. Additionally, the bunches are non-Gaussian at the most of the BPM locations.

The particle distribution has been investigated after some drifts without focussing elements to estimate the longitudinal profile of the bunch. The bunch after each quadrupole

is drifted using linear optical transformation a distance of 0.5 m, 1 m, 2 m, 4 m 6 m 8 m and 10 m but there was no momentum spread considered. Each individual particle is linearly transferred for a given drift d by the 2×2 transfer matrix for the six dimensions where for x - x' and y - y' the transfer matrices written as

$$\begin{pmatrix} x_d \\ x'_d \end{pmatrix} = \begin{pmatrix} 1 & d \\ 0 & 1 \end{pmatrix} \cdot \begin{pmatrix} x_0 \\ x'_0 \end{pmatrix} \quad \text{and,} \quad \begin{pmatrix} y_d \\ y'_d \end{pmatrix} = \begin{pmatrix} 1 & d \\ 0 & 1 \end{pmatrix} \cdot \begin{pmatrix} y_0 \\ y'_0 \end{pmatrix} \quad (4.1)$$

where x_0 , x'_0 , y_0 and y'_0 describe particle position at the Quadrupole, x_d , x'_d , y_d and y'_d describe particle position after a certain drift d . The longitudinal phase spread after a certain drift d is calculated from ϕ - $\Delta p/p$ transfer matrix written as

$$\begin{pmatrix} \phi_d \\ \Delta p_d/p_d \end{pmatrix} = \begin{pmatrix} 1 & d \cdot R \\ 0 & 1 \end{pmatrix} \cdot \begin{pmatrix} \phi_0 \\ \Delta p_0/p_0 \end{pmatrix} \quad (4.2)$$

where ϕ_0 , ϕ_d , $\Delta p_0/p$ and $\Delta p_d/p$ describe particle phase and momentum spread at the Quadrupole and after a certain drift d , respectively. R is the transfer factor which depends on the particle velocity β and γ factor written as

$$R = \frac{2\pi}{\beta\lambda\gamma^2} \quad (4.3)$$

where $\lambda = 0.92$ m. The momentum spread was calculated from

$$\frac{\Delta W}{W} = \frac{\gamma + 1}{\gamma} \cdot \frac{\Delta p}{p} \quad (4.4)$$

Figure 4.6 summarizes the bunch length at 12 locations and after some drifts. One can notice that the broadening of the bunches is more pronounced for lower beam energies than for the higher energy. These calculations are used as a first approximation where the emittance growth caused by space charge effects is not considered. For comparison three cases were chosen to drift the beam in LORASR code where space charge taken into account [75]. It consists of 3950 macro particles but a lot of particles are lost after 4 meters. A comparison in three cases are shown in figure 4.7.

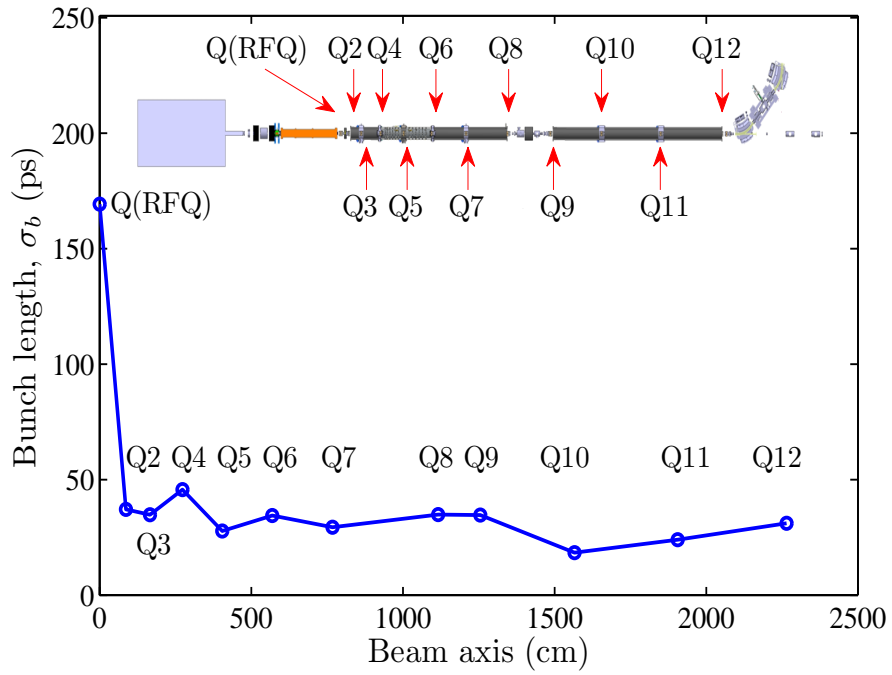


Figure 4.5: rms bunch length after each quadrupole along the proton LINAC.

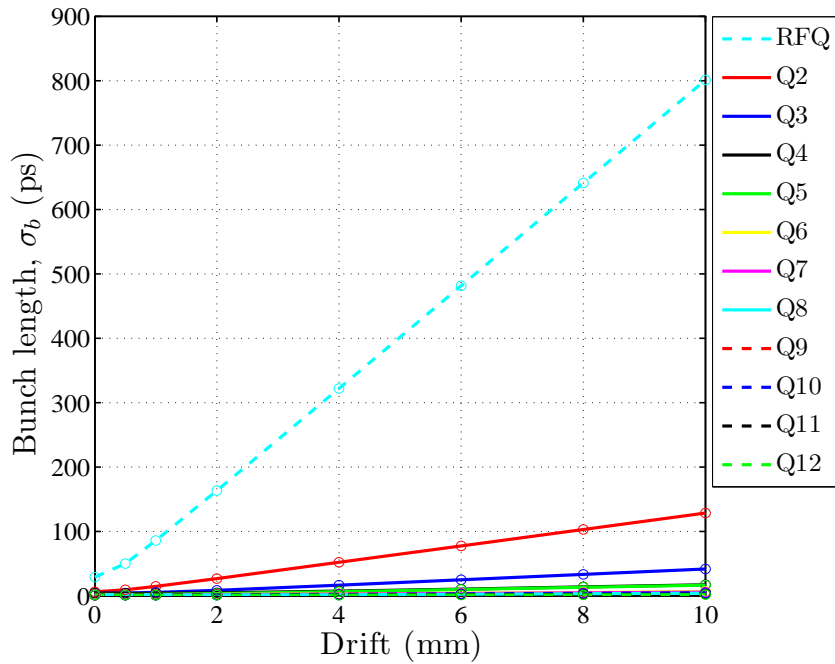


Figure 4.6: Bunch length versus drifts by linear calculations after different focussing elements along the proton LINAC (RFQ, Q2 to Q12).

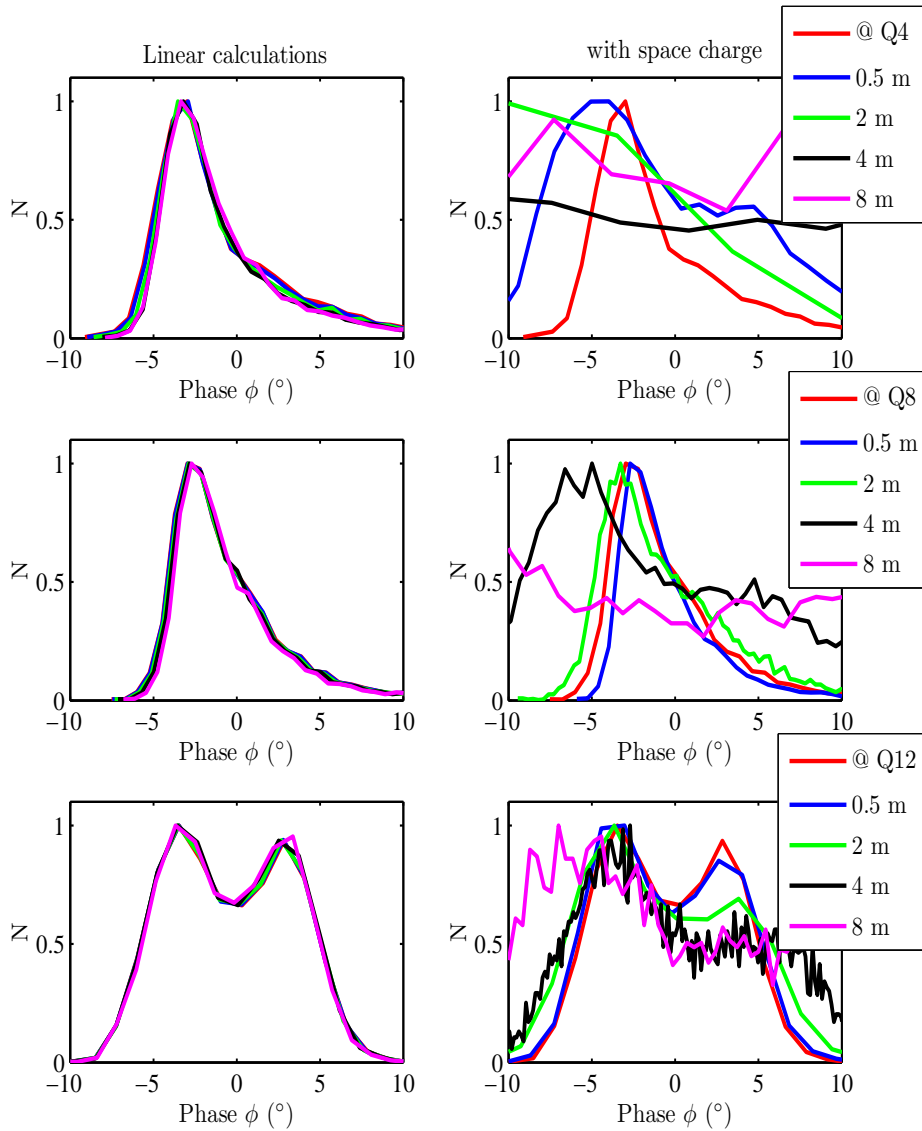


Figure 4.7: Bunch length at several drifts after Q4, Q8 and Q12 calculated by linear calculations (left) and produced from LORASR code with space charge after Q4, Q8 and Q12 (right).

4.3 The BPM Intertank Section

At four locations the BPM will be an integral part of the intertank section between the CCH or CH cavities within an evacuated housing. The mechanical design of those BPMs is most critical due to the tight space which allows only 62 mm insertion length between CCH cavity and magnet walls as shown in figure 4.8.

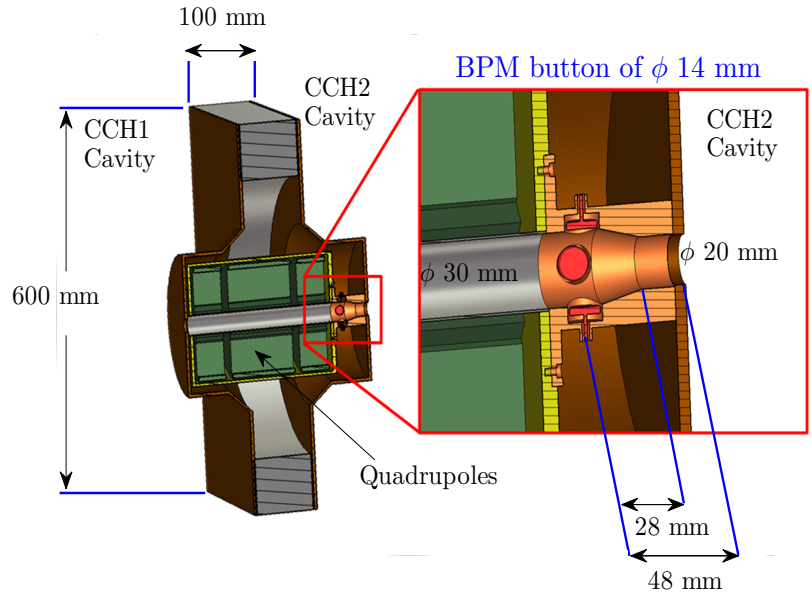


Figure 4.8: The technical layout of the intertank section

On the other hand, as the BPM centre is only 48 mm apart from the upstream cavity boundary, the residual field distribution, so called rf-leakage, generated by the cavity excitation at the BPM location has to be considered. For this purpose numerical simulations were performed to estimate the rf-leakage from the nearby cavity at the BPM coaxial signal path. Special attention was paid to the reduction of the rf-leakage (rf-noise) to an acceptable value in comparison with the beam-induced signal. This section discusses the rf-leakage and shielding properties and the mechanical design of the BPM intertank section.

4.3.1 RF-Leakage Calculations

The maximum electric field gradient along the cavity axis is around 10 MV/m and the distance from the BPM to the center of the last gap is about 10 cm [58]. The first simulation approach handles the realistic situation of rf-field propagation from the cavity into the beam tube and the BPM's plates [76]. In this approach, a very precise CST

model of the first three cavity drift tubes and the intertank section containing the BPM was created. The electric field strength in this simulation is assumed to be $E_{z,peak} = 21.2$ MV/m in the first acceleration gap. The resulting voltage on the BPM's co-axial signal path is calculated as shown in figure 4.9 [77].

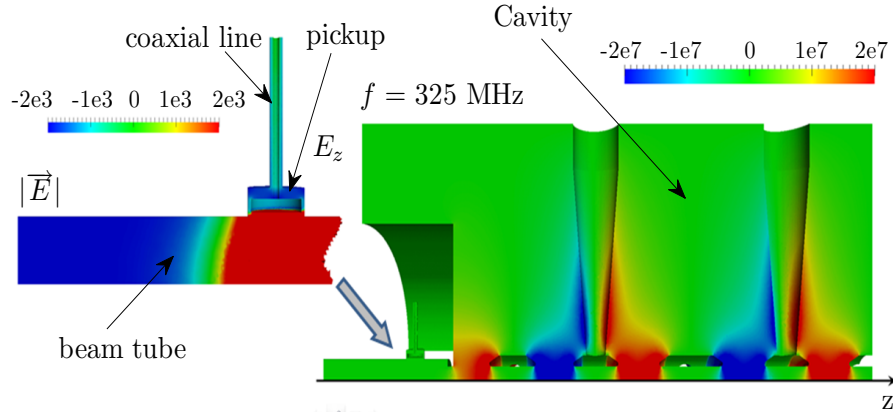


Figure 4.9: Distribution of the electric field strength showing the coupling of the rf-field to the BPM (courtesy of W. Ackermann, TU Darmstadt)

The simulation gives the solution of the large-scale eigenvalue problem which has been handled with a parallel implementation of the Jacobi-Davidson algorithm [78] but requires a large amount of CPU time and memory. The result from the simulation gives a peak voltage of 1.03 V extracted at the coaxial line of the pickup [76]. Additionally, it has been shown that almost the same result can be approximated by a simple electro-static approach using CST electro-static solver when applying a similar static potential on the first drift tube in the cavity. The static potential obtained at BPM's coaxial line from CST electro-static solver is 0.92 V [77].

Based on the above results a 3D model of four button electrodes and first cavity gap is created in CST electro-static solver to improve rf-shielding properties. This relatively fast approach helps to study the rf shielding properties by changing the BPM housing geometries and the BPM locations as shown in figure 4.10. A conical section is introduced to connect the BPM pipe to the CCH entrance due to the different beam pipe apertures. The BPM of 30 mm tube diameter is connected to the CCH entrance flange of 20 mm diameter as shown in figure 4.11. The beam reaches the BPM position after it gets focussed by quadrupole magnet before it enters the CCH cavity.

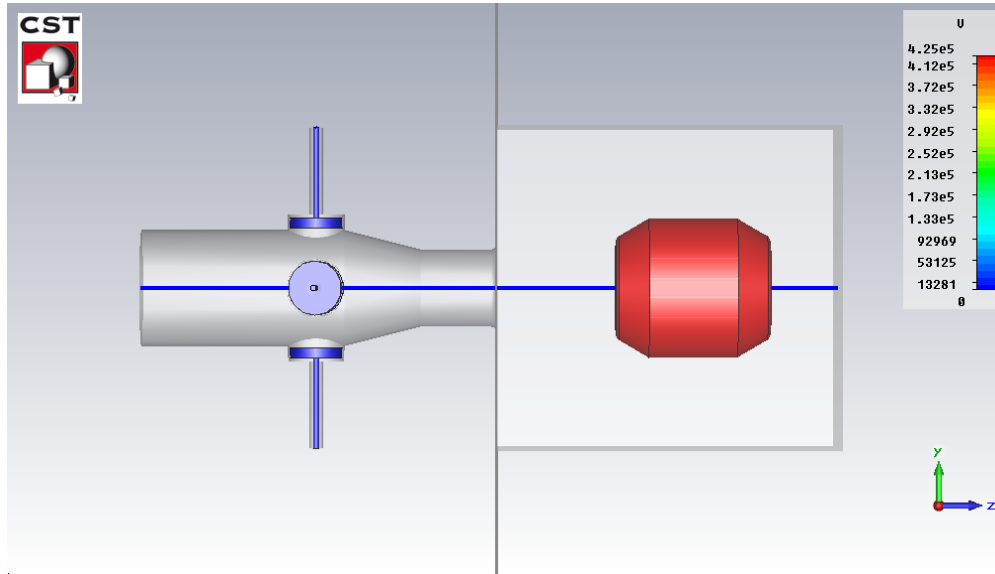


Figure 4.10: A 3D model of four button electrodes and first cavity gap created in CST electro-static solver

In this model, the rf shielding properties are investigated by applying a static potential on the closest drift tube in the cavity. The maximum potential applied on the gap in the cavity proton LINAC is about 450 kV [58]. The applied voltage on the gap was chosen to be 425 kV. The BPM location and the length of the tube and the cone have been modified. The potential along z-axis and the resulting voltage on the BPM's plates have been calculated as a function of cone length l_{cone} for a fixed tube length and as a function of tube length l_{tube} for fixed cone length.

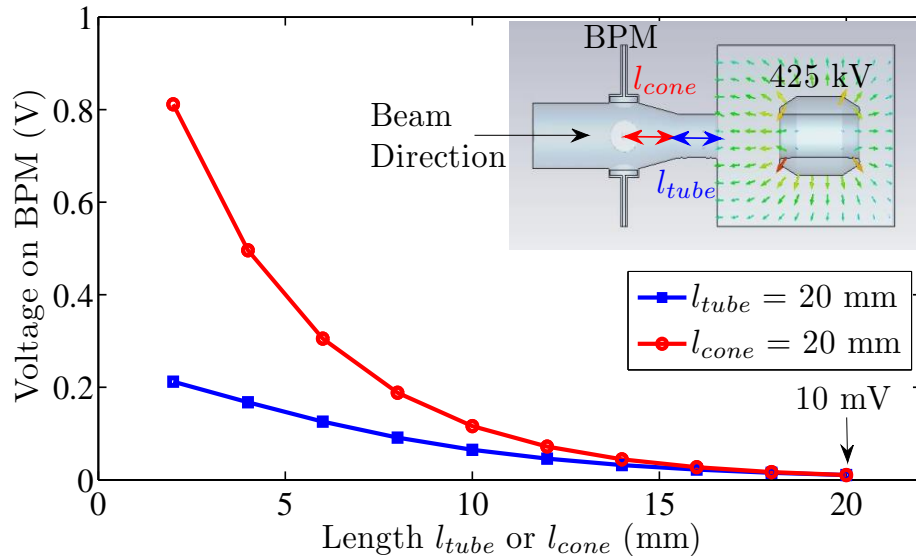


Figure 4.11: Shielding properties as a function of the length of the cone l_{cone} (red) for a fixed length of the tube or as a function of the cylindrical tube length l_{tube} (blue) for fixed cone length. For the electro-static solver the first drift tube is set to 425 kV. Sketch of the geometry and electric field distribution are shown in the up-right corner.

The resulting voltage recorded on the BPM co-axial signal path is demonstrated in figure 4.11 [74]. The results show the influence of BPM locations and housing shape on the field propagation. The important result from these simulations is that the rf-pickup background signal can be reduced to ~ 10 mV amplitude as the length of cone and tube is 20 mm each. This value is satisfactory compared to the signal voltage of ~ 1 V for a nominal beam current of 35 mA. Consequently, it has been decided to fix the BPM housing geometry to 40 mm (20 mm cone and 20 mm tube) so that there is no influence on the beam dynamic. The potential strength along z axis and the corresponding electric field for the chosen geometry (20 mm tube and 20 mm cone) is shown in figure 4.12.

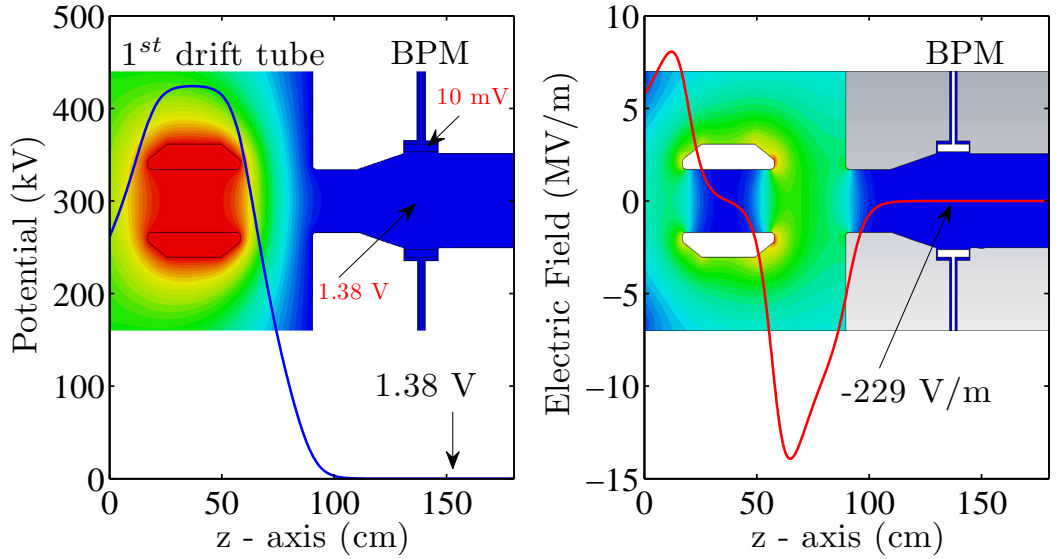


Figure 4.12: Voltage (left) and electric field (right) distribution along z axis. The BPM (tube diameter of 30 mm) is connected to the CCH entrance flange (20 mm) by a conical section with a length of 20 mm

Numerically, one can treat the beam pipe extended from the cavity entrance to the BPM location as a cylindrical waveguide of certain diameter d with a field excited by the CH cavity wave. The cut-off frequency of a TM-mode in cylindrical waveguide of $d = 20$ mm diameter is determined by [79]

$$f_c = c/\lambda_c = \frac{\pi \cdot d}{\chi_{mn}} \quad (4.5)$$

where χ_{mn} is the root of the bessel function $J_0(r)$, c is the speed of light. The first order χ_{21} is 3.054 and the resulting lower cutoff frequency is 14.58 GHz. The cut-off frequency is much higher than excitation frequency from the cavity which is 325.224 MHz. This leads to an exponential damping proportional to $\exp(-z/\lambda_h)$, where z is the distance from the

cavity port and λ_h the wavelength of the excited wave calculated from [79]

$$\lambda_h = \frac{\lambda_0}{\sqrt{1 - \left(\frac{\lambda_0}{\lambda_c}\right)^2}} \quad (4.6)$$

where λ_0 is the wave length in vacuum = 0.923 m, λ_c is the wave length of the cut-off frequency = 0.026 m. The damping of the rf-field in a cylindrical waveguide of radius r along the z -axis is given by [79]

$$E_{z,0,1} = E_{z_0} \cdot J(k_r \cdot r) \cdot \exp\left(\frac{i \cdot 2\pi \cdot z}{\lambda_h}\right) \quad (4.7)$$

where $k_r = \omega/c$. The damping curve for a certain frequency f depends on the applied voltage, wave guide geometry, cut-off frequency and the distance from the cavity l . The exponential damping curve of the rf voltage after a certain distance l can be calculated by [80]

$$U_2 = \frac{U_1}{10^{D/20}} \quad (4.8)$$

where U_1 and U_2 are the voltage applied on the gape and the resulting voltage at distance l , respectively and D is the damping calculated in dB unit from

$$D = 1.832 \times 10^{-9} \times f_c \times \sqrt{1 - \left(\frac{f_0}{f_c}\right)^2} \times l \quad (4.9)$$

The applied voltage on the gap in this calculation is 425 kV. The calculation of the damping and the field strength on z axis are shown in figure 4.13. The resulting voltage on z axis at the BPM location is about 0.25 V.

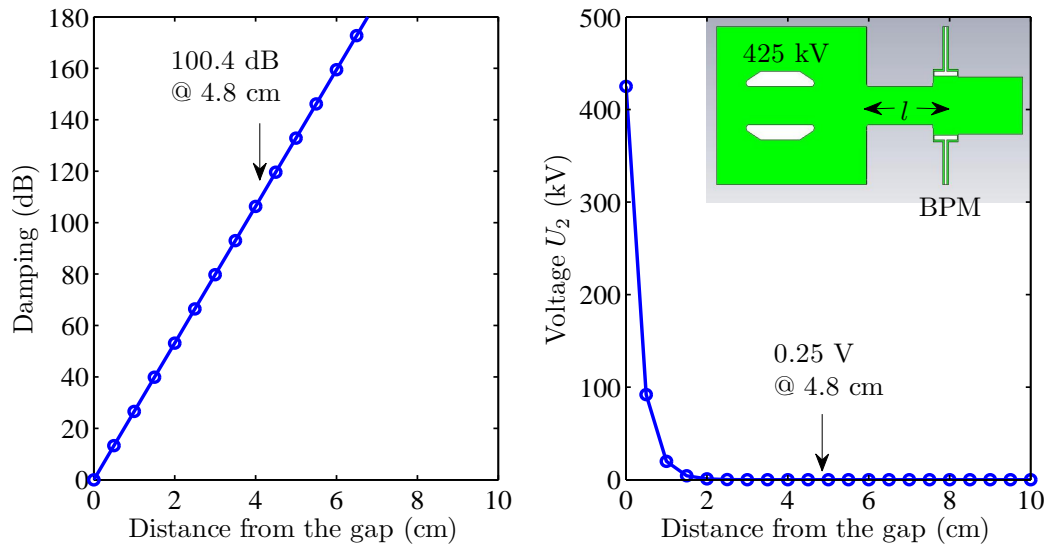


Figure 4.13: Damping versus the distance from the gap (left). Voltage on z axis versus the distance from the gap (right)

For comparison, a 3D model with a tube of 20 mm diameter extended from the cavity entrance to the BPM location was created using the CST static solver. The potential along the axis was calculated. From the electrostatic model the voltage on z axis at the BPM location is about 0.49 V and 2 mV on the BPM coaxial signal path.

4.3.2 The BPM intertank Prototype : Design and Fabrication

The BPM consists of four button pickups delivering signals induced by the proton beam. The beam electric field on the inner surface of the button induces an image current generating a measurable voltage on the pickup electrodes as explained in 3.1. The mechanical model of the pickup is adapted to fit into the intertank section between two CCH cavities so that the same pickup can be used in the other BPMs locations.

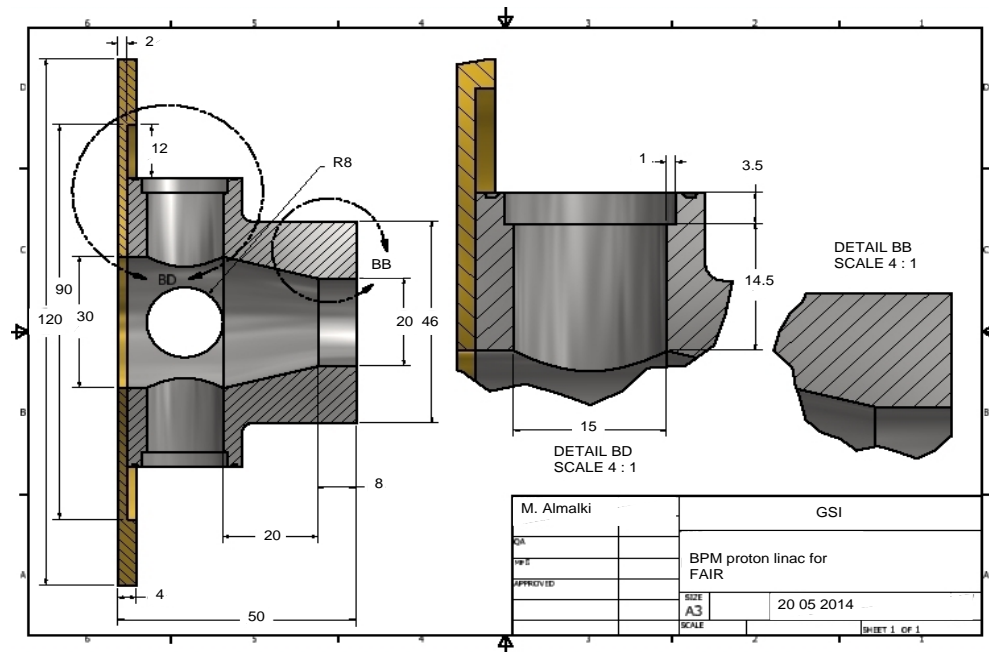


Figure 4.14: CAD drawing in mm unit of the BPM housing and the flange

The BPM intertank will be installed in the available space in the intertank between CCH cavity and quadrupole magnet. It was designed based on the previous numerical simulations as well as on the given intertank dimensions. The intertank section is 300 mm in length which includes a BPM, a flange and a magnet [58]. The BPM tube aperture is 30 mm in diameter connected to the cavity entrance of 20 mm in diameter. The total BPM increment length is 62 mm, CAD drawing is shown in figure 4.14. A separated BPM-body fixed to the quadrupole housing with a flange and dowel pins installed on flanges. A screw

passes through each housing to fit with the flange. The type of flange has to be finally adapted to the quadrupole magnet cylinder. The cable installation within the intertank section must be considered as well.

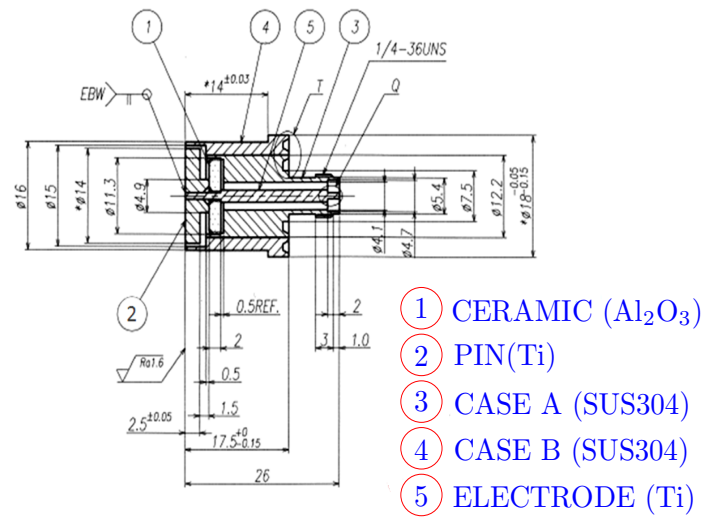


Figure 4.15: Scheme of commercial button from Kyocera



Figure 4.16: Kyocera pickup final assembly.

A commercial 14 mm button pickup produced by Kyocera [73] has been chosen for the first BPM prototype. The button sub-assembly unit consists of a central conductor with a titanium electrode of 2.5 mm thickness connected to a SMA-type connector for signal measurement as shown schematically in figure 4.15. The characteristic impedance

of the structure is 50Ω . The gap size between the electrode and the outer vacuum pipe is 0.5 mm. The Kyocera pickup final assembly is shown in figure 4.16.

The simulation using the CST software and the Time Domain Reflectometer (TDR) measurements show that the gap size and button thickness have a significant influence on the electromagnetic properties of the structure, namely the 50Ω impedance matching. The pickup performance is investigated by simulation calculations to characterize the influence of pickup capacitance on the output signal at a different beam velocity. The goal is to optimize the pickup geometry so that better impedance matching can be archived as will be discussed in detail in chapter 5.

The first prototype of the BPM mechanical design with 30 mm aperture was manufactured at CEA. The prototype will be used for the tests with coaxial wire and for the planned rf-leakage background measurements on a CH prototype cavity at the GSI. The assembly of the BPM consists of four Kyocera buttons of 14 mm diameter, a housing and a flange as shown in figure 4.17. The buttons are recessed 0.5 mm from the inner radius of the tube to protect the electrode from stray beam impingement. Since the BPM is located near the quadropole magnet, a non-magnetic design is mandatory. Therefore, the housing and the flange are fabricated from 316 LN stainless steel. The buttons will be welded to the housing and both will be joined with the flange at the final assembly.

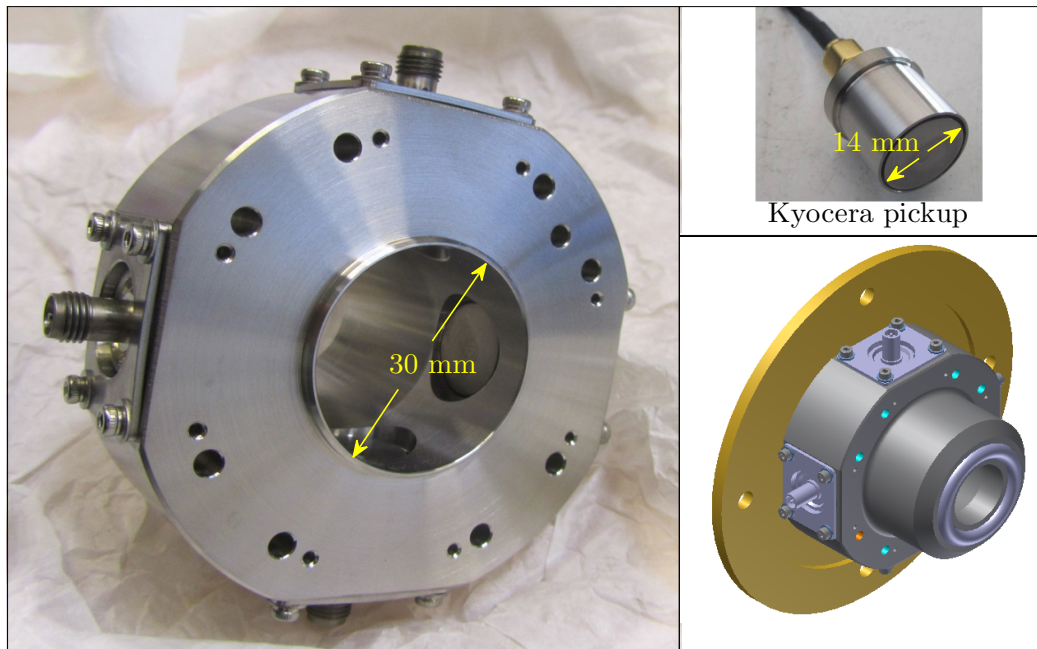


Figure 4.17: The first BPM prototype with four Kyocera buttons (left). The Kyocera pickup and CAD drawing of the BPM with the flange (right)

BPMs Numerical Simulation with CST STUDIO SUITE

This chapter discusses detailed simulations of the pickup design parameters with the finite element code CST [81]. The code is based on the Finite Integration Technique (FIT) and Perfect Boundary Approximation (PBA) algorithms [82,83]. The general purpose of the CST Suite is to simulate electromagnetic fields where the entire volume is discretized. Three CST STUDIO - Solvers are used for the BPM simulations; CST ELECTROMAGNETIC STUDIO - Solver (CST EM), CST MICROWAVE STUDIO (CST MWS) and CST PARTICLE STUDIO (CST PS).

In the first part of this chapter the pickup design and its electrical properties are discussed and investigated with two CST solvers. The CST ELECTROMAGNETIC STUDIO solver is used to calculate the capacitance of the pickup structure for different button geometries. The CST MICROWAVE STUDIO solver is used to investigate and to optimize the pickup geometries to improve the electrical properties of the design, namely the impedance matching of the pickup transmission line.

In the second part of this chapter the Wakefield solver in CST PARTICLE STUDIO is employed to test the BPM response to particle beam. Different pickup geometries are investigated for various beam parameters. The time domain and the frequency domain responses of the BPM output signals reflecting the BPM's interaction with the beam are extracted and compared. These simulations cover the BPM performance test and design optimization. Additionally, some related investigations have been performed such as bunch length variation, button depth in respect to the beam pipe wall, button size, beam pipe diameter, the BPM sensitivity calculations, BPM position map and beam phase variation as a function of the beam position. The Kyocera pickup design introduced in Sec. 4.3.2 is considered as the base geometry for most of the calculations.

5.1 Problem Statement

The first problem statement is to calculate the capacitance of the pickup for different geometries. The importance of pickup capacitance concerns two items; the first is that the shape of the output signal, which is characterized by transfer impedance (as discussed in Sec. 3.2) is influenced by the pickup capacitance. The second is that the pickup button electrode can create severe impedance mismatch in the pickup transmission line due to its capacitance and this can cause a disturbance of the signal propagation. This brings us to the second problem statement which is the optimization of the pickup design to have appropriate 50Ω impedance matching to the attached coaxial cable. A proper impedance matching results in a higher signal amplitude on the one hand and less deformation in signal on the other which is required for Time-of-flight measurements. Therefore, the 50Ω impedance matching of the pickup transmission line must be investigated and improved.

5.2 Pickup Simulations

The BPM consists of four pickup electrodes mounted orthogonally in a beam pipe of 30 or 50 mm diameter. The pickup model in these simulations consists of an inner conductor connected to a pickup electrode called a button electrode. It is assumed that the inner conductor of the pickup electrode is similar to a coaxial cable with a characteristic impedance of 50Ω given by [84]

$$Z_0 = \frac{59.96}{\sqrt{\epsilon_r}} \ln \frac{b}{a} \approx \frac{138}{\sqrt{\epsilon_r}} \log_{10} \frac{b}{a} \quad [\Omega] \quad (5.1)$$

where a is the radius of the inner conductor, b is the radius of the shield, ϵ_r is the relative static permittivity = 1 for vacuum and ~ 1 for air. For a 50Ω impedance, the ratio b/a is important. In these calculations the value of a and b were chosen to be 0.5 mm and 1.151 mm, respectively, which can be different in the practical realization. The presence of the button at the end of the pickup structure creates additional capacitance which can also be calculated from a simple geometrical coaxial model formula as [85]

$$C = \frac{2\pi\epsilon l}{\ln(R_2/R_1)} \quad (5.2)$$

where ϵ is the dielectric constant, l is the button thickness, R_1 and R_2 are the radii of the button and the shield, respectively.

In this section the capacitance and electrical properties of the pickup structure are discussed for the Kyocera model as well as for some other button geometries. The button geometry will be modified by varying the button thickness and the gap between the button

and the housing. The total length of the structure is fixed at 26 mm as shown in the Kyocera sketch in figure 4.15. The influence of the button capacitance on the signal propagation will be explored.

5.2.1 Pickup Capacitance

The CST EM STUDIO - Solver calculates the static capacitance of the pickup directly for the given geometry when applying a certain potential. The button electrode and the inner conductor were set to the perfect electric conductor (PEC). In these calculations 1 V is applied on the button and the inner conductor while the surrounding represents a metallic ground as shown in figure 5.1. The number of mesh cells is $\sim 5 \times 10^6$ and the calculation time needed to perform one run is about 12 minutes.

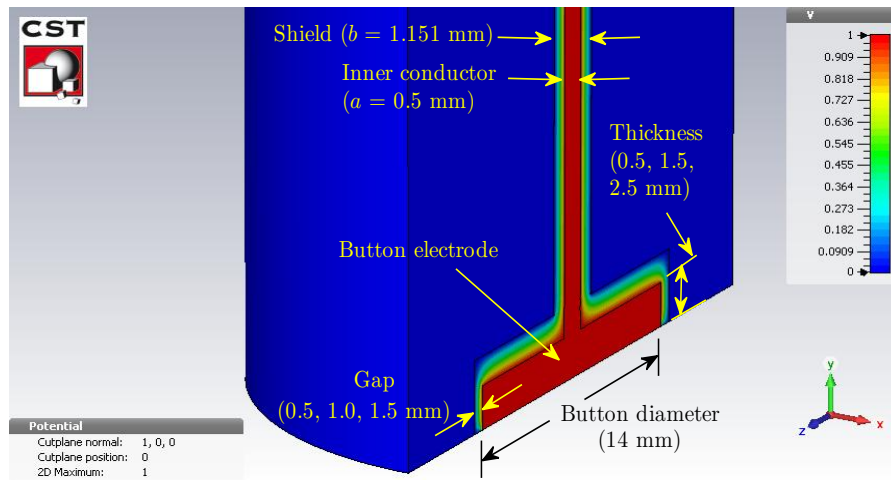


Figure 5.1: The potential distribution on a cut-plane in the pickup structure including a button electrode and an inner conductor set to 1 V

The pickup capacitance is calculated as a function of the button thickness and the gap size between the button and the shield. For a fixed button thickness the gap is given at values of 0.5, 1.0 and 1.5 mm. For a fixed gap the button thickness is varied by values of 0.5, 1.5 and 2.5 mm. The results of the nine simulation runs are shown in figure 5.2. The minimum capacitance value is 4.37 pF obtained as the button thickness is 0.5 mm and the gap is 1.5 mm. The Kyocera model records the highest capacitance value of 6.15 pF which is expected due to its large thickness and small gap. Almost proportional increase in the pickup capacitance is observed in most cases. Only one exception as the button thickness is fixed to 0.5 mm, there is no significant change in pickup capacitance as the gap is varied. It is obvious that a larger button thickness and a smaller gap increase

the pickup capacitance. As the pickup capacitance increases the cut-off frequency of the pickup decreases consequently calculated from $f_{cut} = (2\pi RC)^{-1}$.

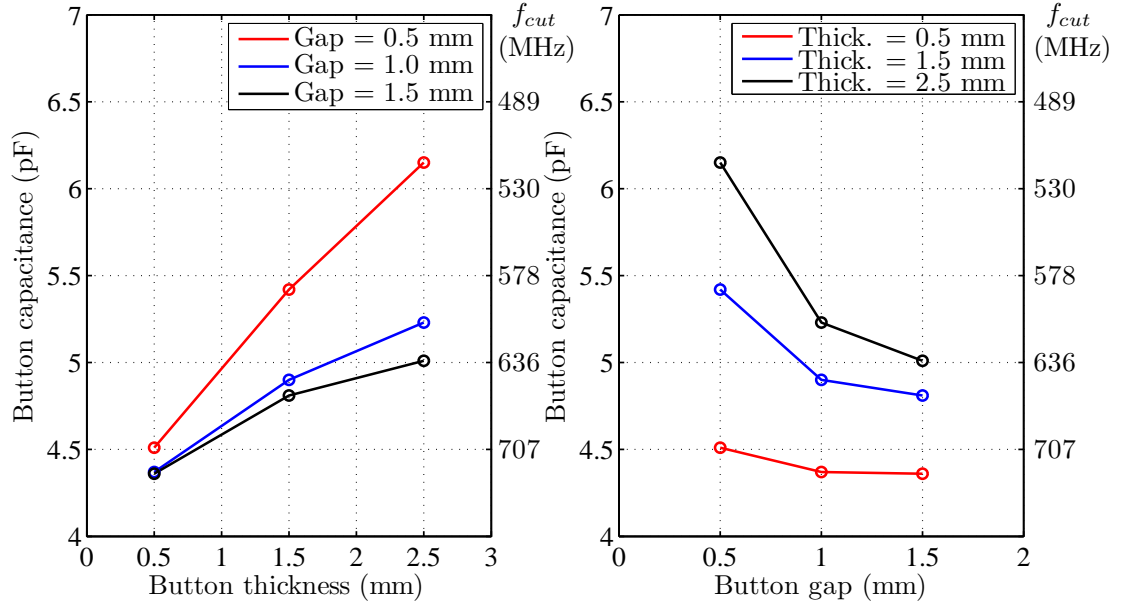


Figure 5.2: The change in pickup capacitance as a function of button thickness at fixed gap size 0.5, 1.0 and 1.5 mm (left) and as a function of gap size at fixed button thickness 0.5, 1.5 and 2.5 mm (right).

5.2.2 Pickup Electrical Properties

The electrical properties of the pickup have been investigated using the CST MICROWAVE STUDIO solver. A 3D model of the pickup has been created to simulate the pickup transmission line response with a pulsed signal. The time impedance profile of the transmission line is obtained from Time Domain Refractometry (TDR). The transmission line impedance as a function of frequency is extracted from the Smith chart. The simulated pickup structure represents an open circuit which fed with a Gaussian pulsed signal. The simulation is executed by defining a discrete port at the end of the coaxial line set to a 50Ω impedance as shown in figure 5.3. The excitation signal is transmitted into the pickup button and the reflected signal is analyzed.

The TDR plot displays the impedance change along the transmission line. It starts with 0 units for the nominal impedance of 50Ω and demonstrates the pickup impedance characteristics over time. The quality of impedance matching Z is calculated by [86]

$$Z = Z_0 \frac{1 + \rho_V}{1 - \rho_V} \quad (5.3)$$

where ρ_V is the voltage reflection coefficient and Z_0 is the $50\ \Omega$ nominal impedance. Considering the coaxial pickup as transmission line, $Z \sim \sqrt{L/C}$ where L is the inductance and C is the capacitance per unit length, respectively. The impedance mismatch along the line occurs only when the ratio of inductance and capacitance changes. The ideal case depicts an open circuit of a coaxial structure with a reflection coefficient of 1 so that the signal is completely reflected with the same amplitude and sign. In the pickup case, the presence of the button at the end of the pickup structure causes impedance mismatch due to its high capacitance. This unpleasant effect is not avoidable but it can be minimized if the pickup geometry is reconsidered.

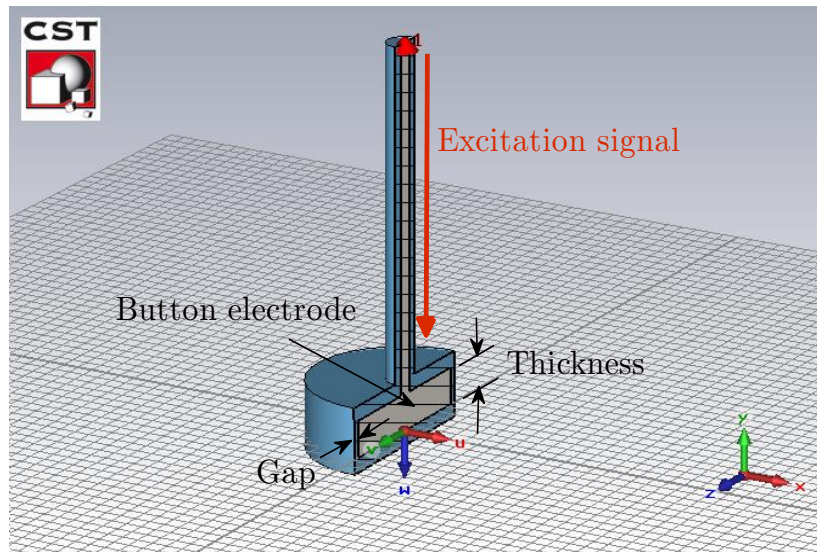


Figure 5.3: 3D model of Kyocera button.

As depicted in the TDR plots in figure 5.4 (right), there is a situation where the impedance mismatch appears. The impedance steps down to the negative side of the plot at the button position. The negative direction of the dip indicates that the reflection is caused by a capacity so that the capacitance is too high compared to the inductance. Consequently, the reflected signal will be distorted and the deformation increases with the dip in the TDR plot. Figure 5.4 (left) shows the excitation signal and the distortion on the reflected signal.

All nine pickup geometries shown in the previous section have been simulated and the TDR plots have been produced. For the sake of simplicity, only three models have been highlighted in this analysis. The first model is the Kyocera design of 2.5 mm thickness and 0.5 mm gap. This design possesses the higher capacitance value of 6.15 pF as already shown in figure 5.2. The second model is chosen to be the model of the lowest capacitance

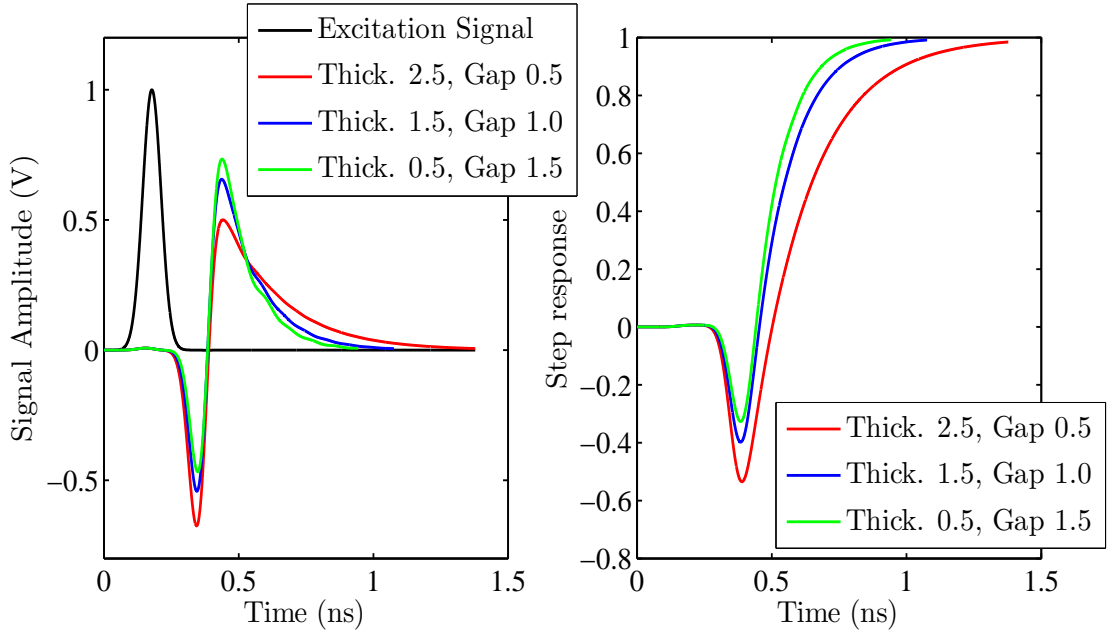


Figure 5.4: The excitation and the reflected signals (left) and the corresponding TDR plots (right) for three button geometries; (2.5 mm thickness, 0.5 mm gap)→ **Kyocera button**, (1.5 mm thickness, 1 mm gap) and (0.5 mm thickness, 1.5 mm gap).

value which is 4.37 pF. This model has 0.5 mm thickness and 1.5 mm gap. The third model is the one with a capacitance value of 4.92 pF. This value is chosen to be in between the previous selected designs. This model has 1.5 mm thickness and 1 mm gap.

Looking at the reflected signal plots in figure 5.4 (left) one can observe that the reflected signal suffers more distortion for the button of higher capacitance; the Kyocera model in this case. The deformation increases with the button capacitance or in other words with the voltage drop in the TDR plot as shown in figure 5.4 (right). The Kyocera model shows the lowest drop in the TDR plot in comparison to the other two designs. It has a drop in the voltage reflection coefficient of $\rho_V = -0.50$ causing an impedance step down to $\sim 17 \Omega$, as calculated from equation 5.3. The second and third designs have impedance step down to 22Ω ($\rho_V = -0.39$) and 25.8Ω ($\rho_V = -0.32$), respectively. These results give the first impression about of the effect of button capacitance on the signal as it is propagating through the pickup structure. Now this effect has to be probed in order to see the impact of such behaviour on the BPM performance. For this reason these nine pickup models will be examined in the following section where the BPM response is investigated with a particle beam.

In parallel to simulations the TDR of the Kyocera pickup is measured. A Tektronix analog TDR signal source is used to transmit a fast signal to the pickup and to measure the reflected signal. The measured TDR plot shows a similar behaviour where the TDR plot

displays the impedance change at the button position due to its capacitance as depicted in figure 5.5. The impedance mismatch causes an impedance step down to $\sim 20 \Omega$. This result shows a good agreement with the simulation value which gives 17Ω . The TDR plot shows that up to the button, the signal experiences no significant disturbance. This indicates that the isolation materials inside the pickup are well-matched.

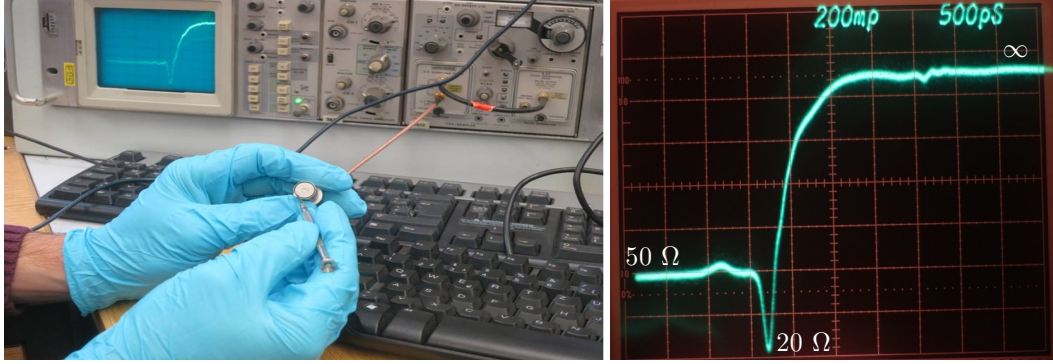


Figure 5.5: The TDR measurements for the 14 mm diameter Kyocera button pickup using a Tektronix analog TDR signal source. The reflection coefficient $\rho_V \approx 400 m\rho$ causes an impedance step down to $\approx 20 \Omega$.

The Smith Chart provides a graphical representation of the reflection coefficient with normalized impedance showing the capacitive and inductive loads of the transmission line as a function of frequency. In essence, it illustrates the characteristic of the equivalent impedance of the pickup transmission line. The equivalent impedance of the open circuit is strictly reactive and has only negative imaginary part given theoretically as [86]

$$Z_{th} = iZ_0 \cdot \cot(k \cdot l) \quad (5.4)$$

where Z_0 is the transmission line impedance of the pickup structure, k is the wave number and l is the length of the pickup structure. The equivalent impedance takes either $1/\omega C$ for the capacitive part or $1/\omega L$ for the inductive one. The negative reactance arc is shown in the lower half of the chart, making the transmission line impedance pure capacitive and the positive reactance sweep the arc in the upper half of the chart, making impedance pure inductive.

Figure 5.6 shows the Smith chart of the Kyocera model extracted from the simulation. The graph rotates clockwise, while the frequency swept from 0 MHz to a given frequency range. In the interesting frequency range; the first two harmonics, 325 MHz, 650 MHz the capacitive load from the button is obvious and the imaginary part of the impedance give -64.54Ω and -17.33Ω . The calculated capacitive load at the first and the second

harmonics are 7.58 pF and 14.12 pF, respectively. At ~ 880 MHz the quarter wave length of the pickup structure is reached and the transmission line impedance will switch to be inductive reactance. This point is close to 0-end of the pure resistance line and represent a short circuit. The geometrical length of the transmission line represented by the pickup is $\lambda/4_{880MHz} \sim 8.5$ cm. At the third harmonic (975 MHz) the reactive load is inductive reactance. Figure 5.7 shows the Smith chart for the pickup structure derived from the measurements using a Network Analyser. The measured capacitive load at the first two harmonics is shown in the graph and they correspond with the simulations.

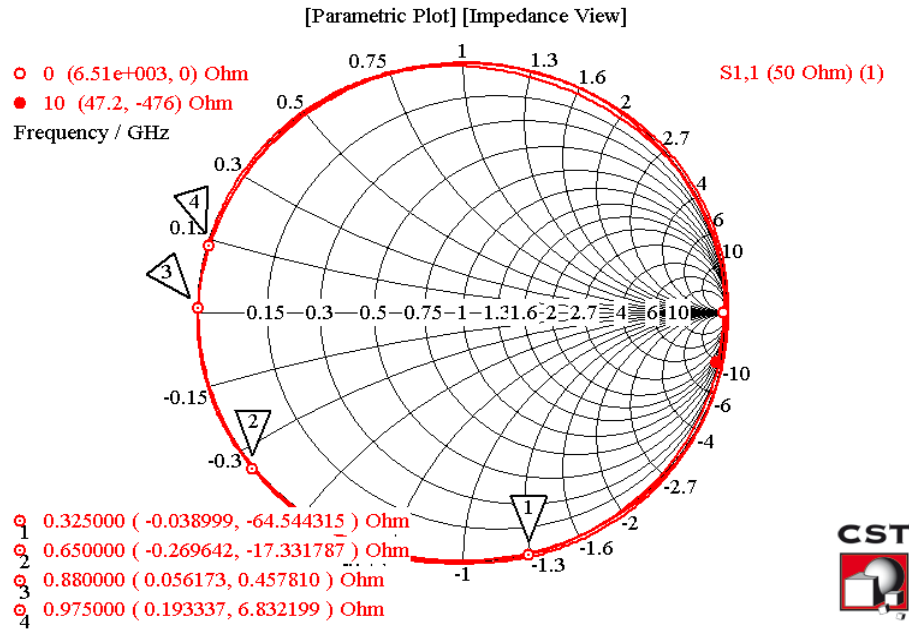


Figure 5.6: Smith chart produced by the simulations of the 14 mm diameter Kyocera button pickup showing the impedance at different frequencies

To conclude, the impedance matching characteristics of the pickup has to be optimized to achieve a suitable 50Ω impedance along the pickup structure. This can be achieved by modifying the button geometry to reduce the capacitance. A large button gap and a small button thickness are required for the pickup optimization. Having proper impedance matching will reduce the disturbance of the signal propagation and will improve the pickup performance. Such disturbance on the signal propagation has minor consequences for beam position determination. However, for the Time-of-flight (TOF) measurements, this effect is critical due to the deformation of the time-domain signal. Moreover, the BPM performance investigations in the next section (Sec. 5.3) will show that a button of better impedance matching delivers a higher amplitude signal.

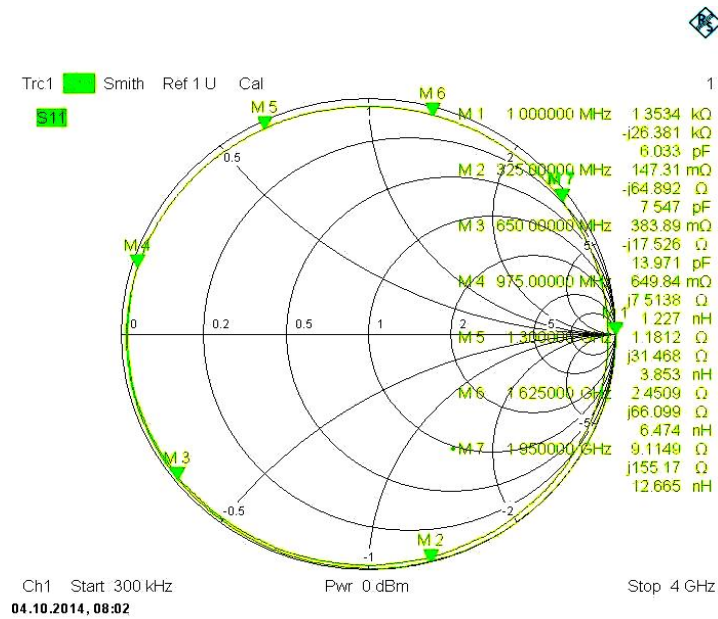


Figure 5.7: Smith chart obtained from the measurement for the 14 mm diameter Kyocera button pickup showing the impedance at different frequencies

5.3 BPM Response Investigations

The CST Particle Studio has been extensively used for the BPM response investigations. It specializes in 3D computations of the charged particles dynamics offering several solvers. The Wakefield solver is the most appropriate for studying the BPM response and the simulations are driven by a bunch of charged particles in the time domain. Like other CST solvers the simulations require discretization of the entire volume but in the CST Particle Studio only a Cartesian (hexahedral) mesh type is available.

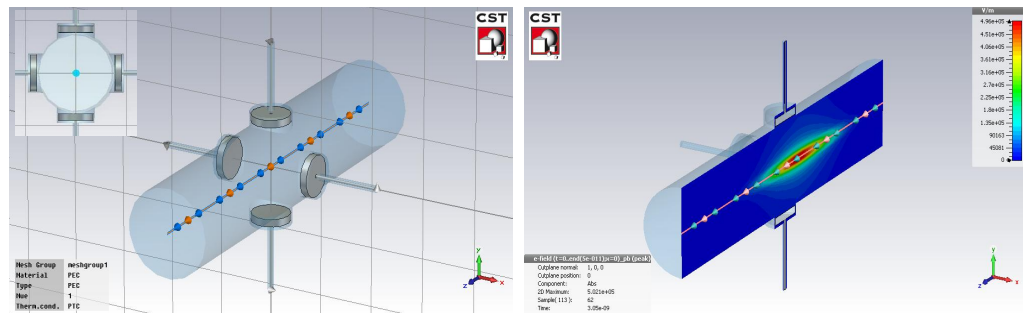


Figure 5.8: A 3D model of the pick-up monitor as simulated in CST Particle Studio (left). The absolute value of the electric field of a bunch of $\sigma = 100$ ps long and $\beta = 0.37$ (right)

A 3D model of a BPM of four button electrodes has been created in the CST Particle Studio as shown in figure 5.8. The background and the pickup electrodes are set to perfect

electric conductor (PEC) and the volume in which the beam is travelling is set to vacuum. The electric field of the particle beam couples to the BPM electrodes inducing measurable signals. The beam-induced pickup signals are measured at predefined discrete output ports located at the end of the pickup feedthroughs shown in figure 5.9.

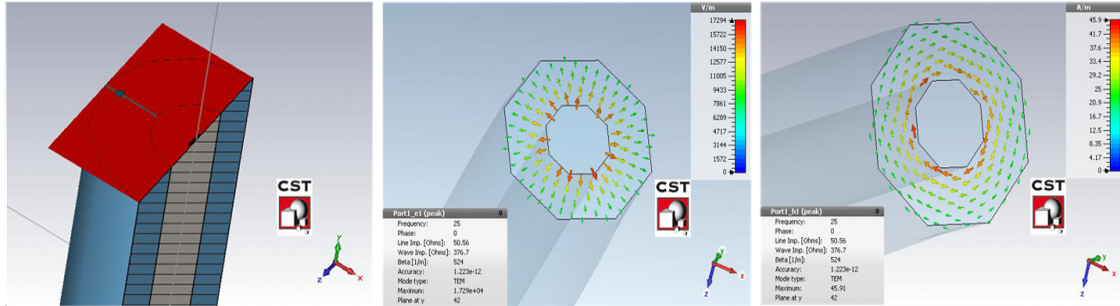


Figure 5.9: a discrete port located at the end of the electrodes feedthroughs (left). Electric field (middle). Magnetic field (right).

The wakefield has been simulated up to a 150 mm length along the beam coordinate for most of the calculations except in bunch length investigation (Sec. 5.7) the length is doubled for bunches longer than $\sigma = 600$ ps. The excitation source is defined by a Gaussian-shaped longitudinal charge distribution with beam bunch charge of 1 nC in the z direction. The ports are set to a 50Ω impedance. The pickup response, expressed as the output signal in time and frequency domains, is obtained for each simulation run reflecting the pickup's interaction with the beam. A typical procedure in the Wakefield solver for extracting time domain signal and its Fourier transformation by the transfer impedance concept are sketched for two signals in figure 5.10.

The output voltages convergence versus mesh size has been investigated prior to utilizing the results. The convergence has been examined at three beam velocity $\beta = 0.08, 0.27$ and 0.37 . The bunch length is chosen to be 150 ps. Figure 5.11 demonstrates the results of the Wakefield solver at different mesh settings. The results show a solid convergence of the output signals and frequency spectrums in the interesting frequency range for $\beta = 0.08, 0.27$ and 0.37 . A visible difference is only observed in the frequency spectrum for $\beta = 0.08$ with the mesh setting of 150000.

All simulations have been performed with the maximum size possible in the range from 0.45×10^6 to 1×10^6 mesh cells depending on the beam velocity and the bunch length. For $\beta = 0.37$ the calculation time needed to perform one run with 1×10^6 mesh cells is between 8 to 15 hours while for $\beta = 0.27$ is between 10 to 20 hours. For $\beta = 0.08$ some simulations for $\beta = 0.08$ need days per run with 0.45×10^6 mesh cells.

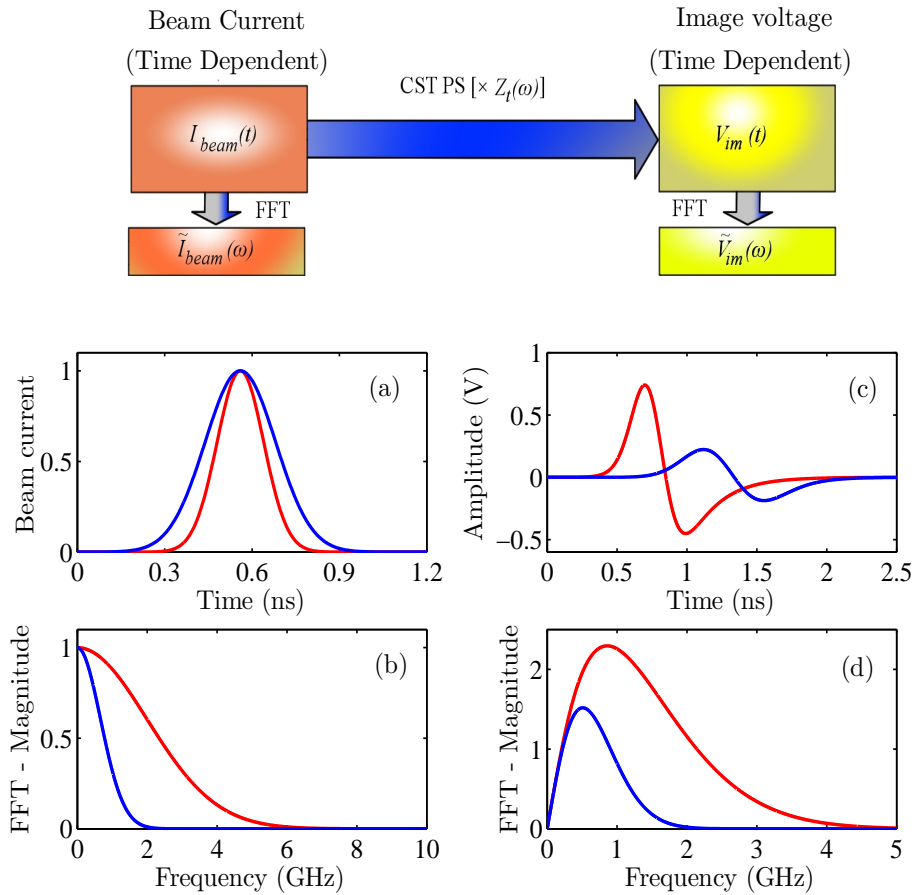


Figure 5.10: Two Gaussian-shaped signals demonstrate the beam current in the time domain (a) are simulated with CST Particle studio (Wakefield solver). They are multiplied by the transfer impedance of the pickup structure to give the time domain voltage output on the pickup coaxial port (c). Post-processing can be performed to obtain Fourier components of the input signal (b) and (d) output signals.

The calculation algorithm needs the bunch to be sent from the outside of the simulated volume. At $\beta = 1$, the field lines are perpendicular to the beam and the pulse can be located just at the entrance of the model. However, for a beam of $\beta \ll 1$ the computed volume needs to be significantly extended outside the defined model in z direction and this makes the simulation much slower. Another constraint is the fact that the shorter bunch requires a significantly denser mesh and, thus, a longer simulation time. Sometimes this makes the algorithm fail to find the stable step size required to perform the calculations or the number of required mesh cells becomes larger than available at the normal computer memory (Pentium(R) Dual-Core CPU E5400, 2.70 GHz, RAM 10 GB, System type 64 Bit). In particular, the simulation becomes unstable for a bunch length shorter than 30 ps and beam velocity of $\beta = 0.08$.

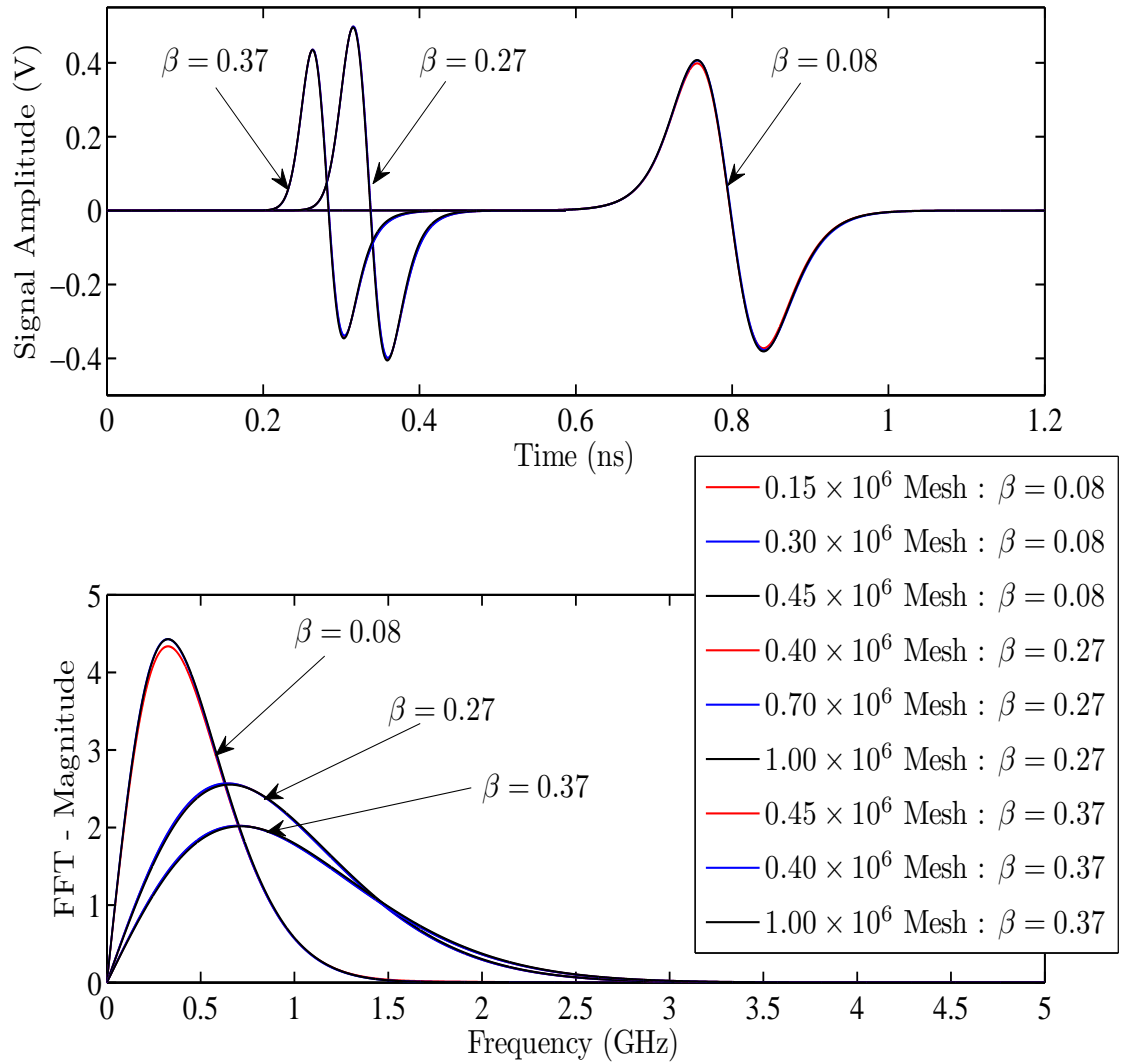


Figure 5.11: BPM output voltage from a single port in time (up) and frequency (down) domains versus mesh size. The beam parameters are $\beta = 0.08, 0.27$ and 0.37 , $\sigma = 150$ ps, 1nC bunch charge.

5.4 Button Design Investigations

All pickup geometries discussed in Sec. 5.2 are simulated in the Particle Studio Wakefield solver. For the sake of simplicity, only the three designs mentioned in Sec. 5.2.2 are shown and discussed. The first design is the Kyocera model of 2.5 mm thickness and 0.5 mm gap. This design requires 15 mm insertion length in the beamline. The second model is the model of 0.5 thickness and 1.5 gap which requires 17 mm insertion length. It possesses the lowest capacitance value and the best TDR behaviour, named here the optimized design. The third model is called the mid-optimized design with a 1.5 thickness and a 1 mm gap and requires a 16 mm insertion length.

Table 5.1: Simulation parameters and button geometries

Parameter	Value
Structure length (mm)	26
Pickup thickness (mm)	0.5, 1.5 and 2.5
Gap between button and wall (mm)	0.5, 1.0 and 1.5
Button depth from the beam pipe (mm)	0.5
Pickup diameter (mm)	14
Beam velocity β	0.08, 0.27 and 0.37
Beam pipe diameter (mm)	30
Bunch length - σ (ps)	100 and 300

Each design has been simulated at three beam velocities ($\beta = 0.08, 0.27$ and 0.37) with two bunch lengths ($\sigma = 100$ and 300 ps). The aim is to compare the response of those designs with a particle beam. The amplitude of the induced signal will be considered for comparison. However, the final statement needs to consider the available space for the BPM along the proton LINAC beamline, in particular the BPM intertank section. Table 5.1 summarizes the simulation parameters of the beam and the pickup design in this section.

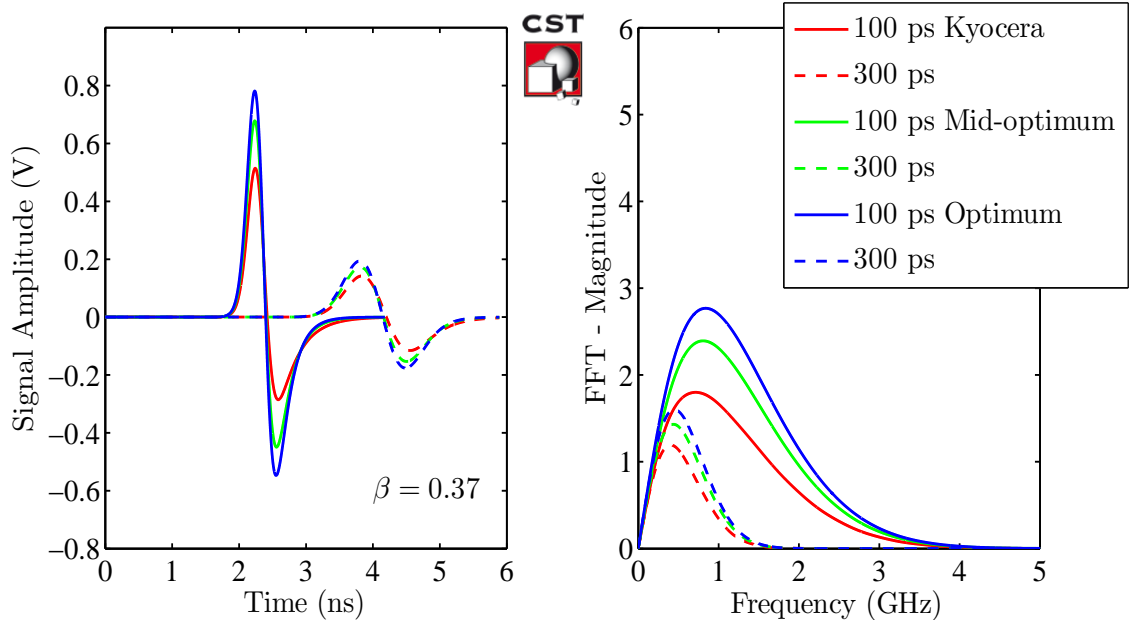


Figure 5.12: BPM output voltage from a single port in time (left) and frequency (right) domains with three button geometries ($\beta = 0.37$, 1nC bunch charge).

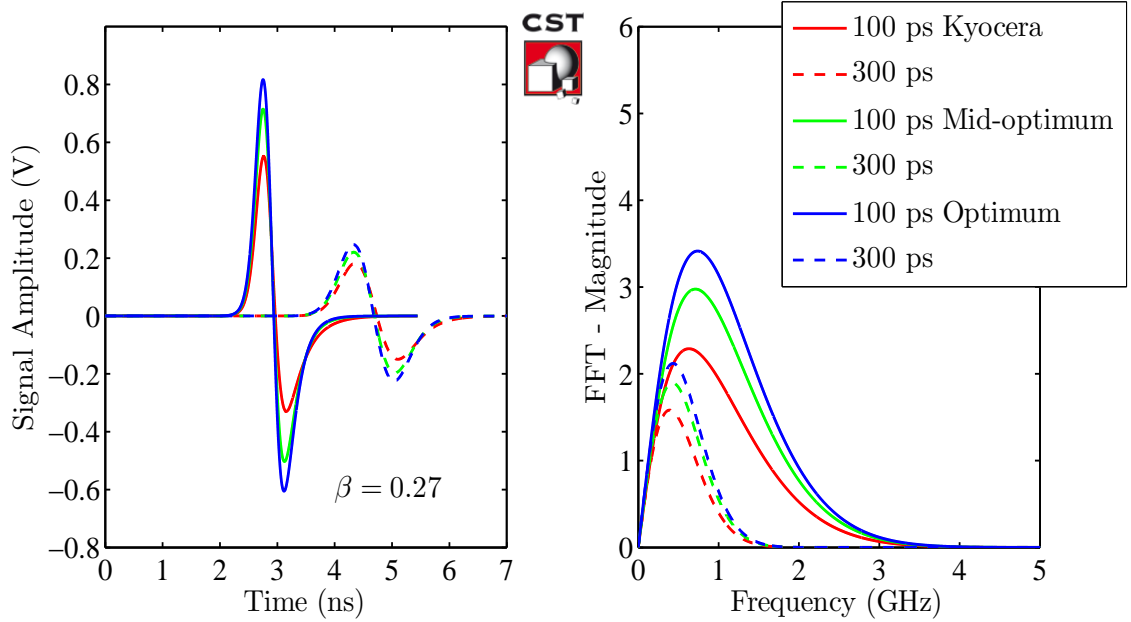


Figure 5.13: BPM output voltage from a single port in time (left) and frequency (right) domains with three button geometries ($\beta = 0.27$, 1nC bunch charge).

The time domain signals and the corresponding Fourier transformation of three pickup geometries are shown in figures 5.12, 5.13 and 5.14. Looking into those figures one can notice that the Kyocera design (red trace) shows the lowest signal strength and the largest signal deviation in all cases due to its large button capacitance in comparison with the other designs. A comparison between the amplitudes of induced signals are depicted in figure 5.15. It is obvious that the amplitude increases with the decrease of capacitance. This shows the influence of button capacitance on the pickup signal. One can observe that the influence of button capacitance is larger in the case of a shorter bunch and high β . For instance, for $\beta = 0.37$ and $\sigma = 100$ ps, the difference between the induced signals by the Kyocera and the optimized design is about 30 % while it is only about 10 % in the case of $\sigma = 300$ ps case.

These results confirm the TDR simulations which show that the disturbance in the signal increases with button capacitance. A point to emphasize here is that the presence of button capacitance is not avoidable in these type of pickups where the button takes a coin shape. The capacitance can be only minimized by reducing the button thickness and expand the gape size between the button and the beam pipe wall. In the next section another design is proposed where the pickup design is modified to be a conical shape [87]. With this design one can improve the impedance matching of the transmission line to a value close to 50Ω .

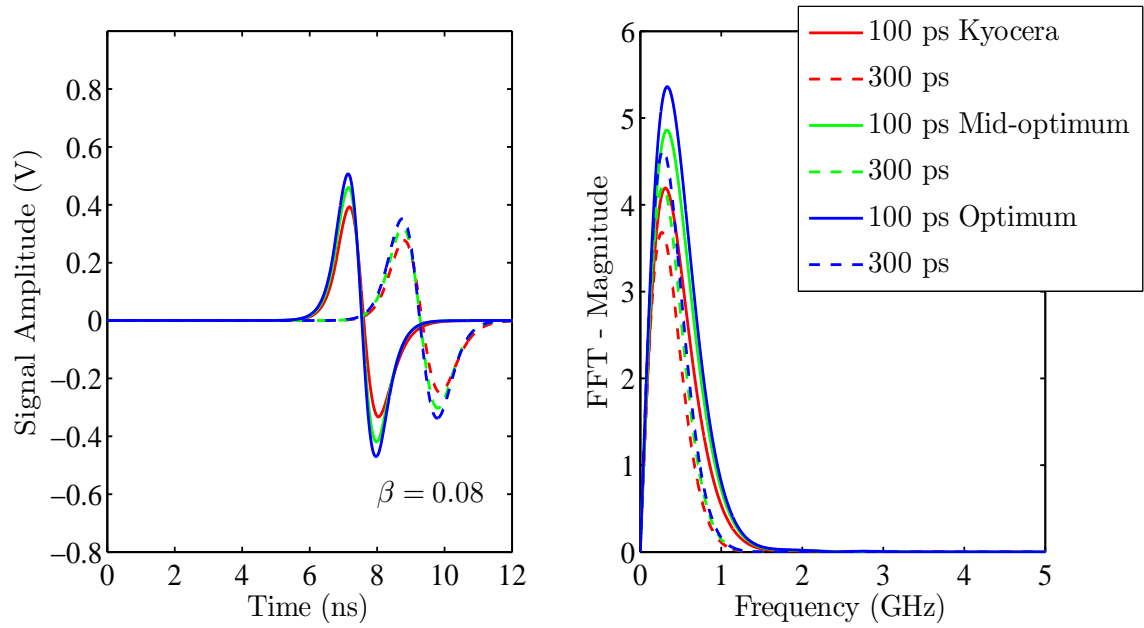


Figure 5.14: BPM output voltage from a single port in time (left) and frequency (right) domains with three button geometries ($\beta = 0.08$, 1nC bunch charge).

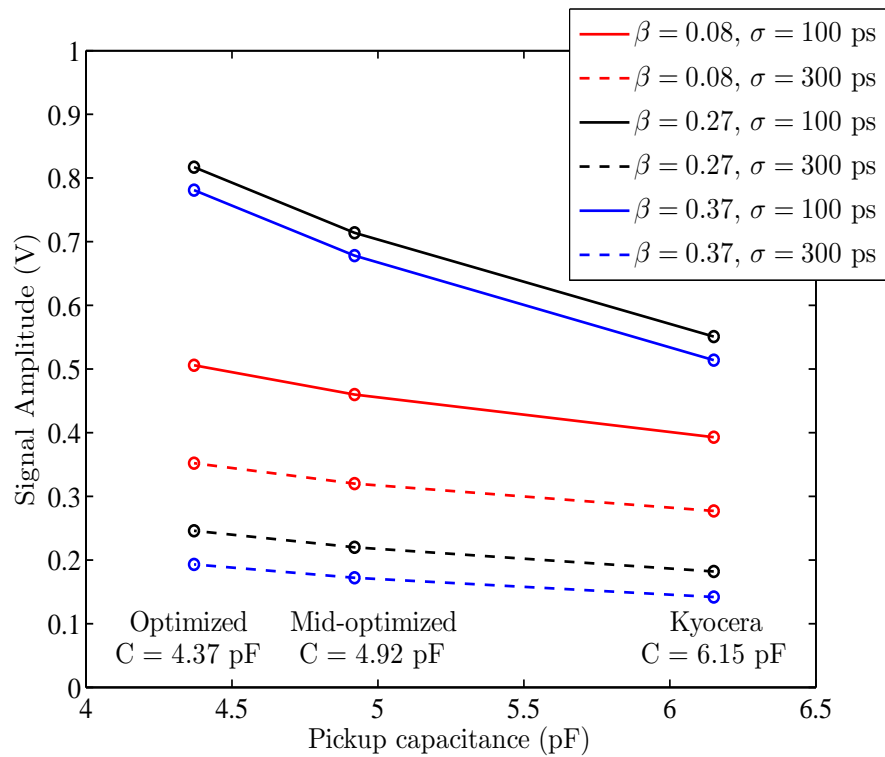


Figure 5.15: A comparison between the amplitudes of induced signals for three designs.

5.5 BPM Optimizations

According to [74], the available insertion for the pickup is 15 mm which includes the button and the gap between the button and the shield. This section discusses the button design optimizations for a coin and a cone designs. Both designs have been optimized and compared to the commercial Kyocera design of 14 mm diameter, 2.5 mm thickness and 0.5 mm gap. The static capacitance and the TDR simulation of all designs were evaluated using the CST ELECTROMAGNETIC STUDIO solver and the CST MICROWAVE STUDIO solver, respectively. Another option to design a good 50Ω impedance matching cone button is to optimize the conical shape to have a curved path of the button volume. However, this design has been excluded due to the expected high production cost.

The coin and cone designs have been optimized using the CST PARTICLE STUDIO Wakefield solver for higher signal by varying button diameter. Both designs were restricted to a 15 mm insertion length so that the gap increases as the button diameter decreases. Figure 5.16 demonstrates a 3D cone button created by CST. In the coin design the button thickness is fixed at 0.5 mm which corresponds to the lowest capacitance value as shown in figure 5.2 and the best TDR performance as shown in figure 5.4.

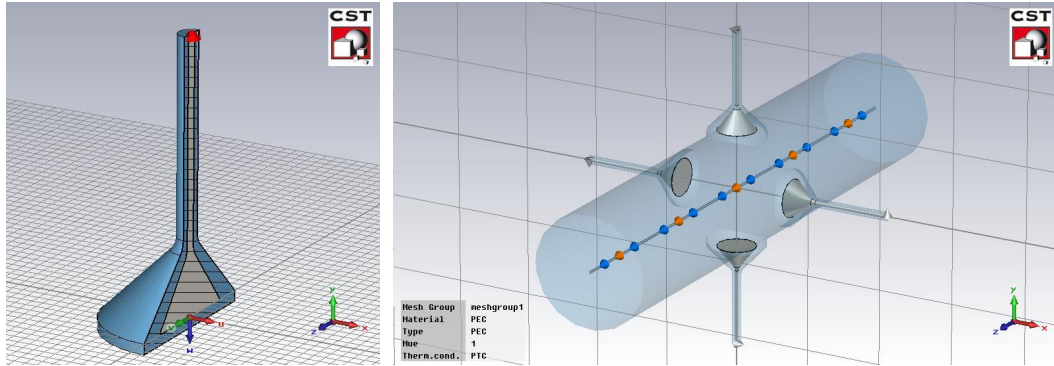


Figure 5.16: Design of one cone button (left). A 3D model of the pickup monitor as simulated in CST Particle Studio (right).

Figure 5.17 shows the optimization curves for the coin and cone design. The maximum signals were obtained at button radius of 5.5 mm and 6.25 mm for the cone and coin design, respectively. Based on this result and the results from Sec.. 5.4, the button radius, the thickness and the gap of the optimized coin design were chosen to be 6 mm, 0.5 mm and 1.5 mm, respectively. The optimized cone design was decided to be 5.5 mm in radius and a gap of 2 mm.

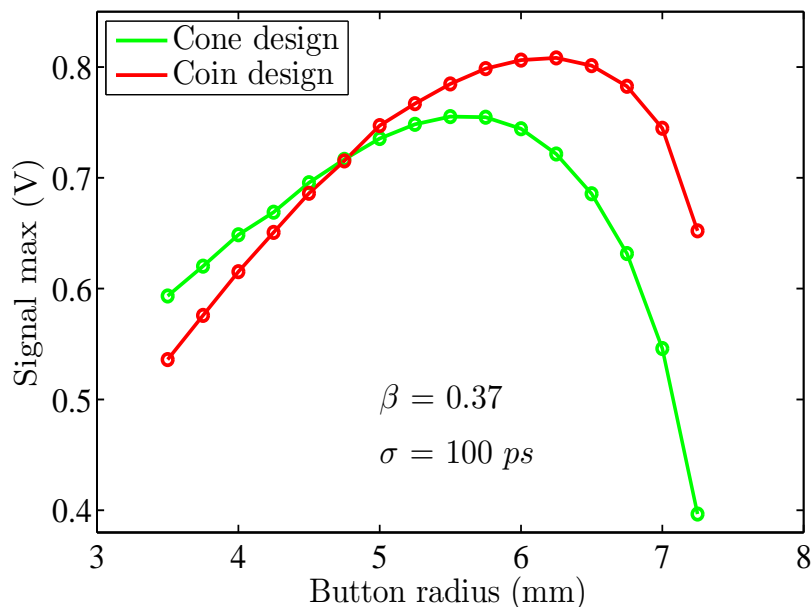


Figure 5.17: The optimization of the coin and cone designs using the CST PARTICLE STUDIO Wakefield solver showing that the higher signals are obtained as cone button diameter is 5.5 mm and coin button diameter is 6.25 mm.

The static capacitance obtained from the CST ELECTROMAGNETIC STUDIO solver are 3.10 pF, 4.1 pF and 6.20 pF for the optimized cone, the optimized coin and the Kyocera designs, respectively. Figure 5.18 shows the excitation and the reflected signals (left) and the TDR plots (right) of the three designs using the CST MICROWAVE STUDIO solver. From the TDR plots, one can notice that the impedance matching is significantly improved in the cone design by a factor of ~ 5 when compared to the Kyocera design. Moreover, the optimized coin design behaves much better than the Kyocera design and the difference in step response is $\sim 100\%$. The impedance step down in the cone, optimized Kyocera and Kyocera designs are $\sim 41\ \Omega$, $\sim 31\ \Omega$ and $\sim 17\ \Omega$, respectively. Table 5.2 summarizes the design parameters and the resulting electrical properties.

The response of the commercial Kyocera design was compared to the optimized cone and coin designs using the CST Particle Studio solver with a beam at $\beta = 0.37$, and bunch lengths of 100 and 300 ps. The time domain signals and the corresponding Fourier transformation of the designs are shown in figures 5.19. The first interesting outcome is the signal deformation in the time domain which is rather obvious in the Kyocera signal in comparison to the optimized cone and the coin designs. The cut-off frequency for the Kyocera design, the optimized cone design and coin designs are 513 MHz, 1026 and 776 MHz, respectively. The deformation or non-symmetry of the output signal becomes significant if the main bunch frequency components are close to the cut-off frequency band of the pickup as discussed in Sec. 3.2.

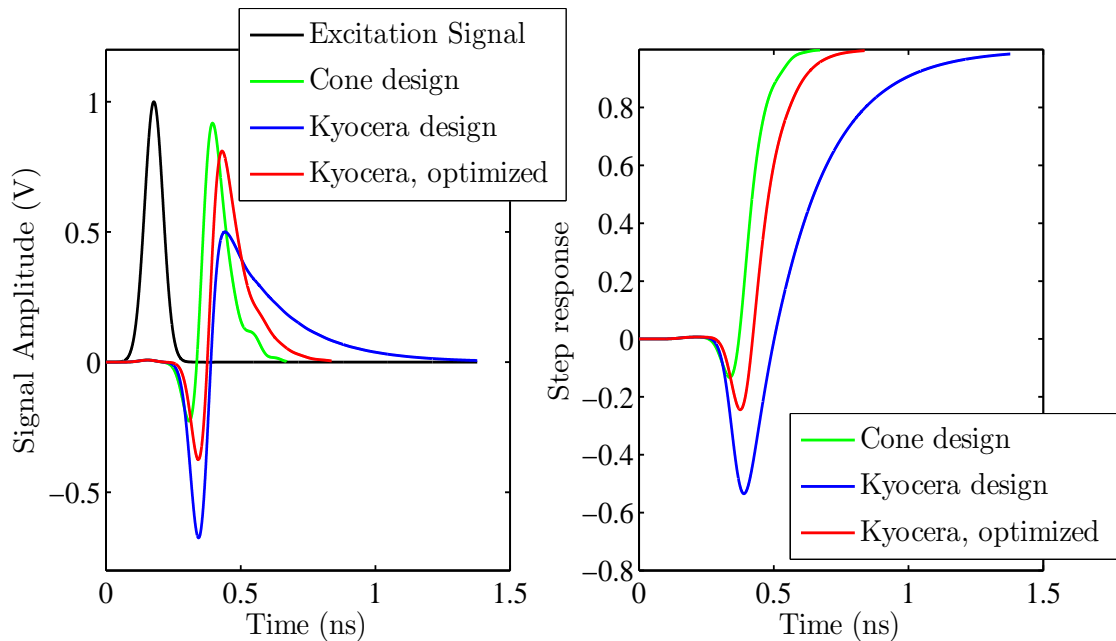


Figure 5.18: The excitation and the reflected signals (left) and the corresponding TDR plots (right) for the cone design, the optimized Kyocera design and the Kyocera design.

It is remarkable to see that the optimized coin design always performs better than the other designs. The optimized cone design shows better impedance matching when compared to the optimized coin design but the optimized coin design delivers a higher signal due to its large button size. For short bunches the optimized coin design gives a signal higher than the optimized cone design and the difference is about 8 %. However, for long bunches the signal amplitude of the Kyocera design exceeds, by a slight difference, the signal produced from the optimized cone design. Such differences in pickup performance can be understood from transfer impedance concept where some geometrical parameters as well as beam parameters contribute to finally form the pickup signal. Some parameters are related to the beam and some others to the pickup geometry and each parameter contributes more than others within a certain range.

Based on the previous results and discussions, three main points should be highlighted before making a final statement; the first point is the signal quality or signal deformation in the time domain. As we have seen this can be improved significantly if the Kyocera design is optimized to achieve proper impedance matching and to have low button capacitance. The second point is the signal amplitude which is directly related to the size of the button and also influenced by the impedance matching of the pickup. The third point is related to the mechanical constraints in the beamline proton LINAC which allows only a limited insertion length for the BPM.

Table 5.2: Geometry parameters of the designs and the resulting electrical properties

Parameter	Button Type		
	Cone design	Kyocera design	Kyocera, optimized
Button Diameter (mm)	11	14	12
Gap size (mm)	2.0	0.5	1.5
Button thickness (mm)	–	2.5	0.5
Capacitance (pF)	3.10	6.2	4.1
Cut-off frequency (MHz)	1026	513	776
Step response, ρ_V	-0.13	-0.50	-0.24
Impedance (Ω)	41	17	31

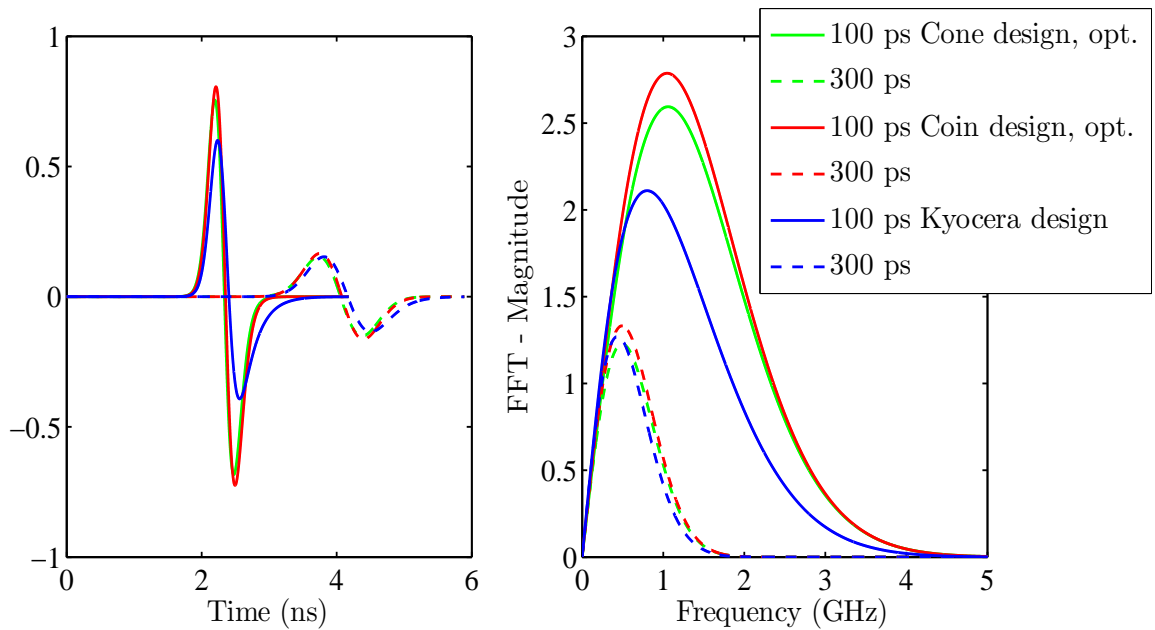


Figure 5.19: BPM output voltage from a single port in time (left) and frequency (right) domains for the cone design, the optimized Kyocera design and the Kyocera design. ($\beta = 0.37$, $\sigma = 100$ and 300 ps, 1 nC bunch charge).

If we consider the previously mentioned points one can state that the optimized coin pickup seems to be favorable when compared to the optimized cone design and to the commercial Kyocera design. The reasons are; firstly, as shown in the simulations, the induced signal from the optimized coin pickup is always higher because of its reasonable button size. Additionally, the large gap size offers smooth signal propagation which also compensates signal amplitude reduction due to reducing the button diameter. Secondly, the impedance matching characteristic seems to be appropriate due to low button capacitance so that signal deformation can be minimized. For this reason the optimized coin

design presents a proper model to reduce the pickup capacitance and thus to have a high cut-off frequency. The third reason is that it does not require additional development costs because it fits with the mechanical setup available for the commercial Kyocera design.

5.6 Button Depth and Size Investigations

The BPM pipe diameters in proton LINAC are 30 and 50 mm and the proposed button diameter is 14 mm. However, the pickup electrodes will be mounted at 0.5 mm depth from the beam pipe inner radius. The reason is to protect the pickup electrodes from the stray beam impingement. Consequently, the amount of the image current induced by the beam on the button surface will be reduced by a certain fraction. On the other hand, the signal produced by the button depends not only on the pickup area but also the beam pipe aperture and the bunch velocity as described in equation 3.7. In this section some parameters related to the button position and the button geometry are investigated.

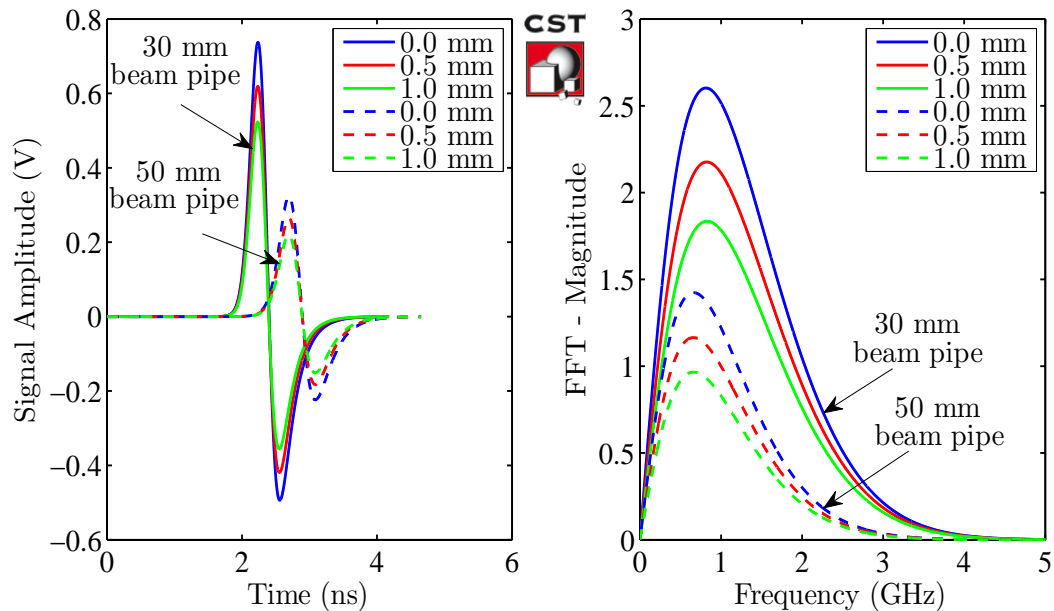


Figure 5.20: BPM output signal from one pickup for 30 mm and 50 mm beam pipe in time (left) and frequency (right) domains mounted at different depths. The beam parameters are $\beta = 0.37$, $\sigma = 100$ ps, 1nC bunch charge.

Lets begin with quantifying the signal amplitude reduction as the button depth is changed for 30 and 50 mm beam pipes. Three cases of button depth have been simulated with a fixed button diameter of 14 mm; in the first case is that the button surface is exactly on the beam pipe inner wall so that the pickup depth is zero; the second case

and the third case the button depth are set to 0.5 mm and 1.0 mm, respectively. The amplitudes of the the output signals are compared.

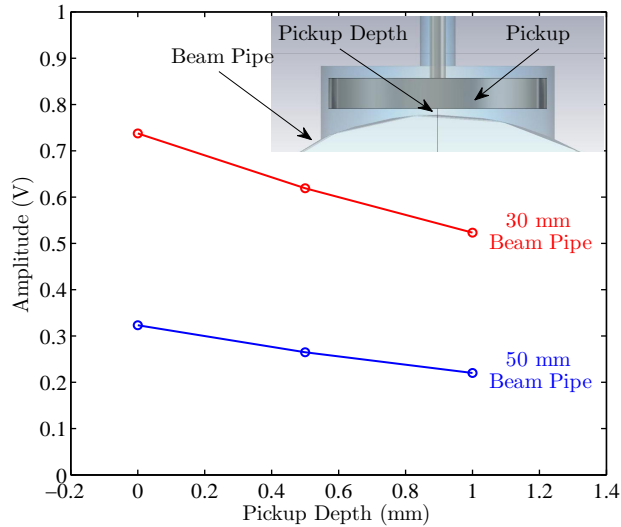


Figure 5.21: Signal amplitudes for 30 and 50 mm beam pipe at different pickup depth

Figure 5.20 shows the pickup signals in the time (left) and the frequency domain (right) for 30 and 50 beam pipes. The plots show that the amplitude of the signal produced by 30 mm beam pipe is higher than the one produced at 50 mm beam pipe by a factor of ~ 2.3 . Looking to figure 5.21, which shows the signal amplitudes differences versus the pickup depth, one can notice an approximated linear decrease of the amplitude signal with the button depth. It is steeper in the case of 30 mm when compared to 50 mm by a factor of 2. The gradients are -0.2 and -0.1 V/mm for 30 and 50 mm respectively.

The second geometrical parameter is the button diameter or button size. The influence of beam pipe radius on the pickup signals was investigated as a function on the button diameter at different β values ($\beta = 0,08, 0,27$ and $0,37$). The pickup diameter was varied from 6 to 28 mm with a fixed gap of 0.5 mm, a button thickness of 2.5 mm and a depth of 0.5 mm. A centered beam was used with a bunch length of 100 ps. Figure 5.22 shows the changes in the maximum and the minimum values of produced signals at different β as a function of button diameter. The signal maximum curves grow almost linearly in both pipes but it tends to curve as the button diameter becomes larger than 20 mm. The slope of the traces depends on the beam velocity which are 0.013 V/mm, 0.024 V/mm and 0.025 V/mm for $\beta = 0,08, 0,27$ and $0,37$, respectively. The signal minima show non-linear behaviour in the case of high β values while a linear response is observed for a low β regime.

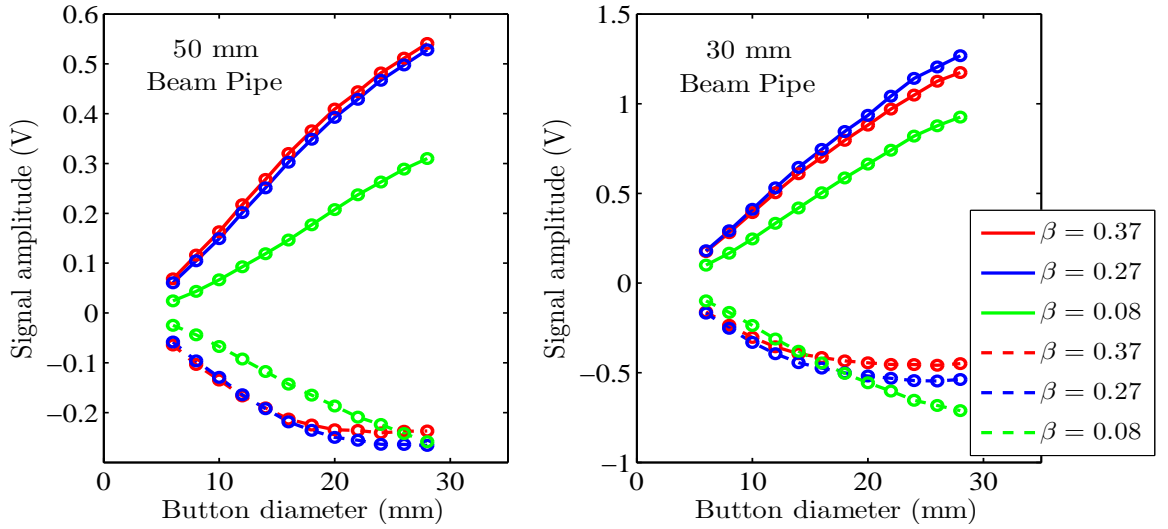


Figure 5.22: The change in signal maximum (solid lines) and minimum (dashed lines) as a function of button diameter for different β values in 50 mm (left) and 30 mm (right) beam pipes. ($\sigma = 100$ ps, 1nC bunch charge).

Figure 5.23 illustrates the ratio between the signal maximum and the button area and the signal minimum and the button area. In the case of $\beta = 0.08$ the change in ratio is not very significant when compared to $\beta = 0.27$ and 0.37 . It is remarkable to see that the minimum ratio traces tend to overlap with the increase of the button area. If the button diameter gets too large, the β should not influence any longer as the concentration of the field does not change any longer the number of mirror charges that generate the voltage.

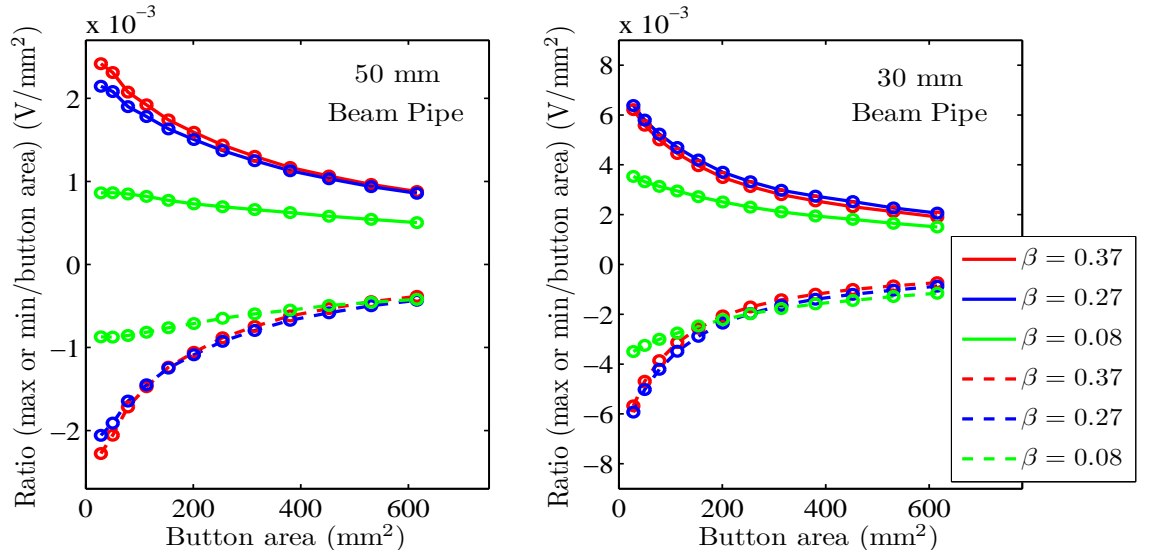


Figure 5.23: The ratio between the signal maximum (solid lines) and minimum (dashed lines) as a function of the button area for different β values in 50 mm (left) and 30 mm (right) beam pipes, same type of CST simulations as shown in figure 5.22 ($\sigma = 100$ ps, , 1nC bunch charge).

5.7 Bunch Length Investigations

The length of the bunch is an important parameter to be investigated for the proton LINAC. The dynamic range of the longitudinal bunch length for the proton LINAC is expected to be between 50 to 700 ps as discussed in Sec. 4.2. Depending on the beam velocity, the signal produced by the pickup is considered as an excellent way to estimate quickly and non-destructively the bunch length.

On the other hand, it is important to keep in mind that the accurate determination of the bunch length is not trivial. The reason is the presence of the advanced Coulomb-field of the moving bunches, in particular for low β range [67]. The geometric length of the bunch Δz along z -axis depends on the particle velocity β which can be calculated from [67]

$$\Delta z = \beta c \Delta t_b \quad (5.5)$$

where $\Delta t_b = 2\sigma_b$. The reason is that the derivative of a Gaussian Function has the maximum and the minimum exactly at $\pm\sigma$. The bunch length Δt_b can be estimated by relating the bunch length with the time difference between the maximum and the minimum values of the pickup signal Δt_s .

The CST simulations have been carried out to investigate the bunch length characteristics for the interesting dynamic range in proton LINAC. Those simulations provide very useful inputs for the BPM system and for the related technical layout. The length of the signal produced by the pickup Δt_s is compared with bunch length $\Delta t_b = 2\sigma_b$ at different beam velocities $\beta = 0.08, 0.27$ and 0.37 , correspond to $E = 3$ MeV, 30 MeV and 70 MeV, respectively. A centered beam is used in the simulations and the bunch length is varied. The Kyocera design of 14 mm button diameter is used and beam pipe is chosen to be 30 mm. The span of simulated bunch length starts from $\sigma_b = 30$ up to 960 ps.

The first set of results are shown in figures 5.27, 5.26 and 5.25 illustrating the pickup signals in the time domain (left) and the corresponding Fourier transformation in the frequency domain (right) as a function of the bunch length σ_b . One can observe the response of the pickup signal σ_s to the change in bunch length. For low β beam the amplitude of the output signal is lower and the signal is longer. The reason is that the electric field components are less perpendicular to the beam direction as for higher values of β . This effect for different velocities β of the moving charge is shown in figure 5.24 [33], where the longitudinal electrical field $E_{\parallel}(t)$ and transversal field $E_{\perp}(t)$ in the lab-frame have been calculated for a single particle with a charge of $1e$ traveling in empty space.

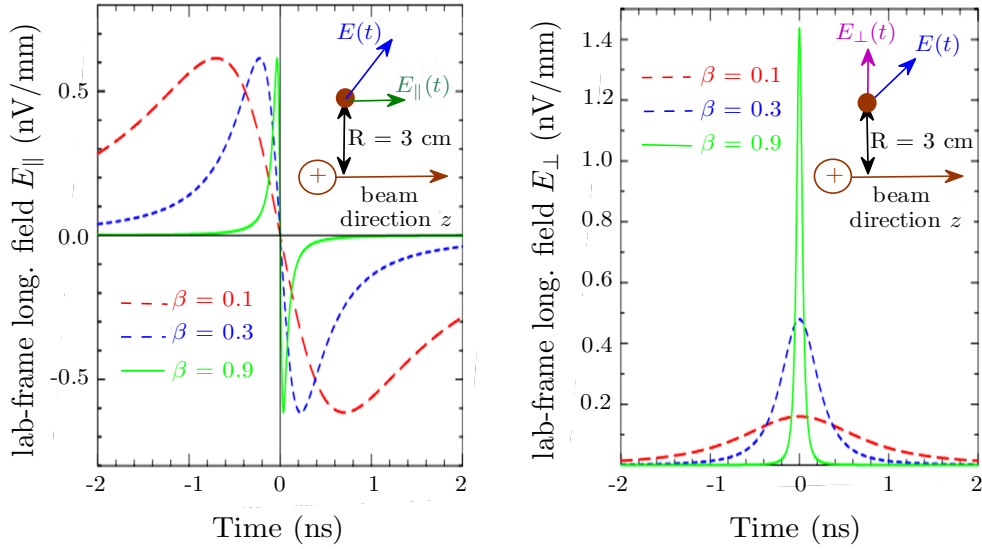


Figure 5.24: Effect of the advanced longitudinal (left) and transverse (right) electric field at an observation point $R = 30$ mm from the beam axis for different velocities of a point-like charge. For $t = 0$ the closest approach is reached (from [33]).

Figure 5.28 shows the change in the signal maximum and the signal minimum values for different β values as a function of bunch length σ_b . One can notice that the maximum of the pickup signals decreases as a function of the bunch length as expected from some theoretical models [66]. For short bunches ($\sigma_b < 300$ ps) and higher beam velocities ($\beta = 0.27$ and 0.37) the maximum and minimum (in the negative side) values of the pickup signal decrease much faster than the low β value ($\beta = 0.08$). For longer bunches ($\sigma_b > 600$ ps) the proportional decrease in the maximum and minimum values is still valid but the change is not significant.

The signal amplitudes expressed in the Fourier components as a function of bunch length is depicted in figure 5.29 for five harmonics. The first observation is that for a short bunch lengths of $\sigma_b < 200$ ps the pickup signal contains a high amplitude value of higher harmonics of the beam-bunching frequency in comparison to the longer bunches. For $\beta = 0.08$, it is noticeable that the first harmonic is always dominant. The major contribution in the spectrum comes from the first two harmonics while the contribution is very weak for higher harmonics, especially for bunches longer than $\sigma_b > 150$ ps. As the beam becomes faster and the bunch is short $\sigma_b < 200$ ps the frequency spectrum is shifted so that the contribution of the first harmonics is smaller than the followings harmonics (2nd, 3rd and 4th harmonics). A very important result for the technical layout of the electronics concerning the data processing aspect is that the second harmonic is present always in the spectrums with sufficient strength.

A very depictive aspect in this investigation is shown in figure 5.30. It shows a linear proportional relationship between the pickup signal and bunch length. This proportionality goes to a certain limit depending on β value. Below that limit there is no more change in the output signal length Δt_s so that the pickup signal remains constant as the bunch length further decreases. Knowing these limits and the proportionality range for each β value are useful for estimating bunch length from the output signal shape. For example, for $\beta = 0.27$ the pickup signal of length $\sigma_s = 526$ ps leads to a bunch length of $\sigma_b = 480$ ps. The linear limit was calculated for each β case by applying a linear fit on the curve from $\sigma_b = 560$ ps for both $\beta = 0.27$ and 0.37 and $\sigma_b = 720$ for $\beta = 0.08$. The slope of the curves a_1 are 0.89, 95 and 0.96 for $\beta = 0,08, 0.27$ and 0.37 , respectively. Figure 5.31 illustrates the linear limits where a_0 are 217 ps, 67.5 ps and 53.8 ps for $\beta = 0,08, 0.27$ and 0.37 , respectively.

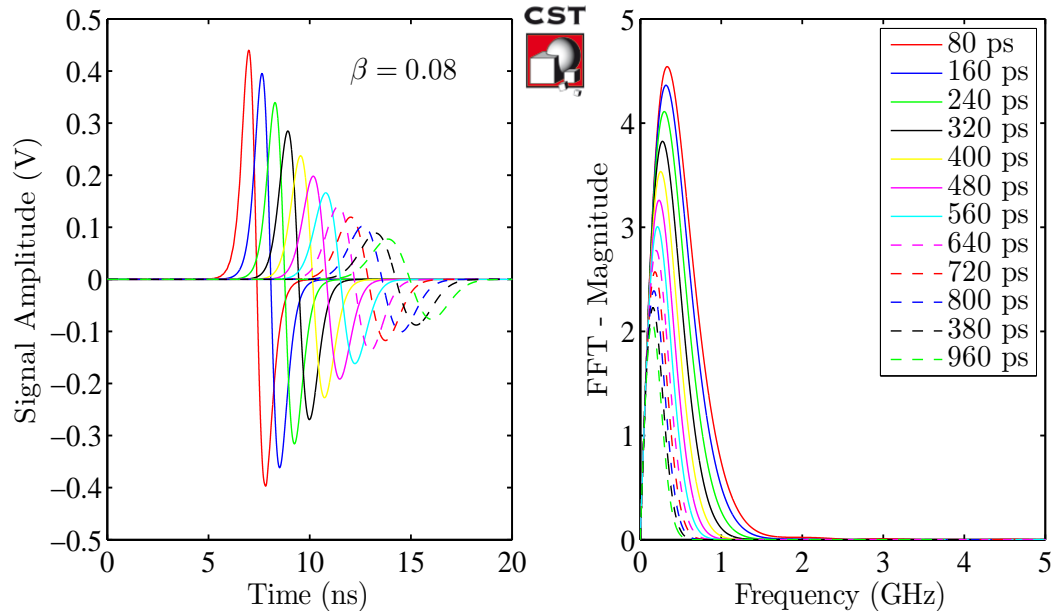


Figure 5.25: The legend shows the bunch length σ_b and the plotted signals represent output voltage from a single port in time (left) and frequency (right) domains for $\beta = 0.08$.

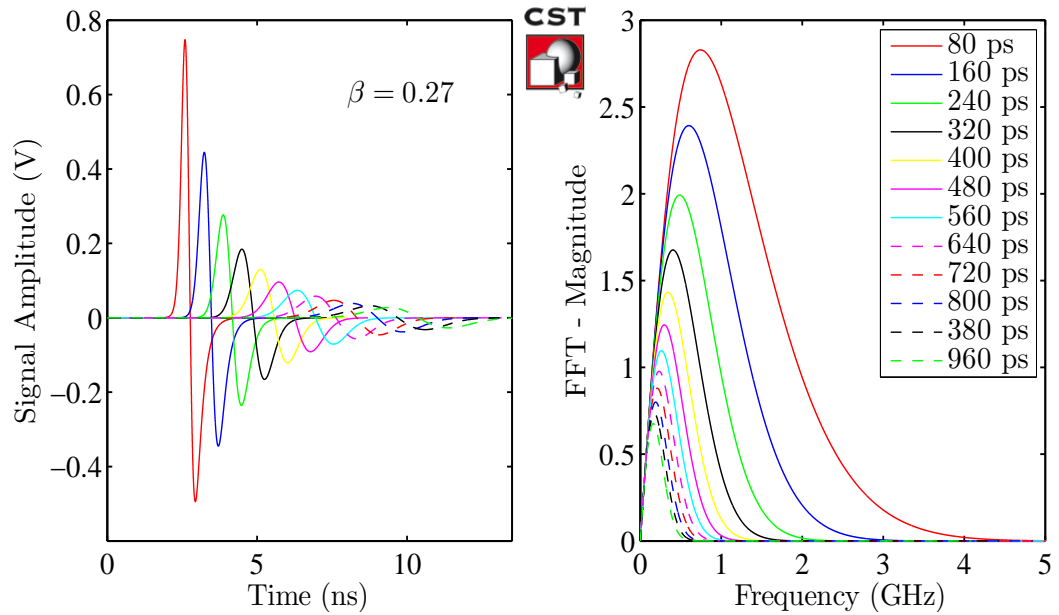


Figure 5.26: The legend shows the bunch length σ_b and the plotted signals represent output voltage from a single port in time (left) and frequency (right) domains for $\beta = 0.27$.

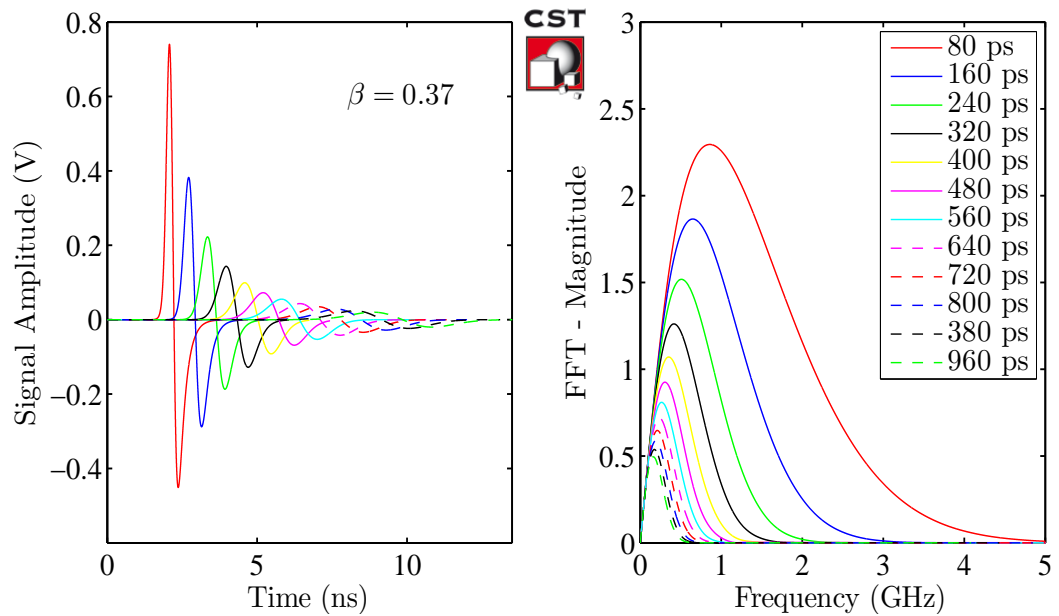


Figure 5.27: The legend shows the bunch length σ_b and the plotted signals represent output voltage from a single port in time (left) and frequency (right) domains for $\beta = 0.37$.

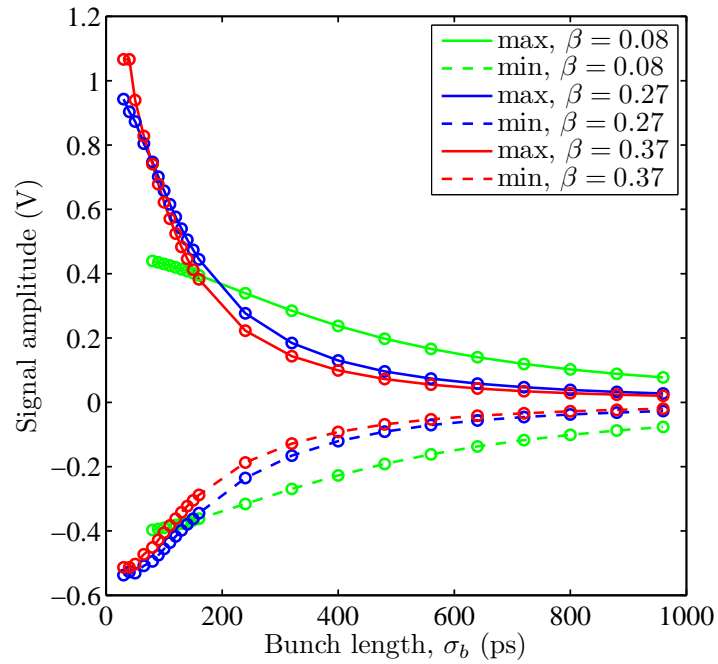


Figure 5.28: The change in the maximum and the minimum values of the pickup signal versus bunch length σ_b .

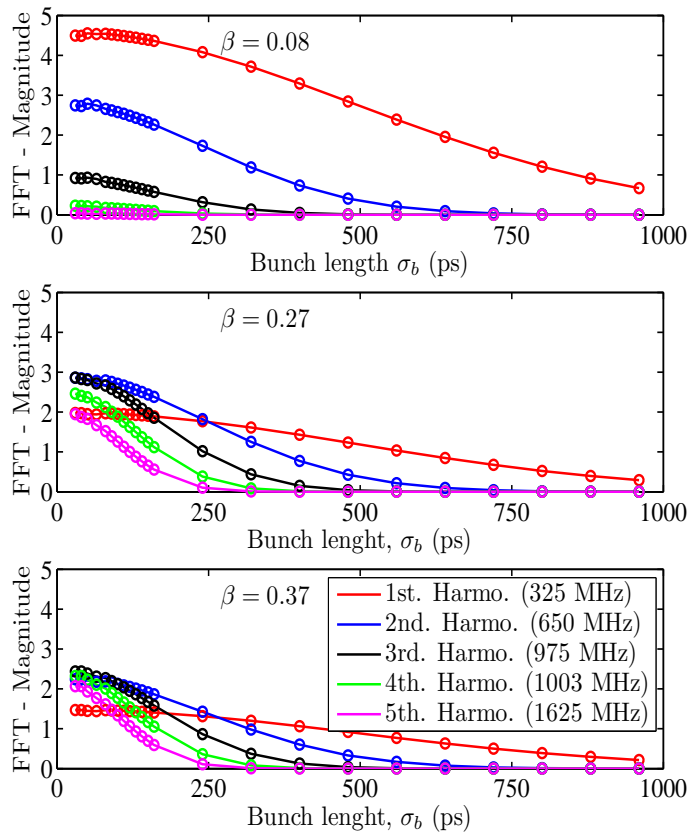


Figure 5.29: The Fourier components of the pickup signals at five harmonics of the bunching frequency versus bunch length.

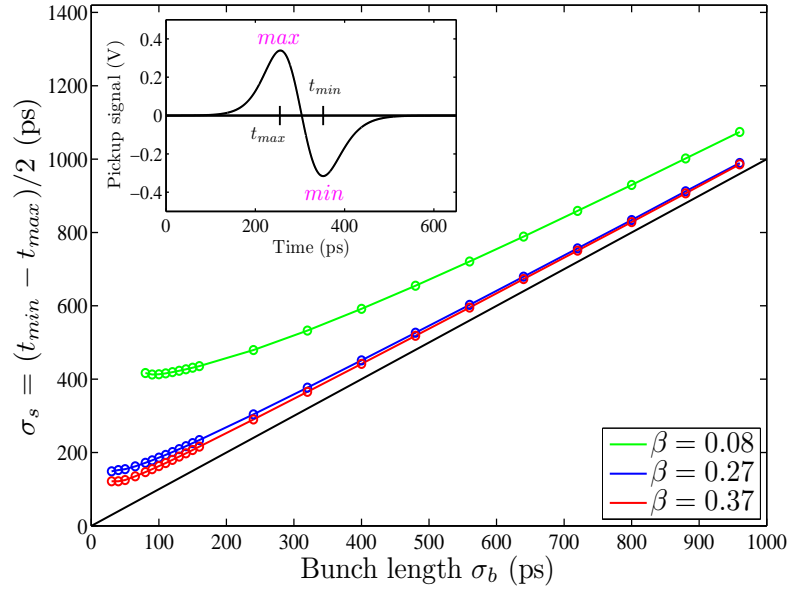


Figure 5.30: The relationship between the bunch length σ_b and the length of the pickup signal σ_s extracted from the time difference between the minimum and the maximum values of the pickup signal.

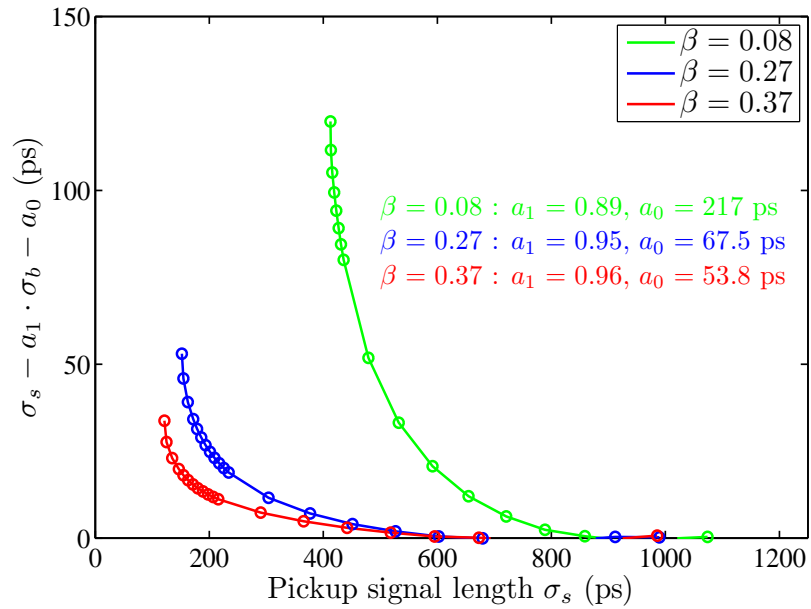


Figure 5.31: The linear limit calculated for $\beta = 0.08, 0.27$ and 0.37 by applying a linear fit on the curve shown in figure 5.30 from $\sigma_b = 560$ ps for both $\beta = 0.27$ and 0.37 and $\sigma_b = 720$ for $\beta = 0.08$.

5.8 BPM Sensitivity, Linearity and Map

An important part of the BPM simulations is the position sensitivity analysis. The position sensitivity curve shows basically the response of the BPM to the beam position changes. The importance of the BPM sensitivity calculations is that it illustrates the non-linearity of the BPM response versus the beam center displacement. It depends on the pickup diameter, beam pipe aperture and the position of the beam with respect to the pickup. The first objective of this section is to calculate the BPM sensitivity at various beam velocities in the frequency domain. This is achieved by extracting the magnitudes of the Fourier components of the accelerating frequency (325 MHz) and the next three harmonics. The second objective is to use the sensitivity results to produce the BPM position map for each harmonic.

The determination of the beam transverse position is performed from the amplitudes of the induced-signals in the opposite pickups using the delta-over-sum method as discussed in section 3.4. In frequency domain analysis the amplitude of the induced-signal is taken at certain harmonic and the beam position coordinates (x, y) are obtained by

$$x \approx \frac{1}{S_x(f)} \cdot \frac{\Delta U_x(f)}{\Sigma U_x(f)} \quad \text{and,} \quad y \approx \frac{1}{S_y(f)} \cdot \frac{\Delta U_y(f)}{\Sigma U_y(f)} \quad (5.6)$$

where $S_x(f)$ and $S_y(f)$ are the BPM sensitivity in horizontal and vertical planes in %/mm unit, respectively and f is the selected frequency component where the signal amplitude is evaluated. In general, the position sensitivity S is a function of the horizontal and the vertical displacements at the evaluated frequency f . At a certain harmonic, $S_x(f)$ and $S_y(f)$ are defined by the derivative for the horizontal and for the vertical directions as

$$S_x(f) = \frac{\partial H(f)}{\partial x(f)} \quad \text{and,} \quad S_y(f) = \frac{\partial V(f)}{\partial y(f)} \quad (5.7)$$

where H and V are the normalized horizontal and vertical beam position defined in equation 3.19. The inverse of the position sensitivities at f harmonic are called the coefficients or the monitor constants $k_x(f)$ and $k_y(f)$ (see equation 3.20) given in the unit of mm.

The simulations have been carried out in the CST Particle Studio Wakefield solver to calculate the BPM position sensitivity and the non-linearity behaviour. The Kyocera model of 14 mm button diameter, 0.5 mm gap and 2.5 mm thickness was used in the simulation. The beam pipe diameter is 30 mm and the button depth set to 0.5 mm from the beam pipe inner radius. Three beam velocities are considered $\beta = 0.08, 0.27$ and 0.37 with bunch lengths of $\sigma = 150$ and 60 ps. The BPM response has been demonstrated at

four frequency harmonics. The position sensitivities S_x and S_y are assumed to be equal due to the BPM symmetry installation.

The BPM sensitivity has been calculated in the vertical plane where the beam is moved along the y-axis in 2 mm steps within a 10 mm range. The BPM sensitivity curves in the y direction for the different β values are shown in figures 5.34, 5.33 and 5.32 (left). It is clear that the BPM sensitivity decreases and the non-linearity increases as the beam center moves away from the center. Moreover, the sensitivity depends on the evaluated frequency. One can also notice that the frequency dependence has more influence on the BPM sensitivity at low β value ($\beta = 0.08$). The corresponding calculated BPM sensitivities S_0 are listed in table 5.3 at different frequency harmonics for $\beta = 0.08, 0.27$ and 0.37 . The values S_0 are calculated using the nearest non-zero beam offset $\Delta x = 2$ mm and $S_0 = \frac{1}{\Delta x} \cdot \frac{\Delta U_x(f)}{\Sigma U_x(f)}$. These numbers are used to convert the calculated signals to position data and to produce the so called BPM position map.

The dependence between the horizontal and vertical plane is usually depicted by the BPM position map. Here the real beam positions with equidistant steps are plotted as well as the calculated beam position obtained using the difference over sum method with S_0 fitted at the central part. The beam position was swept in the vertical plane to cover a half quadrant in the range of ± 10 mm in 2 mm steps.

There are two methods to display the BPM position map; one is by producing the BPM position map from S_0 values calculated for each harmonic (listed in table 5.3). The difference over sum of the induced-signals in the opposite pickups for each harmonic is multiplied by the inverse of the sensitivity $S_0(f)$ to calculate the beam position and, therefore, to produce the BPM position map. The results of the position mapping graphs in this method for four frequency harmonics at $\beta = 0.08, 0.27$ and 0.37 are shown in figures 5.34, 5.33 and 5.32 (right). The plus sign in the figures are the real positions of the beam whereas the circles represent the calculated positions derived from the BPM signals. The distance between adjacent points is 2 mm.

The second method is that only S_0 of the fundamental frequency is used to calculate the beam position and to produce the BPM position map for the fundamental frequency and for the other harmonics. In this method, the difference over sum of the induced-signals in the opposite pickups from each harmonics is multiplied by the inverse of the sensitivity $S_0(325 \text{ MHz})$. The BPM position map with fixed $S_0(325 \text{ MHz})$ for the four frequency harmonics at $\beta = 0.08, 0.27$ and 0.37 are shown in figures 5.34, 5.33 and 5.32

(middle). The BPM sensitivity curves and BPM position maps for all CCH and CH output velocities and the relevant beam pipe diameter (30 and 50 mm) along the proton LINAC have been produced and depicted in Appendix

The BPM position map is used to determine the real position of the beam within a certain range in spite of such a non-linearity response. The effective range is decided by the BPM requirements for a given beam velocity. Theoretically, for the same pickup design and the same β value, the BPM sensitivity for each harmonics is independent from the bunch length. This has been confirmed by the numerical calculations where a similar simulation has been performed at a bunch length of $\sigma = 60$ ps. Figure 5.35 (left) shows the BPM sensitivity curves of the fundamental and the forth harmonics (325 MHz and 1300 MHz) for $\sigma = 150$ and 60 ps with beam velocity of $\beta = 0.37$. One can notice that the sensitivity curves of $\sigma = 150$ and 60 ps are coincided for the same harmonic. This result was used to evaluate the uncertainties or the numerical errors from the simulations as as shown in figure 5.35 (right). The range of variation is about 4×10^{-4} .

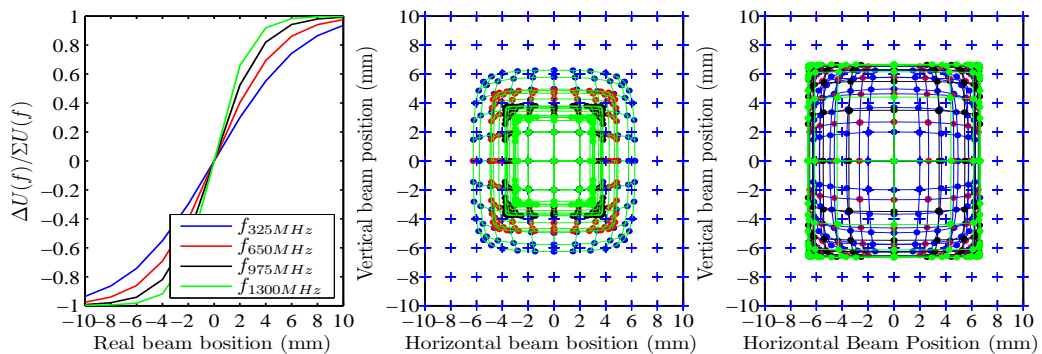


Figure 5.32: Vertical beam position sensitivity curves calculated using the delta-over-sum method at different frequency harmonics with $\beta = 0.08$ for a bunch length = 150 ps (left). The BPM position map from $S_0(f)$ values taken for each frequency harmonic from table 5.3 (right). The BPM position map from $S_0(325 \text{ MHz})$ fixed at the fundamental frequency (middle).

Table 5.3: BPM sensitivities S_0 from the simulation in unit ($\%/mm$) at the center position

β	325 MHz	650 MHz	975 MHz	1300 MHz
0.08	14.94	20.12	26.17	33.00
0.27	12.83	13.47	14.38	15.55
0.37	12.80	13.08	13.55	14.18

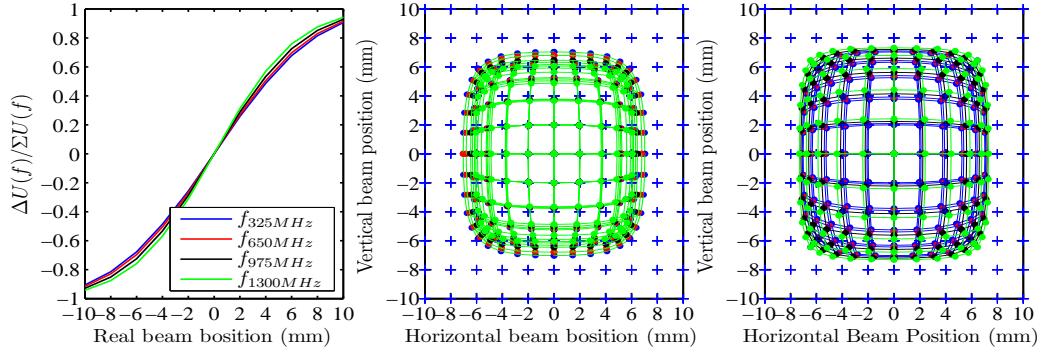


Figure 5.33: Vertical beam position sensitivity curves calculated using the delta-over-sum method at different frequency harmonics with $\beta = 0.27$ for a bunch length = 150 ps (left). The BPM position map from $S_0(f)$ values taken for each frequency harmonic from table 5.3 (right). The BPM position map from $S_0(325 \text{ MHz})$ fixed at the fundamental frequency (middle).

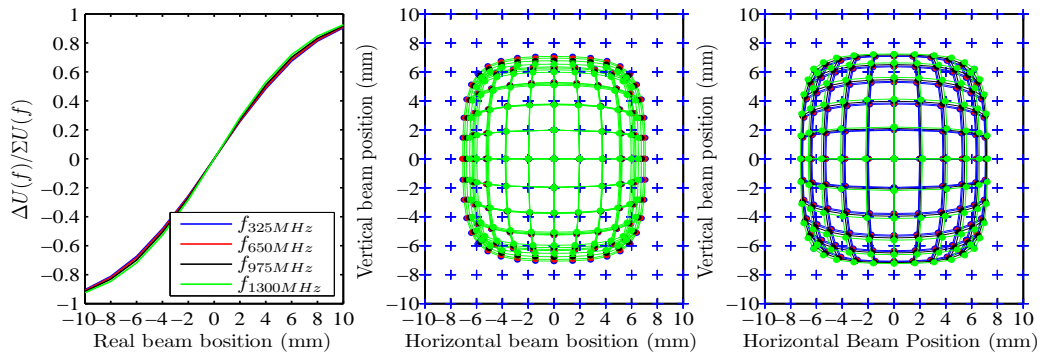


Figure 5.34: Vertical beam position sensitivity curves calculated using the delta-over-sum method at different frequency harmonics with $\beta = 0.37$ for a bunch length = 150 ps (left). The BPM position map from $S_0(f)$ values taken for each frequency harmonic from table 5.3 (right). The BPM position map from $S_0(325 \text{ MHz})$ fixed at the fundamental frequency (middle).

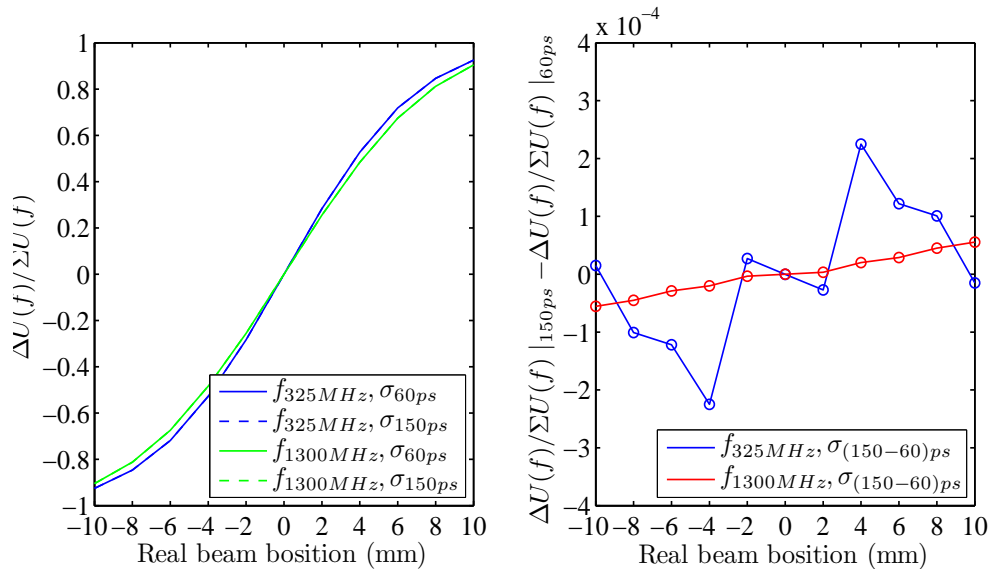


Figure 5.35: Vertical beam position sensitivity curves calculated at $\beta = 0.37$ using the delta-over-sum method for the fundamental frequency and the fourth harmonic for different bunch length $\sigma = 60$ and 150 ps (left). The numerical errors evaluation from the subtraction of $\Delta U(f)/\Sigma U(f)$ values for the same harmonic at $\sigma_b = 150$ ps and 60 ps.

5.9 Signal Phase Investigation

We have seen in the previous section the determination of the beams center-of-mass from the BPM signals and some related parameters such as BPM sensitivity and the non-linearity. These calculations are based on the amplitudes of harmonics of the BPM signals as a function of beam position. The phase of the produced signals as a function of the beam position is also of particular interest. The reason is that the beam phase of two BPMs are used for beam energy measurements by the Time-of-flight (TOF) method (see Sec. 3.5).

For the BPM system, it is very interesting and a useful input to investigate the influence of the beam displacement on the pickup signal phase in a qualitative manner and to see whether this could effect the Time-of-flight measurements. Another application could emerge related to the development of the digital signal processing algorithm (discussed in chapter 6) for the signal phase detection.

Separate simulations have been carried out using the CST Particle Studio Wake-field solver to explore the deviation of the phase reading in one BPM as a function of beam position. In phase analysis requires a large number of mesh cells (factor of 3) to get stable results when compared to the amplitude calculations. Additionally, the phase reading is very sensitive to the different mesh configuration if the model or the beam parameters are changed. Therefore, the same mesh setting and beam parameter are used for all simulations. The Kyocera model of 14 mm diameter and 0.5 mm gap was used with the beam pipe of 30 mm diameter and 0.5 mm depth. The beam velocity is chosen to be $\beta = 0.37$ and the bunch length is set to $\sigma = 100$ ps.

The phase readings are extracted at the first and the second harmonics. For simplification, the BPM pickups are named Up, Down, Left and Right. The beam is moved in two directions sweeping in 0.5 mm steps; the first direction is the vertical axis in the range of ± 12 mm. The beam reaches its extreme position as it is only 3 mm away from the closest pickup and 27 mm from the other. The second direction is the diagonal axis so that the beam position is varied in the range of ± 10 mm. For the BPM system such a large range is not realistic. Nevertheless, it is interesting to observe the tendency of the phase changes with respect to the beam offset.

The phase readings from four pickups are shown in figure 5.36 for vertical direction (left) and for diagonal direction (right). A couple of points are missing in both sweeps due to numerical errors. In these points the mesh configuration blows up to a number of cells

out of the computation capability. From the vertical direction analysis it emerges clearly that the beam phase variation is less than 0.1° in the interesting range of the BPM. This range covers the area between ± 6 mm in vertical and horizontal planes. For the Up and Down pickups the tendency is a curve which starts from the closest beam position (0,+12) and decays to the furthest one (0,-12). These curves are almost identical which proves the credibility of the simulations. The phase readings of the second harmonic also show the exact behaviour taking into account that the phase values are doubled with respect to the first harmonic.

For Left and Right pickups the phases are fluctuating in the central region but then they develop with the same gradient similar to the Up and the Down pickup phases. The fluctuation in the central region could be interpreted as numerical errors in the simulation. In the diagonal direction the same fluctuation is observed in the central region from all pickups but the phase margin is still below 0.1° .

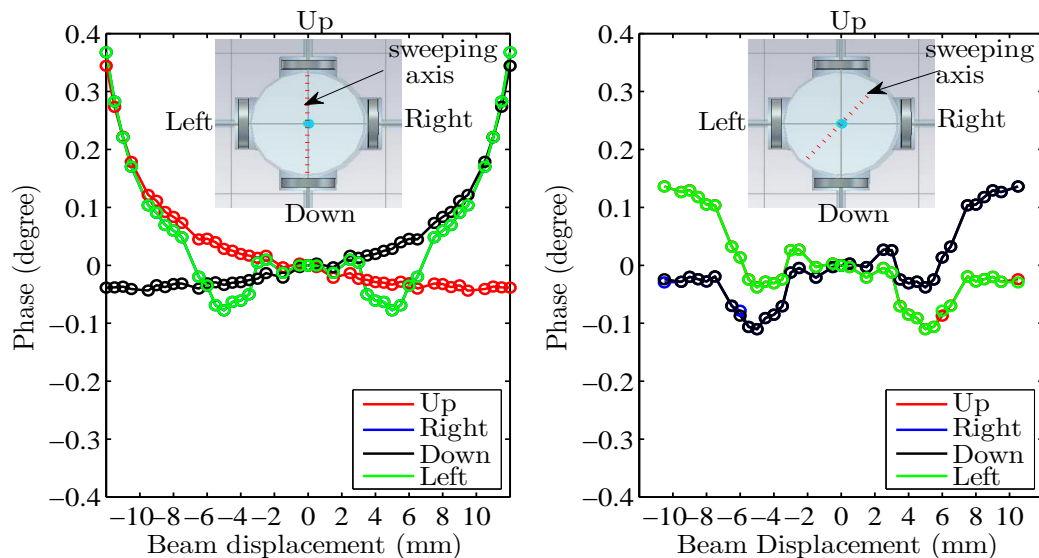


Figure 5.36: The BPM phase deviation from four pickups as a function of the beam displacement in the vertical direction (left) and in the diagonal direction (right).

BPM Electronic and Signal Processing

A digital signal processing system is foreseen for the BPM electronics and DAQ. It is operated by an under-sampling technique, processing data in I/Q demodulation to obtain the beam position from the difference of the electrodes amplitude and the mean energy from the phase value compared to the accelerating frequency. In order to suppress the rf-leakage contribution in the BPM intertank (see Sec. 4.3), the signal information will be obtained from the second harmonic component (650.5 MHz). Therefore, the analogue bandwidth of the digital signal processing should be a band-pass filter matched to the second harmonic of the accelerating frequency [72].

This section gives a general description about the foreseen digital signal processing system for transverse beam position and phase monitoring in the BPM proton LINAC. The motivations, the basic differences between signal processing techniques and the detection algorithm for beam position and phase in digital system - namely Digital Down Conversion (DDC) and IQ modulation techniques - will be briefly introduced.

As a precursor device a Libera Single Pass Hadron (Libera SPH) electronics from the company Instrumentation Technologies [1] is recently under development. The Libera SPH electronic system was tested at the GSI UNILAC. The device functionality, experimental setup, the measurements and the results of the first beam-based test are discussed in this chapter.

6.1 Motivations

Analogue electronics have been used for decades for processing BPM signals in most accelerators facilities. However, the rapid advances in digital systems during the last decade, mainly for telecommunication industry, made digital technology economically

more attractive and easily applicable in the field of particle accelerators. The capabilities of digital systems in terms of sampling rate and voltage resolution have been significantly improved. The high-speed ADC (Analogue to Digital Converter) and FPGA (Field Programmable Gate Array) give digital systems a great advantage to supersede the analogue counterpart in large scale of accelerator applications.

Digital signal processing has several practical advantages with respect to its analogue counterpart. Flexibility is one major advantage for digital systems. Digital systems can be easily reconfigured via software which allows one to upgrade the system to new requirements and operating modes without any hardware modification [88]. In addition, digital systems are remotely controllable and support multi-user operation better than the analogue one [89]. Moreover, the amount of memory which is dependent on the desired resolution (output amplitude bit-width) can be significantly reduced by using digital signal processing. Advantages and drawbacks of using digital and analogue systems in modern accelerators are discussed in [90].

The digital processing scheme is currently under development for the BPM system. The signal will be conditioned by a high resolution ADC (16 bit nominal) and the technique of under-sampling will be applied with a sampling rate matched to a ratio of 4/11 with respect to the accelerating frequency. Using well established digital methods, the amplitude and phase of the individual signal can be evaluated in the FPGA digital electronics. The main features of using the under-sampling technique are; firstly the amount of digital memory needed to record the signal for a given time interval will be significantly reduced. Secondly; the speed requirement of the ADC according to the Nyquist theorem can be decreased [70].

6.2 Signal Processing Methods

To determine the position of the beam and its phase from the BPM, the pickup signals have to be processed and compared. In general, two different techniques are used for processing and evaluating BPM signals, namely the broadband and the narrowband processing depending on the type of measurements and applications [67]. The processing electronics have to be optimized to the machine and the beam parameters in order to obtain the required performance. A detailed comparison of different electronic systems and processing methods is discussed in [65,91].

The choice of signal processing technique significantly influences the position resolution. Broadband signal processing is commonly used for monitoring single bunches. In this type of processing the full signal shape and thus its full power spectrum are recorded, so that the structure of the individual bunches can be observed. This requires that the electronics cover up to at least the 10th harmonics of acceleration frequency [65].

In narrowband processing system, only one harmonic of the acceleration frequency bands with high power density is evaluated. The individual bunch properties are lost due to the bandwidth restriction but the position resolution is enhanced by several orders of magnitude [33]. The reason is that broadband noise contributions are suppressed which leads to better signal-to-noise ratio (SNR).

The background noise in the environment of rf accelerators comes from various sources; mainly the electronic noise, the broadband amplifier noise as well as the stray fields from the rf cavities. The thermal noise is described by an effective voltage drop U_{eff} at a resistor R as given by [67]

$$U_{eff} = \sqrt{4 \cdot k_B T \cdot R \cdot \Delta f} \quad (6.1)$$

with k_B the Boltzmann constant, T the temperature of the resistor R and Δf the bandwidth of the analogue or digital processing. Small bandwidth processing can reduce drastically the contribution of thermal noise and improve position resolution. The achievable resolution for the difference over sum evaluation is usually limited by the thermal noise contribution given by [65]

$$\delta x = \frac{1}{S} \cdot \frac{U_{eff}}{\Sigma U} \quad (6.2)$$

where U_{eff} is the effective voltage calculated from equation 6.1, ΣU is the sum signal from two opposite pickups and S is the BPM sensitivity.

6.3 Amplitude and Phase Detection in BPM Digital Systems

6.3.1 The Sampling Theorem

The process of representing a continuous-time signal with a sequence of discrete data values is called the periodic sampling. The periodic sampling process is mathematically represented as impulse-train sampling in which a band-limited signal $u(t)$ with a bandwidth B is sampled at regular intervals $T_s = 1/f_s$. The sampling frequency f_s should be at least twice the highest frequency component contained in the signal $f_s \geq f$ to avoid the so called “aliasing” and to reconstruct the signal [92]. The periodic impulse-train is the sampling function $s(t)$ described as [93]

$$s(t) = \sum_{n=0}^{\infty} A_m \cdot \delta(t - nT_s) \quad (6.3)$$

where $\delta(t)$ is the unit impulse function, A_m is the modulator amplitude and T_s is the sampling period. The modulator represents a mixer as depicted figure 6.1 and the product of $s(t)$ and $u(t)$ is given by

$$u_s(t) = u(t) \cdot s(t) = u(t) \sum_{n=0}^{\infty} A_m \cdot \delta(t - nT_s) \quad (6.4)$$

using the so called “sifting property” [68] of the impulse function, $u(t)\delta(t) = u(0)\delta(t)$, $u_s(t)$ can be expressed as

$$u_s(t) = A_m \sum_{n=0}^{\infty} u(nT_s) \cdot \delta(t - nT_s) = u(nT_s) \quad (6.5)$$

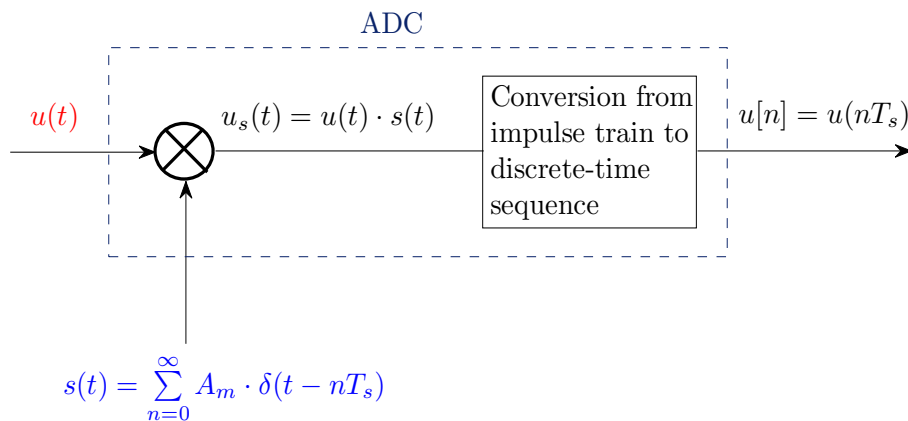


Figure 6.1: The mechanism of impulse-train sampling in which the continuous signal $u(t)$ with a frequency f is sampled at regular intervals $T_s = 1/f_s$. (from [68])

The product of $u(t)$ and $s(t)$ in frequency domain can be derived from the convolution of the fourier transforms $U(\omega)$ and $S(\omega)$ scaled by $1/2\pi$ expressed as

$$U_s(\omega) = \frac{1}{2\pi} \cdot U(\omega) * S(\omega_s) = \frac{1}{T_s} \cdot \sum_{n=0}^{\infty} U(\omega - n\omega_s) \quad (6.6)$$

The result gives spectral replication which consists of the original spectrum and an infinite number of replications, whose period of replication is f_s as shown in figure 6.2. The band of interest can be extracted by applying an appropriate filter.

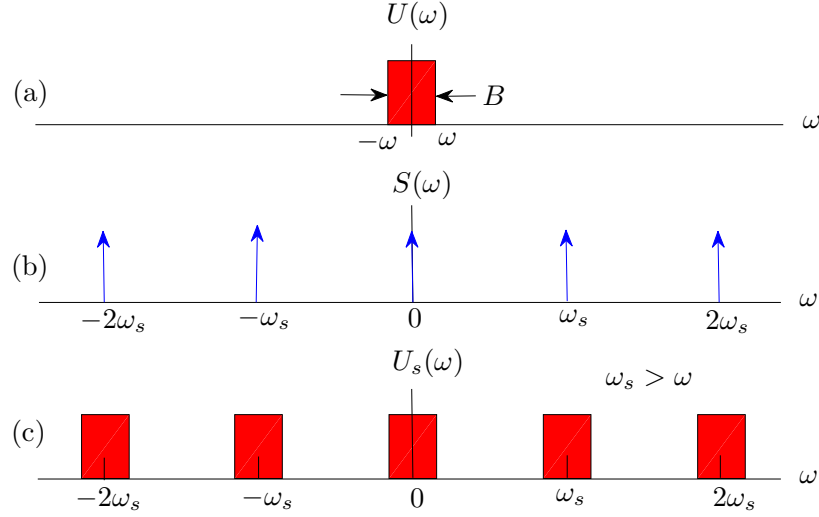


Figure 6.2: Frequency domain representation of sampling in time domain. Spectrum of the original signal $U(t)$ (a). Fourier transformation of the sampling function $S(t)$ (b). Fourier transformation of the sampled signal with $\omega_s > 2\omega$ (c).(from [92])

6.3.2 Phasor Representation of RF Signal

Assuming an input sinusoidal RF signal written as

$$U_{RF}(t) = A_{RF} \cdot \sin(2\pi f_{RF}t + \varphi_{RF}) \quad (6.7)$$

where f_{RF} , A_{RF} and φ_{RF} are signal frequency, amplitude and phase respectively. The $U_{RF}(t)$ signal can be represented in I and Q components by decomposing the signal into its sin and cosine components resulting in so called phasor representation using basic trigonometric functions

$$\begin{aligned} U_{RF}(t) &= A_{RF} \cos(\varphi_{RF}) \sin(2\pi f_{RF}t) + A_{RF} \sin(\varphi_{RF}) \cos(2\pi f_{RF}t) \\ &= I \cdot \sin(2\pi f_{RF}t) + Q \cdot \cos(2\pi f_{RF}t) \end{aligned} \quad (6.8)$$

where $I = A_{RF} \cos(\varphi_{RF})$ is called the in-phase component which represents the amplitude of the sine component in Cartesian coordinates or the real part in polar coordinates;

$A_{RF} \sin(\varphi_{RF})$ is called the quadrature-phase component representing the amplitude of the cosine component in Cartesian coordinates or the imaginary part in polar coordinates. The phasor representation of the RF signal of an amplitude A_{RF} and phase φ_{RF} is shown in figure 6.3. The relationship between I and Q components are;

$$A_{RF} = \sqrt{I^2 + Q^2} \quad \text{and,} \quad \varphi_{RF} = \tan^{-1}(Q/I) \quad (6.9)$$

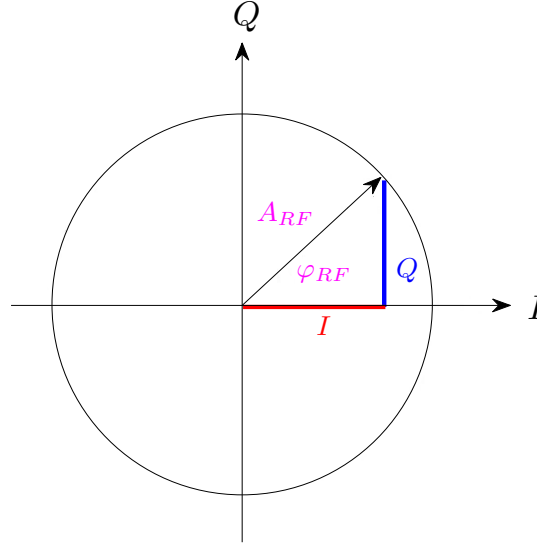


Figure 6.3: Phasor representation of RF signal where $I = A_{RF} \cos(\varphi_{RF})$ (in-phase component) and $Q = A_{RF} \sin(\varphi_{RF})$ (quadrature-phase component)(from [90]).

6.3.3 I/Q modulation and Digital Down Conversion (DDC)

The detection of signal amplitude and phase information in the BPM digital systems is implemented by means of I/Q modulation and Digital Down Conversion (DDC). They are very common and useful techniques for processing signals in many RF applications. In essence, a band-limited high frequency signal is digitized with a lower sampling rate so that the signal is down-converted to a lower frequency while retaining all signal information [70] as shown in figure 6.4. This technique is called harmonic sampling, under-sampling or IF sampling in literature [94].

The Nyquist Shannon's sampling theorem states that, for a full bandwidth sampling, the sampling frequency f_s must be greater than the highest frequency in the signal in order to reconstruct the signal without aliasing as mentioned in Sec. 6.3.1. But this condition will not be applied in the BPM for the proton LINAC because the under-sampling technique will be implemented. The Nyquist Shannon's sampling relates the

sampling frequency and signal bandwidth B and states that in the undersampling case the aliasing can be avoided if the sampling frequency is more than twice the signal bandwidth ($f_s \geq 2B$) [68]. However, the sampling frequency f_s should be chosen anywhere between two boundaries that satisfy the condition [70]

$$\frac{2f_{RF} - B}{m} \geq f_s \geq \frac{2f_{RF} + B}{m + 1} \quad (6.10)$$

where m is an arbitrary, positive integer ensuring that $f_s \geq 2B$. For instance, in the case of the proton LINAC operated at 325.224 MHz and a chance of a signal bandwidth of ~ 1 MHz, the sampling rate can be anywhere in the range of 108.5 to 129.8 MHz if m is chosen to be 5 (See [70] for different possibilities and a more detailed discussion). The optimum sampling frequency in the region between the two boundaries can be chosen based on the specific application, the electronics efficiency and the anti-aliasing filters.

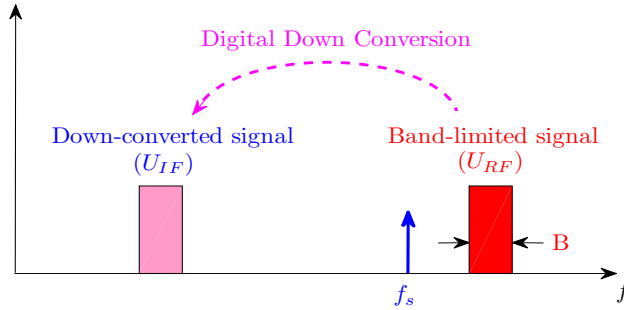


Figure 6.4: In the undersampling technique, a band-limited signal U_{RF} is sampled with a lower sample rate f_s and down-converted to Intermediate Frequency (IF) f_{IF} .

The I/Q (in-phase and quadrature) information are constructed with a sampling rate f_s lower than the RF signal frequency f_{RF} ($f_s < f_{RF}$) as depicted in figure 6.4. Consequently, the incoming RF signal is down-converted to a lower frequency band, so called Intermediate Frequency (IF) f_{IF} . The chosen sampling rate with respect to the RF signal frequency will determine the amount of sample reduction, where [90]

$$f_s = \frac{N}{M} \cdot f_{RF} \quad \Leftrightarrow \quad N \cdot T_s = M \cdot T_{RF} \quad (6.11)$$

At each T_s only one component of the rotating phasor is extracted. If M/N is set to $1/4$ the phase advance between two samples is 90° . This leads to set of the samples defined as $Q, I, -Q$ and $-I$; and the following samples are again $Q, I, -Q$ and $-I$ and so on. Depending on the values chosen for M and N , where M and N are integers, the circle in the IQ plane will be sampled at different locations. The samples only repeat after M

T_{RF} periods. The phase advance between two consecutive ADC readings is [90]

$$\Delta\varphi = 2\pi f_{RF} \cdot T_s = 2\pi \frac{T_s}{T_{RF}} = 2\pi \frac{M}{N} \quad (6.12)$$

The stream of I and Q data reflects the amplitude of the RF signal sampled at intervals and shows a repeating pattern I/Q samples. As long as the input RF signal does not change, it will be sampled at the same location on the circle in the IQ plane.

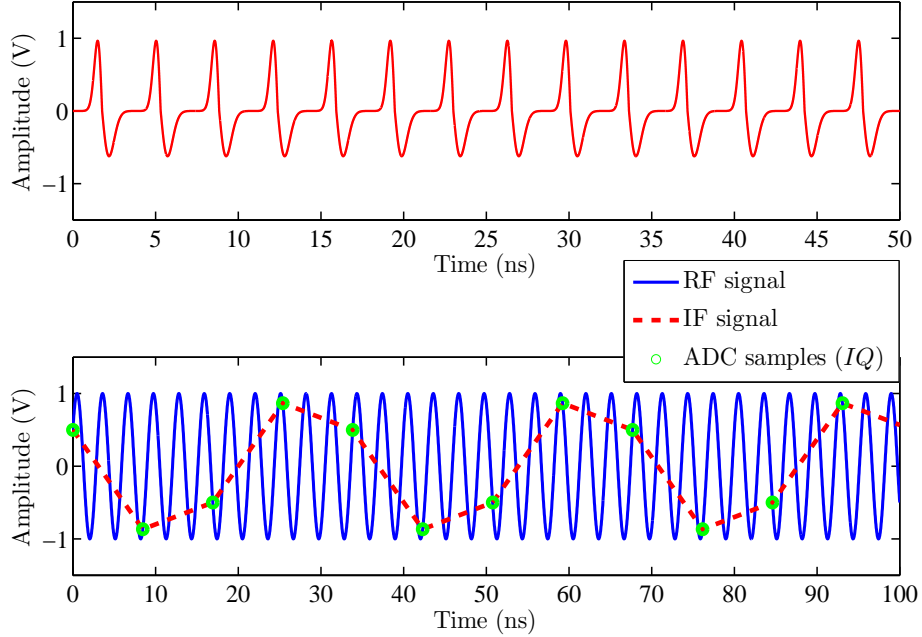


Figure 6.5: The principle of under-sampling as performed for BPM signal (upper panel). The resulting IQ values of the RF signal $f_{RF} = 325$ MHz sampled at $f_s = 4/11 f_{RF} = 118$ MHz, corresponding to 4 samples over 11 bunches. The periodicity of the digital data is 33.82 ns corresponding to a bandwidth of 29.56 MHz for the reconstructed IF signal (down panel).

In the BPM digital system for the proton LINAC the sampling rate f_s is locked to the acceleration frequency f_{RF} which fulfills the condition;

$$f_s = 4/11 \cdot f_{RF} \quad (6.13)$$

The output down-converted IF signal is ~ 29.56 MHz calculated from $f_{IF} = f_s/4$. In time domain view this can be described such that 4 ADC values are equally distributed over 11 bunches as shown in figure 6.5.

The amplitude and phase information of the IF signal can be then extracted in a purely digital way from its I and Q components which are also related to the original RF signal. The process of retrieving the I and Q information is called I/Q demodulation (Sec. 6.3.4) which is performed in the FPGA digital electronics. From I/Q data the beam

position (from the difference of the signal's amplitude of the opposite pickups) and mean energy (from the phase value compared to the accelerating frequency) can be measured in a flexible manner with a selectable time resolution.

6.3.4 I/Q Demodulation

As mentioned previously the signal amplitude and phase information are preserved in the I and Q data stream which consists of a repeating pattern of I and Q values. In the digital I/Q demodulator, a numerically controlled oscillator (NCO) is implemented as a quadrature digital oscillator [90]. It generates a stream of sine and cosine samples with a 90° phase shift and frequency matches to the digital down-converted signal $f = f_{IF}$ as shown in figure 6.6.

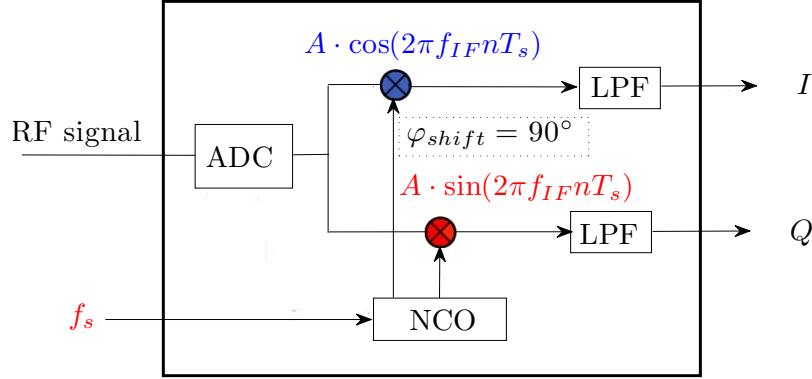


Figure 6.6: The digital I/Q demodulator producing I and Q data stream includes a numerically controlled oscillator (NCO) generating a stream of sine and cosine samples with a 90° phase shift and frequency matches to IF signal (from [90]).

The mixing product of the the IF signal and NCO's signals produces I and Q data. The result of of each mixing path gives two terms; written as

$$\begin{aligned}
 I &= U_{IF}(t) \cdot A \cdot [\sin(2\pi f_{IF} n T_s)] \\
 &= A_{IF} \cdot \sin(2\pi f_{IF} n T_s + \varphi_{IF}) \cdot A \cdot \sin(2\pi f_{IF} n T_s) \\
 &= 0.5 \cdot A_{IF} \cdot A [\cos(2\pi \cdot 2f_{IF} n T_s - \varphi_{IF}) - \cos \varphi_{IF}]
 \end{aligned} \tag{6.14}$$

$$\begin{aligned}
 Q &= U_{IF}(t) \cdot A \cdot [\cos(2\pi f_{IF} n T_s)] \\
 &= A_{IF} \cdot \sin(2\pi f_{IF} n T_s + \varphi_{IF}) \cdot A \cdot \cos(2\pi f_{IF} n T_s) \\
 &= 0.5 \cdot A_{IF} \cdot A [\sin(2\pi \cdot 2f_{IF} n T_s + \varphi_{IF}) + \sin \varphi_{IF}]
 \end{aligned} \tag{6.15}$$

The higher order terms $0.5 \cdot A_{IF} \cdot A \cdot \sin(2\pi 2f_{IF} n T_s + \varphi_{IF})$ and $0.5 \cdot A_{IF} \cdot A \cdot \cos(2\pi \cdot 2f_{IF} n T_s + \varphi_{IF})$ are filtered out and the dc baseband terms $0.5 \cdot A_{IF} \cdot A \cdot \sin \varphi_{IF}$ and

$0.5 \cdot A_{IF} \cdot A \cdot \cos \varphi_{IF}$ are selected as I/Q data which correspond to the I/Q of the original RF signal. The sign inversion in each path is removed by multiplying each data stream by +1 and -1 alternatively. After N successive samples the sum of I and Q output are [90];

$$Q = \frac{2}{N} \cdot \sum_{i=0}^{N-1} U_{IF_i} \sin(i \cdot \Delta\varphi) \quad \text{and,} \quad I = \frac{2}{N} \cdot \sum_{i=0}^{N-1} U_{IF_i} \cos(i \cdot \Delta\varphi) \quad (6.16)$$

where i is integer and $\Delta\varphi$ is given from equation 6.12.

6.3.5 Libera SPH Digital Electronics for Proton LINAC

The proton LINAC operates with an accelerating frequency of 325.224 MHz and the technique of under-sampling will be applied with a sampling rate of ~ 118 MSa/s [95]. The digital signal processing for the transverse beam position and the phase monitoring could be realized by using the Libera SPH which involves a fast I/Q digital sampling and digital down conversion processing [96]. From I/Q data stream the beam position and phase of the individual signal are evaluated in the FPGA digital electronics in a flexible manner with a selectable time resolution between 1 to 70 μs [97].

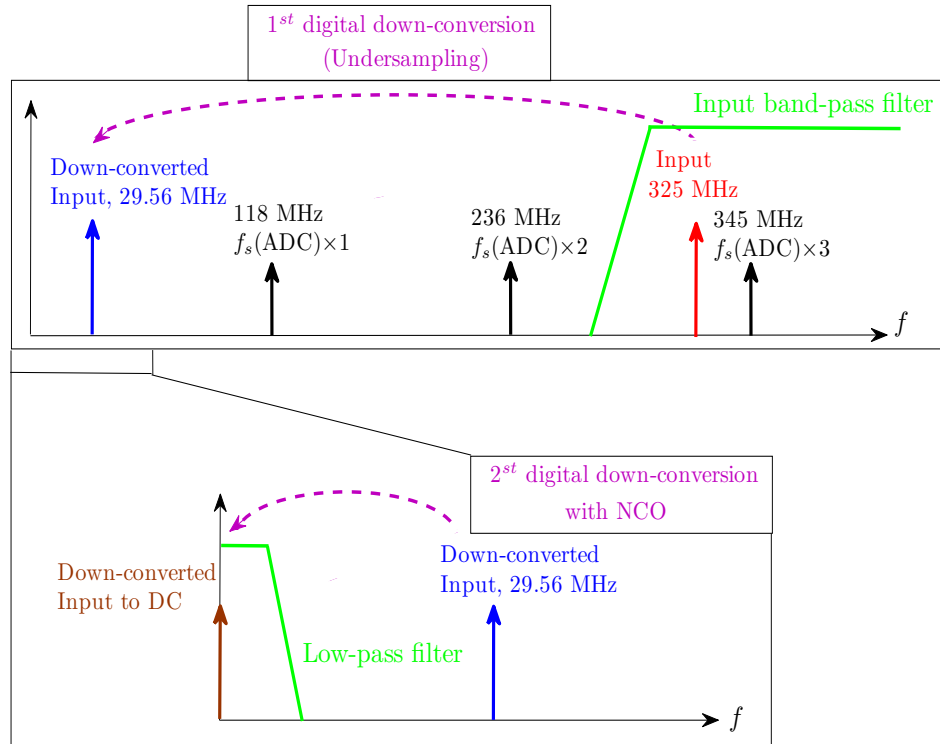


Figure 6.7: Input signal is digitized (1st digital down conversion) with sampling rate $f_s = 118$ MHz locked to the acceleration frequency $f_{RF} = 325.224$ MHz. The output down-converted IF signal is ~ 28.22 MHz and the I/Q data is retrieved by applying a numerically controlled oscillator (NCO) (2nd digital down conversion).

After pre-amplification, the analogue signal from the BPM pickups are fed to the Libera SPH front-end. In order to suppress the rf-leakage from the nearby CH-cavity a band-pass filter matched to the second harmonic (650.45 MHz) of the accelerating frequency is placed into the analogue front-end chain. The signal is then digitized using a high resolution ADC and the I/Q data stream is constructed (first digital down conversion) as shown in figure 6.7 [98]. The I/Q data is retrieved through a sophisticated digital signal processing module by applying a numerically controlled oscillator (NCO) to obtain the amplitude and phase information from the processed harmonic.

6.4 Experimental Setup

A beam-based test was conducted at the GSI UNILAC to investigate the performance of the Libera SPH electronics system for beam position and phase measurements. The Libera SPH unit consists of 5 input channels as shown in figure 6.8 [98]. Four of them measure amplitude and phase of individual input signal from each button of the BPM. The unit features a 117.44 MSa/s ADCs of nominal 14 to 16 bits, large field programmable gate array circuits (FPGA) and fast memory. From amplitudes the beam position is calculated from the difference over sum method. The beam phase is determined from the average phase measured by the four channels with respect to an external master oscillator rf signal. The phase calculation includes a wrapping algorithm to prevent incorrect phase calculations.

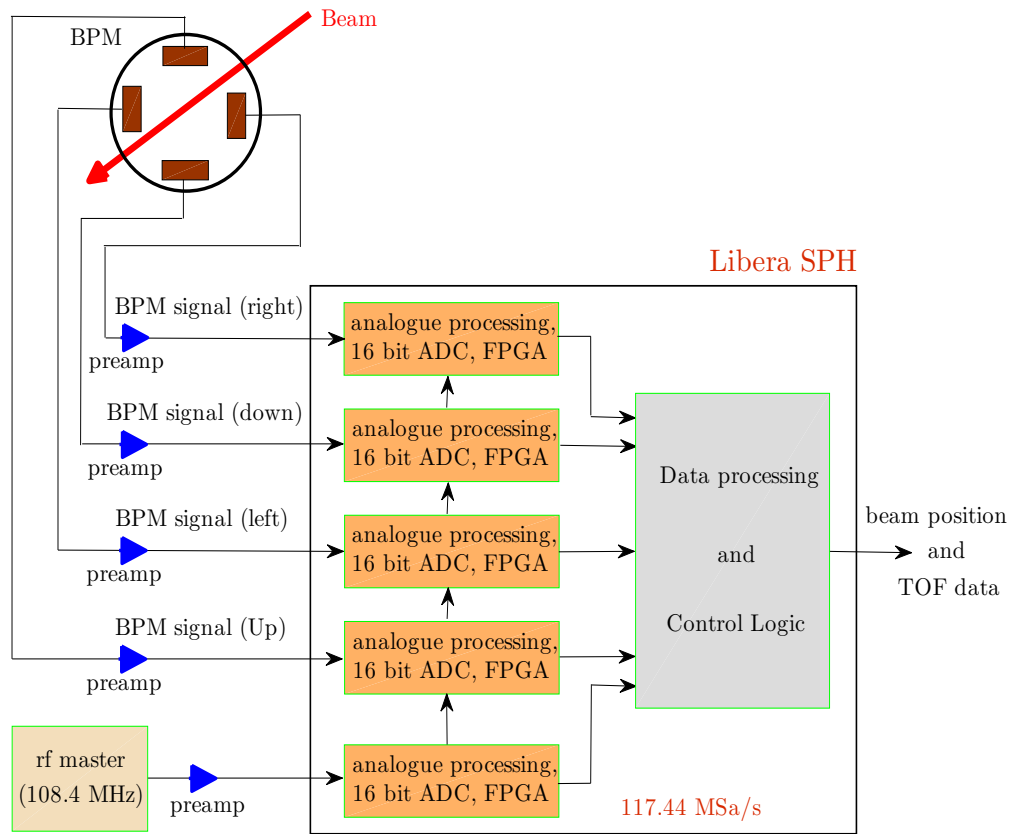


Figure 6.8: The Libera SPH phase and position processing and block diagram

For the test, the Libera SPH electronics were customized to process the signals at the base frequency of the UNILAC (108.4 MHz). The BPM signals were adapted by low noise, 3 GHz broadband amplifiers up to 44 dB amplification. The characteristic of the input impedance matching the device is shown in figure 6.9.

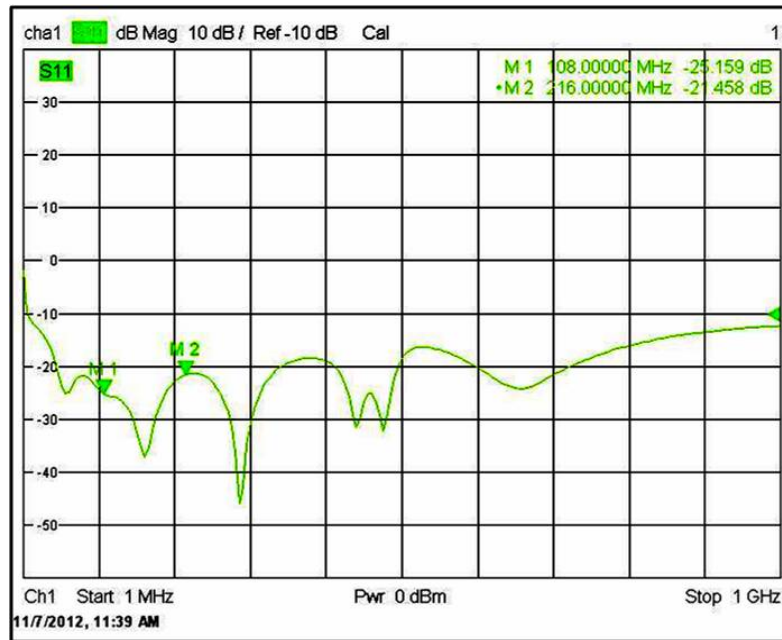


Figure 6.9: The input matching at 108.408 MHz and 216.8 MHz frequencies are at -25 dB and -21 dB return loss.

The experiment described here was carried out using a Ca^{10+} beam from the High Charge State Injector (HLI) with an energy of 1.4 MeV/u and a bunch repetition rate of 108.408 MHz. The macro pulse structure for the measurements was 200 μs length and 1 Hz repetition rate. As shown in figure 6.10, the beamline optical elements consist of a re-buncher for longitudinal focussing, quadrupole doublet for beam transverse focussing and dipole for horizontal position variation. The diagnostic section is installed at the end of the beamline. It consists of a four electrode capacitive BPM for beam position and phase detection, a phase probe for phase measurements and a SEM-grid for beam profile measurements. The capacitive BPM has an aperture of 50 mm and an electrode length of 20 mm as shown in figure 6.11 (left). The phase probe in 50 Ω geometry has an inner diameter of 35 mm as shown in figure 6.11 (right). The beamline configuration allows one to vary the beam position as well as the formation of different bunch shapes by changing the re-buncher setting. The peak-to-peak voltage V_{pp} of the output signal depends on the resulting bunch shape due to longitudinal focussing.

The experiment was divided into three parts. In the first part, the resolution of the Libera SPH unit was investigated for beam position and phase measurements at different signal amplitude levels under various forms. This part was conducted without comparison to any other system. The second part of the test was dedicated to evaluate the Libera SPH phase readings measured at the base frequency of UNILAC. The aim was to characterize

the dependence of beam arrival time on bunch shape. The resulting phase obtained by the Libera SPH were compared to the phase calculated from Fourier transformation and the phase determined time domain sampling by a fast oscilloscope (LeCroy Waverunner 6200A). The third part was performed to investigate the Libera SPH position accuracy. The beam position was varied vertically in five locations and the beam position measured by the Libera SPH was compared to SEM grid measurements. In the following three sections the results of these tests are presented and discussed.

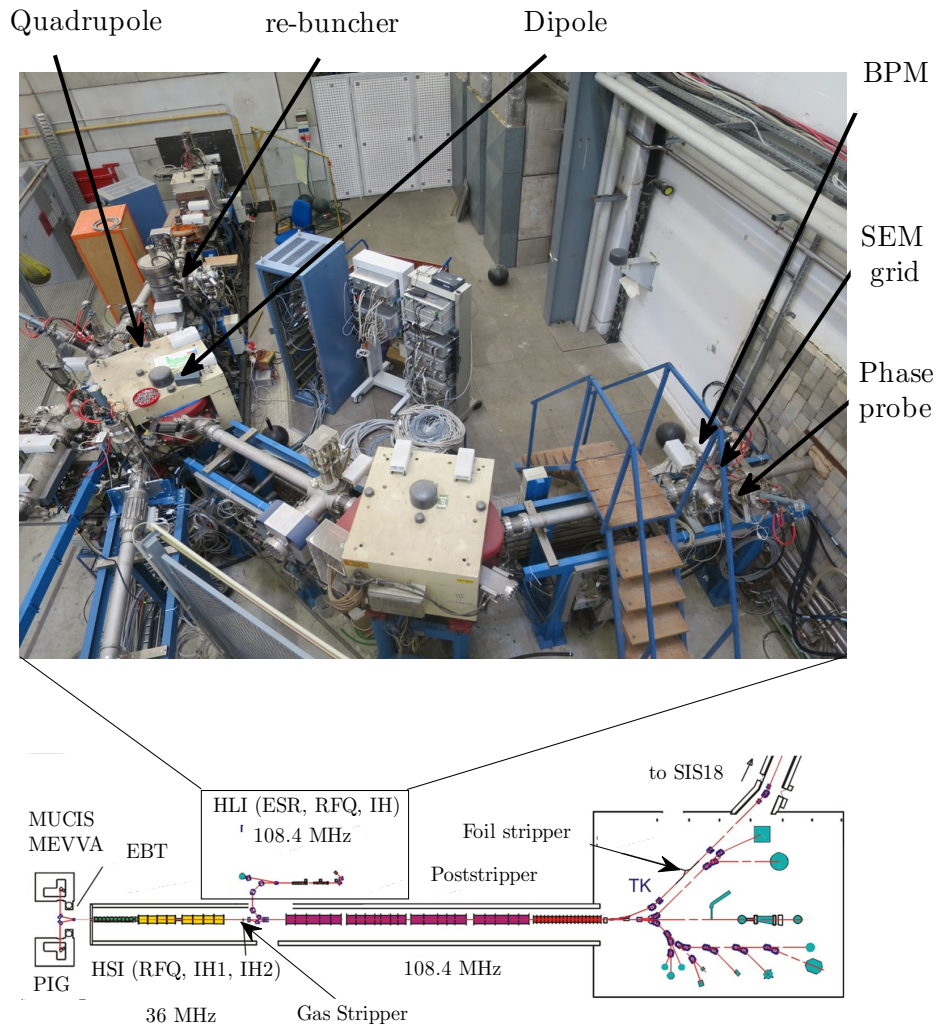


Figure 6.10: The beamline optical elements in the High Charge State Injector (HLI) at UNILAC consisting of a re-buncher, quadrupole doublet, dipole and a diagnostic section.

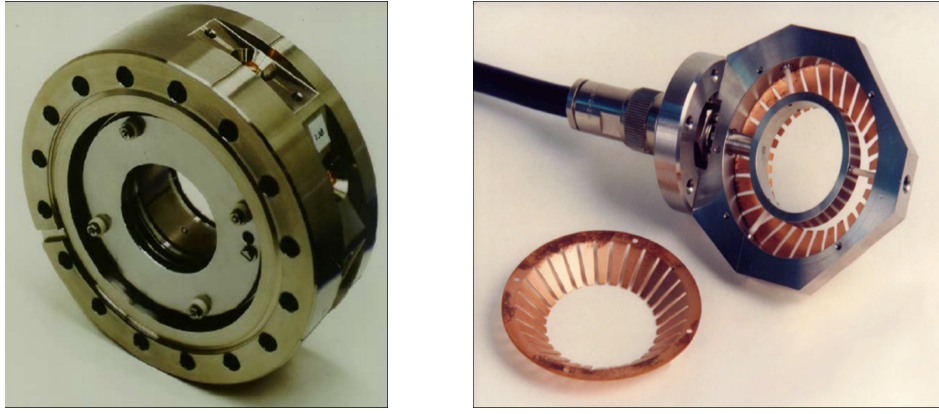


Figure 6.11: The capacitive BPM of a 50 mm aperture and a 20 mm electrode length at the GSI-LINAC (left). The phase probe in 50 Ω geometry and a 35 mm inner diameter as used for the longitudinal bunch observation and phase measurements at the 108 MHz GSI-LINAC (right).

6.4.1 Libera SPH Data Evaluation

The signals from the four electrode BPM were sampled at 117.440 MSa/s (not fixed to the acceleration frequency $f_{RF} = 108.408$ MHz) with nominal 16-bit ADC and digitally processed by the Libera SPH unit. The unit processes the signal and calculates the beam position and phase from the base frequency. The data has been stored in the device in steps of 1 μs (correspond to ~ 108 bunches) for a train of data sets of 129 μs each. Every data set corresponds to one macropulse and contains the signal amplitude of four pickups, the calculated beam position and phase reading in respect to rf signal master oscillator. The mean value and the standard deviation σ_M were calculated and used. The standard deviation of the mean σ_{mean} was obtained from $\sigma_{mean} = \sigma_M / \sqrt{N}$, where $N = 129$ is the number of measured data within a macropulse.

Four input signals U_A (Up), U_B (Left), U_C (Down) and U_D (Right) carry beam position and phase information. Figure 6.12 shows a typical example of the Libera SPH data-set for pickup amplitudes and phase during one macropulse. The device calculates the output phase directly for each signal subtracted from the phase of rf master oscillator. The final phase reading is the average of the four phases from the BPM signals.

The device calculates the position of the beam from signal amplitudes of two opposite pickups using the difference over sum method:

$$\Delta U_x = U_A - U_C \quad \text{and,} \quad \Delta U_y = U_B - U_D \quad (6.17)$$

$$\Sigma U_x = U_A + U_C \quad \text{and,} \quad \Sigma U_y = U_B + U_D \quad (6.18)$$

The ratio between difference over sum in the horizontal H and vertical V plane are

$$H = \frac{\Delta U_x}{\Sigma U_x} \quad \text{and,} \quad V = \frac{\Delta U_y}{\Sigma U_y} \quad (6.19)$$

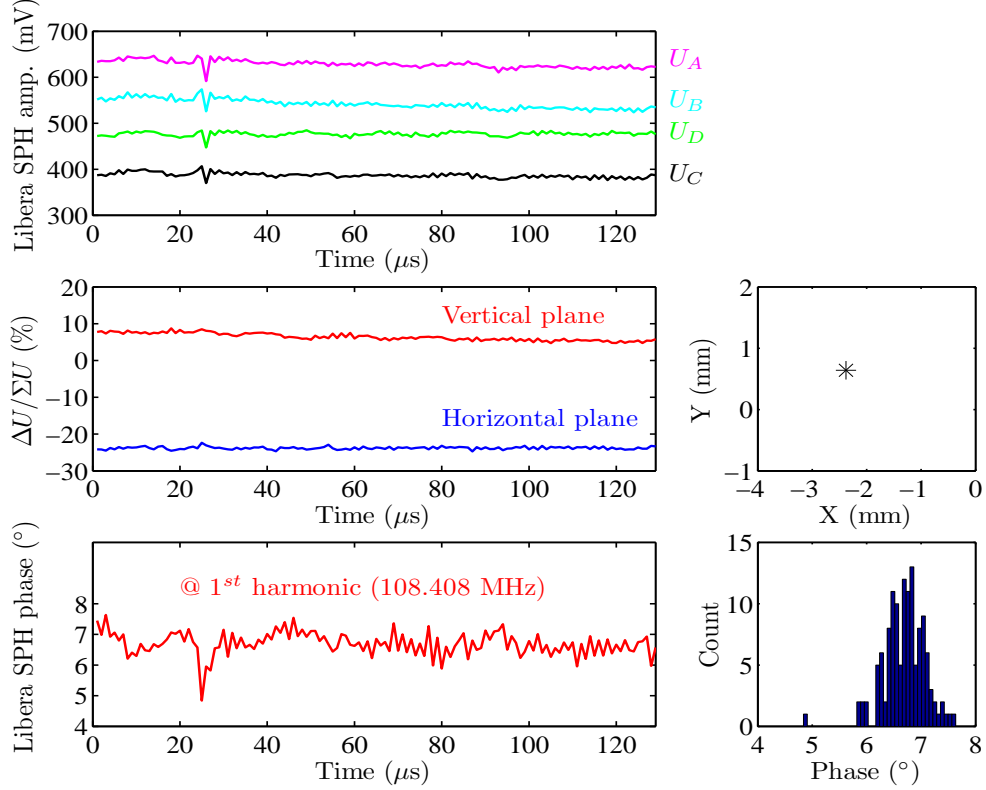


Figure 6.12: Single electrode amplitude (up), the difference over sum of H and V in % and the calculated beam position for $S = 10$ %/mm (middle), the corresponding phase reading with respect to 108.408 MHz and the histogram (bottom) during one macro-pulse (train of data sets of $129 \mu s$ and $1 \mu s$ time resolution).

The position sensitivity S_x and S_y of the BPM was set to be $10\%/mm$. The standard deviation for the sum or for the difference was calculated from

$$\sigma_{\Delta(H,V)} = \sigma_{\Sigma(H,V)} = \sqrt{\left(\sigma_{(U_A,U_C)}^2 + \sigma_{(U_B,U_D)}^2\right)} \quad (6.20)$$

where σ_{U_A} , σ_{U_B} , σ_{U_C} and σ_{U_D} are the standard deviation of output signals. The standard deviation for the calculated ratio between difference over sum was calculated using fractional errors as

$$\sigma_H = H \times \sqrt{\left(\frac{\sigma_{\Delta H}}{\Delta U_x}\right)^2 + \left(\frac{\sigma_{\Sigma H}}{\Sigma U_x}\right)^2} \quad \text{and,} \quad \sigma_V = V \times \sqrt{\left(\frac{\sigma_{\Delta V}}{\Delta U_y}\right)^2 + \left(\frac{\sigma_{\Sigma V}}{\Sigma U_y}\right)^2} \quad (6.21)$$

The results for such evaluation are depicted in figure 6.14 (right).

6.5 Test of Libera SPH Resolution

The aim of this test was to investigate the Libera SPH resolution for measuring beam position and phase at different amplification levels for different bunch shapes. The Libera SPH resolution was determined from the standard deviation of four successive macropulses. Three bunch shapes were produced as shown in figure 6.13 by the variation of the re-buncher settings. The position and phase measurements were taken systematically for each bunch shape at different signal levels. The signal amplification was swept from 14 dB to 44 dB with gain step of 6 dB steps using a switchable pre-amplifier. The sum signals of the BPM pickups was displayed on a 10 GSa/s oscilloscope during measurements to monitor the bunch shape.

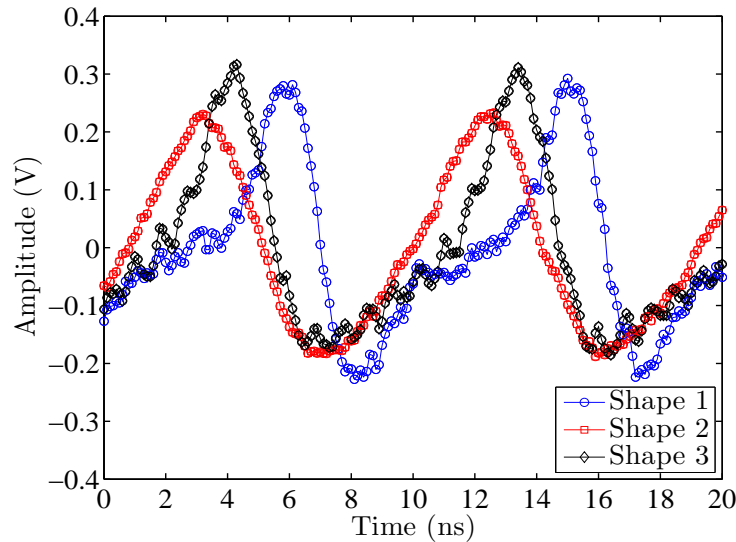


Figure 6.13: Three different bunch shapes (200 samples) at 44 dB amplification as displayed on a 10 GSa/s oscilloscope (LeCroy Waverunner 6200A).

6.5.1 Position Measurements

The Libera SPH unit records the signal amplitude values of the BPM's pickups and calculates directly the position of the beam. The position of the beam was calculated for x and y coordinates from

$$x = \frac{1}{S_x} \cdot H \quad \text{and,} \quad y = \frac{1}{S_y} \cdot V \quad (6.22)$$

Figure 6.14 shows the position variation on x and y coordinates as a function of the signal level (left) and the standard deviation of the measurements (right). The results show a stable response for most of the measurements especially for large signal amplitudes but the position resolution decreases with signal level decrease. The standard deviation is $\sim 50 \mu m$

for signal amplification level of higher than 25 dB. Such resolution level fulfills the BPM requirements which is $100 \mu m$ spatial resolution for beam position determination [57]. The position resolution for x and y differ by roughly factor of ~ 2 for the same bunch and the reason could be due to beam offset.

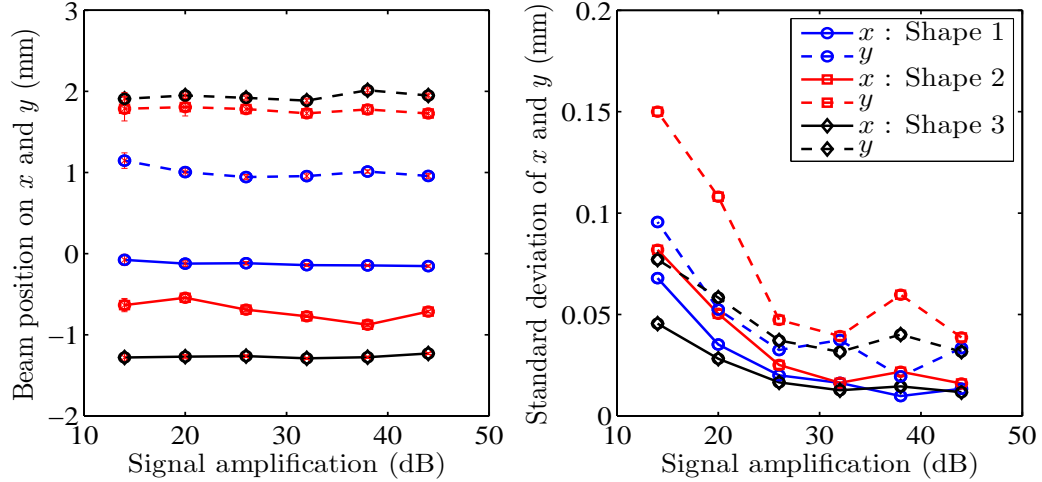


Figure 6.14: Libera SPH position variation on x and y coordinates for three bunch shapes as a function of the signal level (left) and the standard deviation of the measurements (right).

6.5.2 Phase Measurements

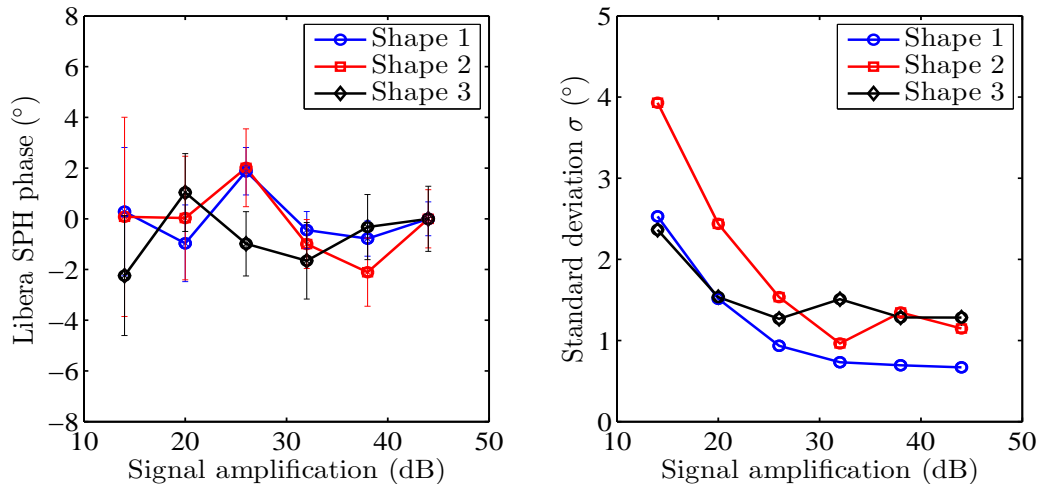


Figure 6.15: Libera SPH phase reading variation for three bunch shapes as a function of the signal level (left) and the standard deviation of the measurement (right).

The Libera SPH unit calculates the average phase from the four BPM's signals in respect to the rf master oscillator. Figure 6.15 shows the phase reading variation of the

three bunch shapes as a function of the signal level (left) and the standard deviation of the measurements (right). One can observe that phase reading is fluctuating in a range of $\pm 4^\circ$. The variation of the measured phase for each bunch shape does not show a clear tendency. But it is obvious that the phase resolution is amplitude dependent so that it increases with the signal level decrease. The phase resolution is larger than the value required in the specification of the BPM [57].

For instance, the standard deviation of shape 1 is less than 1° for amplification level of 44 to 26 dB but for the other shapes it gives more than 1° and some fluctuation. The reason for such behaviour is still not understood but it could be related to the position of the bunch. As it seen in figure 6.14, shape 2 and shape 3 have more offset from the beam pipe centre. The effect of such displacement on the measured phase still needs to be investigated.

6.6 Beam Phase Evaluation by Different Methods

The conventional time domain method uses broad-band signal processing so that the signal shape and its full power spectrum are recorded. As a representation for arrival time the zero-crossing point of the signal (see figure 6.24) is used which depends mainly on the particle distribution in the bunch forming a certain bunch shape.

The produced signal has a discrete spectrum in the frequency domain reflecting the bunch shape. The Libera SPH applies a narrow-band processing and the arrival time is determined from the phase of the processed harmonic in the spectrum. The advantage as equation 6.1 clearly shows that the noise power is proportional to the measurement bandwidth. Making the measurement bandwidth as narrow as possible gives a significant increase in the signal-to-noise ratio, and thus improves the measurement resolution. As a drawback for phase measurement, processing only one harmonic does not give all the information about the bunch shape. The reason is that the signal phase information not only exists in the interesting harmonic but the other harmonics also contribute. These harmonics are neglected or filtered out by the system.

In the proton LINACs machine it is expected that the bunch will be deformed due to the space charge effect especially in the low β range. Therefore, processing only one

harmonic might be not sufficient to determine bunch arrival time if there is significant change in the bunch shape between two successive BPMs. Therefore, it was required to conduct a dedicated phase test with different bunch shapes to characterize the phase dependence on the bunch shape. The results obtained by the Libera SPH were compared to the zero-crossing time domain evaluation as well as to the Fourier transformation in frequency domain.

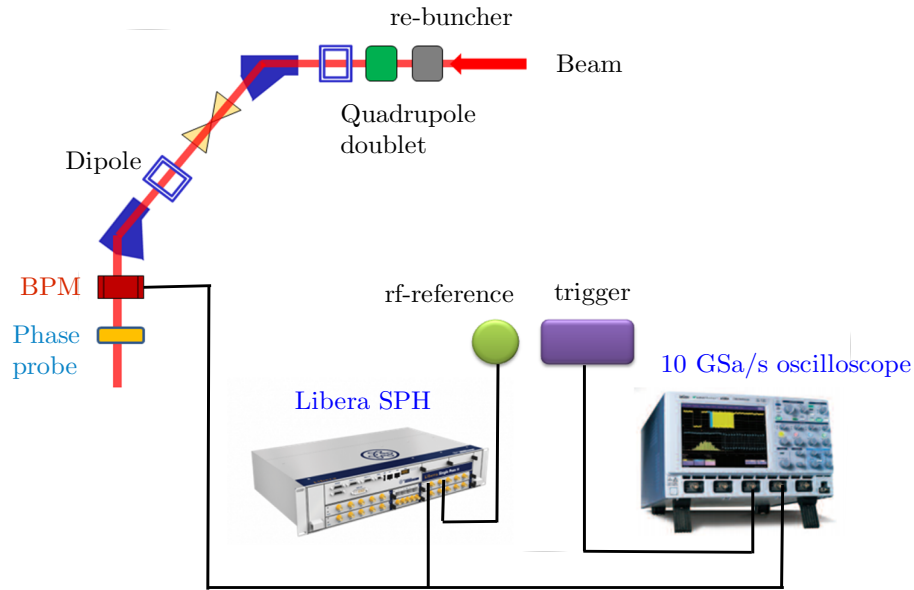


Figure 6.16: Experimental setup where the BPM's signal is split into Libera SPH unit and a 10 GSa/s oscilloscope (LeCroy Waverunner 6200A) and both systems were triggered to the rf master oscillator

Six different bunch shapes were generated by adjusting the re-buncher setting. The experiment conducted using a Ca^{10+} beam from with an energy of $1.4 MeV/u$ and a bunch repetition rate of 108.408 MHz. The macro pulse structure for the measurements was 200 μs length and 1 Hz repetition rate. The BPM acts as a bunch arrival monitor detecting the longitudinal profile of the bunch. The BPM's signals were split into the Libera SPH unit and a 10 GSa/s oscilloscope (LeCroy Waverunner 6200A) and both systems were triggered to the rf master oscillator as shown in figure 6.16. Four channels in the Libera SPH were fed with the pickup signals and the sum of those signals was displayed and stored by the oscilloscope. The correlation between the Libera SPH and the oscilloscope time domain data was studied. For further investigations, the time domain data obtained from the oscilloscope was Fourier-transformed to compare with the frequency-domain results measured by the Libera SPH.

6.6.1 Libera SPH Phase Evaluation

The phase was measured by the Libera SPH for each bunch shape. The measurements were conducted in a systematic manner at three different amplification levels 44, 32 and 20 dB using the BPMs' signals and the phase probe. First, the BPMs' signals were fed to the device and the measurements were performed by the Libera SPH unit. After that, the cables from the BPMs' electrodes to the Libera SPH were disconnected and they were replaced with the phase probe signal after being split into four channels. The purpose was to eliminate the influence of the beam offset in order to compare with the phase produced by the BPM. Figures 6.17 and 6.18 show the measured Libera SPH phase (left) and the standard deviation (right) using the BPM and the phase probe, respectively.

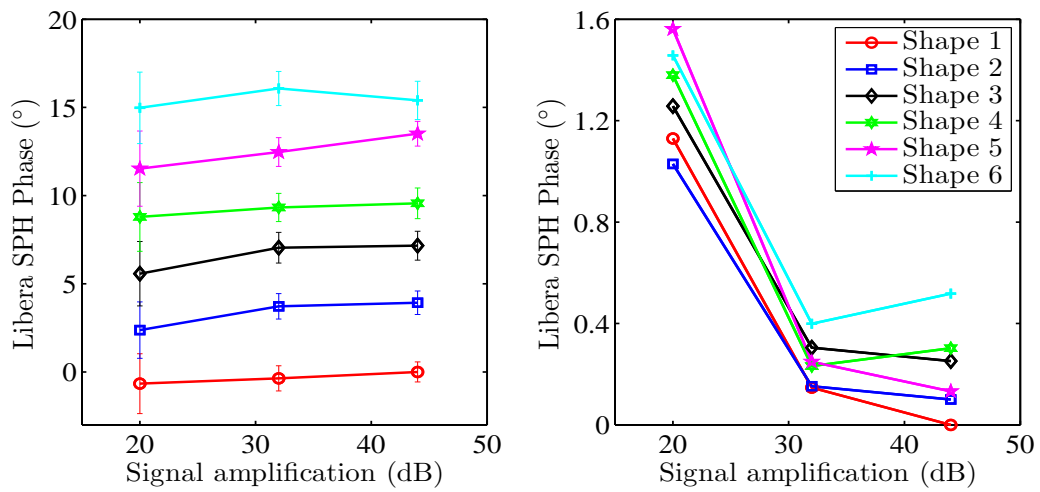


Figure 6.17: Libera SPH phase reading for six bunch shapes @ 44, 32 and 20 dB amplification using BPM signals (left) and the standard deviation (right).

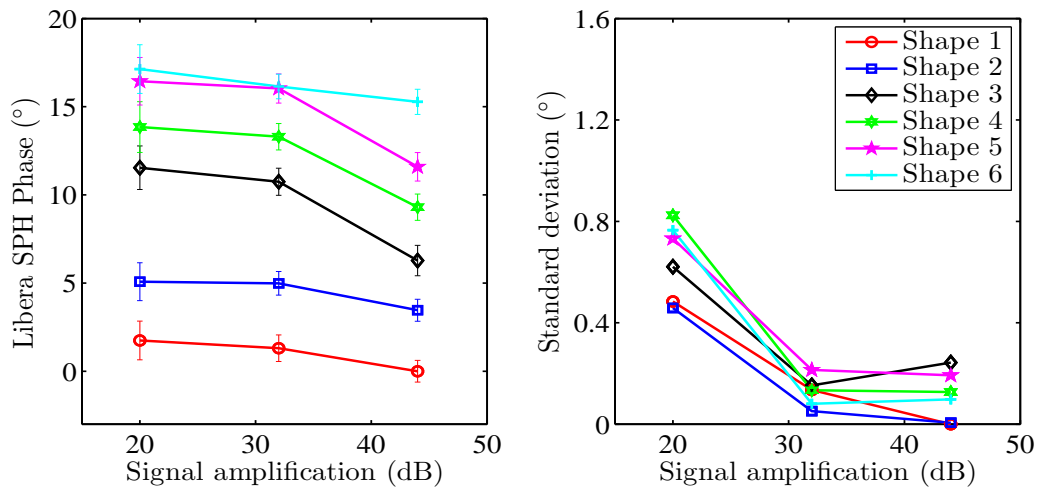


Figure 6.18: Libera SPH phase reading for six bunch shapes @ 44, 32 and 20 dB amplification using phase probe signal (left) and the standard deviation (right).

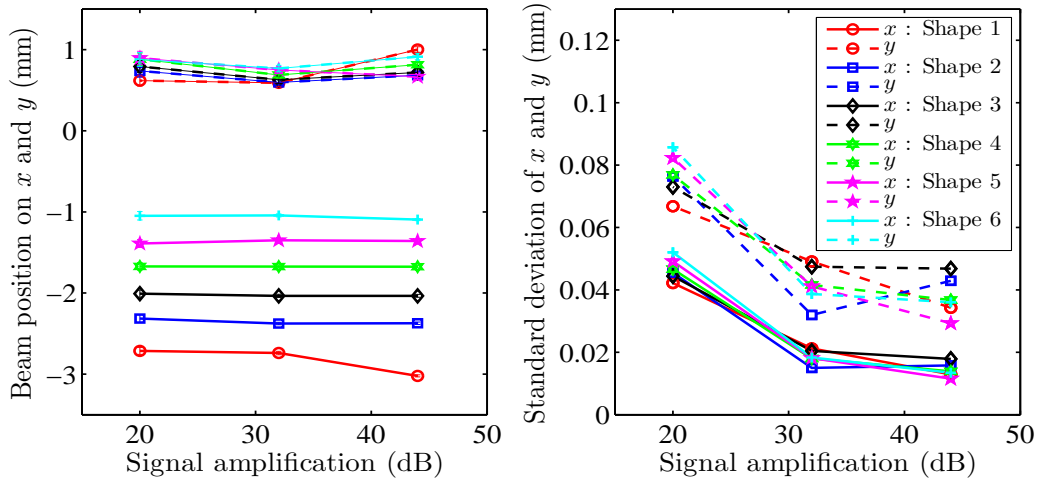


Figure 6.19: Beam position variation on x and y coordinates as a function of the signal level for six bunch shapes (left) and the standard deviation of the measurements (right).

Looking into figures 6.17 and 6.18 one can observe a compatibility between BPM and phase probe readouts in most shapes. The discrepancy in some phase readings were expected in such measurements for two reasons; first the phase is very sensitive to the any intervention in the setup such as cables bending or cable unscrew / screw, which may cause some uncertainty. Second, the beam offset was canceled in the phase probe reading since the phase probe signal is equally distributed into four inputs to the Libera SPH unit. The beam position in x and y coordinates measured by the Libera SPH and the standard deviation are shown in figure 6.19 which shows a large offset in the x -axis. The phase reading is amplitude dependent, although the change is not significant but the measurement resolution changes significantly. With 44 dB and 32 dB pre-amplification, the Libera SPH readouts show good resolution with standard deviation less than 0.4° for most of shapes. The measurements proves the feasibility that the Libera SPH can measure a phase within a 1° resolution but only if the signal level is high enough.

6.6.2 FFT Analytical Approach

A code was written in MATLAB software [99] to manipulate the time domain signal stored by the oscilloscope and to perform the Fast Fourier Transform. The MATLAB function `fft` computes $X(m)$ function in equation 3.17 for a given N input sequence. The amplitude and phase spectrums of the time domain sequence can then be produced from the calculated $f_a(m)$ frequencies or FFT bins. Then, the phase at 108.408 MHz in FFT phase spectrum can be extracted and used to verify with the time-domain reading and to compare with the frequency-domain processing obtained by the Libera SPH.

- FFT for a single bunch

The signal curve obtained from the time domain data for a single bunch was Fourier transformed to obtain the amplitude and phase of the the shape in the frequency domain. Prior to applying FFT on the input time sequence of a single bunch, the time domain data was manipulated. The original input time domain signal of one single bunch which contains 92 samples was extracted, and then spline interpolated with 2^{13} points increasing the granularity by factor of ~ 90 . The curve of the reference shape was shifted to place a zero-crossing point on the origin of the x and y axes (0,0). The other shapes were shifted depending on the zero-crossing time difference.

Next, the zero padding technique [70] was used to improve the resolution of the FFT amplitude and phase spectrum. This process involves the addition of zero-values data samples to the interpolated time domain input curve. In each side of the curve 28672 zeros were appended to have a curve with a total point of 2^{16} . This process increases the FFT frequency resolution by a factor of 8. The FFT function was then applied on the curve to produce the amplitude and phase spectrum of the signal. The phase at 108.408 MHz was extracted to be compared with other approaches. Figure 6.20 shows the amplitude and phase spectrums of two bunch shapes obtained from FFT calculations.

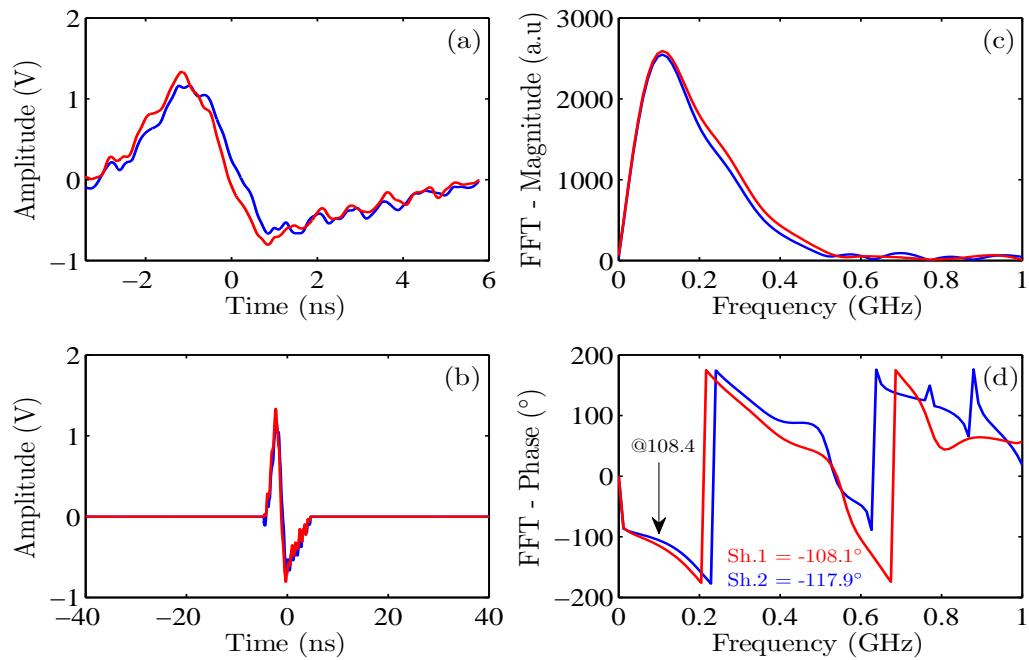


Figure 6.20: A single bunch of two different shapes recorded by the oscilloscope were extracted, spline interpolated and shifted to zero (a). The signal is zero padded in both sides with 28672 each zeros to create a curve with a total point of 2^{16} (b). The FFT is applied to produce the amplitude (c) and phase (d) spectrum.

- FFT for a stream of bunches

For further investigation a stream of bunches (~ 170000) was stored during the measurements along 1.5 ms from the oscilloscope for each bunch shape. Due to the limited memory size only 45000 bunches were used to be Fourier transformed but it was sufficient to recognize the characteristics of amplitude and phase spectrums at several harmonics. A zero-valued samples were appended to the end of the time domain sequence to match 2^{22} which is the next largest radix-2 FFT.

The FFT function was then applied on the curve of the time domain sequence to produce the amplitude and phase spectrum in the frequency domain. The amplitude spectrum shows discrete peaks at each frequency component which correspond to a phase shift of 180° in the phase spectrum. This can be interpreted as resonance frequencies for the stream. The phase shift at 108.408 MHz was extracted and used for comparison with a single bunch and with other approaches. Figure 6.21 shows an example of the amplitude and phase spectrum for two shapes.

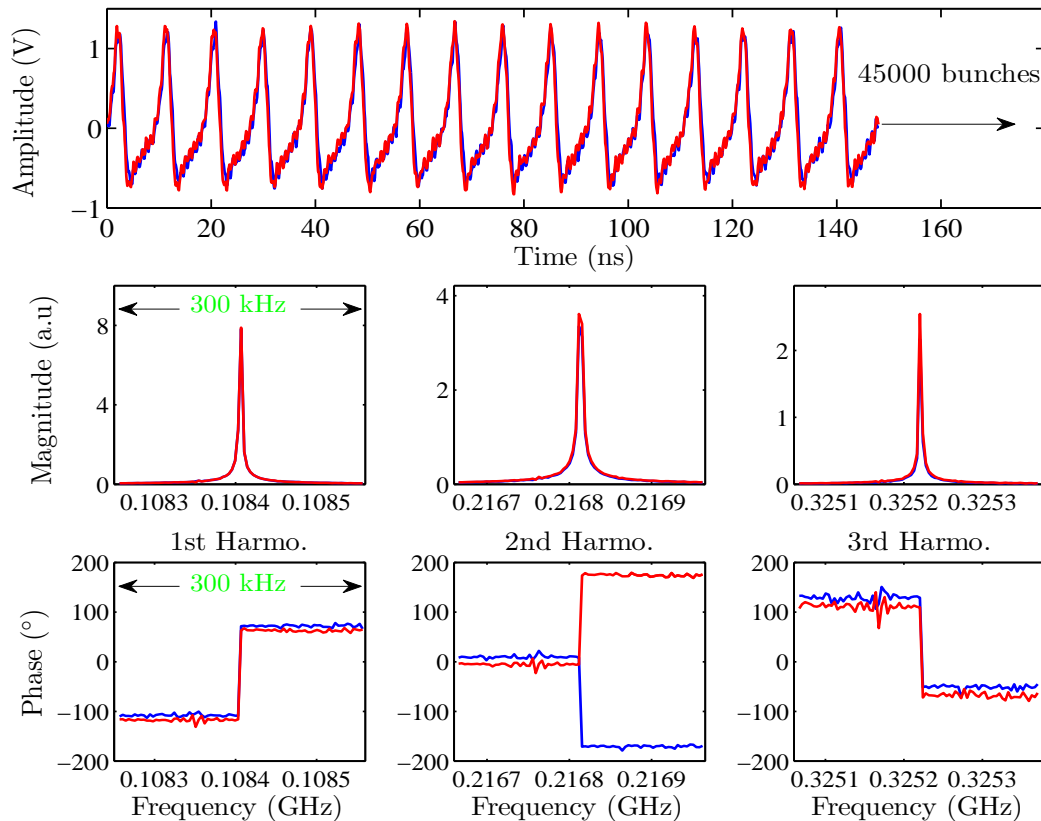


Figure 6.21: A stream of two different shapes stored by the oscilloscope (up). The FFT is applied on 45000 bunches to produce the amplitude peaks spectrum (the amplitude spectrum nearly coincided) (middle) and the corresponding phase spectrum (down).

6.6.3 I/Q Demodulation Method

The I/Q demodulation described in Sec. 6.3.4 was applied to calculate the phase of each shape from I and Q values. In the I/Q demodulation the RF signal is mixed (multiplied) with two sinusoidal signals which have a 90° phase shift as shown in figure 6.6. Those signals have a frequency matches to the RF signal, $f_{dem} = f_{RF}$ and the mixing process produces the I and Q signals as explained equations 6.14 and 6.15. The frequency spectrum of I and Q signals has a dc baseband term centered at zero Hz where the signal amplitude and phase could be retrieved as discussed in equation 6.9. Practically, the higher order terms are filtered out using low pass filter (LPF) as shown in figure 6.6.

A stream of 108 bunches obtained from the time domain data was used for the calculations. This number corresponds to the number of bunches stored and processed by the Libera SPH unit in one macropulse step as mention in Sec. 6.4.1. The stream of bunches was mixed with stream of two sinusoidal signals under the condition $f_{dem} = f_{RF} = 108.408$ MHz. The I and Q dc term were extracted and used to calculate bunch phase. Figures 6.22 and 6.23 show the results of multiplication and the I and Q spectrum in frequency domain which contain the continues quadrature phase term of the signals.

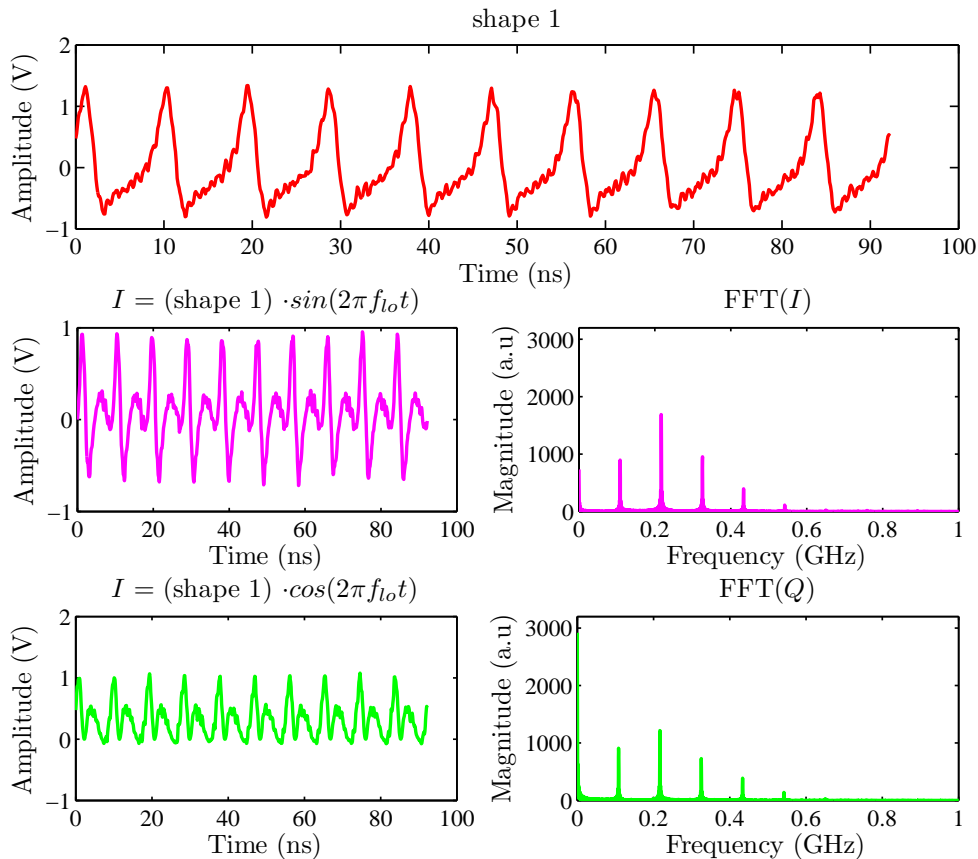


Figure 6.22: A stream of shape 1 recorded by a 10 GSa/s oscilloscope. The I and Q signals and its spectrum which contain the continues quadrature phase term of the signal.

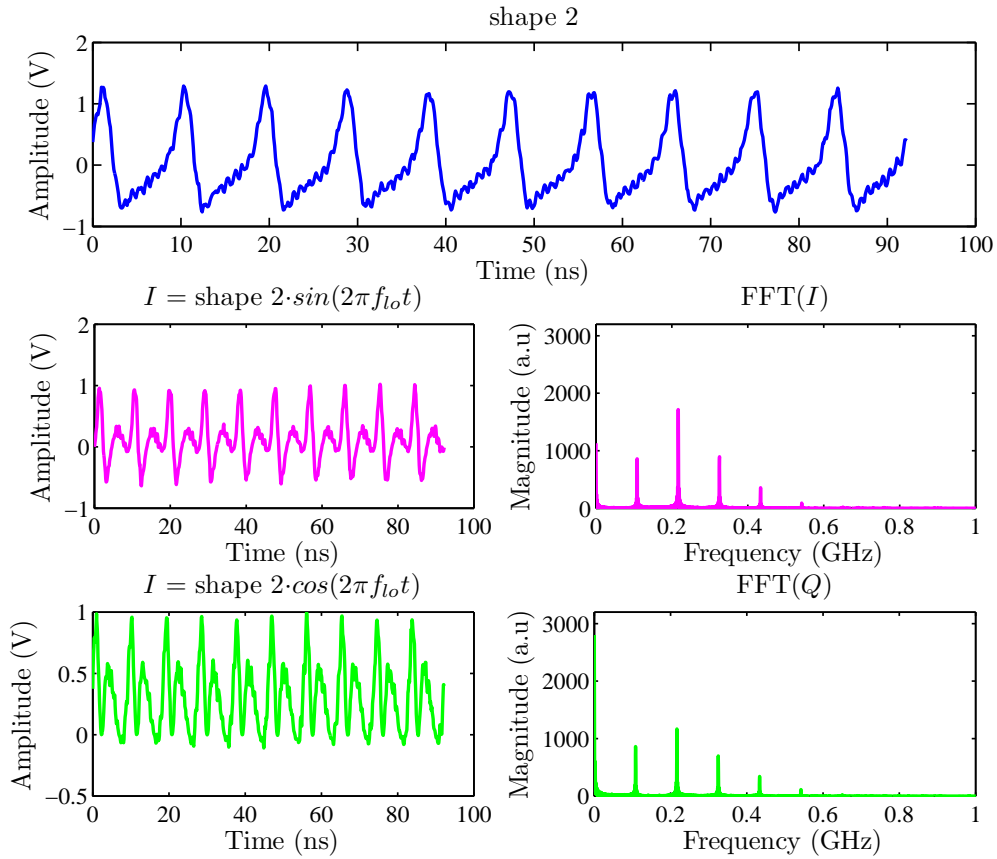


Figure 6.23: A stream of shape 2 recorded by a 10 GSa/s oscilloscope. The I and Q signals and its spectrum which contain the continues quadrature phase term of the signal.

6.6.4 Time Domain Evaluation

From the average over many macropulses, each individual shape was displayed and stored on a 10 GSa/s oscilloscope (LeCroy Waverunner 6200A) by summing the BPM signals. The recorded curve by the oscilloscope contains ~ 92 samples for each single bunch. A typical time domain for two bunch shapes displayed on the oscilloscope shown in figure 6.24, each shape corresponds to a different re-buncher setting.

The bunch trace on the oscilloscope was triggered with the master oscillator - the RF accelerating frequency as well as the Libera SPH. The trigger and the interpolator jitter accuracy of the oscilloscope is ~ 3 ps rms (typical) [100]. In the time domain the phase - or arrival time - of the bunch was determined from the zero-crossing point which corresponds to the maximum point of the signal integration. All bunch curves were non-symmetric and thus the integration was not a perfect Gaussian-shape.

For data evaluation the first shape was selected as a reference shape. The resolution of the original curves recorded by the oscilloscope was 100 ps. In order to increase the resolution of the curve as the zero-crossing is determined, the granularity of the curve was improved from 100 ps to 1.12 ps by the spline interpolation containing 2^{13} points. Using the interpolated curve, the points of interest were extracted. Figure 6.25 illustrates the time domain signals for six bunch shapes. For all shapes the maximum zero-crossing deviation was 400 ps.

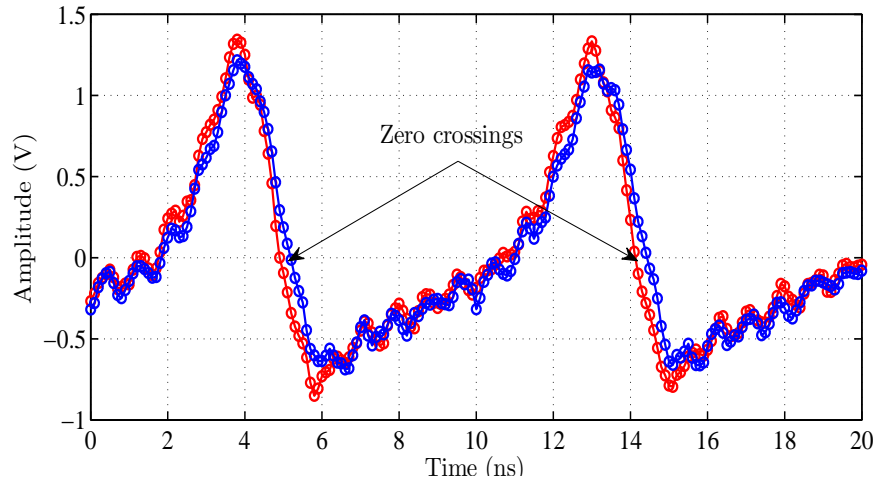


Figure 6.24: Two bunch curves (shape 1 and shape 2) recorded by a 10 GSa/s oscilloscope (LeCroy Waverunner 6200A).

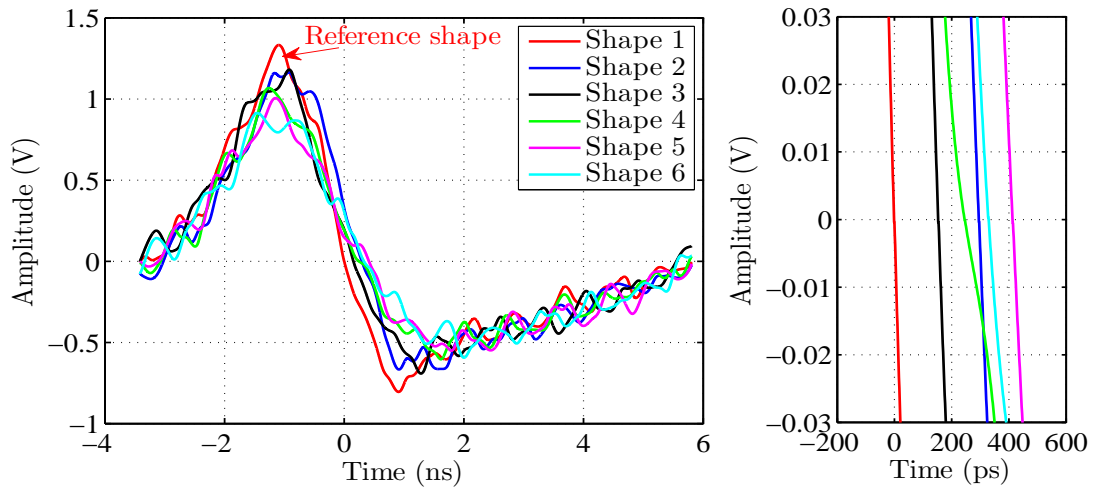


Figure 6.25: The time domain signals and the zero-crossing points (left). The magnification of the zero-crossing region showing the arrival time differences showing 400 ps maximum arrival time difference.

- Zero-Crossing Jitter

The point of zero-crossing was determined from a single bunch chosen arbitrarily from a macro-bunch. But when looking into a stream of bunches the zero-crossing points were jittering within one macro bunch. Therefore, it was required to investigate the jitter of zero-crossing for many bunches and to quantify the deviation within the macro-pulse. The first step to perform this delicate investigation was to determine bunches periodicity very precisely. The FFT was applied to the stream of bunches stored by the oscilloscope to extract the first harmonic where the phase was shifted by 180° .

For example, applying FFT on 45000 bunches of the reference shape produced an amplitude and the phase spectrum shown in figure 6.21. The periodicity was then determined using the first harmonic where $T = 1/f_n$ where $f_n = 108.408$ MHz. This time (periodicity) was corrected by $\sim 1 \times 10^{-5}$ for 1000 bunches where a straight plot is observed. The correction is below the typical accuracy needed for the accelerations.

The second step was to determine the exact zero-crossing points for a sequence of bunches. Starting from the first stored sample at the beginning of the stream, 92 successive samples of the first bunch were spline-interpolated. The interpolated curve was integrated and the maximum point which corresponds to the zero-crossing of the bunch was extracted. The same procedure was applied on each bunch sequence individually where the second bunch starts from 92 to 180 sampling points and so on. The zero-crossing deviation from the periodicity for each bunch was determined by;

$$Jitter_b = |Z_c - N \cdot T_p| \quad (6.23)$$

where N is the number of the bunch, T_p is the periodicity calculated from the first frequency harmonic. The errors of zero-crossing points referred as the zero-crossing jitter of the stream. The zero-crossing jitter from 500 successive bunches for the RF reference signal is shown in figure 6.26. Figures 6.27 and 6.28 illustrate the fluctuation of zero-crossing jitter from 500 successive bunches for bunch shape 1 and bunch shape 2, respectively. The results show that the zero-crossing jitter σ_{Z_c} depends on the bunch shape as listed in table 6.1 for the six bunch shapes and for the RF reference signal from the acceleration cavity.

The calculated jitter can be called time resolved jitter because the zero-crossing variation has been calculated for each individual bunch. It was observed that the variation has a systematic behaviour with a repetition of ~ 7.5 MHz common for all bunch shapes. This systematic fluctuation was caused by the wrong functionality of the LeCroy oscillo-

scope (LeCroy Waverunner 6200A) which was difficult to identify at the beginning. For this purpose the LeCroy oscilloscope was tested and compared with Tektronix and Agilent oscilloscopes in a separated beam time as well as in a series of lab-test investigations using signal generator HP 8648C [9kHz 3200MHz]. This behaviour was observed again and, therefore, it was clear that the systematic fluctuation was caused by the internal routine of the LeCroy oscilloscope electronic used during the experiment.

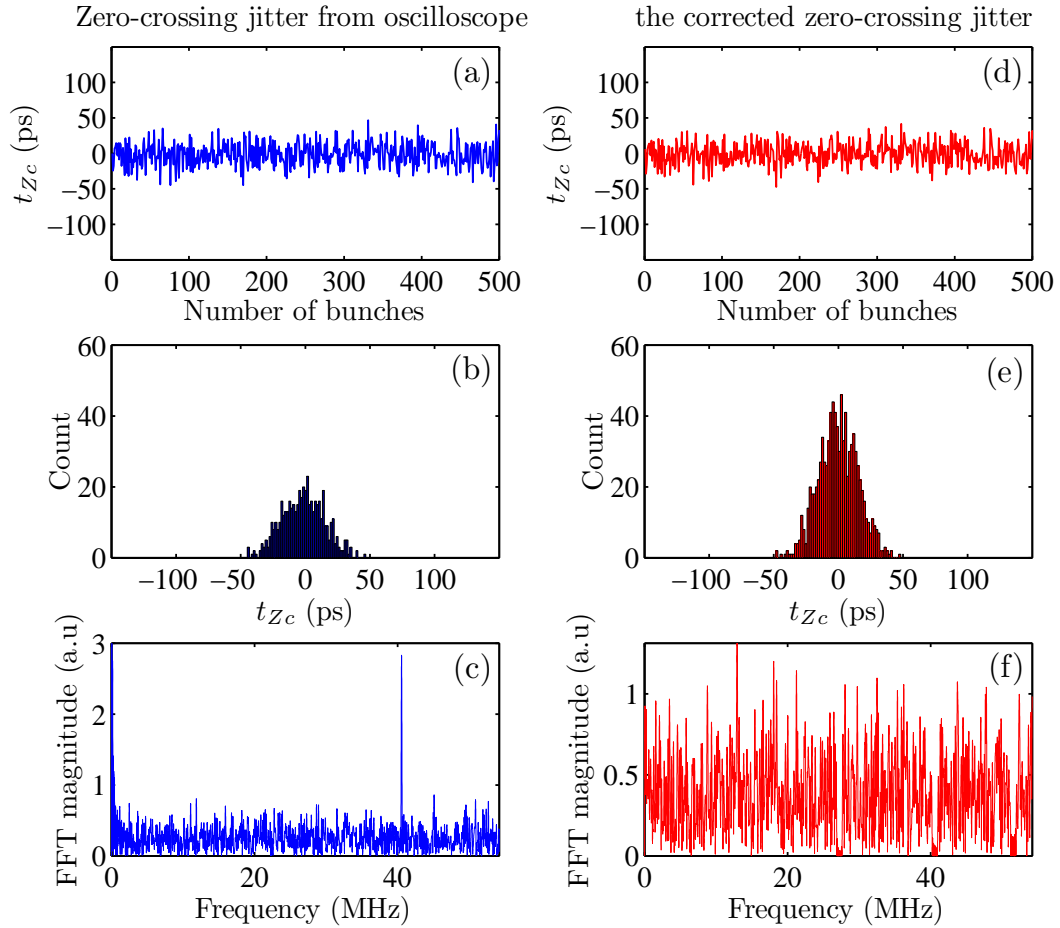


Figure 6.26: The jitter of zero-crossing points for 500 bunches for RF signal and the histogram (left). FFT applied on zero-crossing jitter for 1000 bunches showing a systematic behaviour with a repetition of ~ 40 MHz (right).

The zero-crossing jitter was corrected by removing the unintended frequency, 7.5 MHz and 40.75 MHz shown in the subplot (c) in figures 6.26, 6.27 and 6.28. This was required to eliminate the influence of the wrong functionality of the LeCroy oscilloscope in order to match the real condition of the beam for each bunch shape and the RF signal.

The artificial frequencies were suppressed to zero in the fourier transform of the zero-crossing jitter sequence as shown in the subplot (f) in figures 6.26, 6.27 and 6.28. The new frequency domain sequence - after suppressing the peak frequency and ± 3 bins - was decomposed to its real and imaginary components. A MATLAB function `ifft` was used to apply the inverse discrete fourier transform (described in Sec. 3.4) to reconstruct the time domain sequence. The resulting time domain sequence corresponds to the zero-crossing jitter sequence as shown in the subplot (d) in figures 6.26, 6.27 and 6.28. The corrected zero-crossing jitter were listed in table 6.1 representing the error bars for the time domain data.

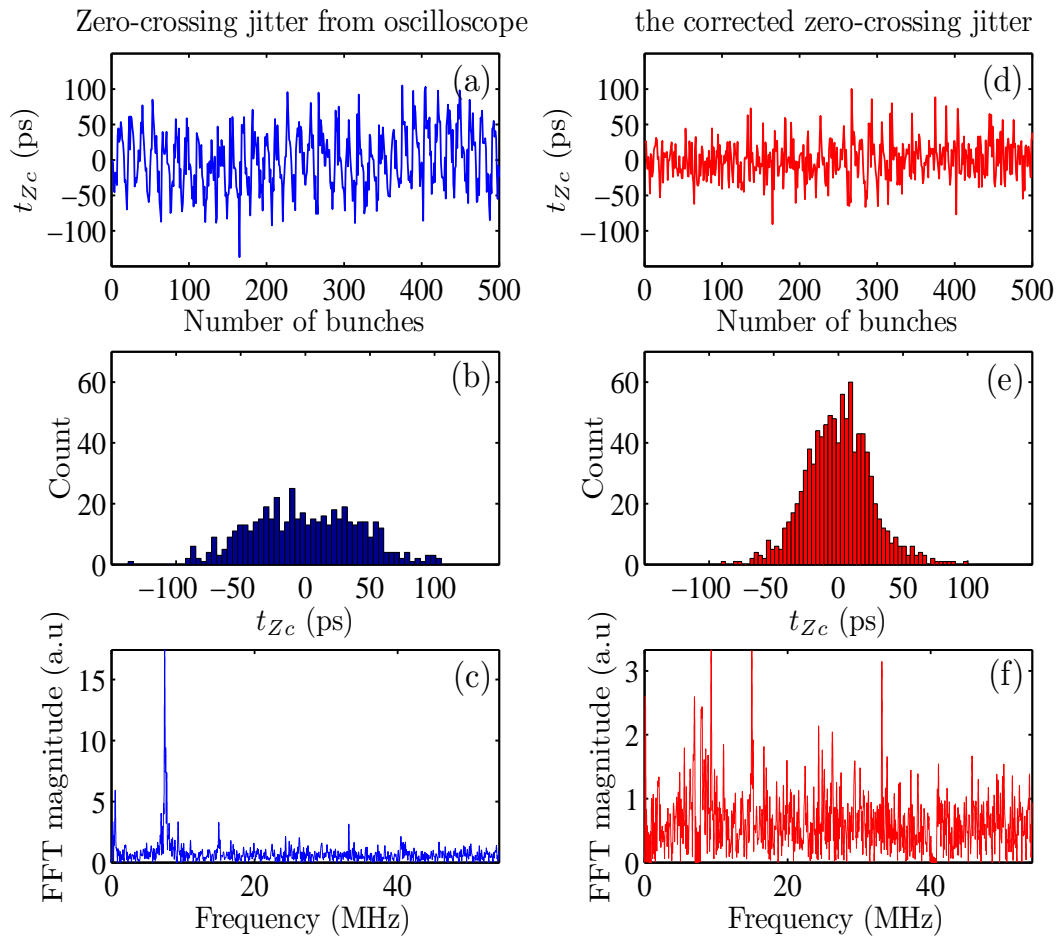


Figure 6.27: The jitter of zero-crossing points for 500 bunches for bunch shape 1 and the histogram (left). FFT applied on zero-crossing jitter for 1000 bunches showing a systematic behaviour with a repetition of ~ 7.5 MHz (right).

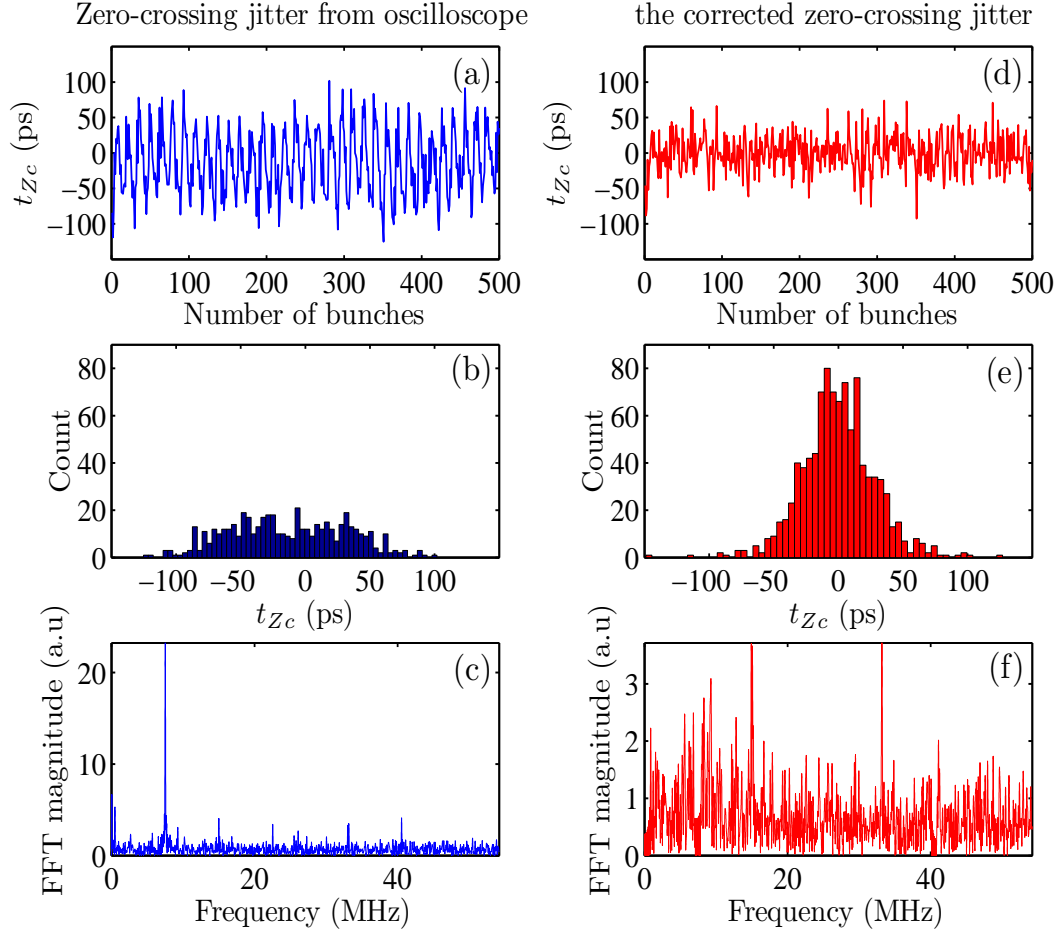


Figure 6.28: The jitter of zero-crossing points for 500 bunches for bunch shape 2 and the histogram (left). FFT applied on zero-crossing jitter for 1000 bunches showing a systematic behaviour with a repetition of ~ 7.5 MHz (right).

Table 6.1: σ_{Z_c} of zero-crossing jitter within one macro-pulse for six bunch shapes in ps unit and the corresponds to degree @ 108.4 MHz (9.22 ns = 360°)

	RF signal	shape 1	shape 2	shape 3	shape 4	shape 5	shape 6
σ_{Z_c} (ps)	16.19	40.99	46.41	55.61	68.92	87.24	101.49
($^\circ$)	0.63°	1.56°	1.81°	2.16°	2.68°	3.40°	3.95°
corr. σ_{Z_c} (ps)	14.65	23.38	26.72	32.63	43.43	52.68	66.04
($^\circ$)	0.57°	0.91°	1.04°	1.27°	1.69°	2.05°	2.57°

6.6.5 Data Evaluation and Results

The correlation between phase (bunch arrival time) for each bunch shapes obtained from the different methods was analyzed. The phase obtained by the oscilloscope from the time domain processing $Z_c - Z_c(1)$ (shape 1 as reference) was represented on the x -axis while Libera SPH system, FFT calculations (for a single bunch and a stream of bunches) and I/Q demodulation were assigned on the y -axis as depicted in Figure 6.29.

Looking at figure 6.29 one can notice a correlation between the different methods. The straight line represents the ideal linear correlation between the time domain and the other methods. A linear regression fit was applied on the measured data to analyze this correlation. The simple linear regression was obtain in a form of

$$Y = a_1 \cdot X + a_0 \quad (6.24)$$

where

$$a_1 = \frac{n \sum X_i Y_i - \sum X_i \sum Y_i}{n \sum X_i^2 - (\sum X_i)^2} \quad \text{and,} \quad a_0 = \bar{Y} - a_1 \bar{X} \quad (6.25)$$

Then, the coefficient of determination R^2 was calculated to measure the goodness of the fitted regression line from

$$R^2 = \frac{SSR}{SST} = 1 - \frac{SSE}{SST} \quad (6.26)$$

where SSE is the sum of squares due to the error, SSR is the sum of squares due to the regression and SST is the total sum of the squares. The larger R^2 is, the more variability is explained by the linear regression model. The fit slope and the goodness of the fit from different methods were listed in table 6.2.

Table 6.2: A linear regression fit and the goodness of the fit for different methods

Method	a_0	a_1	R^2
I/Q demodulation	0.710	0.605	76.17 %
FFT stream of bunches	0.893	0.630	79.03 %
FFT for one bunches	0.892	0.717	82.00 %
Libera SPH	0.251	0.850	67.25 %

The first observation is that there is a compatibility between the FFT calculation methods for a single bunch and a stream of bunches. However, the FFT calculations for a stream of bunches are better matched to the I/Q demodulation method. The lower fluctuation is observed from the FFT calculations for a stream of bunches with a

goodness of 82.00 %. The phase measurements obtained from the Libera SPH unit shows good correlation with ideal slope but the fluctuation is larger than the other methods. The goodness of the linear regression fit of the Libera SPH is 67.25 %.

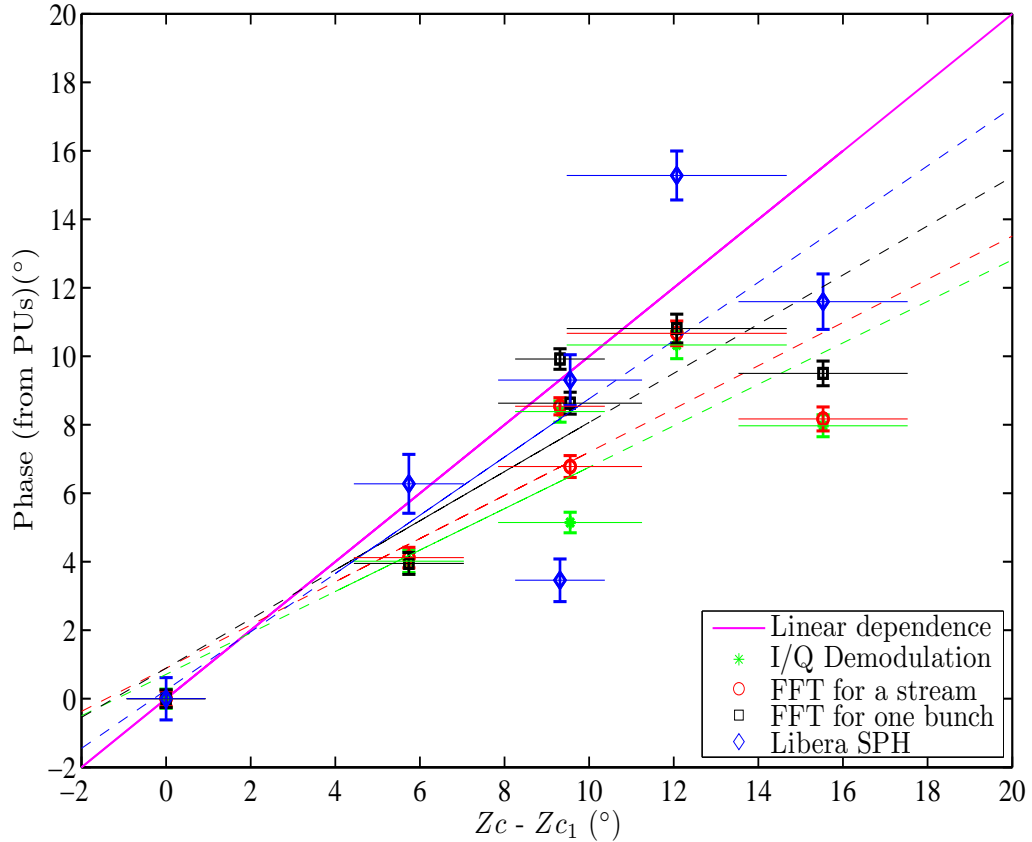


Figure 6.29: The signal phase - arrival time - obtained from the time domain processing $Z_c - Z_c(1)$ (shape 1 as reference) is represented on the x -axis and the Libera SPH phase reading and phase calculated from FFT (for a single bunch and for a stream of bunches) and I/Q demodulation are assigned on the y -axis.

The results from this test with a real beam show that the Libera SPH seems to be promising, although it still does not fulfill the requirements yet. Thus, some modifications and further investigations might lead to the desired accuracy. It has to be stressed that there are some limitations related to the achievable accuracy. The first is related to the strength of the processed harmonic versus the applied bunch shape. The second is the fact that a large variation in the bunch shape influences the phase contribution of the processed harmonic. The Libera SPH system is recently under development and more investigations and lab-based tests have already been planned to improve the performance based on a comprehensive modelling of the digital signal processing algorithm [101].

6.7 Beam Position Evaluation

This test aimed to compare the position of the beam obtained by the Libera SPH unit from the BPM signals to the beam profile displayed by a Secondary Electron Monitor (SEM) profile grid. The SEM grid is an intersecting diagnostic method using the emission of secondary electrons from metallic wires. The grid has 15 wires for both planes interspaced at 1.5 mm intervals and each individual wire has a current-to-voltage amplifier. When the beam hits a wire, secondary electrons are emitted from the wire's surface and all signals are collected and to display the horizontal and the vertical profile of the beam [33, 102].

The grid is placed behind the BPM so that the position can be measured simultaneously by both devices. The beam position was adjusted using a dipole magnet (called vertical steerer). The beam swept along the y -axis at 2 mm steps while the x -axis was fixed. The points on the y -axis were -5, -3, 0, 3, 5 mm. The measured profiles of SEM grids displaying the horizontal profile left and the vertical right in mm for five locations are shown in figure 6.31. Figure 6.30 show the response of the Libera SPH unit as compared to the SEM grid. One can observe that the beam position measured by the Libera SPH matches with the variation seen by the SEM profile for both coordinates. One can state that the Libera SPH digital electronics seems to be suitable for beam position determination. The resolution tests concerning the position reading were depicted in figures 6.14 and 6.19.

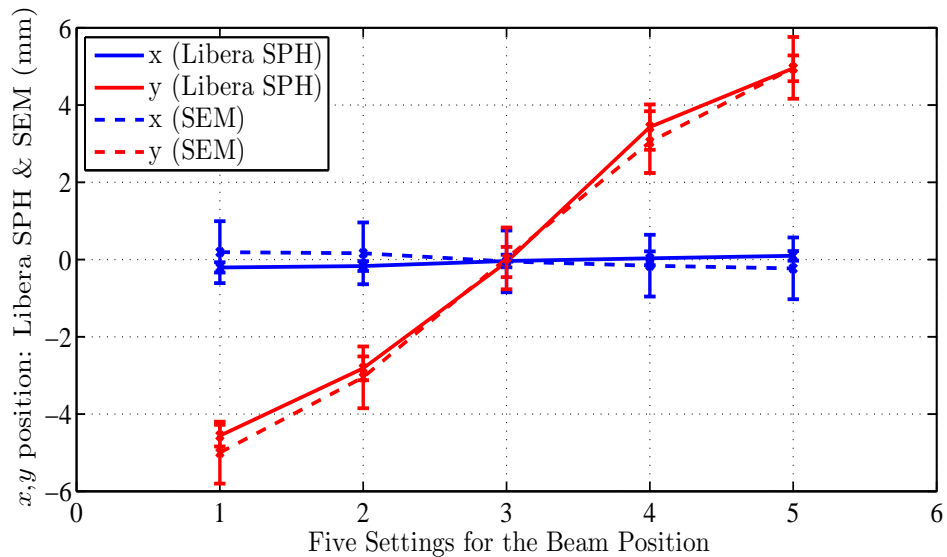
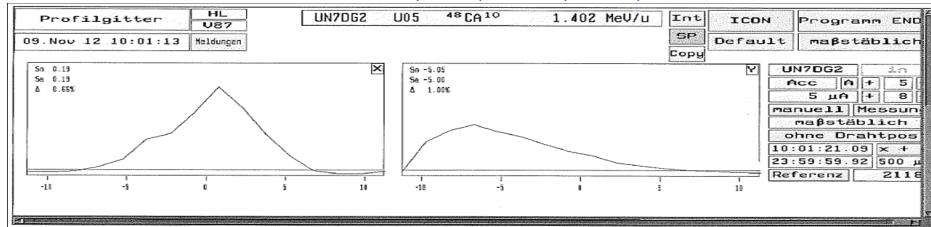
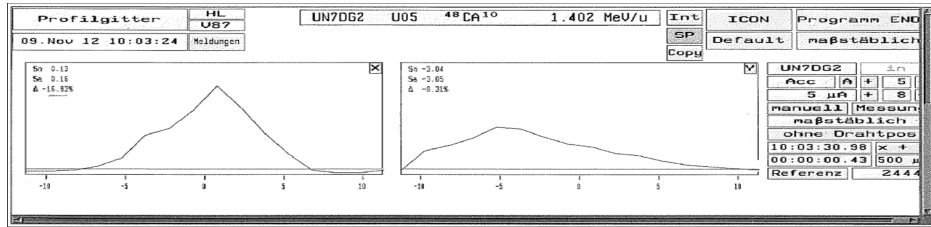


Figure 6.30: The variation of x and y coordinates of the beam obtained by Libera SPH (solid lines) and SEM grid (dashed lines) where x is always fixed at 0 and y is varied from -5 to 5 mm in 2 mm steps.

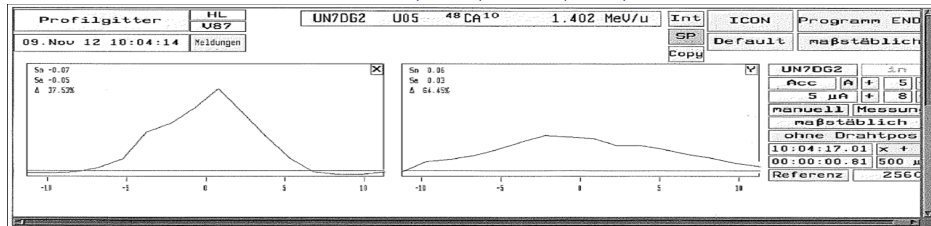
$$(x,y) = (0,-5)$$



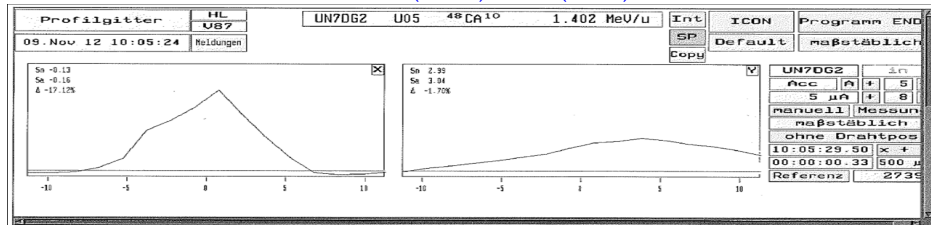
$$(x,y) = (0,-3)$$



$$(x,y) = (0,0)$$



$$(x,y) = (0,3)$$



$$(x,y) = (0,5)$$

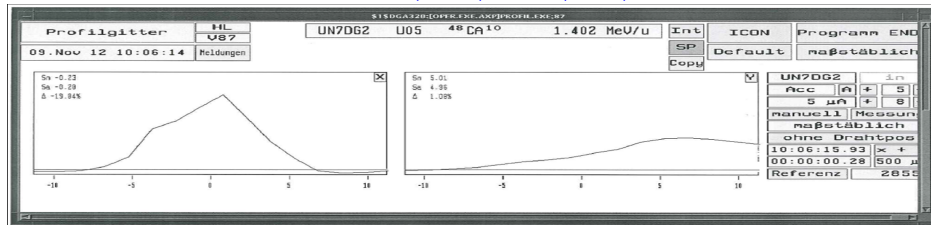


Figure 6.31: The measured profiles of SEM grid displaying the horizontal profile (left) and the vertical (right) in mm for five locations.

Summary and Outlook

7.0.1 Summary

In this thesis, a high precision and a high resolution beam position and beam energy system has been developed for the proton linac injector for the FAIR. The Beam Position Monitor (BPM) system as non-destructive devices will be installed at 14 locations along the proton linac. They will serve for transverse beam position determination, beam energy from the Time-of-flight (TOF) method and the relative beam current from the sum signal of four BPM electrodes.

The system's specifications are 0.1 mm spatial resolution for the transverse beam position determination and 8.5 ps (1° @ 325 MHz) for the time-of-flight measurements. Depending on the location the BPM design has to be optimized for a 30 mm (nine locations) and a 50 mm (five locations) beam pipe aperture taking into account the beam energy range from 3 to 70 MeV and the limited space for the BPM installation. A capacitive button type pickup was chosen for its easy mechanical realization and for its short insertion length.

An overview about the GSI and the FAIR project is given in chapter 1. The basic principles of the RF linear accelerators as well as the design and the main parameters of the FAIR proton LINAC injector are introduced in chapter 2. The theory of the capacitive BPMs and the signal estimation are discussed in chapter 3. The layout and the main parameters of the BPM system for the FAIR proton LINAC injector as well as the mechanical design and the production of the first BPM prototype are described in chapter 4. The CST simulations for the button pickup design optimization and the BPM response with a beam are discussed in chapter 5. The digital signal processing algorithm for the BPM system as well as the experimental results of the beam-based test using the Libera SPH electronics are presented in chapter 6.

The outcomes of this work can be divided into three major segments. The first segment is the contribution in the technical realization of the BPM intertank section and the calculations of the rf-leakage from the nearby CH cavity. At four locations the BPM will be an integral part of the intertank section between the CCH or CH cavities together with the magnetic triplet lenses within an evacuated housing. The tight space allows only 62 mm insertion length between CCH cavity and magnet walls so that the BPM centre is only 48 mm apart from the upstream cavity boundary.

Numerical simulations were performed to estimate the rf-leakage from the nearby cavity and to improve the rf shielding properties. The rf-pickup background signal was reduced to ~ 10 mV amplitude. This value is satisfactory compared to the signal voltage of ~ 1 V for a nominal beam current of 35 mA. Based on the simulations the first prototype of the BPM intertank with 30 mm aperture was manufactured and produced. The assembly of the BPM prototype consists of four Kyocera buttons of 14 mm in diameter and a housing.

The second segment of this work discusses detailed simulations of the pickup design parameters with the finite element code CST. Three CST STUDIO - Solvers have been used for the BPM simulations. The CST ELECTROMAGNETIC STUDIO solver was used to calculate the capacitance of the pickup structure as a function of the button thickness and the gap size between the button and the shield. The electrical properties of the pickup design, namely the impedance matching of the pickup transmission line, were investigated by the CST MICROWAVE STUDIO solver from the Time Domain Refractometry (TDR).

The Wakefield solver in CST PARTICLE STUDIO was used to investigate the BPM response to particle beam for different pickup geometries and various beam parameters. The time domain and the frequency domain responses of the BPM output signals reflecting the BPM's interaction with the beam were extracted and compared. A coin and a cone designs restricted to a 15 mm insertion length have been optimized by varying button diameter and the button thickness and the gap.

Additionally, the CST simulations were performed to investigate bunch length variation, button depth with respect to the beam pipe wall, button size, beam pipe diameter, the BPM sensitivity, BPM position map and beam phase variation as a function of the beam position. Those simulations are required for the BPM analogue band width for signal processing and the related technical layout.

The third segment of this work involves a beam-based test which was conducted at the GSI UNILAC to investigate the performance of the Libera SPH electronics system for beam position and phase measurements. The Libera SPH involves a high resolution ADC (16 bit nominal) and applies the technique of under-sampling with a sampling rate of ~ 117.4 MHz. The experiment was carried out using a Ca^{10+} beam from the High Charge State Injector (HLI) with an energy of 1.4 MeV/u and a bunch repetition rate of 108.408 MHz. The beamline optical elements allow one to vary the beam position by a dipole as well as the formation of different bunch shapes by changing the re-buncher setting.

Firstly, the Libera SPH resolution was tested for beam position and phase. The results show a stable response for position measurements especially for large signal amplitudes with standard deviation of $\sim 50 \mu m$ which fulfills the BPM requirements. For the phase measurements, the results shows that the phase resolution is amplitude dependence and for some signal shapes the standard deviation is less than 1° for high signal amplification level.

Secondly, the phase measurement accuracy was investigated by studying the phase correlation between Libera SPH unit and other methods, namely the time domain approach from the zero-crossing, FFT analytical calculations and the I/Q demodulation. A single BPM was used to act as a bunch arrival monitor and six bunch shapes were generated to characterize the phase dependence on the bunch shape. The time domain data was obtained by a 10 GSa/s oscilloscope (LeCroy Waverunner 6200A). Some correlation between methods were observed but the Libera SPH phase reading shows large fluctuation. However, the results show that the Libera SPH seems to be promising, although it still does not fulfill the requirements yet. Some modifications and further investigations might lead to the desired accuracy.

Finally, the Libera SPH accuracy for the beam position was investigated by the comparison with the beam profile displayed by a Secondary Electron Monitor (SEM) profile grid. The results show that the Libera SPH digital electronics seems to be suitable for the beam position determination.

7.0.2 Outlook

Several issues are already planned to continue the development on the BPM system. Firstly, the BPM prototype will be tested with a wire test bench. The test aims to investigate BPM electrical characteristics and to determine accurately the electrical center of the BPM. The test bench is being constructed at CEA-Saclay, France.

Secondly, it is intended to use the BPM prototype for the rf-leakage background measurements on the CH prototype cavity which is under preparation at the GSI. The simulations of the rf-leakage were performed and it would be required to be verified with measurements.

Thirdly, based on the CST simulation the pickup button geometry will be modified and the new design will be produced. The new design will be used for the BPM intertank section and for the other beamline BPMs. The fabrication of the optimized BPM design and mechanical environments of the beamline BPMs are ongoing.

Finally, since the resolution of the Libera SPH unit limits the performance of the BPM system, the next step will be to further improve the unit. The most prominent challenge would be to investigate the bunch shape variation and its influence on the bunch arrival time. Recent modifications to the signal processing hardware and to the improvements of data analysis software have been suggested. In order to successfully achieve those goals, several technical challenges must be overcome. Additionally, a detailed understanding of the unit functionality is essential. On the other hand, a theoretical model studies the phase as a function of bunch shape deformation could be advantageous. This would lead to define a range in which the narrowband processing system is creditable.

Appendix

The BPM sensitivity curves and the BPM Position Maps for all CCH and CH output velocities along the proton LINAC are shown in the figures from 8.1 to 8.11 at different frequency harmonics. The corresponding calculated BPM sensitivities S_0 for all cases are listed in table 8.1.

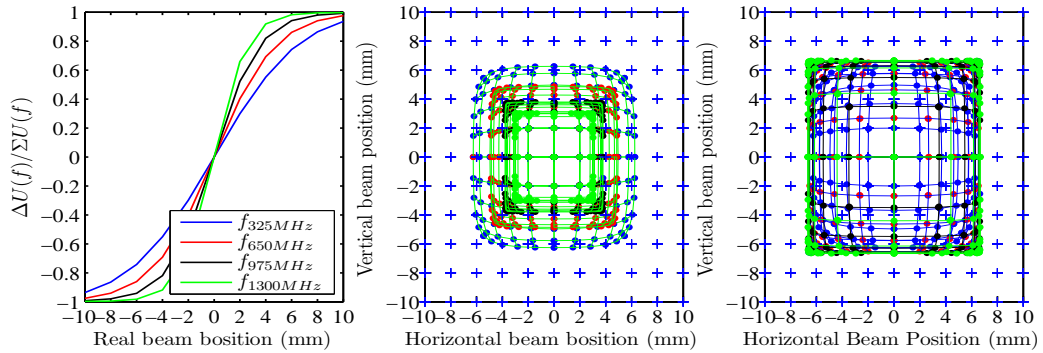


Figure 8.1: Vertical beam position sensitivity curves (left) and the BPM position maps (right) at different frequency harmonics at CCH1 entrance ($\beta = 0.08$, $\sigma_{bunch} = 150ps$).

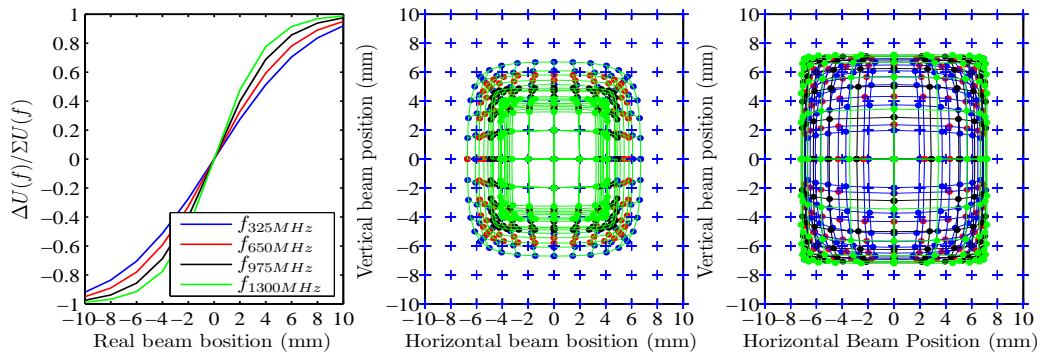


Figure 8.2: Vertical beam position sensitivity curves (left) and the BPM position maps (right) at different frequency harmonics after one half CCH1 ($\beta = 0.12$, $\sigma_{bunch} = 150ps$).

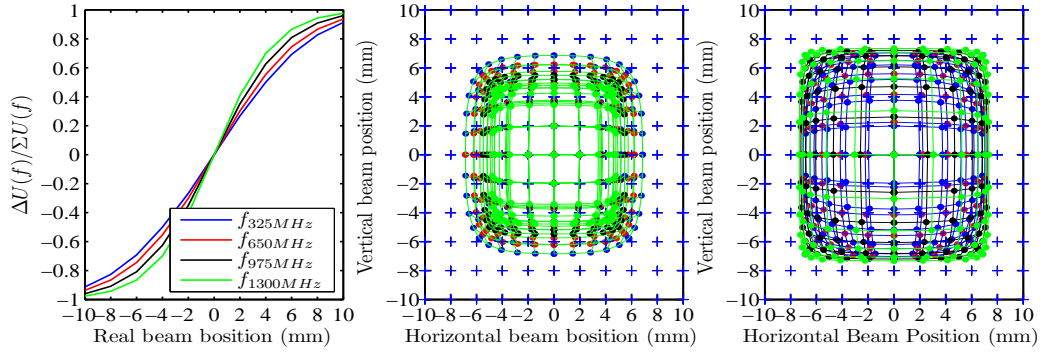


Figure 8.3: Vertical beam position sensitivity curves (left) and the BPM position maps (right) at different frequency harmonics at CCH2 entrance ($\beta = 0.15$, $\sigma_{bunch} = 150ps$).

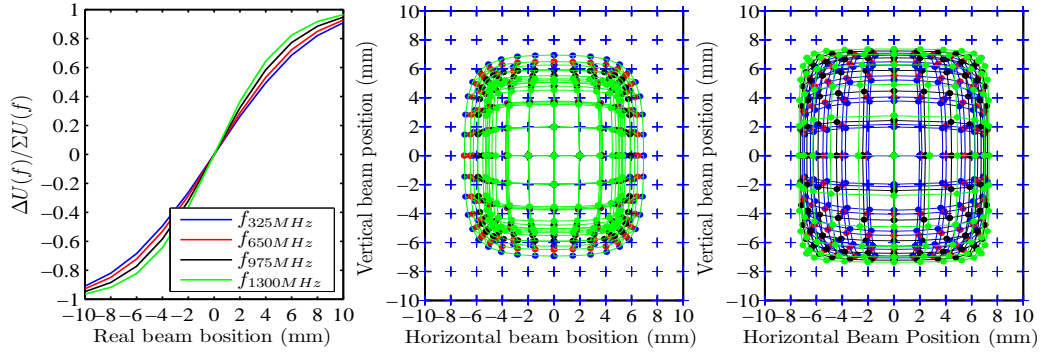


Figure 8.4: Vertical beam position sensitivity curves (left) and the BPM position maps (right) at different frequency harmonics after one half CCH2 ($\beta = 0.18$, $\sigma_{bunch} = 150ps$).

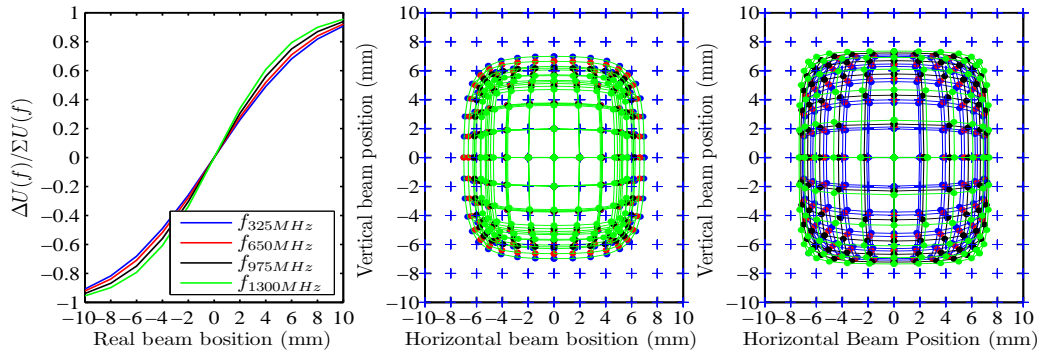


Figure 8.5: Vertical beam position sensitivity curves (left) and the BPM position maps (right) at different frequency harmonics at CCH3 entrance ($\beta = 0.22$, $\sigma_{bunch} = 150ps$).

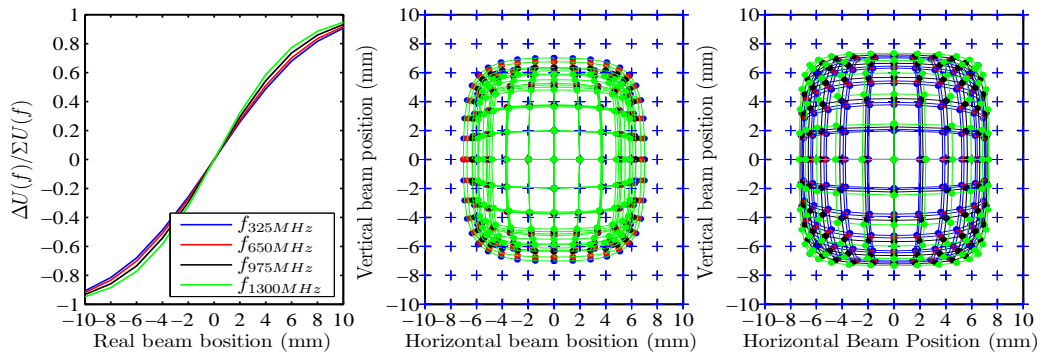


Figure 8.6: Vertical beam position sensitivity curves (left) and the BPM position maps (right) at different frequency harmonics after one half CCH3 ($\beta = 0.24$, $\sigma_{bunch} = 150ps$).

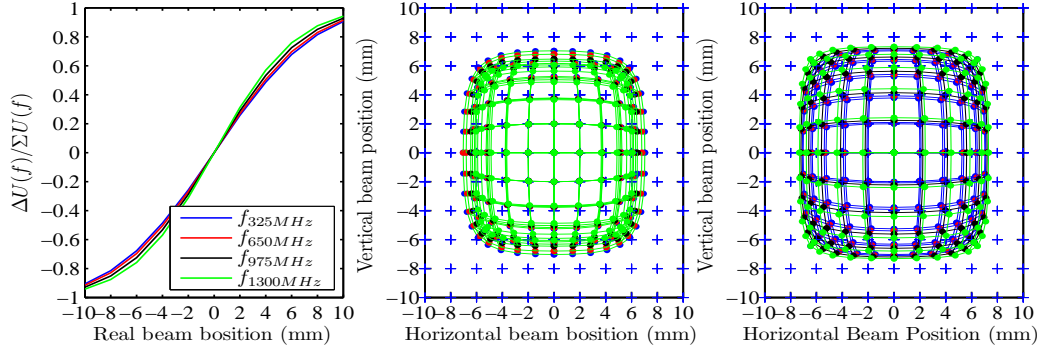


Figure 8.7: Vertical beam position sensitivity curves (left) and the BPM position maps (right) at different frequency harmonics after CCH3 ($\beta = 0.27$, $\sigma_{bunch} = 150ps$).

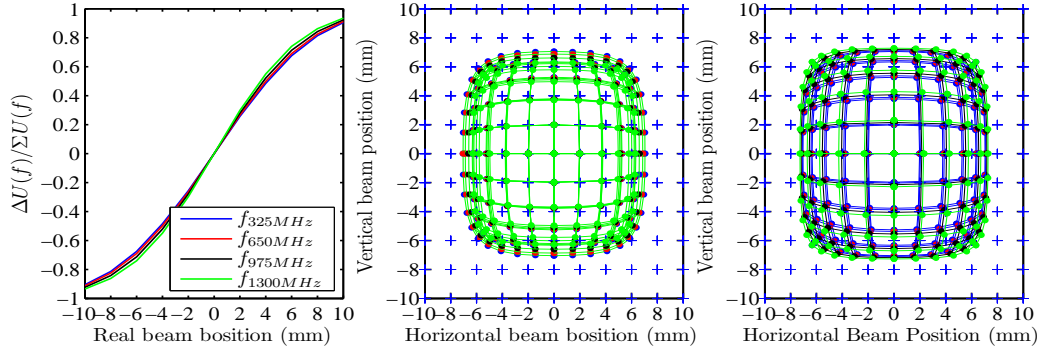


Figure 8.8: Vertical beam position sensitivity curves (left) and the BPM position maps (right) at different frequency harmonics after CH4 ($\beta = 0.30$, $\sigma_{bunch} = 150ps$).

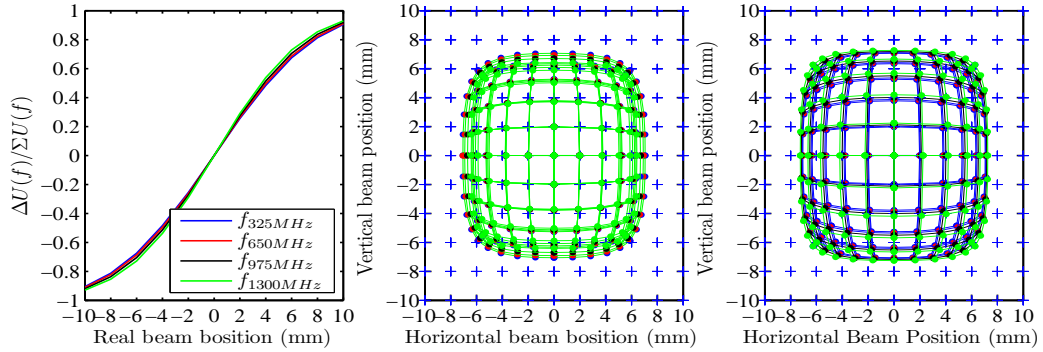


Figure 8.9: Vertical beam position sensitivity curves (left) and the BPM position maps (right) at different frequency harmonics after CH5 ($\beta = 0.33$, $\sigma_{bunch} = 150ps$).

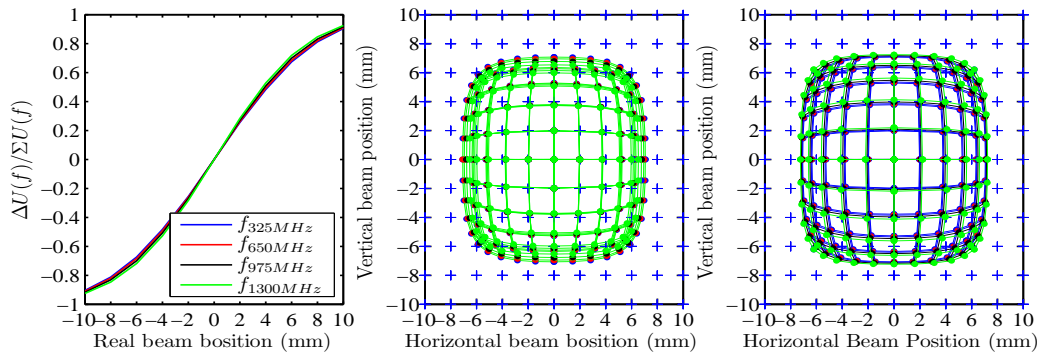


Figure 8.10: Vertical beam position sensitivity curves (left) and the BPM position maps (right) at different frequency harmonics after CH6 ($\beta = 0.37$, $\sigma_{bunch} = 150ps$).

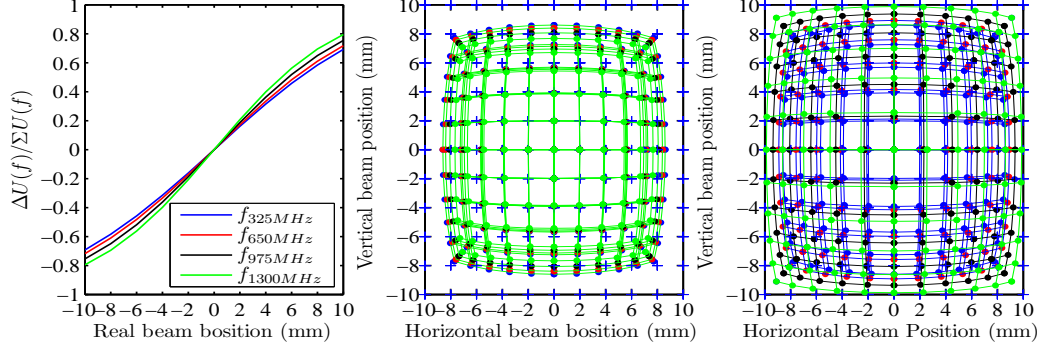


Figure 8.11: Vertical beam position sensitivity curves (left) and the BPM position maps (right) at different frequency harmonics in the inflation region ($\beta = 0.37$, $\sigma_{bunch} = 150ps$).

Table 8.1: The BPM sensitivity S_0 from the simulation in unit ($\%/mm$) at the center position for all CCH and CH output velocities and the relevant beam pipe diameter along the proton LINAC.

β	BPM Location	beam pipe	325 MHz	650 MHz	975 MHz	1300 MHz
0.08	at CCH1 entrance	30 mm	14.94	20.12	26.17	33.00
0.12	after one half CCH1	30 mm	13.71	16.39	19.92	23.86
0.15	at CCH2 entrance	30 mm	13.33	15.08	17.54	20.44
0.18	after one half CCH2	30 mm	13.12	14.30	16.07	18.21
0.22	at CCH3 entrance	30 mm	13.00	13.88	15.22	16.92
0.24	after one half CCH3	30 mm	12.93	13.62	14.70	16.07
0.27	after CCH3	30 mm	12.83	13.47	14.38	15.55
0.30	after CH4	30 mm	12.85	13.28	13.98	14.90
0.33	after CH5	30 mm	12.82	13.17	13.73	14.51
0.37	after CH6	30 mm	12.80	13.08	13.55	14.18
0.37	the inflation region	50 mm	8.05	8.55	9.34	10.36

Bibliography

- [1] <http://www.i-tech.si/>.
- [2] <http://repository.gsi.de/>.
- [3] <https://www.gsi.de/en/gsiwork/forschungsabteilungen.htm>.
- [4] H. H. Gutbrod, I. Augustin, H. Eickhoff, K.-D. Groess, W. F. Henning, D. Kraemer, G. Walter. “FAIR-Baseline technical report”. technical report, GSI, Darmstadt, 2006.
- [5] W. Henning. “FAIR-an international accelerator facility for research with ions and antiprotons”. In High Intensity and High Brightness Hadron Beams, Proc. of AIP Conference. vol. 773, pp.3-5, EPAC-2004-TUXCH02, 2005.
- [6] W. Henning, H. H. Gutbrod, K. D. Gross, and V. Metag. “An international accelerator facility for beams of ions and antiprotons”. Conceptual Design Report, GSI, Darmstadt, 2001.
- [7] H. Stoecker, C. Sturm. “The FAIR start”. Nuclear Physics A, 855(1):506509, 2011.
- [8] O. Boine-Frankenheim. “The FAIR accelerators: Highlights and challenges”. Proc. of IPAC10, Japan, 2010.
- [9] U. Ratzinger. “The New GSI Prestripper Linac for High Current Heavy Ion Beams”. LINAC96, Geneva, Switzerland, p.288, 1996.
- [10] U. Ratzinger. “Commissioning of the new GSI high current Linac and HIF related rf Linac aspects”. Nuclear Instruments and Methods in Physics Research Section A:

- Accelerators, Spectrometers, Detectors and Associated Equipment, 464(1):636645, 2001.
- [11] A. Hollinger, R. Adonin and J. Pfister. “High current ion sources for the FAIR accelerator facility”. Proc. of RUPAC2012, Saint-Petersburg, Russia, 2012.
- [12] J. Klabunde. “The high charge state injector for GSI”. Proc. of the Linear Accelerator Conference, Ottawa, Ontario, Canada. 1992.
- [13] B. Franczak. “SIS parameter list”. technical report, GSI, 1987.
- [14] B. Franzke. “Heavy ion storage rings for atomic physics”. Nuclear Science, IEEE Transactions on, 32(5):3297.3301, 1985.
- [15] B. Franzke. “The heavy ion storage and cooler ring project ESR at GSI”. Nuclear Instruments and Methods in Physics Research Section B: Beam Interactions with Materials and Atoms, 24:18.25, 1987.
- [16] F. Nolden, K. Beckert, F. Caspers, B. Franczak, B. Franzke, R. Menges, A. Schwinn, and M. Steck. “Stochastic cooling at the ESR”. Nuclear Instruments and Methods in Physics Research Section A: Accelerators, Spectrometers, Detectors and Associated Equipment, 441(1):219.222, 2000.
- [17] P. Spiller, K. Blasche, U. Blell, O. Boine-Frankenheim, P. Forck, P. Hülsmann, G. Moritz, H. Ramakers, and S. Ratschow. “SIS100/300 Conceptual Design Studies”. technical report, GSI, 2004.
- [18] W. Barth, W. Bayer, L. Dahl, L. Groening, S. Richter, and S. Yarymyshev. “Upgrade program of the high current heavy ion UNILAC as an injector for FAIR”. Nuclear Instruments and Methods in Physics Research Section A: Accelerators, Spectrometers, Detectors and Associated Equipment, 577(1):211.214, 2007.
- [19] P. Spiller. “FAIR at GSI”. Proc. of HB2006, Tsukuba, Japan, MOBP02, pp.24-28, 2006.
- [20] “SNS Parameter list”, SNS-100000000-PL0001-R13, technical Report, ORNL, Oak Ridge, 2005.
- [21] S. Peggs. “The European spallation source”. Proc. of IPAC11, New York, USA, 2011.

- [22] R. C. York, G. Bollen, C. Compton, A. C. Crawford, M. Doleans, T. Glasmacher, W. Hartung et al. "FRIB: a new accelerator facility for the production of rare isotope beams". In International Conference on Radio Frequency Superconductivity, pp. 888-894, 2009.
- [23] O. Meusel, L. P. Chau, I. Mueller, U. Ratzinger, A. Schempp, K. Volk, C. Zhang, and S. Minaev. "Development of an Intense Neutron Source FRANZ in Frankfurt". Proc. of LINAC, Knoxville, Tennessee USA, vol. 6, p. 159, 2006.
- [24] H. Podlech, S. Barbanotti, A. Bechtold, J. L. Biarrotte, M. Busch, S. Bousson, F. Dziuba et al. The 600 MeV EUROTRANS proton driver linac". In International Topical Meeting on Nuclear Research Applications and Utilization of Accelerators, Wien, Austria, 2009.
- [25] IFMIF INTERNATIONAL TEAM. "IFMIF Comprehensive Design Report: An Activity of the International Energy Agency (IEA), Implementing Agreement for a Program of Research and Development on Fusion Materials". International Energy Agency, 2004.
- [26] Y. Yamazaki. "Accelerator Technical Design Report for High-Intensity Proton Accelerator Facility Project", J-PARC, KEK-Report 2002-13. JAERI-Tech 44, 2003.
- [27] F. Gerigk, M. Vretenar. "Linac4 technical design report". CERN document AB-2006-084ABP/RF, 2006.
- [28] H. V. Smith, D. E. Rees, W. P. Lysenko, P. M. McGehee, L. J. Rybarczyk, T. L. Figueroa, M. E. Schultze et al. "Commissioning results from the low-energy demonstration accelerator (LEDA) Radio-Frequency Quadrupole (RFQ)". Proc. of EPAC2000, Vienna, 2000.
- [29] L. Groening, W. Vinzenz, S. Yaramyshev, W. Barth, L. Dahl, R. Tiede, G. Clemente, U. Ratzinger, and A. Schempp. "The 70 MeV proton LINAC for the facility for antiproton and ion research FAIR". technical report, 2006.
- [30] T. Wangler. "RF Linear Accelerators". WILCY-VCH Verlag GmbH & Co. KGaA, Weinheim, Germany, 2008.
- [31] E. Wilson. "An Introduction to Particle Accelerator". Oxford University Press, 2001.

- [32] M. Vretenar. “Linear accelerators”. CERN Accelerator School (CAS), Course on High Power Hadron Machines, Bilbao, Spain, CERN Yellow Report CERN-2013-001, pp.225-249, 2013.
- [33] P. Forck. “Lecture notes on beam instrumentation and diagnostics”. Joint Universities Accelerator School (JUAS), 2010.
- [34] H. Podlech. “Entwicklung von normal-und supraleitenden CH-Strukturen zur effizienten Beschleunigung von Protonen und Ionen”. Habilitationsschrift, Angew. Physik, Goethe Universität Frankfurt, 2008.
- [35] L. Alvarez. “The design of a proton linear accelerator”. In Physical Review, vol. 70, pp.799-800. American Physical Society one Physics Ellipse, College PK, MD 20740-3844 USA, 1946.
- [36] U. Ratzinger. “H-type linac structures”. CERN Accelerator School on Radio Frequency Engineering 2000, Seeheim, Germany. CERN Yellow Report CERN-2005-003, pp.351-380, 2005.
- [37] U. Ratzinger. “High current IH structures”. Proc. of EPAC94, London,UK, vol.1,p.264, 1994.
- [38] G. Clemente. “The room temperature CH-DTL and its application for the FAIR proton injector”. PhD dissertation, Goethe Universität Frankfurt, 2007.
- [39] J. Broere, H. Kugler, B. Krietenstein, U. Ratzinger, and M. Vretenar. “High power conditioning of the 202 MHz IH tank 2 at the CERN LINAC3”. No. CERN-PS-98-050-RF, 1998.
- [40] A. Almomani. “RF acceleration of intense laser generated proton bunches”. PhD dissertation, Goethe Universität Frankfurt, 2012.
- [41] A. Almomani, U. Ratzinger. “High gradient room temperature cavity development for 10 - 100 AMeV beams”. Proc. of LINAC2014, Geneva, Switzerland, 2014.
- [42] <http://www.helmholtz.de/artikel/superschwer-und-superkurzlebig-2517/>.
- [43] R. Tiede, U. Ratzinger. “Teilchendynamische untersuchungen an einer kombinierten null grad struktur KONUS mit quadrupoltriplett-fokussierung”. GSI-Arbeitsnotiz ALG10077SI, 1997.

- [44] U. Ratzinger. “Effiziente Hochfrequenz-Linearbeschleuniger für leichte und schwere Ionen”. Habilitationsschrift, Angew. Physik, Goethe Universität Frankfurt, 1998.
- [45] U. Ratzinger, R. Tiede. “Status of the HIF RF LINAC study based on H-mode cavities”. Nuclear Instruments and Methods in Physics Research Section A: Accelerators, Spectrometers, Detectors and Associated Equipment 415.1: 229-235, 1998.
- [46] R. Tiede. “Simulationswerkzeuge für die Berechnung hochintensiver Ionenbeschleuniger”. PhD dissertation, Goethe Universität Frankfurt, 2009.
- [47] U. Ratzinger, E. Nolte, R. Geier, N. Gaertner, H. Morinaga. “The upgraded Munich linear heavy ion postaccelerator”. Nuclear Instruments and Methods in Physics Research Section A: Accelerators, Spectrometers, Detectors and Associated Equipment 263, no. 2: pp.261-270, 1988.
- [48] R. Tiede, A. C. Sauer, H. Podlech, S. Minaev, U. Ratzinger, G. Clemente. “LORASR code development. No. CARE-Conf-2006-006-HIPPI, 2006.
- [49] M. Vretenar. “The radio-frequency quadrupole”. CERN Accelerator School (CAS), Course on High Power Hadron Machines, Bilbao, Spain, CERN Yellow Report CERN-2013-001, pp.207-223, 2011.
- [50] I. M. Kapchinsky, V. A. Tepliakov. “Linear ion accelerator with spatially homogeneous focusing”. Prib. Tekh. ksp 2: 119, 1970.
- [51] A. Schempp. “Radio-Frequency Quadrupole Linacs”. CERN Accelerator School on Radio Frequency Engineering, Seeheim, Germany, May 2000, CERN Yellow Report CERN-2005-003, pp.305-314, 2005.
- [52] A. W. Chao, K. H. Mess, M. Tigner, F. Zimmermann. “Handbook of Accelerator Physics and Engineering”. Handbook of Accelerator Physics and Engineering (2nd Edition). Edited by A. W. Chao et al. Published by World Scientific Publishing Co. Pte. Ltd., 2013. ISBN-9789814415859 1, 2013.
- [53] J. Schmidt. “Tuning and optimization of the field distribution for 4-rod radio frequency quadrupole linacs”. PhD dissertation, Goethe Universität Frankfurt, 2014.
- [54] E. D. Courant and H. S. Snyder. “Theory of the alternating-gradient synchrotron”. Annals of physics 3, no. 1 (1958): 1-48, 1958.

- [55] L. Groening, W. Barth, R. Berezov, G. Clemente, P. Forck, R. Hollinger, A. Krämer, C. Mühle, J. Pfister, G. Schreiber, J. Trüller, W. Vinzenz, C. Will, N. Chauvin, O. Delferrere, O. Tuske, B. Koubek, H. Podlech, U. Ratzinger, A. Schempp, R. Tiede, B. Laun, J. Lesrel, C. S. Simon. “Status of the FAIR 70 MeV Proton Linac”. 26th International Linear Accelerator Conference, LINAC12, Tel Aviv, Israel, 927-929, 2013.
- [56] G. Clemente, W. Barth, L. Groening, S. Yaramishev, R. Brodhage, U. Ratzinger, R. Tiede. “The FAIR proton LINAC: The first LINAC based on a room temperature CH-DTL”. Proc. ICFA ABDW HB2010, Morschach, Switzerland, 2010.
- [57] W. Barth. “Technical design report FAIR proton LINAC”. technical report, FAIR, 2008.
- [58] G. Clemente, U. Ratzinger, H. Podlech, L. Groening, R. Brodhage, and W. Barth. “Development of room temperature crossbar-H-mode cavities for proton and ion acceleration in the low to medium beta range”. Physical Review Special Topics-Accelerators and Beams 14, no. 11: 110101, 2011.
- [59] N. Chauvin, O. Delferrere, P. Girardot, Y. Gauthier, J. L. Jannin, A. Lotode, A. Maugueret et al. “Status of the FAIR proton source and LEBT”. Proc. of LINAC2014, Geneva, Switzerland, 2014.
- [60] C. Ullmann, R. Berezov, J. Fils, R. Hollinger, V. Ivanova, O. Kester, W. Vinzenz, Germany N. Chauvin, and O. Delferrere. “Status and computer simulations for the front end of the proton injector for FAIR”. Proc. of IPAC2014, Dresden, Germany, 2014.
- [61] L. Groening, W. Vinzenz, W. Barth, R. Höllinger, L. Dahl, P. Spädtke, and S. Yaramishev. “A Dedicated 70 MeV Proton LINAC for the Antiproton Physics Program of the Future Facility for Antiproton and Ion Research (FAIR) at Darmstadt”. No. CARE-CONF-2004-018-HIPPI, 2004.
- [62] U. Ratzinger, G. Clemente, C. Commenda, H. Liebermann, H. Podlech, R. Tiede, W. Barth, and L. Groening. “A 70-MeV proton LINAC for the FAIR facility based on CH-cavities”. Linear Accelerator Conference (LINAC2006), Knoxville, Tennessee, USA, 2006.
- [63] H. Koziol. “Beam diagnostics for accelerators”. No. CERN-PS-2001-012-DR. CERN, 2001.

- [64] T. Sieber, M. Almalki, C. Dorn, J. Fils, P. Forck, R. Haseitl, W. Kaufmann, W. Vinzenz, M. Witthaus, B. Zwicker. “Beam diagnostics layout for the FAIR proton LINAC”. Proc. of LINAC2014, Geneva, Switzerland, 2014.
- [65] P. Forck, P. Kowina, D. Liakin. “Beam position monitors”. CERN accelerator school on beam diagnostics (2008). CERN Yellow Report CERN-2009-005, pp.187-228, 2009.
- [66] R. E. Shafer. “Beam position monitor sensitivity for low- β beams”. Beam Instrumentation Workshop, vol. 319, no. 1, pp. 303-308. AIP Publishing, 1994.
- [67] P. Strehl. “Beam Instrumentation and Diagnostics, Particle Acceleration and Detection”. Springer, Berlin, 2006.
- [68] J. R. Buck, A. V. Oppenheim, R. W. Schafer. “Discrete-time signal processing”. Prentice Hall, 1999.
- [69] J. W. Cooley, J. W. Tukey. “An algorithm for the machine calculation of complex fourier series”. Mathematics of computation, 19(90):297.301, 1965.
- [70] R. G. Lyons. “Understanding digital signal processing”. Pearson Education, 2010.
- [71] P. Forck, De. Antoni, G. Clemente, P. Galdemard, L. Groening, M. Kaiser, W. Kaufmann et al. “Design of the BPM system for the FAIR proton LINAC”. GSI Scientific Report, 2010.
- [72] M. Almalki, P. Forck, W. Kaufmann, P. Kowina, G. Clemente, L. Groening, R. Singh et al. “Layout of the BPM system for proton LINAC at FAIR and the digital methods for beam position and phase monitoring”. Proc. of IBIC2013, Oxford, UK, 2013.
- [73] <http://global.kyocera.com/>.
- [74] M. Almalki, P. Forck, J. Fils, W. Kaufmann, O. Kester, P. Kowina, C. Krüger, T. Sieber, C. Simon. “Mechanical Design for the proton LINAC BPMs Inter-tank Section”. GSI Scientific Report 2013, 2014-1, p.320, 2014.
- [75] R. Brodhage. “Particle distribution with space charge using LORASAR code”. private communication, 2013.
- [76] W. Ackermann, W. F. O. Müller, and T. Weiland. “Unintentional coupling of accelerating field to the BPM pickups”. GSI Scientific Report 2011. p. 312, 2012.

- [77] W. Ackermann. “GSI cavity simulation”. presentation, 2012.
- [78] W. Ackermann, G. Benderskaya, T. Weiland. “State of the art in the simulation of electromagnetic fields based on large scale finite element eigenanalysis”. International COMPUMAG Society Newsletter 17, no. 2 (2010): 2012.
- [79] H. Brunswig, O. Zinke, A. Vlcek, H. L. Hartnagel, and K. Mayer. “Hochfrequenztechnik 2: Elektronik Und Signalverarbeitung”. Springer, 1998.
- [80] W. Vinzenz. “Durchgriff der HF-spannung ins strahlrohr der CH-struktur”. private communication, 2013.
- [81] www.cst.com.
- [82] T. Weiland. “A discretization model for the solution of Maxwell’s equations for six-component fields”. Archiv Elektronik und Uebertragungstechnik 31 : 116-120, 1977.
- [83] Krietenstein, Bernd, R. Schuhmann, P. Thoma, T. Weiland. “The perfect boundary approximation technique facing the big challenge of high precision field computation”. Proc. of the XIX International Linear Accelerator Conference (LINAC98), Chicago, USA, pp. 860-862, 1998.
- [84] D. M. Pozar. “Microwave Engineering”. John Wiley & Sons, 2009.
- [85] G. A. Mesyats. “Pulsed Power”. Springer Science & Business Media, 2007.
- [86] J. F. White. “High frequency techniques: an introduction to RF and microwave engineering”. John Wiley & Sons, 2004.
- [87] Yin, Yan, E. Schulte, T. Ekelof. “Recovery of CTF beam signals from a strong wakefield background”. Proceedings of Particle Accelerator Conference 1995, vol. 4, pp. 2622-2624. IEEE, 1995.
- [88] Simrock, Stefan, W. Cichalewski, M. K. Grecki, G. W. Jablonski, W. J. Jalmuzna. “Universal controller for digital RF control”. Proc. of EPAC2006, TUPCH190, 2006.
- [89] M.E. Angoletta, “Digital Low Level RF”. EPAC06, Edinburgh, Scotland, p.1847, 2006.

- [90] T. Schilcher. “RF applications in digital signal processing”. CERN Accelerator School on Digital Signal Processing, CERN Yellow Report CERN-2005-003, pp.249-283, 2008.
- [91] G. Vismara. “Signal processing for beam position monitors”. Proc. of AIP Conference 2000, vol.546, no. CERN-SL-2000-056-BI, pp. 36-60, 2000.
- [92] M. Hoffmann. “Digital signal processing mathematics”. CERN Accelerator School on Digital Signal Processing, CERN Yellow Report CERN-2005-003, pp.11-72, 2008.
- [93] A. V. Oppenheim, S. A. Willsky, S. H. Nawab. “Signals and systems”. Prentice Hall, 1996.
- [94] J. Belleman. “From analog to digital”. CERN Accelerator School on Digital Signal Processing, CERN Yellow Report CERN-2005-003, pp.131-165, 2008.
- [95] W. Kaufmann. “Detailed Specification of the Beam Position Monitor (BPM) and Time Of Flight (TOF) system for the proton LINAC”. GSI Beam Diagnostic Department, 2012.
- [96] B. Baricevic, J. S. Menart, M. Znidarcic, A. Kosicek. “Evaluation of new generation heavy particle beam diagnostics instrumentation”. Proc. of IPAC2011, San Sebastin, Spain, 2011.
- [97] Instrumentation Technologies. “Hadron beam phase and position processor, user manual”. SI-5250 Solkan Slovenia, Velika Pot 22, 2013.
- [98] Instrumentation Technologies, Conceptual Design Report (CDR). SI-5250 Solkan Slovenia, Velika Pot 22, 2013.
- [99] MATLAB. version 7.10.0 (R2010a). The MathWorks Inc., Natick, Massachusetts, 2012.
- [100] Lecroy waverunner 6200a datasheet, “test equipment solutions datasheet”.
- [101] P. Lemut. “Libera single pass Hadron (Libera SPH) evaluation measurements at rf 325 MHz”. Instrumentation Technologies, Solkan Slovenia, 2013.
- [102] M. Plum. “Interceptive beam diagnostics-signal creation and materials interactions”. In Beam Instrumentation Workshop 2004, volume 732, pages 23.46, 2004.

List of Figures

1	Der FAIR Protonen Linearbeschleuniger ist dargestellt mit den Einbauorten der 14 BPMs mit einem Strahlrohrdurchmesser von entweder \varnothing 30 mm (neun Stellen) oder \varnothing 50 mm (fünf Stellen). Vier BPMs werden in der Zwischentank-Sektion zwischen den Beschleunigungskavitat installiert. Weiterhin ist Strahlenergie an spezifischen Positionen angegeben.	v
2	Links: Das technische Layout der Zwischentank-Sektion. Rechts: Berechnung der Abschirmeigenschaften in Abhangigkeit von der Lange des Kegels (rot) fur eine festgehaltene Lange des Rohres sowie in Abhangigkeit der zylindrischen Rohrlange (blau) fur feste Kegellange. Fur die Berechnungen mit dem CST elektro-statischen Solver wurde die erste Driftrohre innerhalb der Kavitation auf eine Spannung von 425 kV gelegt.	vi
3	Der erste Prototyp der BPM Installation fur die Zwischentank-Sektion mit vier Button-Elektroden.	vi
4	Die Optimierung des so genannten Munz- und Kegel-Designs mit dem CST PARTICLE STUDIO zeigt, dass die hochsten Signale mit einem Munze Radius von 6,25 mm (Button Dicke = 0,5 mm) und einem Kegel Radius von 5,5 mm erzeugt werden.	vii
5	Links: Vertikale Strahlpositionskurven unter Verwendung des Differenz-durch-Summe-Verfahrens bei unterschiedlichen Auswertefrequenzen mit $\beta = 0,27$ fur eine Bunchlange von $\sigma_{bunch} = 150$ ps. Rechts: Die BPM Positionskarte.	viii

6	Darstellung der Signalphasenmessung für verschiedene Bunchformen. Dargestellt ist auf der y -Achse die Phasenmessung mit der Libera SPH, die Phase der Fourier-Transformation für einen einzelnen Bunch und für eine Folge von Bunchen, sowie die Phase mit Hilfe der I/Q-Demodulation als Funktion der im Zeitbereich aufgezeichneten Bunche charakterisiert durch den jeweiligen Nulldurchgang $Zc - Zc_1$ (Bunchform 1 dient als Referenz).	x
1.1	Layout of the existing GSI facility (UNILAC, SIS18, ESR) on the left and the planned FAIR facility on the right (proton linac, SIS100 and SIS300, CR, RESR, NESR, the rare isotope production target, Super-FRS, the antiproton production target, HESR, FLAIR and the experimental stations for plasma physics and atomic physics	4
2.1	The time structure of the beam at a pulsed linac and the definition of different currents (according to [33]).	12
2.2	Schematic of the axial electric field $E_z(r, z)$ in an accelerating gap	13
2.3	A cylindrical and a pillbox cavity (left). The distribution of electric and magnetic fields in an empty cylindrical cavity excited in $TE_{111} - mode$ in IH-cavity and $TE_{211} - mode$ in CH-cavity (right), from [34].	15
2.4	The resulting electric field in adjacent gaps in a cavity : a) $2\pi - mode$ or $\beta\lambda$ structure, b) $\pi - mode$ or $\beta\lambda/2$ structures.	16
2.5	The IH cavity $TE_{11(0)} - mode$ (left) [42]. The CH cavity $TE_{21(0)} - mode$ of the FAIR proton linac injector operates at 325 MHz (right) (Courtesy of R. Brodhage).	17
2.6	Accelerating field lines in an accelerating gap of length g	18
2.7	On top the accelerating electric field E_z as a cosine function of the phase ϕ where the synchrous phase ϕ_s is shown as negative value. Some trajectories in the longitudinal phase space are shown including the separatrix and the limit trajectory for stable motion (a). The potential function has its minimum at $\phi = \phi_s$ illustrating the meaning of the synchrous phase in the phase space (b). The particle motion in the longitudinal phase space for zero synchrous phase 0° (c) and the longitudinal potential well (d) as applied in KONUS beam dynamics.	21

2.8	A schematic representation of KONUS period in H-DTL. A KONUS period consists of a transverse focusing element, longitudinal focusing and matching section with negative synchronous phase (rebunching) and the main acceleration stage with a multi gap 0° - synchronous phase.	22
2.9	a quadrupole field of the RFQ (left). A sinusoidal modulated electrode form acceleration cells with a mid to mid distance of $\beta\lambda/2$ where the bunch to bunch distance is $\beta\lambda$ (right) [from [53]].	23
2.10	The conceptual layout of the FAIR proton linac	24
2.11	3D Sketch of the CCH power prototype	26
2.12	The scheme for the diagnostics along the proton LINAC.	27
3.1	Scheme of inductive (left) and capacitive (right) signal extraction [67].	31
3.2	Extracting a signal from moving charged particles bunches by measuring the image current flowing with reverse polarity to the beam current (left). Four electrodes mounted orthogonally around the vacuum pipe aperture to measure how far the beam is from each in order to determine beam position (right).	32
3.3	Schematic plot for the relativistic increase of the transverse electric field (left). The electric field lines of charged particle beam moving at much less than the speed of light and close to the speed of light (right)	32
3.4	The equivalent circuit of the electrostatic pickup device.	34
3.5	The beam current $I_{beam}(t)$ is Fourier transformed resulting $\tilde{I}_{beam}(\omega)$ and then multiplied by $Z_t(\omega)$ to give the frequency dependent voltage $\tilde{V}_{im}(\omega) = Z_t(\omega) \cdot \tilde{I}_{beam}(\omega)$. Next, the inverse Fourier transformation is applied to get back the time dependent signal $V_{im}(t)$	34
3.6	Principle of the Time-of-flight (TOF) measurements using two BPMs	38
4.1	The FAIR proton LINAC, showing the positions of the 14 BPMs for the 30 mm (nine locations) or 50 mm (five locations) beam pipe aperture. Four of these BPMs are located in the intertank section between two coupled cavities. The proton beam energy is given as well	43

4.2	95% transversal beam envelope along the proton LINAC in XZ plane (Up). 95% beam energy envelope with respect to the bunch center (Middle). 95% beam phase envelope with respect to the bunch center (Down).	44
4.3	Phase space distribution at three locations. The output phase space after RFQ at 3 MeV (Up), The output phase space at after Q4 at 20 MeV (Middle), the output phase space after Q12 at 70 MeV (Down).	45
4.4	The phase projection (histogram) of the particles distribution after the RFQ, Q4 and Q12.	46
4.5	rms bunch length after each quadrupole along the proton LINAC.	48
4.6	Bunch length versus drifts by linear calculations after different focussing elements along the proton LINAC (RFQ, Q2 to Q12).	48
4.7	Bunch length at several drifts after Q4, Q8 and Q12 calculated by linear calculations (left) and produced from LORASR code with space charge after Q4, Q8 and Q12 (right).	49
4.8	The technical layout of the intertank section	50
4.9	Distribution of the electric field strength showing the coupling of the rf-field to the BPM (courtesy of W. Ackermann, TU Darmstadt)	51
4.10	A 3D model of four button electrodes and first cavity gap created in CST electro-static solver	52
4.11	Shielding properties as a function of the length of the cone l_{cone} (red) for a fixed length of the tube or as a function of the cylindrical tube length l_{tube} (blue) for fixed cone length. For the electro-static solver the first drift tube is set to 425 kV. Sketch of the geometry and electric field distribution are shown in the up-right corner.	52
4.12	Voltage (left) and electric field (right) distribution along z axis. The BPM (tube diameter of 30 mm) is connected to the CCH entrance flange (20 mm) by a conical section with a length of 20 mm	53
4.13	Damping versus the distance from the gap (left). Voltage on z axis versus the distance from the gap (right)	54
4.14	CAD drawing in mm unit of the BPM housing and the flange	55

4.15	Scheme of commercial button from Kyocera	56
4.16	Kyocera pickup final assembly.	56
4.17	The first BPM prototype with four Kyocera buttons (left). The Kyocera pickup and CAD drawing of the BPM with the flange (right)	57
5.1	The potential distribution on a cut-plane in the pickup structure including a button electrode and an inner conductor set to 1 V	62
5.2	The change in pickup capacitance as a function of button thickness at fixed gap size 0.5, 1.0 and 1.5 mm (left) and as a function of gap size at fixed button thickness 0.5, 1.5 and 2.5 mm (right).	63
5.3	3D model of Kyocera button.	64
5.4	The excitation and the reflected signals (left) and the corresponding TDR plots (right) for three button geometries; (2.5 mm thickness, 0.5 mm gap)→ Kyocera button , (1.5 mm thickness, 1 mm gap) and (0.5 mm thickness, 1.5 mm gap).	65
5.5	The TDR measurements for the 14 mm diameter Kyocera button pickup using a Tektronix analog TDR signal source. The reflection coefficient $\rho_V \approx 400 m\rho$ causes an impedance step down to $\approx 20 \Omega$	66
5.6	Smith chart produced by the simulations of the 14 mm diameter Kyocera button pickup showing the impedance at different frequencies	67
5.7	Smith chart obtained from the measurement for the 14 mm diameter Kyocera button pickup showing the impedance at different frequencies	68
5.8	A 3D model of the pick-up monitor as simulated in CST Particle Studio (left). The absolute value of the electric field of a bunch of $\sigma = 100$ ps long and $\beta = 0.37$ (right)	68
5.9	a discrete port located at the end of the electrodes feedthroughs (left). Electric field (middle). Magnetic field (right).	69

5.10	Two Gaussian-shaped signals demonstrate the beam current in the time domain (a) are simulated with CST Particle studio (Wakefield solver). They are multiplied by the transfer impedance of the pickup structure to give the time domain voltage output on the pickup coaxial port (c). Post-processing can be performed to obtain Fourier components of the input signal (b) and (d) output signals.	70
5.11	BPM output voltage from a single port in time (up) and frequency (down) domains versus mesh size. The beam parameter are $\beta = 0.08, 0.27$ and $0.37, \sigma = 150$ ps, 1nC bunch charge.	71
5.12	BPM output voltage from a single port in time (left) and frequency (right) domains with three button geometries ($\beta = 0.37, 1\text{nC}$ bunch charge). . . .	72
5.13	BPM output voltage from a single port in time (left) and frequency (right) domains with three button geometries ($\beta = 0.27, 1\text{nC}$ bunch charge). . . .	73
5.14	BPM output voltage from a single port in time (left) and frequency (right) domains with three button geometries ($\beta = 0.08, 1\text{nC}$ bunch charge). . . .	74
5.15	A comparison between the amplitudes of induced signals for three designs.	74
5.16	Design of one cone button (left). A 3D model of the pickup monitor as simulated in CST Particle Studio (right).	75
5.17	The optimization of the coin and cone designs using the CST PARTICLE STUDIO Wakefield solver showing that the higher signals are obtained as cone button diameter is 5.5 mm and coin button diameter is 6.25 mm. . . .	76
5.18	The excitation and the reflected signals (left) and the corresponding TDR plots (right) for the cone design, the optimized Kyocera design and the Kyocera design.	77
5.19	BPM output voltage from a single port in time (left) and frequency (right) domains for the cone design, the optimized Kyocera design and the Kyocera design. ($\beta = 0.37, \sigma = 100$ and 300 ps, 1nC bunch charge).	78
5.20	BPM output signal from one pickup for 30 mm and 50 mm beam pipe in time (left) and frequency (right) domains mounted at different depths. The beam parameters are $\beta = 0.37, \sigma = 100$ ps, 1nC bunch charge.	79
5.21	Signal amplitudes for 30 and 50 mm beam pipe at different pickup depth .	80

5.22	The change in signal maximum (solid lines) and minimum (dashed lines) as a function of button diameter for different β values in 50 mm (left) and 30 mm (right) beam pipes. ($\sigma = 100$ ps, 1nC bunch charge).	81
5.23	The ratio between the signal maximum (solid lines) and minimum (dashed lines) as a function of the button area for different β values in 50 mm (left) and 30 mm (right) beam pipes, same type of CST simulations as shown in figure 5.22 ($\sigma = 100$ ps, , 1nC bunch charge).	81
5.24	Effect of the advanced longitudinal (left) and transverse (right) electric field at an observation point $R = 30$ mm from the beam axis for different velocities of a point-like charge. For $t = 0$ the closest approach is reached (from [33]).	83
5.25	The legend shows the bunch length σ_b and the plotted signals represent output voltage from a single port in time (left) and frequency (right) domains for $\beta = 0.08$	84
5.26	The legend shows the bunch length σ_b and the plotted signals represent output voltage from a single port in time (left) and frequency (right) domains for $\beta = 0.27$	85
5.27	The legend shows the bunch length σ_b and the plotted signals represent output voltage from a single port in time (left) and frequency (right) domains for $\beta = 0.37$	85
5.28	The change in the maximum and the minimum values of the pickup signal versus bunch length σ_b	86
5.29	The Fourier components of the pickup signals at five harmonics of the bunching frequency versus bunch length.	86
5.30	The relationship between the bunch length σ_b and the length of the pickup signal σ_s extracted from the time difference between the minimum and the maximum values of the pickup signal.	87
5.31	The linear limit calculated for $\beta = 0.08, 0.27$ and 0.37 by applying a linear fit on the curve shown in figure 5.30 from $\sigma_b = 560$ ps for both $\beta = 0.27$ and 0.37 and $\sigma_b = 720$ for $\beta = 0.08$	87

5.32	Vertical beam position sensitivity curves calculated using the delta-over-sum method at different frequency harmonics with $\beta = 0.08$ for a bunch length = 150 ps (left). The BPM position map from $S_0(f)$ values taken for each frequency harmonic from table 5.3 (right). The BPM position map from $S_0(325\text{ MHz})$ fixed at the fundamental frequency (middle).	90
5.33	Vertical beam position sensitivity curves calculated using the delta-over-sum method at different frequency harmonics with $\beta = 0.27$ for a bunch length = 150 ps (left). The BPM position map from $S_0(f)$ values taken for each frequency harmonic from table 5.3 (right). The BPM position map from $S_0(325\text{ MHz})$ fixed at the fundamental frequency (middle).	91
5.34	Vertical beam position sensitivity curves calculated using the delta-over-sum method at different frequency harmonics with $\beta = 0.37$ for a bunch length = 150 ps (left). The BPM position map from $S_0(f)$ values taken for each frequency harmonic from table 5.3 (right). The BPM position map from $S_0(325\text{ MHz})$ fixed at the fundamental frequency (middle).	91
5.35	Vertical beam position sensitivity curves calculated at $\beta = 0.37$ using the delta-over-sum method for the fundamental frequency and the fourth harmonic for different bunch length $\sigma = 60$ and 150 ps (left). The numerical errors evaluation from the subtraction of $\Delta U(f)/\Sigma U(f)$ values for the same harmonic at $\sigma_b = 150$ ps and 60 ps.	91
5.36	The BPM phase deviation from four pickups as a function of the beam displacement in the vertical direction (left) and in the diagonal direction (right).	93
6.1	The mechanism of impulse-train sampling in which the continuous signal $u(t)$ with a frequency f is sampled at regular intervals $T_s = 1/f_s$.(from [68])	99
6.2	Frequency domain representation of sampling in time domain. Spectrum of the original signal $U(t)$ (a). Fourier transformation of the sampling function $S(t)$ (b). Fourier transformation of the sampled signal with $\omega_s > 2\omega$ (c).(from [92])	100
6.3	Phasor representation of RF signal where $I = A_{RF} \cos(\varphi_{RF})$ (in-phase component) and $Q = A_{RF} \sin(\varphi_{RF})$ (quadrature-phase component)(from [90]).	101

6.4	In the undersampling technique, a band-limited signal U_{RF} is sampled with a lower sample rate f_s and down-converted to Intermediate Frequency (IF) f_{IF}	102
6.5	The principle of under-sampling as performed for BPM signal (upper panel). The resulting IQ values of the RF signal $f_{RF} = 325$ MHz sampled at $f_s = 4/11 f_{RF} = 118$ MHz, corresponding to 4 samples over 11 bunches. The periodicity of the digital data is 33.82 ns corresponding to a bandwidth of 29.56 MHz for the reconstructed IF signal (down panel).	103
6.6	The digital I/Q demodulator producing I and Q data stream includes a numerically controlled oscillator (NCO) generating a stream of sine and cosine samples with a 90° phase shift and frequency matches to IF signal (from [90]).	104
6.7	Input signal is digitized (1^{st} digital down conversion) with sampling rate $f_s = 118$ MHz locked to the acceleration frequency $f_{RF} = 325.224$ MHz. The output down-converted IF signal is ~ 28.22 MHz and the I/Q data is retrieved by applying a numerically controlled oscillator (NCO) (2^{nd} digital down conversion).	105
6.8	The Libera SPH phase and position processing and block diagram	107
6.9	The input matching at 108.408 MHz and 216.8 MHz frequencies are at -25 dB and -21 dB return loss.	108
6.10	The beamline optical elements in the High Charge State Injector (HLI) at UNILAC consisting of a re-buncher, quadrupole doublet, dipole and a diagnostic section.	109
6.11	The capacitive BPM of a 50 mm aperture and a 20 mm electrode length at the GSI-LINAC (left). The phase probe in 50Ω geometry and a 35 mm inner diameter as used for the longitudinal bunch observation and phase measurements at the 108 MHz GSI-LINAC (right).	110
6.12	Single electrode amplitude (up), the difference over sum of H and V in % and the calculated beam position for $S = 10 \%/mm$ (middle), the corresponding phase reading with respect to 108.408 MHz and the histogram (bottom) during one macro-pulse (train of data sets of $129 \mu s$ and $1 \mu s$ time resolution).	111

6.13	Three different bunch shapes (200 samples) at 44 dB amplification as displayed on a 10 GSa/s oscilloscope (LeCroy Waverunner 6200A).	112
6.14	Libera SPH position variation on x and y coordinates for three bunch shapes as a function of the signal level (left) and the standard deviation of the measurements (right).	113
6.15	Libera SPH phase reading variation for three bunch shapes as a function of the signal level (left) and the standard deviation of the measurement (right).	113
6.16	Experimental setup where the BPM's signal is split into Libera SPH unit and a 10 GSa/s oscilloscope (LeCroy Waverunner 6200A) and both systems were triggered to the rf master oscillator	115
6.17	Libera SPH phase reading for six bunch shapes @ 44, 32 and 20 dB amplification using BPM signals (left) and the standard deviation (right).	116
6.18	Libera SPH phase reading for six bunch shapes @ 44, 32 and 20 dB amplification using phase probe signal (left) and the standard deviation (right).	116
6.19	Beam position variation on x and y coordinates as a function of the signal level for six bunch shapes (left) and the standard deviation of the measurements (right).	117
6.20	A single bunch of two different shapes recorded by the oscilloscope were extracted, spline interpolated and shifted to zero (a). The signal is zero padded in both sides with 28672 each zeros to create a curve with a total point of 2^{16} (b). The FFT is applied to produce the amplitude (c) and phase (d) spectrum.	118
6.21	A stream of two different shapes stored by the oscilloscope (up). The FFT is applied on 45000 bunches to produce the amplitude peaks spectrum (the amplitude spectrum nearly coincided) (middle) and the corresponding phase spectrum (down).	119
6.22	A stream of shape 1 recorded by a 10 GSa/s oscilloscope. The I and Q signals and its spectrum which contain the continues quadrature phase term of the signal.	120

6.23	A stream of shape 2 recorded by a 10 GSa/s oscilloscope. The I and Q signals and its spectrum which contain the continuous quadrature phase term of the signal.	121
6.24	Two bunch curves (shape 1 and shape 2) recorded by a 10 GSa/s oscilloscope (LeCroy Waverunner 6200A).	122
6.25	The time domain signals and the zero-crossing points (left). The magnification of the zero-crossing region showing the arrival time differences showing 400 ps maximum arrival time difference.	122
6.26	The jitter of zero-crossing points for 500 bunches for RF signal and the histogram (left). FFT applied on zero-crossing jitter for 1000 bunches showing a systematic behaviour with a repetition of ~ 40 MHz (right). . .	124
6.27	The jitter of zero-crossing points for 500 bunches for bunch shape 1 and the histogram (left). FFT applied on zero-crossing jitter for 1000 bunches showing a systematic behaviour with a repetition of ~ 7.5 MHz (right). . .	125
6.28	The jitter of zero-crossing points for 500 bunches for bunch shape 2 and the histogram (left). FFT applied on zero-crossing jitter for 1000 bunches showing a systematic behaviour with a repetition of ~ 7.5 MHz (right). . .	126
6.29	The signal phase - arrival time - obtained from the time domain processing $Z_c - Z_c(1)$ (shape 1 as reference) is represented on the x -axis and the Libera SPH phase reading and phase calculated from FFT (for a single bunch and for a stream of bunches) and I/Q demodulation are assigned on the y -axis.	128
6.30	The variation of x and y coordinates of the beam obtained by Libera SPH (solid lines) and SEM grid (dashed lines) where x is always fixed at 0 and y is varied from -5 to 5 mm in 2 mm steps.	129
6.31	The measured profiles of SEM grid displaying the horizontal profile (left) and the vertical (right) in mm for five locations.	130
8.1	Vertical beam position sensitivity curves (left) and the BPM position maps (right) at different frequency harmonics at CCH1 entrance ($\beta = 0.08$, $\sigma_{bunch} = 150ps$).	138

8.2	Vertical beam position sensitivity curves (left) and the BPM position maps (right) at different frequency harmonics after one half CCH1 ($\beta = 0.12$, $\sigma_{bunch} = 150ps$).	138
8.3	Vertical beam position sensitivity curves (left) and the BPM position maps (right) at different frequency harmonics at CCH2 entrance ($\beta = 0.15$, $\sigma_{bunch} = 150ps$).	139
8.4	Vertical beam position sensitivity curves (left) and the BPM position maps (right) at different frequency harmonics after one half CCH2 ($\beta = 0.18$, $\sigma_{bunch} = 150ps$).	139
8.5	Vertical beam position sensitivity curves (left) and the BPM position maps (right) at different frequency harmonics at CCH3 entrance ($\beta = 0.22$, $\sigma_{bunch} = 150ps$).	139
8.6	Vertical beam position sensitivity curves (left) and the BPM position maps (right) at different frequency harmonics after one half CCH3 ($\beta = 0.24$, $\sigma_{bunch} = 150ps$).	139
8.7	Vertical beam position sensitivity curves (left) and the BPM position maps (right) at different frequency harmonics after CCH3 ($\beta = 0.27$, $\sigma_{bunch} = 150ps$).	140
8.8	Vertical beam position sensitivity curves (left) and the BPM position maps (right) at different frequency harmonics after CH4 ($\beta = 0.30$, $\sigma_{bunch} = 150ps$).	140
8.9	Vertical beam position sensitivity curves (left) and the BPM position maps (right) at different frequency harmonics after CH5 ($\beta = 0.33$, $\sigma_{bunch} = 150ps$).	140
8.10	Vertical beam position sensitivity curves (left) and the BPM position maps (right) at different frequency harmonics after CH6 ($\beta = 0.37$, $\sigma_{bunch} = 150ps$).	140
8.11	Vertical beam position sensitivity curves (left) and the BPM position maps (right) at different frequency harmonics in the inflation region ($\beta = 0.37$, $\sigma_{bunch} = 150ps$).	141

List of Tables

1.1	A comparison between some of the most recent worldwide LINAC accelerators	8
2.1	The FAIR Proton Linac Parameters	25
2.2	The main parameters of the second CCH cavity of the FAIR proton injector	26
4.1	Parameters for the BPM system for the LINAC	43
5.1	Simulation parameters and button geometries	72
5.2	Geometry parameters of the designs and the resulting electrical properties	78
5.3	BPM sensitivities S_0 from the simulation in unit $(\%/mm)$ at the center position	90
6.1	σ_{Z_c} of zero-crossing jitter within one macro-pulse for six bunch shapes in ps unit and the corresponds to degree @ 108.4 MHz ($9.22 \text{ ns} = 360^\circ$) . . .	126
6.2	A linear regression fit and the goodness of the fit for different methods . .	127
8.1	The BPM sensitivity S_0 from the simulation in unit $(\%/mm)$ at the center position for all CCH and CH output velocities and the relevant beam pipe diameter along the proton LINAC.	141

Acknowledgements

This work would not have been possible without help and guidance of many individuals that have contributed to the project in different ways. I will humbly attempt to acknowledge them here.

I am thankful to Prof. Dr. Oliver Kester for accepting me as a PhD student in his group. I thank him for the encouragement and intellectual freedom he provided me throughout the past three years. I have got used to the friendly atmosphere established in the group and his enthusiasm. It is an honour to be one of his PhD students. I thank Prof. Dr. Holger Podlech for his recommendations and his support as a member of my HGS-HIRe PhD committee.

I would like to express my sincere gratitude to Dr. Peter Forck, who provided me with a seemingly endless amount of support, encouragement, recommendations and constructive criticism. Without his numerous scientific contributions and permanent support this thesis would not be in its present form. He especially helped with his careful and detailed inputs in the writing phase of this dissertation. Additionally, he gave me the opportunity to work in his group and introduced me to the field of beam diagnostics, such an interesting research topic. I have been able to benefit from his scientific knowledge and experience throughout the years of my studies. His balanced way of supervision enabled me, while having clear objectives, to work independently and take important decisions myself, which is something to appreciate on a personal level.

I would like to thank Dr. Thomas Sieber, who provided insightful comments and a lot of stimulating discussions on various stages of this work. I appreciate all his assistance with solving some problems. My special thanks goes to W. Kaufmann and K. Krüger for their help in numerous aspects of my research and for the continual willingness to lend a hand in the lab. I always enjoyed working together with them and I am deeply grateful to them for teaching me to a lot of practical things in RF technology and on the BPM electronics. I have been trying to learn from them as much as possible and I look forward to further collaborations.

I would like to express my gratitude and very deep appreciation to Dr. Rahul Singh for his many useful discussions, critical consideration and for the constructive critiques of my work from an early stage. Moreover, a few key ideas in the supplement of this dissertation have been based on his knowledge and valuable advice. I would like to thank Dr. Piotr Kowina for our useful discussions and his ideas, especially for the designing

of the BPM prototype. I owe special thanks to Thomas Reichert and Jan Latzko for helping me as I started to learn the CST program and for transferring to me various bits of invaluable arcane knowledge about the program.

I would like to thank the entire Beam Instrumentation group at the GSI. Our group leader, Dr. Marcus Schwickert is gratefully acknowledged for his continuous encouragement. By name I wish to thank Tobias, Kevin, Oleksandr, Michael, Rainer, Carsten, Christoph, Tino, Timo, Andreas, Beata, Serban, Hansjörg, Vladimir, Alice, Yulia, Benjamin, Frank, Christiane and Febin. These people have made me feel welcome and they were always willing to assist, support and offer help in various matters over the course of my doctorate.

Many thanks go to the administrators of Helmholtz Graduate School for Hadron and Ion Research (HGS-HIRE) for the perfect coordination of courses and the structured PhD studies: Prof. Dr. Henner Büsching, Ms. Johanna Dilley, Ms. Helena Correa dos Santos, Ms. Sylke Schneider, Dr. Sascha Vogel and Dr. Gerhard Burau. I attended several scientific courses and activities which helped me a lot, not only to improve my scientific knowledge for my PhD study but also to establish a network of friends from various fields.

I would like to thank KACST and the Saudi Arabian government for giving me one of their scholarships and for their financial support to attend conferences and courses. Many thanks goes to the administrators of the Saudi Cultural Bureau in Berlin and KACST in Riyadh, namely Dr. Hamoud Alharbi, Dr. Lamya Alnaim and Basmah Zrida, for their help during my studies and for their cooperation and support to improve my English in England. I also thank Linda Bishop and Dr. Hasan Alfaify for taking care of me during my time in England.

My previous education, especially during my MSc. degree, enabled me to go that step further. I would like to express my sincerest gratitude to Prof. Dr. S. EL-Kameesy, who directed my energy and enthusiasm without a clear view of the perspectives, when I was a student at the King Saud University. I appreciate the fascinating discussions with him, which sometimes even extended outside the field of science.

Words are inadequate to express my sincere thanks to Prof. Dr. Reinhard Dörner for his support in the most critical time of my doctorate. Prof. Dr. Ratzinger deserves a special mention and thanks for his valuable lectures that I attended as well as for the help and valuable suggestions in the rf-leakage calculations. I feel highly indebted to my friend in Frankfurt university Dr. Ali Almomani for his discussions and valuable explanations in

the accelerator field and other related topics which helped me a great deal to capture the key concepts and develop meaningful insights. I want to express my gratitude to Dr. Dirk Lipka from DESY for his valuable hints, suggestions and ideas in CST simulations and for his time spent reading and commenting on the chapter 5 draft. I want to thank Janet Schmidt very much for her help with her translation of the Zusammenfassung. I want also to thank the people from GSI proton linac department, namely Robert Brodhage for providing me with the required inputs related to the BPM mechanical design and for Dr. Lars Groening for his discussions with me. I want to thank Dr. Gianluigi Clemente for providing me with the input files for the CST simulation to extend my calculations.

It was a pleasure to spend an interesting experience of a few months in the first year of my doctoral study with Dr. Kurt Stiebing, Dr. Dirk Tiedemann and Frederik King. I want to thank all of them for their help and support when I first came to Germany. I also want to thank other people I met here in Germany for the wonderful friendship they offered me. By names I would like to thank Husam Al Omari, Alhussain Abuhoza, Khalid Teilab, Samir Amar, Frederik, Sabrina, Marcel, Anja, Carmen, Cathrina and AlJioani.

Many thanks to the collaborators directly involved in this project from CEA-Saclay, France and Instrumentation Technologies, Solkan, Slovenia. Our mutual communication helped me a great deal in solving a lot of the problems related to the layout of the BPM system and I look forward to further collaborations. I must acknowledge the contribution of Instrumentation Technologies for the development of the Libera SPH unit and for the valuable information and fruitful discussions about the BPM digital signal processing, namely B. Baricevic, M. Znidarcic, R. Hrovatin, P. Lemut. A special thanks goes to C. Simon and Jerome Fils from CEA-Saclay, France for the participation in the BPM prototype manufacturing and for the productive discussion in the CST calculations.

I dreamt of sharing this success with my father who has been an endless source of support for me but, unfortunately, he died two years ago, so I am unable to do so. My deepest gratitude goes to my mother for her patience and other family members for their constant encouragement and moral support. A heartfelt thanks goes to my wife, Dalal, for her great emotional support, love and her loving care for our two children. Surely, it was not possible for me to complete this dissertation without her standing beside me through this journey.

Goethe-Universität Frankfurt
Mohammed Almalki

Curriculum Vitae (CV)

Mohammed Almalki, MSc.



1. PERSONAL DATA

- Date of Birth: 01.07.1981
- Place of Birth: Bani Malk
(Saudi Arabia)
- Nationality: Saudi
- Marital Status: Married
- Address (Business): GSI Helmholtzzentrum für Schwerionenforschung GmbH
Beam Instrumentation (LOBI)
Planckstraße 1, 64291 Darmstadt
- E-mail: m.almalki@gsi.de
- Phone: + 49 (0) 6159 71 1523

2. EDUCATION

- 01.01.2011 - 00.00.2015 : Ph.D student with Prof. Dr. Oliver Kester at IAP - Goethe-Universität Frankfurt, scholarship by KACST, Riyadh, Saudi Arabia (Disputation date: 00.00.2015). Title: “Beam Position Monitor System for Proton-LINAC for FAIR”.
- 14.09.2002 - 29.01.2006 : Master’s degree of Science in physics with Prof. Dr. S. EL-Kameesy in Nuclear Physics group at College of Science, King Saud University, Riyadh, Saudi Arabia. Title: “Nuclear structure properties of some deformed nuclei in the region of mass number $A \sim 150$ ”, grade: 4.45/5.
- 07.09/1997 - 16.06.2001 : Bachelor degree of Science in the field of physics, College of Science, King Saud University, Riyadh, Saudi Arabia, grade: 3.25/5.
- 1994 to 1997 : General Secondary Education, Naamah Secondary School, Jazan, Saudi Arabia, grade: 90/100.

3. PROFESSIONAL EXPERIENCE

- 10.12.2007 - 15.10.2009 : Lecturer, King Abdulaziz City for Science and Technology (KACST), National Center for Mathematics & Physics, Riyadh, Saudi Arabia.
- 11/09/2006 - 19/1/2008 : Lecturer collaborator, part time for teaching the practical experiments in college of science - physics department at King Saud University, Riyadh, Saudi Arabia.
- 02.09.2001 - 10.12.2007 : Teacher (all levels of high secondary schools), Ministry of Education, Riyadh, Saudi Arabia.

4. TRAINING

- CERN Summer Student Program 2008, project at ATLAS unit, B. Di. Girolamo (beniamino.di.girolamo@cern.ch), 01.06 - 05.08.2008.
- A guest scientist at Max Planck Institut, Heidelberg University, QUASAR group, C. Welsch (c.p.welsch@liverpool.ac.uk). Simulation of the Electrostatic Storage Ring using OPERA (TOSCA) software, 08.01 - 05.03.2009.
- MATLAB Fundamentals, Eindhoven, Netherland, 10 - 12.01.2012.
- CST PARTICLE STUDIO and MICROWAVE STUDIO Training, CST Office, Darmstadt, Germany, 11 - 12.06.2013.

5. COURSES

- The Joint US-CERN-Japan-Russia Accelerator School (JAS) course on “Synchrotron Radiation & Free Electron Lasers”, Erice, Italy, 05.04.2011 - 16.04.2011.
- CERN Accelerator School in “High Power Hadron Machines”, Bilbao, Spain, 24.05 - 02.06.2011.
- HGS-HIRe for FAIR Lecture Week in Accelerator Physics, “Introduction to Accelerator Physics”, Puidoux, Switzerland, 09 - 15.10.2011.
- HGS-HIRe for FAIR Lecture Week in Atomic Physics, “Precision experiments with stored highly charged ions”, Kloster Marienburg, Germany, 13 - 18.11.2011.
- HGS-HIRe for FAIR Lecture Week in Nuclear Structure, “Nuclear Structure Physics: Gamma-ray Spectroscopy”, Kloster Höchst, Germany, 15 - 20.04.2012.
- HGS-HIRe for FAIR Lecture Week in Accelerator Physics, “Linear Accelerators”, Kloster Höchst, Germany, 23 - 28.09.2012.

- Third Joint Helmholtz-Rosatom School, “Aspects of the new FAIR accelerator complex”, Crete, Greece, 06 - 13.10.2013.
- Joint HGS-HIRe & RS-APS Lecture Week in Atomic & Laser/Plasma Physics, “X-ray spectroscopy as diagnostic tool in atomic and plasma physics”, Buchenau, Germany, 16 - 20.11.2014.
- CERN Accelerator School in “Accelerators for Medical Applications”, Vösendorf, Austria, 26.05 - 05.06.2015.

6. ACTIVITIES & WORKSHOPS

- HGS-HIRe Graduate Days, Mainz, Germany, 25 - 26.10.2012.
- The 9th Libera Workshop, Smartno, slovenia, 25.04.2013.
- HGS-HIRe Graduate Days, Worms, Germany 24 - 25.10.2013.
- HGS-HIRe Graduate Days, Gründau, Germany 23 - 24.10.2014.
- Lander-Tag, IAP - Goethe Universität, Frankfurt, Germany, 24.10.2014
- HIC for FAIR Workshop “Current Topics in Accelerator-, Astro- and Plasma-physics”, Lungau, Austria, 23.02 - 01.03.2014.
- HIC for FAIR Workshop “Current Topics in Accelerator-, Astro- and Plasma-physics”, Riezlern, Austria, 08 - 14.03.2015.

7. CONFERENCES

- The 23rd Particle Accelerator Conference (IPAC09), Vancouver, Canada, 2009.
- DPG spring meeting, Dresden, Germany, 2013.
- DPG spring meeting, Frankfurt, Germany, 2014.
- DPG spring meeting, Heidelberg, Germany, 2015.
- The 2nd International Beam Instrumentation Conference (IBIC 13), Oxford, UK, 2013
- The 5th International Particle Accelerator Conference (IPAC14), Dresden, Germany, 2014.

8. SCIENTIFIC MEETINGS

- The 5th Meeting of the p-LINAC BPM Collaboration, 03.12.2013, CEA Saclay, France.

- Meeting of the Libera Single PASS H (Libera SPH), BPM Data Acquisition for p-LINAC, Slovenian In-Kind Contribution, 09.04.2013, GSI Darmstadt, Germany.
- The 6th Meeting of the p-LINAC BPM Collaboration, 03.02.2014, GSI Darmstadt, Germany.
- The 7th Meeting of the p-LINAC BPM Collaboration, 12.11.2014, CEA Saclay, France.

9. PUBLICATIONS

- M. El-Ghazaly, V. Aleksandrov, **M. Almalki**, A. Almandil, A. Papash, S. Schmid, C. Welsch, “Layout of a Versatile Injector for a Low-energy Experimental Platform at KACST”. Applied Mathematics & Information Sciences, vol 3, issue 3 pp, 2009.
- M. El-Ghazaly, **M. Almalki**, A. Papash, C. Welsch, “A Highly Flexible Low Energy Ion Injector at KACST”. Proceedings of Particle Accelerator Conference (IPAC09), Vancouver, Canada, 2009.
- M. El-Ghazaly, **M. Almalki**, A. Papash, C. Welsch, “Layout of an Electrostatic Storage Ring at KACST”. Proceedings of Particle Accelerator Conference (IPAC09), Vancouver, Canada, 2009.
- S. Behery, A. Almukhum, **M. Almalki**, S. Alshemmeri, A. Mandil, A. Alrashdi, M. El-Ghazaly, “A Flexible Low Energy Ion injector at KACST”, ESD 2011, Gatlinburg, Tennessee, 2011.
- **M. Almalki**, P. Forck, W. Kaufmann, P. Kowina, R. Singh, C. Krüger, B. Baricevic, M. Znidarcic, R. Hrovatin, “Test of Digital Electronics for the p-LINAC BPMs at UNILAC”, GSI Scientific Report 2013-1, 227 p. (2013).
- **M. Almalki**, P. Forck, W. Kaufmann, P. Kowina, G. Clemente, L. Groening, R. Singh, C. Krüger, C. Simon, W. Ackermann, B. Baricevic, M. Znidarcic, R. Hrovatin, P. Lemut, “Layout of the BPM system for proton LINAC at FAIR and the digital methods for beam position and phase monitoring”. Proc. of IBIC2013, Oxford, UK, 2013.
- **M. Almalki**, P. Forck, J. Fils, W. Kaufmann, O. Kester, P. Kowina, C. Krüger, T. Sieber, C. Simon. “Mechanical Design for the proton LINAC BPMs Inter-tank Section”. GSI Scientific Report 2013, 2014-1, p.320, 2014.

- T. Sieber, **M. Almalki**, C. Dorn, J. Fils, P. Forck, R. Haseitl, W. Kaufmann, W. Vinzenz, M. Witthaus, B. Zwicker. “Beam diagnostics layout for the FAIR proton LINAC”. Proc. of LINAC2014, Geneva, Switzerland, 2014.
- **M. Almalki**, R. Brodhage, P. Forck, W. Kaufmann, O. Kester, P. Kowina, T. Sieber, J. Balaguer, P. Girardot, C. Simon, “The mechanical design of the BPM inter-tank for p-Linac at FAIR”, IPAC14, Dresden, p. 3474, 2014.
- C. Simon, V. Bellego, **M. Almalki**, P. Forck, W. Kaufmann and T. Sieber, “Numerical Calculations for the FAIR Proton LINAC BPMs”, Proceedings of IBIC2014, Monterey, CA, USA, 2014.
- **M. Almalki**, P. Forck, W. Kaufmann, T. Sieber, P. Kowina, C. Krüger, O. Kester, C. Simon, “Extensive CST Simulations for the p-LINAC BPMs”, GSI Scientific Report 2014, (2015).

10. RELEVANT EXTERNAL TALKS

- “System Design for the FAIR Proton LINAC BPMs”, DPG spring meeting 2013, Dresden, Germany, March 2013.
- “Beam-Based Test for Libera Single Pass H at UNILAC at GSI”, DPG spring meeting 2013, Dresden, Germany, March 2013.
- “A development of BPM for P-LINAC at FAIR”, DPG spring meeting 2013, Frankfurt, Germany, March 2014.
- “CST Calculations for the layout of a button BPM system for the FAIR proton LINAC”, DPG spring meeting 2015, Heidelberg, Germany, March 2015.
- “Mechanical Design for the Inter-tank Section for FAIR p-linac BPM”, 5th Meeting of the p-Linac BPM Collaboration, CEA Saclay, France, December 2013.
- “Drifting Calculations and beam Dynamics at BPMs along p-LINAC”, 6th Meeting of the p-Linac BPM Collaboration, GSI Darmstadt, Germany, February 2014.
- “CST STUDIO SUITE Simulation for Button BPMs for p-linac for FAIR”, 7th Meeting of the p-Linac BPM Collaboration, CEA Saclay, France, November 2014.
- “Beam-Based Test for Libera Single Pass Based Test for Libera Single Pass H at UNILAC at GSI”, The 9th Libera Workshop, Smartno, slovenia, April 2013.

- “Layout of the BPM System for p-LINAC at FAIR & the Digital Methods for Beam Position and Phase Monitoring”, HIC for FAIR Workshop, Lungau, Austria, March 2014.
- “CST Calculations for the Layout of a Button BPM System for the FAIR Proton Linac”, HIC for FAIR Workshop, Riezlern, Austria, March 2015.

11. RELEVANT POSTERS

- “Layout of the BPM System for p-LINAC at FAIR and the Digital Methods for Beam Position and Phase Monitoring”, IBIC13, Oxford, UK, September 2013.
- “Digital Methods for Beam Position and Phase Monitoring for the BPM System for p-LINAC at FAIR ”, HGS-Hire Graduate days, Worms, Germany, October 2013.
- “The mechanical design of the BPM inter-tank for p-Linac at FAIR”, IPAC14, Dresden, Germany, June 2014.

12. COMPUTER SKILLS

- Windows Operating System.
- C++ (Basic).
- Origin, MATLAB (very good), Mathematica, Microsoft Office.
- Experience in running several codes, TRACE-3D code, SIMION Ion and Electron Optics Simulator, CST Program, OPERA software.

13. LANGUAGE SKILLS

- Arabic (native)
- English (very good)
- German (good)

14. REFERENCES

- Prof. Dr. Oliver Kester (O.Kester@gsi.de), IAP - Goethe Universität, Frankfurt, Germany, Max-von-Laue Str. 1, 60438 Frankfurt am Main, Germany.
- Prof. Dr. Holger Podlech (H.Podlech@iap.uni-frankfurt.de), IAP - Goethe Universität, Frankfurt, Germany, Max-von-Laue Str. 1, 60438 Frankfurt am Main, Germany.

- Dr. Peter Forck (P.Forck@gsi.de), GSI, Planckstr. 1, 64291 Darmstadt, Germany.
- Dr. Thomas Sieber (T.Sieber@gsi.de), GSI, Planckstr. 1, 64291 Darmstadt, Germany.